University of Nottingham
UK | CHINA | MALAYSIA

Damage modelling in fibre-reinforced composite laminates using phase field approach

A Thesis Submitted to The University of Nottingham
for the Degree of Doctor of Philosophy

Udit Pillai, M.Sc., B.E.(Hons.)

Aug 2021

Abstract

Thin unidirectional-tape and woven fabric-reinforced composites are widely utilized in the aerospace and automotive industries due to their enhanced fatigue life and impact damage resistance. The increasing industrial applications of such composites warrants a need for high-fidelity computational models to assess their structural integrity and ensure robust and reliable designs. Damage detection and modelling is an important aspect of overall design and manufacturing lifecycle of composite structures.

In particular, in thin-ply composites, the damage evolves as a result of coupled in-plane (membrane) and out-of-plane (bending) deformations that often arise during critical events, e.g., bird strike/ hail impact or under in-flight service loads. Contrary to metallic structures, failure in composites involves complex and mutually interacting damage patterns, e.g., fibre breakage/ pull-out/ bridging, matrix cracking, debonding and delamination. Providing high-fidelity simulations of intra-laminar damage is a challenging task both from a physics and a computational perspective, due to their complex and largely quasi-brittle fracture response. This is manifested by matrix cracking and fibre breakage, which result in a sudden loss of strength with minimum crack openings; subsequent fibre pull-outs result in a further, although gradual, strength loss. To effectively model this response, it is necessary to account for the cohesive forces evolving within the fracture process zone. Furthermore, the in-

teraction of the failure mechanisms pertinent to both the fibres and the matrix necessitate the definition of anisotropic damage models.

In addition, the failure in composites extends across multiple scales; it initiates at the fibre/ matrix-level (micro-scale) and accumulates into larger cracks at the component/ structural level (macro-scale). From a simulation standpoint, accurate prediction of the structure's critical load bearing capacity and its associated damage thresholds becomes a challenging task; accuracy necessitates a fine level of resolution, which renders the corresponding numerical model computationally expensive. To this point, most damage models are applied at the meso-scale based on local stress-strain estimates, and considering material heterogeneity. Such damage models are often computationally expensive and practically inefficient to simulate the failure behaviour in real-life composite structures. Moreover at the macro-scale, the effect of local stresses is largely minimised, which necessitates definition of a homogenised failure criterion based on global macro-scale stresses.

This thesis presents a phase field based MITC4+ (Mixed Interpolation of Tensorial Components) shell element formulation to simulate fracture propagation in thin shell structures under coupled membrane and bending deformations. The employed MITC4+ approach renders the element shear- and membrane- locking free, hence providing high-fidelity fracture simulations in planar and curved topologies. To capture the mechanical response under bending-dominated fracture, a crack-driving force description based on the maximum strain energy density through the shell-thickness is considered. Several numerical examples simulating fracture in flat and curved shell structures which display significant transverse shear and membrane locking are presented. The accuracy of the proposed formulation is examined by comparing the predicted critical fracture loads against analytical estimates.

To simulate diverse intra-laminar fracture modes in fibre reinforced composites, an anisotropic cohesive phase field model is proposed. The damage anisotropy is captured via distinct energetic crack driving forces, which are defined for each pertinent composite damage mode together with a structural

tensor that accounts for material orientation dependent fracture properties. Distinct 3-parameter quasi-quadratic degradation functions based on fracture properties pertinent to each failure mode are used, which result in delaying or suppressing pre-mature failure initiation in all modes simultaneously. The degradation functions can be calibrated to experimentally derived strain softening curves corresponding to relevant failure modes. The proposed damage model is implemented in Abaqus and is validated against experimental results for woven fabric-reinforced and unidirectional composite laminates. Furthermore, a dynamic explicit cohesive phase field model is proposed to capture the significantly nonlinear damage evolution behaviour pertinent to impact scenarios. A strategy is presented to combine the phase field and the cohesive zone models to perform full composite-laminate simulations involving both intra-laminar and inter-laminar damage modes.

Finally, the developed phase field model is employed within the framework of a multiscale surrogate modelling technique. The latter is proposed to perform fast and efficient damage simulation involving different inherent scales in composites. The technique is based on a multiscale FE^2 (Finite Element squared) homogenisation approach, however the computationally expensive procedure of solving the meso- and macro-scale models simultaneously is avoided by using a robust surrogate model. The meso-scale is defined as a unit-cell representative volume element (RVE) model, which is analysed under a large number of statistically randomised mixed-mode macro-strains, applied with periodic boundary conditions. The complex damage mechanisms occurring at the meso-scale are captured using the anisotropic cohesive phase field model, and the homogenised stress-strain responses post-damage evolution are obtained. These anisotropic meso-scale fracture responses are used to train the Polynomial Chaos Expansion (PCE) and Artificial Neural Network (ANN) based surrogate models, which are interrogated at the macro-scale using arbitrary macro-strain combinations. The accuracy of the surrogate model is validated against high-fidelity phase field simulations for a set of benchmarks.

Acknowledgements

First and foremost, I would like to express my deep and sincere gratitude to my academic supervisor, Dr. Savvas Triantafyllou for providing me an opportunity to work on this exciting research topic and his immense support and guidance throughout this project. His patience, enthusiasm, vision and profound scientific knowledge have deeply inspired me during the execution and writing of this thesis. Even after he left Nottingham, he remained a member of the supervisory team and was the acting primary supervisor for this project.

I am also thankful to the remaining members of the supervisory team, Dr. Panos Psimoulis, Prof. Ian Ashcroft and Dr. Dimitrios Chronopoulos, for providing me with valuable advice and suggestions from time to time. I am grateful to my industrial supervisors Dr. Yasser Essa and Dr. Federico Martin de la Escalera, and other colleagues at the Aernnova Engineering Division for sharing their technical expertise and industrial insights, which have greatly enhanced my practical understanding and shaped the work performed during this PhD project.

I sincerely thank my examiners Prof. José Antonio Reinoso Cuevas and Dr. Jelena Ninić for their constructive feedback which has helped improving the overall quality of this thesis. I would like to acknowledge the generous financial support provided by European Union's Horizon 2020 research and innovation programme under the Marie Sklodowska-Curie SAFE-FLY Project,

Grant Agreement No. 721455. I express my gratitude to the University of Nottingham for providing a supportive environment to conduct my research.

It had been a privilege working with Dr. Bassam Elsaied from University of Bristol; I would like to thank him for introducing me to the field of surrogate modelling and providing extensive supervision during and after my academic secondment with him. A special thanks to my colleagues at SAFE-FLY for all the insightful technical discussions and help throughout the project.

And finally, a big thanks to my family and my wife for always standing by me and supporting me in every possible way. Without you all, it would have been impossible to push through this challenging yet, exciting phase of my life. Thanks for always being there, and I owe it all to you.

Contents

List of Acronyms

ALM	Augmented Lagrange Method
ANN	Artificial Neural Network
APDL	ANSYS Parametric Design Language
B.C.	Boundary Conditions
BEM	Boundary Element Method
BFGS	Broyden–Fletcher–Goldfarb–Shanno
CDF	Cumulative Density Function
CDM	Continuum Damage Mechanics
CFM	Computational Fracture Mechanics
CLT	Classical Lamination Theory
CSM	Cohesive Segments Method
CT	Compact Tension
CZM	Cohesive Zone Modelling
DENT	Double-Edge Notched Tension
DOF	Degree Of Freedom
EOS	Equation of State
FEM	Finite Element Method
FETI	Finite Element Tearing and Interconnecting
FFM	Finite Fracture Mechanics
FPZ	Fracture Process Zone
GFEM	Generalized Finite Element Method

IGA	IsoGeometric Analysis
LEFM	Linear Elastic Fracture Mechanics
LFRC	Long Fibre Reinforced Composites
LHC	Latin HyperCube
LM	Levenberg-Marquardt
MITC	Mixed Interpolation of Tensorial Components
MKL	Math Kernel Library
MM	Meshless Method
MPC	Multi Point Constraints
MPM	Material Point Method
MSE	Mean Squared Errors
MsFEM	Multiscale Finite Element Method
NURBS	Non-Uniform Rational B-spline
PARDISO	Parallel Direct Solver
PBC	Periodic Boundary Condition
PCE	Polynomial Chaos Expansion
PDE	Partial Differential Equation
PDF	Probability Density Function
PFM	Phase Field Method
PU	Partition of Unity
RHS	Right Hand Side
RTM	Resin Transfer Moulding
RUL	Remaining Useful Life
RVE	Representative Volume Element
SBFEM	Scaled Boundary Finite Element Method
SBIGA	Scaled Boundary IsoGeometric Analysis
SFRC	Short Fibre Reinforced Composites
SHM	Structural Health Monitoring
SIF	Stress Intensity Factor
SPH	Smooth Particle Hydrodynamics
SSA	Stacked Shell Approach

SSE	Sum of Squared Errors
STF	Spread-Tow Fabric
UD	Uni-Directional
UEL	User Element subroutine for Abaqus/Standard
UMAT	User Material subroutine for Abaqus/Standard
VCCT	Virtual Crack Closure Technique
VEM	Virtual Element Method
VUMAT	User Material subroutine for Abaqus/Explicit
XFEM	eXtended Finite Element Method
XIGA	eXtended IsoGeometric Analysis

List of Tables

List of Figures

List of Algorithms

1 Introduction

Modelling of damage initiation and propagation plays an important role in assessing the structural integrity and the load-bearing capacity of composite structures. This chapter highlights the context and motivation of the current work performed on multiscale damage modelling of composites, and outlines the key research objectives and original contributions of this PhD thesis.

1.1 Motivation and Problem Statement

The demand for lighter, stronger, and durable structures has led to the widespread application of fibre-reinforced composites, especially in the aerospace and the automobile industries. Driven by an ever-increasing requirement for resilient and more sustainable structures, composites are nowadays extensively used in manufacturing various aircraft parts. Composites provide a compatible solution, which demonstrates favourable strength to weight, stiffness to weight and damping to weight ratios as compared to standard aluminium and in general metallic alloys [30, 31]. However, the inherent complex microstructure of composites significantly affects and largely determines their performance and resilience. This however poses important challenges both in terms of manufacturing as well as material characterization and numerical simulation.

Amongst the various types of advanced composites, e.g. laminated, sandwich, braided, auxetic, ceramic, metal matrix and nano composites, laminated

composites are the most frequently used in the aerospace industry [32], as their layups can be conveniently tailored for specific applications. These composites are fabricated using multiple stacked plies, each comprising fibres reinforced within matrix materials, and bonded with adhesive layers. However, a principle drawback with conventional thick-ply laminated composites is their poor through-thickness performance especially during impact scenarios [33]. This has particularly steered the focus of aerospace industry since past 15 years towards thin-ply laminated composites, which provide remarkably improved transverse strength under static, fatigue and impact loadings along with significant reduction in laminate weight [33]. Based on the fibre reinforcement direction, the thin-ply composites can be broadly classified into two types, i.e. unidirectional or woven fabric-reinforced composites, in which the fibres are aligned either in single or multiple directions respectively, within each ply of the laminate.

Compared to unidirectional composites, traditional woven fabric-reinforced composites exhibit lower in-plane stiffness and critical strength due to the waviness effect of the fibres [5, 34]. However, woven fabric-reinforced composites possess higher through-thickness damage resistance and are capable of dissipating higher energy during critical impact events. These properties render them an ideal solution for improving the crash-worthiness of composite structures. Amongst these, thin uni-directional (UD) tapes and woven-fabric reinforced composites manufactured using the spread-tow technology [35] are a special class of advanced composites that have been of significant research interest in the past few years. In spread tow technology, the fibres are spread into thinner, wider and flatter reinforcements thereby producing ultra lightweight composites with improved stiffness, strength and impact resistance [2]. In particular, spread-tow textile fabrics are known to possess a significantly lower fibre-waviness, reduced resin-rich pockets, lower crimp angles and crimp frequencies [36]. As a result, a higher number of thin plies with smaller relative fibre angles can be stacked within the same laminate width, resulting in composites with increased toughness against interfacial fracture between the plies

[37, 38]. Spread-tow fabrics (STF) provide a similar mechanical performance as that of a cross plied unidirectional ply, but with improved drapability and delamination resistance [39].

To ensure increased strength and resilience of the manufactured parts, the possibility of defects should be detected in the early stages of the design cycle so that preventive measures could be taken. Materials have inherent discontinuities at the micro-mechanical level, which accumulate to cracks and evolve across multiple scales before the part is completely fractured. Hence, it is important to evaluate the failure and damage characteristics, and subsequently load carrying capacity, of composite laminate structures to create an economic and reliable design [40–42]. Depending upon the loading conditions and micro-structure, various failure modes may emerge and lead to the complete damage of laminates; numerical simulation can provide an improved fundamental understanding of this process, which is crucial for the practical design of composite structures [42, 43].

In the aerospace industry, damage modelling is often performed to assess structural integrity of different aircraft composite structures and their capability in sustaining critical bird-strike and hail-impact events. An effective damage modelling approach must predict not only the critical fracture loads, but also capture the post damage-initiation and progressive crack propagation behaviour accurately. Damage modelling in composites is a challenging task due to the variety of the mutually interacting damage mechanisms involved. Furthermore, the damage in composites extends across multiple scales, which necessitates implementation of efficient multiscale modelling techniques that effectively characterise the material behaviour and failure characteristics at all inherent size scales.

Spread-tow composite laminates typically contain a large number of significantly flatter and thinner plies stacked over each other. Modelling such thin plies with conventional hexahedral elements becomes a challenging task as it requires multiple element layers through each ply's thickness to accurately capture its bending response. This results in excessive computational over-

head due to significantly increased number of elements and system degrees-of-freedom (DOFs). In such case, shell elements provide advantage vis-à-vis numerical modelling of composite plies, as they reduce the kinematics to their mid-surface and simulate the complete 3-D mechanical response, whilst requiring much lesser computational efforts. Both membrane and bending response of thin plies can be accurately modelled using shell elements, provided their locking effects are alleviated.

The multiscale damage modelling of composite structures involves analysing the failure behaviour at both macro-scale and micro/meso-scales simultaneously. The macro-scale (structural level) analysis is often performed using effective or homogenized material and fracture properties, however, localized stress-strain estimates are required to effectively characterise the anisotropic damage evolution at meso-scale (ply-level) [44]. In particular, damage modelling at the meso-scale involves predicting diverse families of complex intra-laminar and inter-laminar composite damage mechanisms. This necessitates development of robust damage modelling methods that can simulate these failure modes and resulting crack patterns in an automated and physically-consistent way. Since past 10 years, phase field method (PFM) has emerged as a powerful approach backed by consistent variational framework, for accurately characterising the fracture behaviour in solid materials. PFM does not require crack-paths to be pre-defined and naturally models crack branching and merging, which renders it highly beneficial vis-à-vis modelling of anisotropic and mutually-interacting intra-laminar damage modes. However, a downside of PFM is that it requires finer mesh-size and smaller time-increments to resolve the crack-paths accurately. This presents a notable challenge in effectively using them to analyse large macro-scale composite structures.

1.2 Research Scope

The current work focuses on developing a novel damage modelling method for thin-ply composites, specifically focusing on the spread-tow unidirectional

and spread-tow woven-fabric reinforced variants. The diverse anisotropic composite failure modes, e.g. fibre cracking, fibre pullouts, fibre bridging, plastic shear deformation of the matrix and its cracking under tensile and in-plane shear loads are considered. However, the effects of transverse matrix cracking and subsequent triggering of delamination are ignored as they are negligible and practically suppressed in the case of thin-ply spread-tow composites [45]. The numerical modelling of thin composite plies is performed using degenerated Reissner-Mindlin shell elements based on MITC4+ approach. The implementation assumes small strain deformations, and the damage evolution in flat and curved shell plies subjected to in-plane and out-of-plane deformations is modelled using phase field method. A 3-parameter anisotropic cohesive phase field model is implemented to capture the complex anisotropic intra-laminar composite failure modes. The approach is further extended to full composite laminate analysis, by combining it with cohesive zone method to model inter-laminar failure at the interface. To enable fast and efficient macro-scale simulation of large composite structures, a multiscale technique using machine-learning based surrogate models is applied to minimize the computational costs incurred during composite damage modelling.

1.3 Research objectives

The overarching aim of this project is to propose a novel multiscale damage modelling framework that predicts the vast variety of anisotropic failure modes in thin-ply composites, pertinent to the aerospace industry, in a computationally inexpensive manner. Within this context, the following key research objectives are identified.

1.3.1 Research Objective I

To develop a robust damage modelling approach that simulates damage evolution in thin plies subjected to combined membrane and bending deformations.

The implementation needs to be computationally robust and efficient, and the transverse shear and membrane locking effects must be alleviated for accurate fracture predictions. The accuracy of the numerical model must be established against analytically predicted critical fracture loads. The model should predict realistic crack paths and post-fracture behavior for planar and curved 3-D shell geometries, which display significant transverse shear and membrane locking.

1.3.2 Research Objective II

To deliver a numerical model for high-fidelity intra-laminar damage simulations involving all pertinent failure mechanisms in thin-ply unidirectional tapes and woven fabric-reinforced composites. The model must predict both critical fracture loads and the crack propagation paths accurately, and capture different anisotropic fibre and matrix based damage mechanisms that evolve under mixed-mode stress states. The quasi-brittle fracture behaviour under fibre-dominated failure scenarios must be accurately captured, accounting for the cohesive forces evolving within fracture process zone, which is formed due to fibre pullouts and bridging. The damage model must be flexible enough to control the shape of cohesive softening law, so that the numerical fracture response can be effectively calibrated against experimental results.

1.3.3 Research Objective III

To validate the anisotropic fracture response obtained from numerical damage model against experimental results with a set of benchmark tests. The damage behaviour under different loading scenarios must be analysed, and the predicted crack path, critical fracture loads and the post-fracture response must be compared against experiments.

1.3.4 Research Objective IV

To effectively extend the numerical damage model to perform full composite-laminate analysis involving both intra-laminar and inter-laminar fractures. The extended model must be robust and efficient to simulate the significantly non-linear and dynamic damage evolution behaviour pertinent to impact scenarios.

1.3.5 Research Objective V

To develop a multiscale damage modelling workflow, which facilitates faster and efficient prediction of failure behaviour in large macro-scale composite structures and simulates wide variety of composite failure modes with minimal computational efforts. The multiscale approach must effectively bridge the gap between different inherent scales of composites, i.e. it must be able to capture complex physics of damage evolution at micro/meso scale, and provide fast and efficient failure predictions in large macro-scale structures. The approach should also be easy to implement in commercial software Abaqus for it to be readily implemented for industrial practice, and must involve minimal modifications to the model geometry and mesh.

1.4 Methodology

The scientific methodology employed to accomplish the research objectives listed in Sec. (1.3.1)-(1.3.5) is described as individual work-packages (W.P.) listed below (see also Fig. 1.1).

- ***WP1* :** A phase field modelling framework to simulate brittle fracture in thin-plies using MITC4+ based Reissner-Mindlin shell elements is developed, wherein damage initiates and evolves due to coupled membrane/bending deformations. The employed MITC4+ approach renders the element free of transverse-shear and membrane locking effects, hence providing high-fidelity fracture simulations in planar and curved topolo-

gies. To capture the mechanical response under bending-dominated fracture, a crack-driving force description based on the maximum strain energy density through the shell-thickness is considered. The plane stress assumptions are imposed directly on the tangent constitutive matrix, which results in optimum convergence rates. Several numerical examples providing realistic and accurate fracture predictions in flat and curved shell structures are presented, which display significant membrane and transverse shear locking due to the coupling of membrane and bending deformations. The accuracy of the proposed formulation is examined by comparing the predicted critical fracture loads against analytical estimates both in the isotropic and anisotropic phase field case. The implementation was initially performed in MATLAB, but was later translated into in-house FORTRAN code to improve the computational efficiency.

- ***WP2*** **:** A novel anisotropic cohesive phase field model that can accurately model the vast variety of intra-laminar composite damage modes in thin unidirectional (UD) and woven fabric-reinforced composite laminates is proposed. The model effectively captures the quasi-brittle behaviour exhibited by most thin-ply composites due to fibre-dominated failure mechanisms, and accounts for cohesive forces evolving within the fracture process-zone. The formulation relies on the definition of a single phase field variable that describes each composite failure mode. However, the stresses and elastic properties in each direction are degraded using distinct degradation functions that depend on the critical energy release rate and the fracture stress along that direction. The crack driving state functions and stress-degradation functions corresponding to each individual damage mechanism, e.g., in-plane longitudinal/transverse cracks in the fibres and shear cracks in the matrix, are determined separately. This provides a robust and versatile simulation tool custom fit for materials with strong anisotropies both in their elastic and fracture properties. An anisotropic structural tensor is defined to orient the crack-path in the direction associated with the lower fracture strength and critical energy

release rate. The cohesive phase field model incorporates 3 parameters to provide higher flexibility in controlling the shape of the cohesive softening law and post-peak fracture behaviour. This is important because the damage models in which the initial and the final stages of the cohesive softening curve cannot be controlled independently have only limited capability in accurately predicting the post-fracture material response. The anisotropic cohesive phase field formulations are modified to incorporate elasto-plasticity with isotropic hardening for the in-plane shear behaviour. The implementation is performed in commercial software Abaqus via a user-material (UMAT) subroutine coupled with parallel direct solver (PARDISO) available within Intel's Math Kernel Library (MKL) to solve phase field equations.

- ***WP3* :** The numerical damage model in WP2 is validated against benchmark experiments to demonstrate its effectiveness in accurately capturing damage evolution due to diverse intra-laminar composite damage mechanisms, namely fibre fracture, fibre pull-outs/bridging, and matrix shear cracking. The proposed method is validated for woven carbon and glass fabric-reinforced composites, as well as unidirectional flax-ply composites. The accuracy of predicted crack-paths and overall load deflection response from the numerical model are compared against the experiments.

- ***WP4* :** The phase field damage model is further extended to perform full composite-laminate simulations using a stacked shell approach with multiple shell and surface element layers. The inter-laminar fracture (delamination) is modelled using the cohesive zone surface interaction model available in Abaqus. A dynamic explicit cohesive phase field model is implemented in Abaqus using a VUMAT subroutine to alleviate convergence issues pertinent to highly nonlinear impact-driven damage evolution. The combined damage model is used to perform dynamic explicit simulations for quasi-static indentation and low-velocity impact on a full composite laminate comprising thin woven fabric-reinforced plies.

- ***WP5 :*** A multiscale modelling technique based on surrogate models is proposed to perform simultaneous meso- and macro-scale damage simulations in composites. The approach uses concurrent FE^2 multiscale approach as its foundation, but replaces the computationally inefficient procedure of simulating unit-cell representative volume element (RVE) under periodic boundary conditions at each time-step, with a surrogate model. The surrogate model defines an equivalent constitutive law for the macro-scale simulations, and provides homogenized macro-stress components as outputs for different imposed macro-strain combinations. Two different types of surrogate models based on Polynomial Chaos Expansion (PCE) and Artificial Neural Network (ANN) have been implemented and the predicted fracture responses are compared. A database is first populated by solving large number of meso-scale unit cell RVEs, subjected to averaged macro-strains applied at their boundary under periodic boundary conditions. Damage modelling of fibre and matrix-based failure modes at the meso-scale is performed using the anisotropic cohesive phase field model described in ***WP2***. The homogenized post-fracture stress components are extracted as equivalent macro-scale stresses in response to applied macro-strains. The surrogate models based on ANN and PCE algorithms are then trained with macro-strains and stresses as inputs and outputs respectively; these are used to replace the FE-RVE feedback loop in macro-scale FE^2 analysis, which requires meso-scale RVEs to be solved at each time-increment. The proposed surrogate model is validated against the high-fidelity phase field model using a set of benchmark tests. The multiscale framework is implemented using Abaqus UMAT and Python scripting interface.

1.5 Original contributions

The original contributions of this PhD thesis are

- The phase field modelling approach is applied within the context of

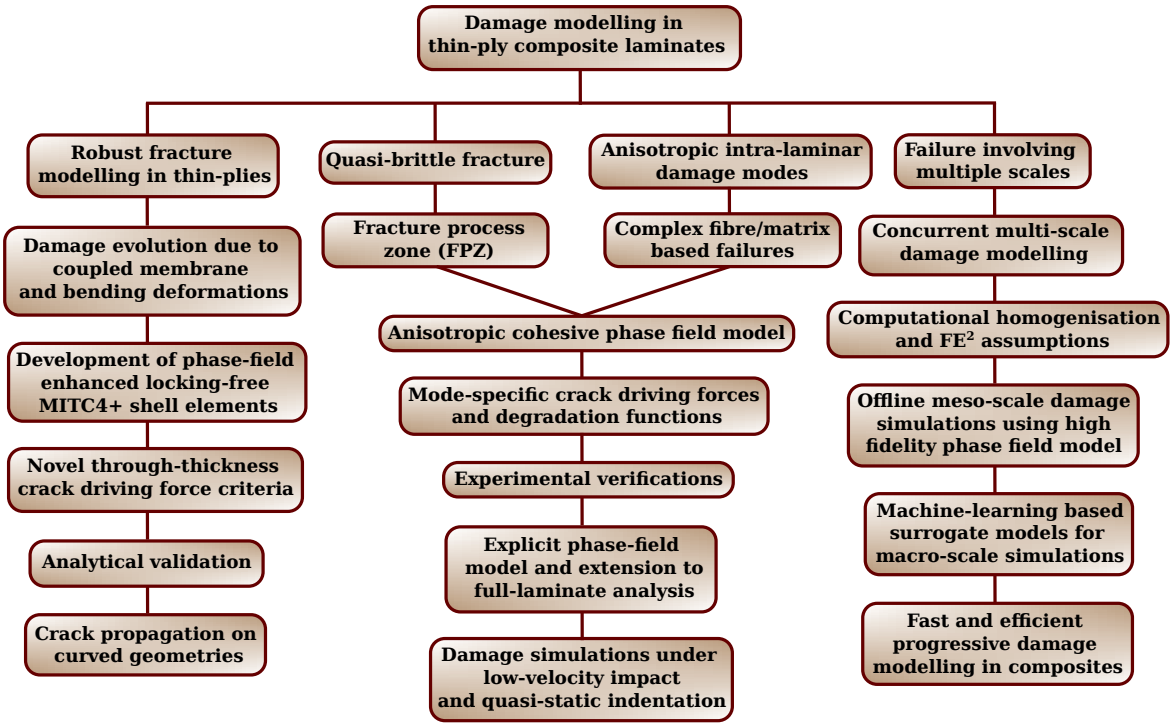

Figure 1.1: Project overview and methodology

MITC4+ based Reissner Mindlin shell elements. Brittle fractures are simulated under coupled membrane and bending deformations for the first time in the literature using phase field method. The method is validated using a set of benchmark tests involving brittle fracture in both flat and curved shell-geometries which display significant transverse shear and membrane locking.

- A novel maximum through-the-thickness crack driving force definition is proposed to obtain accurate fracture predictions for thin-shells in bending-dominated deformations scenarios. The results obtained with the proposed formulation are shown to be highly accurate demonstrating excellent agreement with the analytical estimates.

- A strategy to obtain improved and optimal convergence rates during damage evolution in Mindlin shell elements is provided by imposing the plane-stress assumptions directly on the tangent constitutive matrix.

- A novel anisotropic cohesive phase field damage model is developed to simulate quasi-brittle fractures in composites, and model complex intra-

laminar failure modes in thin-ply composites like fibre cracking, fibre pullouts, fibre bridging and matrix cracking under tensile/ shear loads.

- The anisotropic crack driving forces and degradation functions are defined based on critical fracture stresses and energy release rates corresponding to each composite failure mode. This enables the accurate intra-laminar fracture predictions for plies with arbitrary fibre orientations when these are subjected to mixed loading conditions.

- The plastic deformation of the matrix under shear stresses in woven fabric-reinforced composites, and their subsequent fracture is captured for the first time using an elastic-plastic cohesive phase field model in shear mode.

- Extensive validations are performed against a set of benchmark experiments for intra-laminar damage simulations in woven fabric-reinforced (carbon-fibre/glass-fibre), and unidirectional composite laminates.

- A strategy to calibrate the phase field model with experimental response corresponding to each composite failure mode is suggested. The length-scale independence of the results obtained from the proposed cohesive phase field model is established.

- A new strategy to implement a staggered scheme for phase field fractures in Abaqus is proposed, by coupling the Abaqus user-material (UMAT) subroutine with an external MKL-PARDISO solver to rapidly solve the phase field equations.

- A novel approach to extend the intra-laminar phase field model for performing full-laminate analysis is suggested. A dynamic explicit cohesive phase field model is proposed, which is used to simulate damage evolution in composite laminates subjected to low-velocity impact and quasi-static indentation for the first time.

- The proposed cohesive phase field model is applied in conjunction with a fast and computationally efficient multiscale surrogate modelling method

to accelerate composite damage simulations at different inherent scales.

- A consistent and automated workflow is developed employing PCE and ANN based surrogate models for macro-scale damage simulations. The surrogates are trained using the high-fidelity constitutive response obtained from robust phase field simulations at the meso-scale.

1.6 Publications

The outcomes of this research have been disseminated in a variety of formats as per the list below

1.6.1 Publications in peer-reviewed scientific journals

1. Egger, A., **Pillai, U.**, Agathos, K., Kakouris, E., Chatzi, E., Aschroft, I.A. and Triantafyllou, S.P., 2019. Discrete and phase field methods for linear elastic fracture mechanics: a comparative study and state-of-the-art review. Applied Sciences, 9(12), p.2436

2. **Pillai, U.**, Triantafyllou, S.P., Ashcroft, I., Essa, Y. and de la Escalera, F.M., 2020. Phase-field modelling of brittle fracture in thin shell elements based on the MITC4+ approach. Computational Mechanics, pp.1-20

3. **Pillai, U.**, Triantafyllou, S.P., Essa, Y. and de la Escalera, F.M., 2020. An anisotropic cohesive phase field model for quasi-brittle fractures in thin fibre-reinforced composites. Composite Structures, 252, p.112635.

1.6.2 Publications in International Conference Proceedings

1. Martin De La Escalera, F., Essa, Y., Castello, M.A., **Pillai, U.**, Chiminelli, A., Lizaranzu, M. and Maimi, P., 2018, June. Challenges of Hybrid Laminar Flow Control (HLFC) in Aircraft Design and Manufacturing. In ECCM18-18th European Conference on Composite Materials.

2. **Pillai, U.**, Triantafyllou, S.P., Ashcroft, I., Essa, Y. and de la Escalera, F.M., 2020. A review of damage modelling approaches for layered composites. *In proceedings of Transport Research Arena (TRA)-2020 conference, Helsinki*

1.6.3 Presentations in International Conferences

1. **Pillai, U.**, Triantafyllou, S., Ashcroft, I., Essa, Y. and Martin de la Escalera, F., Phase-field modelling of brittle fracture in thin shell elements based on MITC4+ approach. 6th European Conference on Computational Mechanics ECCM (11-15 June, 2018), Glasgow, United Kingdom

2. **Pillai, U.**, Triantafyllou, S., Ashcroft, I., Essa, Y. and Martin de la Escalera, F., A cohesive phase-field model for intra-laminar damage in fabric composite laminates. VI International Conference on Computational Modeling of Fracture and Failure of Materials and Structures (12-14 June, 2019), Braunschweig, Germany

3. **Pillai, U.**, Triantafyllou, S., Ashcroft, I., Essa, Y. and Martin de la Escalera, F., Intra-laminar Damage Modelling In Fabric Composite Laminates Using Phase-field Method. 7th International Conference on Computational Methods in Structural Dynamics and Earthquake Engineering (24-26 June, 2019), Crete, Greece

4. **Pillai, U.**, Triantafyllou, S., Ashcroft, I., Essa, Y. and Martin de la Escalera, F., An anisotropic cohesive phase-field model for intra-laminar damage in fabric-reinforced composites. 7th ECCOMAS Thematic Conference on The Mechanical Response of Composites (18-20 Sept, 2019), Girona, Spain

5. **Pillai, U.**, Triantafyllou, S., Ashcroft, I., Essa, Y. and Martin de la Escalera, F., Phase Field Modelling For Robust Damage Evolution In Thin Composite Laminates. 12th HSTAM International Congress on Mechanics (22-25 Sept, 2019), Thessaloniki, Greece

6. **Pillai, U.**, Elsaied B., Triantafyllou, S., A Multiscale Surrogate Damage Model for Thin-ply Woven Composite Laminates Based on a Cohesive

Phase-Field Approach. Engineering Mechanics Institute Conference and Probabilistic Mechanics Reliability Conference (26-28 May, 2021), Virtual event

1.7 Thesis layout

The thesis is structured as follows: In Chapter 2, a comprehensive literature survey for the numerical modelling of thin-ply composites, damage modelling approaches and multiscale methods is provided. Chapter 3 discusses the brittle phase field damage model for MITC4+ based Reissner-Mindlin shell elements. In Chapter 4, the anisotropic cohesive phase field model for quasi-brittle intra-laminar damage in thin-ply composites is introduced. Experimental validations for unidirectional and woven-fabric reinforced composites are performed, and the model is subsequently extended to perform full laminate analysis involving both intra and inter-laminar fractures. Chapter 5 proposes the novel multiscale damage modelling approach for fibre-reinforced composites using PCE and ANN surrogate models, followed by final conclusions and discussion on future work in Chapter 6.

2

Literature review

Numerical simulation of damage evolution in thin-ply composite laminates, which are widely used in aerospace structures, involves several challenges. First, thin-ply composites often fail due to combined in-plane (membrane) and out-of-plane (bending) deformations that may occur during day-to-day in-flight operations or critical events, e.g, bird strike and hail impact (Fig. 2.1). To provide a sound assessment of the overall structural integrity of such composites, it is important that the damage model accurately captures such coupled effects and also predict diverse composite failure modes, e.g., ply-cracking and delamination. Second, the damage modelling method must capture the complex anisotropic damage patterns that arise as a result of mutually interacting intra-laminar failure mechanisms in composites. Finally, failure in composites extends across multiple scales; it initiates at the fibre/matrix-level (micro-scale) and accumulates into larger cracks at the component/structural level (macro-scale).

Modelling of damage in fibre-reinforced composite laminates involves two stages at a broader level: 1) Implementation of a robust meso-scale damage model that predicts the diverse failure modes in composites 2) Incorporating a multiscale model to capture the composite damage behaviour based on the global macro-scale stresses. The primary requirement for the meso-scale damage model is that it must be able to accurately predict the diverse intra-laminar and inter-laminar crack propagation patterns, as well as the subsequent re-

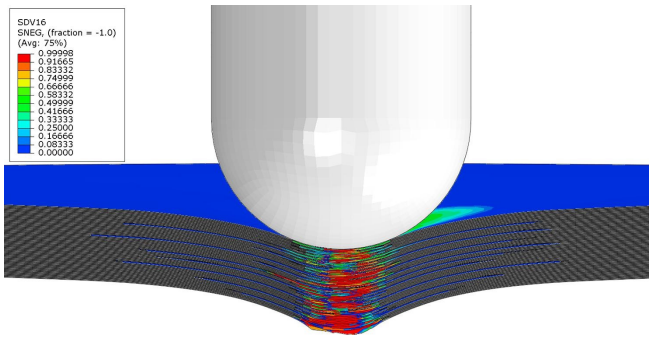

Figure 2.1: Damage evolution in composite laminates due to combined membrane and bending deformations (image reproduced from Soto et al. [2], with permission from Elsevier)

duction in overall laminate strength and load-bearing capacity. Intra-laminar damage occurs due to complex and often interacting failure mechanisms such as fibre fracture, fibre pullouts, fibre bridging, shear and tensile matrix cracks, and debonding, whereas the inter-laminar damage occurs in the form of delamination of composite plies, caused due to failure of adjoining adhesive layers. The interaction between diverse intra-laminar damage modes pertaining to fibre and matrix further necessitates the definition of anisotropic damage models.

This literature survey presents the current state-of-the-art in numerical methods available for damage modelling of materials, specifically fibre-reinforced composites. The advantages and drawbacks/limitations for each method are highlighted and their suitability with regards to the prediction of composite intra-laminar and inter-laminar failure modes is discussed. The review crafts a way to select an appropriate damage modelling approach which is capable of predicting realistic estimates for crack initiation and evolution including precise crack paths and critical stress estimates, across different scales in composites. In addition, different multiscale modelling approaches vis-à-vis composites that incorporate both macro- and meso-scale effects in a unified numerical framework are comprehensively reviewed.

This chapter is organised as follows: Sec. 2.1 reviews the different discretization methods available for damage modelling in solid materials. Sec. 2.2 provides a general overview of numerical modelling of damage in com-

posite laminates and the challenges associated with capturing intra-laminar damage modes in composites. In Sec. 2.2.1, different finite shell element implementations vis-à-vis modelling of thin composite plies are reviewed. Sec. 2.3 provides an overview of different damage modelling approaches, which are reviewed in detail based on discrete and smooth representation of cracks in Sec. 2.4 and 2.5, respectively. Their applicability with regards to modelling intra- and inter-laminar fracture in composites is also discussed. Sec. 2.6 reviews the different multi-scale strategies that are used for numerical modelling of layered composite laminates. The emphasis throughout this survey is on thin-ply composites used in aerospace structures that pose significant challenges with regards to ensuring their structural integrity.

2.1 An overview of discretization methods for damage simulation

Within the different discretization methods proposed till date, the finite element method (FEM) has become the industry standard to solve variety of numerical problems pertinent to computational mechanics. However, FEM faces challenges when characterizing sharp numerical singularities that arise as a result of crack propagation in solid materials. Typically, numerical modelling of damage in solids involves introduction of discontinuities in the displacement fields, which results in a challenging mathematical treatment to achieve automatic initiation, propagation and growth of cracks. In particular, the following select challenges in FEM need to be addressed [17].

- The accurate representation of the crack contour requires the mesh topology to conform with the crack path
- The standard polynomial based FEM shape functions cannot reproduce singular stresses and discontinuous solution fields at the crack tip
- Crack nucleation, branching, merging and modelling of curvillinear crack

paths are algorithmically challenging tasks, and are difficult to treat in a uniform and theoretically sound manner

- Calculation of stress-intensity factors (SIFs) need to be performed using additional post-processing methods

Numerous techniques have been proposed to tackle the issue of singular stress fields around the sharp crack-tip, e.g. remeshing algorithms [46, 47], the introduction of quarter point elements [48], and the evaluation of fracture parameters like SIFs [49, 50]. However, such methods are highly mesh-dependent and computationally expensive, with significant efforts resulting due to repeated remeshing of the structure [17].

To address the issue of mesh-dependency, Zhou and Molinari [51] proposed an enrichment to cohesive element theories in the form of their strength distribution based on modified weakest link Weibull distribution. Meshless methods (MM) were also proposed with an objective of eliminating mesh-dependent problems; they rely on distributed set of nodes and hence, overcome the FEM issues associated with mesh-distortion and remeshing [17]. However, meshless methods require higher-order shape functions and rely on an intricate treatment of essential boundary conditions that leads to increased computational costs in comparison to FEM [52]. The material point method (MPM) offers computational advantage over purely meshless methods as it avoids time-consuming neighbour searching algorithms. In MPM, the solution to governing partial differential equations (PDEs) is performed over a set of material points that move within a non-deformable (Eulerian) computational grid. The crack can be modelled by introducing multiple velocity fields [53] or phase fields [54].

The boundary element method (BEM) [55] was introduced to reduce the mesh-generation complexity by discretizing only the boundary and the crack-front, and solving initial value problems described as boundary integral equations. The method is more accurate as compared to FEM, however, it requires specially tailored numerical methods to solve the resulting discrete equations

[56, 57].

To effectively resolve mesh dependency and treat stress singlarities, the extended finite element method (XFEM) [50, 58] was introduced, which relies on partition of unity to enrich the standard finite element shape functions. Such singular enrichment functions are employed locally in the vicinity of the crack-tip, thereby allowing the representation of cracks independent of underlying mesh and improving the accuracy of asymptotic stress fields. Instead of applying additional enrichment techniques, the scaled boundary finite element method (SBFEM) [59] naturally resolves the singular stress fields by extracting the generalized stress-intensity factors at negligible computational cost [17]. SBFEM requires discretization only along the tangential boundary, whereas it retains analytical solution in the radial direction. Such damage modelling methods are reviewed in detail in Sec. 2.3-2.5.

Despite the select shortcomings of FEM with regards to damage modelling in solids, it has reached a highly matured development status in terms of element technology and is readily available in most commercial software. This motivates its further development to enhance its capability in modelling complex damage scenarios pertinent to large-scale industrial applications.

2.2 Finite element modelling of 3-dimensional composite laminates

Typically, the simulation of thin composite laminates is performed on the basis of the classical lamination theory (CLT), which originated in the 1960s [60]. The underlying assumption made in CLT is that each composite lamina/ply is composed of fibres that are oriented in arbitrary directions and embedded in a binding matrix (Fig. 2.2). The plies exhibit anisotropic material behaviour due to different fibre-orientations and variable stiffness associated with the fibre and matrix phases. The thickness of the plies is considered very smaller in comparison to the other characteristic dimensions and plane-stress assump-

tions hold for each ply. The plies are further considered to be stacked and bonded with a thin adhesive layer to form a laminate structure (Fig. 2.2). These assumptions lay the foundation of the CLT and allow for the analysis of the entire composite laminate.

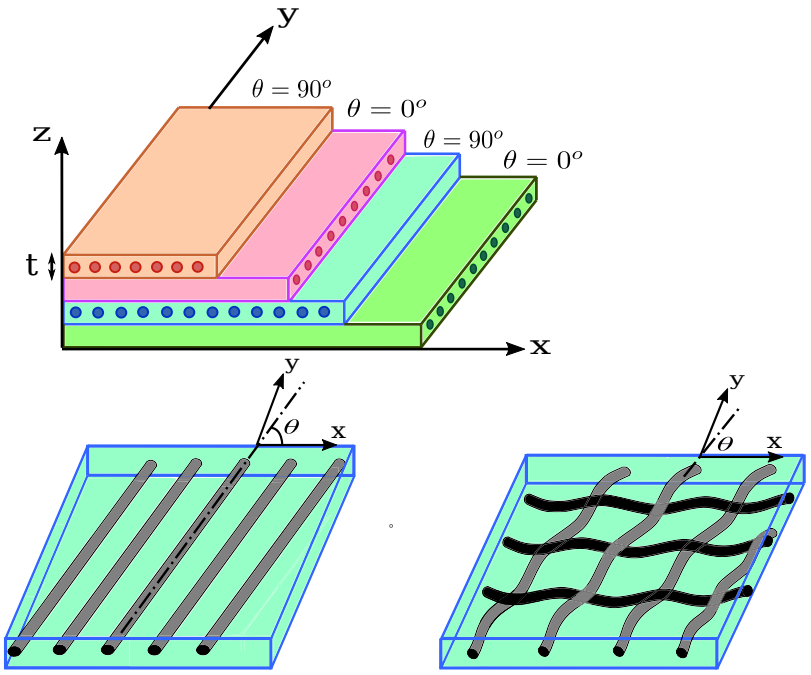

Figure 2.2: Stacked thin plies with different fibre orientations, and configuration of unidirectional (UD) and woven-fabric reinforced composite laminate plies based on classical lamination theory (CLT)

Numerical modelling of thick-ply composites has extensively been performed over the past using conventional 3-D hexahedral elements [61, 62], as they are capable of incorporating the complete 3-D deformation behaviour of composite plies, whilst considering through-thickness variation of the induced stresses. In laminates, hex elements are used in a layer-wise modelling of the plies, which are comprised of different fibre lay-ups; in this way the explicit modelling of the bonding adhesive layers between the plies is also feasible. However, when used in thin-ply laminates, hex elements suffer from transverse shear locking and fail to capture accurate out-of-plane bending response of plies.

To circumvent shear locking effects and calculate the bending stresses accurately, the mesh must be substantially refined with at-least 3-4 element layers along the ply-thickness, or higher-order elements must be used [63]. This leads

to significant computational overhead, as the number of degrees of freedom (DOFs) to solve for increase considerably. In such cases, plies are often modelled using Reissner- Mindlin shell elements, which offer convenient choice for modelling both membrane and bending deformations accurately at a reduced computational cost [64].

2.2.1 Shell element implementations

Mindlin shell elements, see, e.g. [65–68], offer a better alternative for modelling composite plies. Compared to 3-D models, shell elements rely on a set of kinematical assumptions stemming from shell theory [8, 69], hence reducing the order of the finite element problem. Furthermore, Mindlin shell elements explicitly treat shear locking, and hence they are computationally ideal candidates for modelling even complex fracture problems, e.g., impact driven damage scenarios.

Significant computational gains can be achieved especially when using an explicit time-integration scheme, as Reissner-Mindlin shell elements do not penalize the stable time increment [2]. A basic requirement of any shell element formulation is that it passes all basic tests, e.g., the patch test, isotropy, and zero energy mode conditions [8]. In addition, it must display an optimal convergence behaviour for membrane-dominated, bending-dominated and mixed shell deformation behaviours on both uniform and distorted meshes [23]. Shell elements can be categorized into the following types based on their underlying numerical formulations [70].

- Curved shell elements based on general shell theory
- Degenerated shell elements with their kinematics derived from the 3-D solid element formulation
- Flat shell elements that combine the kinematics of plane-stress and plate elements individually to define membrane and bending behaviour respectively

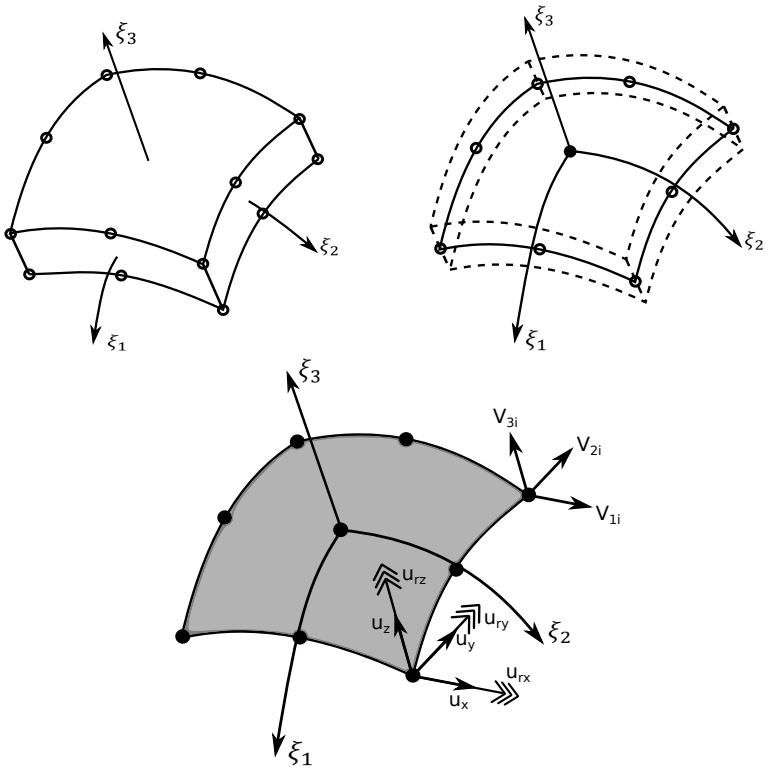

Figure 2.3: Reissner-Mindlin shell element with translational and rotational degrees of freedom, degenerated from the mid-surface of 3-D hexahedral solid element [8]

Shell elements can also be classified based on their thickness as: Thin shells based on Kirchhoff-Love theory that neglects the effect of transverse shear strains, and Thick shell elements based on Reissner-Mindlin shell theory that considers these effects [70]. Amongst these, the degenerated shell elements based on Mindlin theory (Fig. 2.3) have garnered much attention in the past as they are suitable for both thin and thick shell applications, and realistically represent the coupled membrane and bending behaviour of shells at considerably lower computational cost.

An inherent issue with Mindlin shell elements is that they display membrane and transverse shear locking [23] when they are too thin. This can significantly affect the evolution of the simulated crack path and may provide erroneous fracture predictions. Transverse shear locking occurs purely because the linear displacement based interpolation used in the calculation of transverse shear strains in Mindlin shells do not accurately reflect the Kirchhoff-Love thin-shell assumptions. Hence, the shell element predicts an artificial or parasitic shear stress even when a constant bending moment is applied. This leads to a

significant over-prediction of the bending stiffness and an under-prediction of the transverse deformations which are lower than the analytical estimates by orders of magnitude [22].

In addition, spurious coupling may occur between the membrane and transverse shear strains when the shell elements are curved or become overly distorted due to nonlinear deformation, e.g., during out-of-plane bending. This also results in increased element stiffness and subsequent membrane locking [23]. The membrane stiffness can be significantly larger than the bending stiffness in thin shells, and hence, membrane locking leads to the exclusion of the desired bending modes from the overall element response [8].

Locking is typically observed in beam, plate and shell element formulations that are based on a linear interpolation scheme. An illustration of transverse shear locking in simple cantilever beam subjected to bending loads is shown in Fig. 2.4 [9]. The numerical solution obtained from linear (1^{st} order) and quadratic (2^{nd} order) elements are compared against the exact analytical solution. It can be clearly seen in Fig. 2.4 that the 2^{nd} order elements perform well, but the 1^{st} order elements severely under-predict the tip displacements due to shear locking [9].

To this point, several approaches have been proposed to alleviate locking in shell elements. Reduced/ selective integration schemes have been employed in the past that has been greatly successful in alleviating membrane and transverse shear locking effects [71–73]. In reduced integration, the order of the, typically Gauss, integration rule is lower than the one required for optimum accuracy. This results in a less stiffer shell element and improves the computational efficiency. However, reduced integration introduces an additional zero-energy mode that results in spurious hourglass deformations and necessitates implementation of hourglass stabilization techniques [73, 74]. Moreover, shell elements based on reduced integration suffer from rank deficiency; hence they do not represent the rigid body modes properly and require additional projection techniques [23].

A popular remedy is also to use selective reduced integration technique

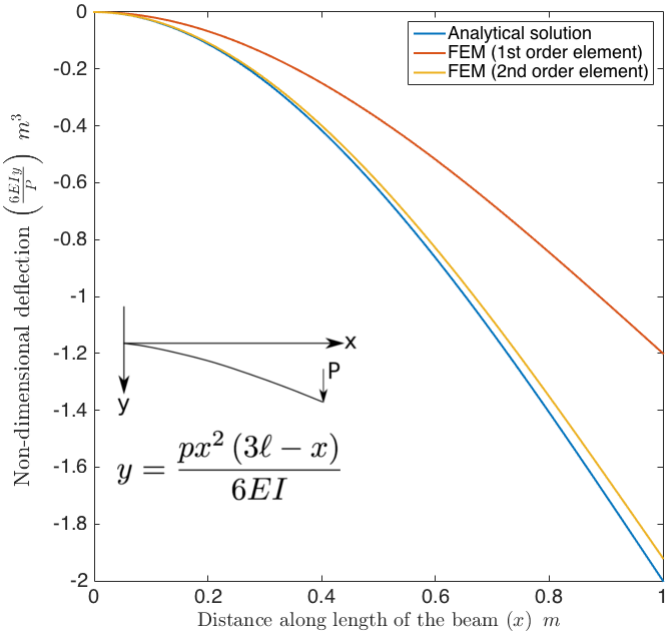

Figure 2.4: Illustration of transverse shear locking in linear (1^{st} order) elements (image reproduced from Harish [9])

[75, 76], in which an exact integration is performed for the shear deformation components whereas a reduced integration is preformed for the volumetric components. In general, using reduced integration elements with damage or strain softening models negatively affects the accuracy and stability of simulations [77]. Especially for nonlinear phenomena like damage, the precise prediction of crack paths using elements based on selective/reduced integration necessitates an even finer mesh discretisation in the critical regions which adds up to the computational complexity.

An alternative to alleviate shell locking effects is to use the assumed strain approach based on the Mixed Interpolation of Tensorial Components (MITC) formulation proposed in the works of Dvorkin and Bathe [22], Bathe [74], Bathe and Dvorkin [78]. The idea is to use the standard displacement-based approach to calculate the transverse shear strains only at a set of discrete tying points within the shell element. The strain values at all other points in the element are then assumed based on these tying point strains using a different interpolation technique [22]. The MITC formulations were originally proposed to reduce transverse shear locking in 4-noded continuum mechanics based shell element

(referred as MITC4). MITC4 elements have been dominantly used in the engineering practice as they provide much better locking alleviation and hence superior performance over the 3-noded triangular shell elements MITC3 [79, 80]. Later, the MITC4 formulations were extended to treat both membrane and transverse shear locking in higher-order and initially curved shell elements, see e.g. MITC9, MITC16 elements in [69, 81]. Membrane locking was not addressed in the original MITC4 formulations as they are relatively flat in their initial geometry. However, some membrane locking occurs when the MITC4 elements are used to model curved geometries or when it gets significantly distorted due to nonlinear deformations during the analysis [23, 82]. In such cases, membrane locking becomes dominant and may cause solution accuracy to deteriorate, especially in damage prediction scenarios. Several attempts have been made to treat membrane locking in MITC4 shell elements [23, 82–86]. Choi and Paik [83] proposed an assumed strain field based approach that efficiently treats membrane locking in MITC4 shells, however it fails the membrane patch test. Other efforts include implementation of 4-noded exact geometry shell elements with assumed membrane strains [84, 85] which relies on exact representation of shell mid-surface and subsequent treatment of membrane locking. The recently proposed MITC4+ continuum mechanics based shell formulation by Ko et al. [23, 82] provides a more general approach and has been successful in alleviating both transverse and shear locking. More importantly, the MITC4+ shell element does not depend on any adjustable numerical factor and passes all basic patch tests in an optimal convergence behaviour for both uniform as well as significantly distorted meshes [23].

Carrera et al. [10] performed a comparison between reduced/selective integration and MITC methods, with regards to their effectiveness in treating transverse shear locking, using a cantilever beam bending test (Fig. 2.5). It can be seen in Fig. 2.5b that the fully integrated linear element display significant shear locking, resulting in significantly lower displacements (relative error 97.5%) than the analytical estimate for the single element case. The reduced integration method displays slightly better predictions (error 24.9%) and con-

vergence rates for the displacement solution, than the selective reduced and MITC methods (error 32.8%). However, the reduced integration method performs poorly in predicting the transverse shear stresses accurately, whereas the predictions from MITC and solid hexahedral elements match closely with each other (see Fig. 2.5c). Hence, the MITC method provides an accurate description of the complete 3-D state of stresses, rendering it ideal for the purpose of damage simulations [10]. Furthermore, Laulusa et al. [11] evaluated the performance of different shell elements in alleviating membrane locking using several benchmarks, and compared their results against the deep shell solution. Fig. 2.6 illustrates that MITC performs significantly better than other methods in treating membrane locking, and provides less stiff response with more accurate membrane strains [11].

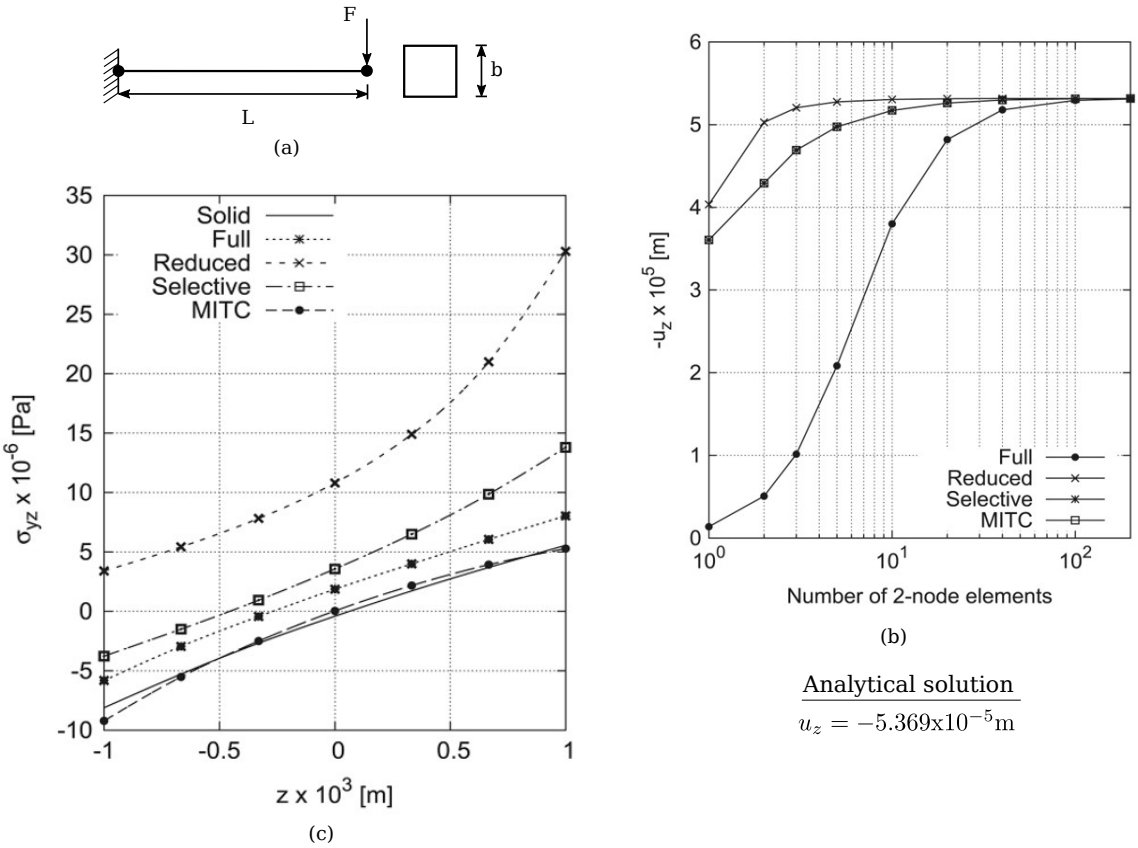

Figure 2.5: (a) Schematic for 1-D beam subjected to vertical bending load. Comparison of its (b) maximum vertical tip deflection u_z against analytical solution $(u_z = -5.369 \times 10^{-5})$ m, and (c) transverse shear stresses σ_{yz} against solid hexahedral elements, predicted by full-integration/ reduced/ selective/ MITC methods. All images reproduced from Carrera et al. [10] with permission from Wiley, refer to [10] for more details.

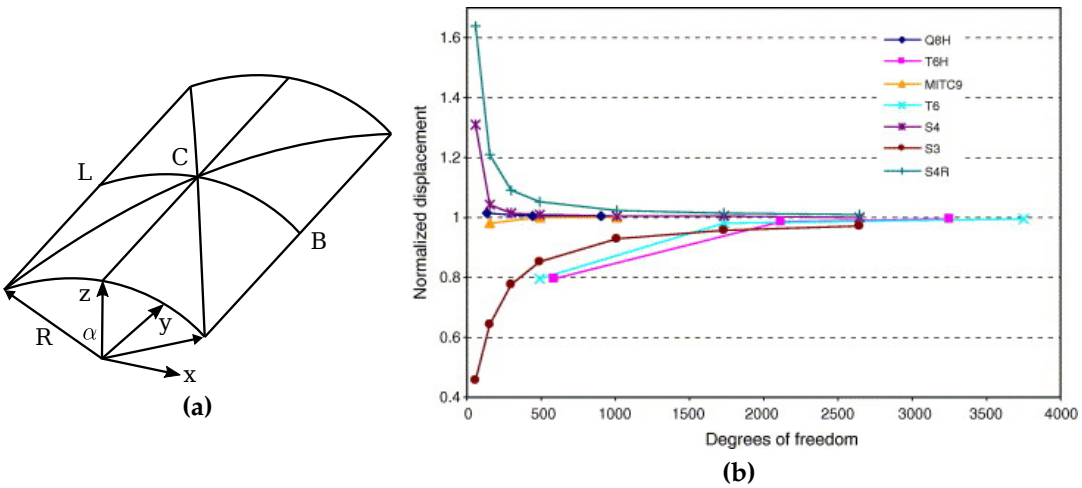

Figure 2.6: (a) Schematic for Scordelis-Lo barrel roof under distributed load used to test membrane locking (b) Comparison of normalised displacement of barrel roof at point C, for different types of shell elements with respect to increasing number of DOFs. All images reproduced from Laulusa et al. [11] with permission from Elsevier, refer to [11] for more details.

2.3 Damage Modelling - an Overview

An appropriate shell element formulation as discussed in the previous section is necessary to model the 3-D deformation of thin plies accurately. From a computational perspective, shell elements are more efficient than a full 3-D discretization scheme using hexahedral elements. Furthermore, employing Mindlin shell elements ensures that the damage in composite plies initiates and evolves due to coupled membrane/bending deformations. However, it is also important that the constitutive damage model itself captures the diverse composite failure modes accurately. In contrast to ductile metal materials, composites fail due to wide range of complex anisotropic failure modes that interact with each other. Typical failure modes in layered composite laminates can be primary classified into two types, i.e. intra-laminar and inter-laminar damage as shown in Fig. 2.7. The former, e.g., delamination, involves separation of composite plies due to failure of adjoining adhesive layers. Delamination is one of the primary modes of failure in composite laminates that is often barely visible, but causes significant degradation of the structural strength. The latter involves evolution of damage within individual plies due to fibre cracking un-

der tensile loads, matrix cracking under tensile/shear loads, fibre microbuckling, fibre pullout, fibre bridging and debonding, or a combination of these modes. Intra-laminar failure in thick-ply composites initiates within resin rich

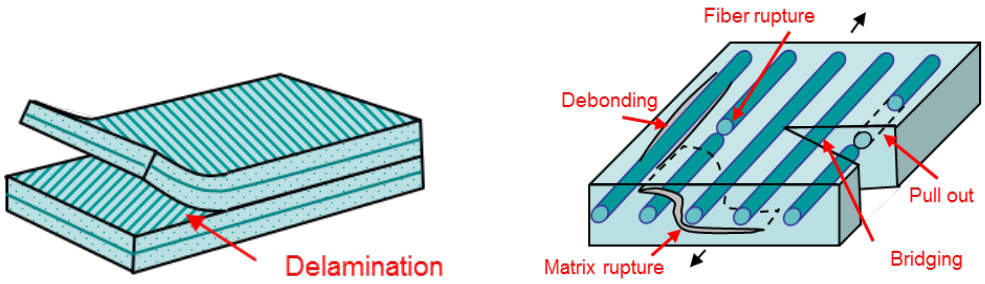

Figure 2.7: Illustration of diverse inter-laminar and intra-laminar damage modes in composite laminates (image reproduced from Noels [12])

matrix pockets which further evolve to cause delamination, and also fibre failure in some cases. However in thin-ply spread-tow composites (Fig. 2.8), the fibre bundles are flatter and wider, and the resin rich areas are considerably reduced. As a result, sub-critical damage mechanisms like transverse matrix cracking and delamination are practically suppressed leading to an improved fatigue life and damage resistance [2, 38, 87–90]. In such cases, fibre failure

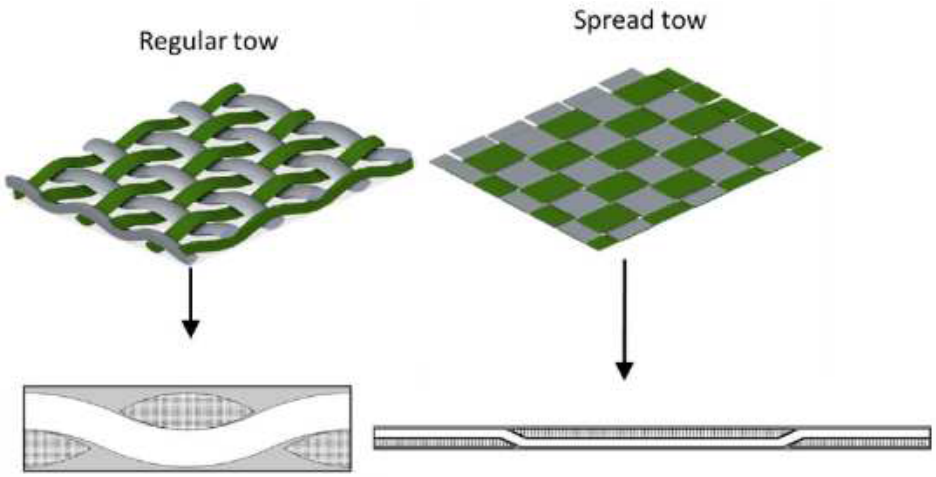

Figure 2.8: Regular-tow vs Spread-tow woven fabric reinforced composite (image reproduced from Olsson et al. [13])

becomes more relevant and acts as the primary mode of intra-laminar failure [45]. Modelling of fibre-based failures has been difficult as fibre cracks are often accompanied by subsequent fibre-pullout events, which leads to fibre-bridging between crack faces. This renders the intra-laminar damage response

quasi-brittle, which is characterized with a gradual degradation of induced stresses as the crack evolves. This is in contrast to brittle fractures which are manifested by a sudden drop in the induced stresses and subsequent structural collapse. Both intra- and inter-laminar damage can occur simultaneously; however in thin-ply composites, they are largely uncoupled due to the suppression of transverse shear cracking [45]. This warrants the need for a robust meso-scale damage modelling framework that:

- Is computationally cheaper, efficient and provides accurate predictions of composite fracture behaviour both in terms of curvillinear crack-paths and strength degradation
- Captures damage initiation and evolution due to coupled membrane and bending deformations
- Models diverse anisotropic intra-laminar failure modes and facilitates reliable assessment of the overall strength of composite laminate structures
- Simulates both intra-laminar and inter-laminar composite damage modes accurately

In Linear Elastic Fracture Mechanics (LEFM) methods, damage initiation and propagation are described within the remit of brittle and quasi-brittle fracture [17]. LEFM methods can be classified broadly under two distinct theoretical frameworks, i.e. methods that rely on discrete (sharp) or diffuse (smooth) representation of damage based on Computational Fracture Mechanics (CFM) (see, e.g., [91]) and Continuum Damage Mechanics (CDM) (e.g., [92]) approaches respectively, wherein the latter is also applied vis-à-vis nonlinear ductile damage. In the former, the crack is introduced as an explicit geometrical discontinuity in the finite-element mesh, whereas the latter relies on a smooth representation of damage that is homogenized over a representative volumetric domain. In CDM approaches, the damage variable is embedded directly into the constitutive model, and thus facilitates implicit modelling of stiffness degradation effects. The smeared/diffused crack approaches, e.g.,

gradient enhanced damage and phase field approach, lie effectively at the boundary of CFM and CDM methods [17]. The phase field method (PFM) [93, 94], that falls under the realm of diffused crack methods [95], performs implicit treatment of strain localization by replacing the sharp crack interface with a scalar damage variable. The damage variable, also known as the phase field, is diffused into the crack surrounding domains, with the diffusion zone width controlled by a length-scale parameter.

To this point, several theories and criteria pertaining to numerical prediction of damage in isotropic and orthotropic materials such as composites have been proposed. Some of the early versions of discrete crack models based on CFM originated from the works of Ngo and Scordelis [96], which predicted crack paths via the splitting of mesh nodes, thus constraining the crack-paths to coincide with the element edges. This made the discrete models highly mesh dependent and improvements were needed to reduce the mesh-bias problem. Constraining the crack propagation to lie only over the element edges leads to over-estimation of fracture energy unless an additional correction is applied. This results in predicted crack-path to diverge significantly from the actual crack-path, especially when a coarser mesh is used [97]. One way to alleviate the mesh-bias problems is by using automatic remeshing techniques during crack propagation [98]. Several techniques incorporating sophisticated remeshing algorithms [47, 99] have been introduced to model singular stress fields. In addition, diverse methods based on calculation of the fracture parameters, e.g., stress-intensity factors (SIFs) have been proposed, see e.g. path-independent integrals [100, 101], virtual crack closure technique [102, 103], hybrid element approach [104] and Irwin's crack closure integral [105]. The computational efficiency of such methods is low, primarily due to the requirement of remeshing algorithm for maintaining fine mesh in the vicinity of crack tip.

The extended finite-element methods (XFEM) [49, 50] was introduced to efficiently and accurately treat LEFM and cohesive fractures, which allows for automatic propagation of crack independently of the underlying mesh and is highly flexible, resolving crack-tip stress singularities with a much coarser dis-

cretization compared to the standard FEM. However, to define the crack topology, XFEM requires additional DOFs and individual crack segments, which increase significantly as the problem size grows and makes XFEM computationally expensive. In addition, the extension of XFEM for 3-D applications is not straightforward, as the crack-propagation increment in 3-D becomes difficult to specify [17]. XFEM models are primarily based on the assumption of LEFM, and uses crack-tip stress intensity factors (SIFs) to evaluate crack propagation. A direct disadvantage is that standard XFEM fails to predict the exact crack behaviour for ductile damages, where significant plastic deformations and non-linearities are involved. There have been attempts to model ductile damage by combining XFEM with continuum mechanical models [106–108] which takes the softening and damage effects into account, arising due to microscopic voids initiated at inclusions in the material matrix [109].

Cohesive zone modelling (CZM) [110, 111] is an alternative discrete method based on the partition of unity framework, which predicts the crack topology with the help of discrete, overlapping segments. CZM effectively overcomes numerical stress singularities by considering a small fracture process zone (FPZ) ahead of the crack tip that exhibits some ductility. As a result, the fracture energy is gradually released at the crack-tip based on the length of FPZ and the crack opening displacement, as opposed to sudden release of energy that is witnessed during pure brittle fractures. CZM is a highly efficient and flexible approach that has become the industry standard for realistic prediction of structure's critical strength and load bearing capacity. A downside, however is that it requires the crack-propagation path to be pre-defined before the analysis. This limits it's applicability to problems where crack-paths are already known, e.g., delamination of composite plies. A variant of CZM is the Cohesive Segments Method (CSM) [112] that introduces cohesive segments arbitrarily within the finite-element mesh to incorporate discontinuity in the displacement field. CSM utilizes a set of overlapping cohesive segments to model a continuous crack-path, and has been used in various partition-of-unity methods that use cohesive theories within a meshless discretization

approach, see e.g. [113, 114].

Discrete models are useful in describing the crack behaviour at finer scales, starting from crack initiation to propagation and ultimately coalescence. The approaches based on fracture mechanics and micro-damage mechanics attempt to model each individual crack and their interaction with other defects. This requires high amount of computational resources and are practically inefficient for large-scale industrial problems. The discrete models are also inefficient for analyzing problems with high-strain rates, wherein a fine scale spatial discretization is used to model complex crack patterns.

In such cases, methods based on either a continuum representation of damage, e.g., continuum damage modelling [115, 116], diffused crack approaches, e.g., the phase field method [93, 94] or the thick level set methods [117], provide higher advantage as they do not rely on explicit representation of crack, and hence overcome the numerical issues associated with the presence of sharp discontinuity in the domain. Rather, they represent crack using a damage variable whose evolution causes the degradation of material stiffness. Such methods have proved to be highly successful in predicting complex crack patterns and failure characteristics in wide range of materials, including composites [118–122].

CDM provides an efficient alternative to formulate constitutive models for damaged composites by representing the complete damage effect by means of a homogeneous damage field. However, CDM models when considered at a purely local level are ill-posed and mesh-dependent within a finite element setting. Hence, regularization [123, 124] or continuum homogenization techniques [125] are often required to prevent the spurious localization of damage. To circumvent these deficiencies, an integral-type non-local model is defined to provide non-local strain measures by using a weighted mean of local strain values considered over a small volume. Traditional approaches relied on predicting the crack evolution based on a strength criteria, but they suffered from presence of stress singularities at the crack tip producing incorrect results [126]. This can be overcome by replacing strength based approach with energy based

fracture criteria, refer [127], in which the fracture energy is utilized as a material parameter in addition to the fracture strength. This causes another mesh bias problem of the energy rate being dependent on element size, which can be addressed with a crack band model [128].

Diffused crack approaches resolve the issue of mesh-dependence during crack propagation by replacing the sharp discontinuous crack with a continuous damage field that is smeared/diffused into the crack surrounding domains within a length-scale. Diffused crack approaches, in particular the phase field method (PFM), have displayed a highly promising behaviour in predicting localized and complex crack patterns without needing to keep track of sharp crack interfaces and discontinuities [24, 129]. In particular, the damage model incorporates the effects associated with crack formation such as stress release or stiffness degradation into the constitutive model rather than attempting to model the actual crack topology [97]. Started with the work of Rashid [95], which defined a cracking criterion for pre-stressed concrete pressure vessels, a smeared approach works on the principle of loss of material stiffness in the direction normal to crack (plane of degradation), as crack evolves and propagates through the structure. Phase field methods (PFM), proposed by Francfort and Marigo [93], Bourdin et al. [94], are based on the variational theory of fracture that helps overcoming certain limitations of the Griffith's theory and enabling automatic crack initiation, branching, merging and handling curved crack paths without any modification of the underlying finite-element mesh. The main advantage of PFM is that the crack-path does not need to be predefined; rather it emerges as a solution to a physical energy-based partial differential equation that is solved over the entire computational domain. However a minimum length scale parameter is needed for the accurate resolution of crack which results in extremely fine mesh sizes in the regions where crack is expected to propagate.

In the subsequent Sec. 2.4-2.5, different discrete and diffuse damage modelling approaches are comprehensively reviewed and their advantages/limitations with regards to applicability for modelling composite damage is discussed.

2.4 Discrete Damage Modelling

2.4.1 Remeshing

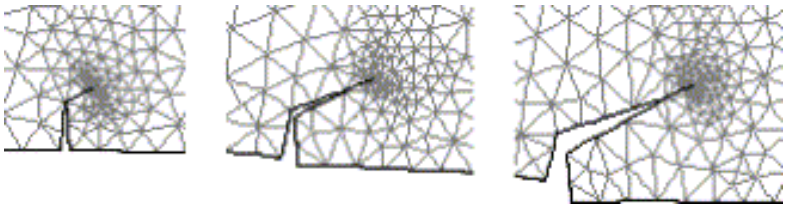

Figure 2.9: Damage modelling using an automatic evolutionary remeshing algorithm (image reproduced from Bouchard et al. [14], with permission from Elsevier)

In the 70s, remeshing was introduced as a necessary component to predict discrete fracture propagation using FEM, particularly in elastic and elastic-plastic materials (Fig. 2.9). Remeshing approaches can be of two types, i.e. one which involves remeshing of the entire model in each time-increment, and another that involves modification of only certain number of elements in the vicinity of the crack tip and locally remeshing them, thus minimally impacting the original model. The former approach has been reported in [130, 131] and allows generation of elements with better aspect ratios. However, it poses computational challenges in transferring a large number of state variables from the old mesh and interpolating them for the new mesh, especially for elastic-plastic materials. For the latter approach, since only a small number of elements close to the crack tip need to be remeshed, the number of variables that need to be transferred decrease, thus involving lesser computational overheads. However, this leads to other challenges as the already existent mesh in far-away regions restricts creation of new well-shaped elements, which need to fit into the small confined region that is being remeshed.

Some of the earlier endeavours in CFM, see e.g. [96, 132, 133], were based on the principle of nodal release, wherein the crack propagation was constrained along predefined mesh lines. Several remeshing techniques, in particular the h-adaptive remeshing [134], have been proposed till date, see e.g. [135–141]. H-adaptive remeshing modifies only the element geometry,

shape and sizes based on a posteriori error estimator, but keeps the element formulations unchanged [142]. Such methods are highly mesh dependent as the cracks propagate only along element edges, and over-estimate the fracture energy especially when the predicted crack-path deviates from the actual crack-path.

Trädegård et al. [143] used a combination of nodal relaxation and automatic remeshing algorithms to model crack propagation in elastic-plastic materials using Abaqus, and was able to enhance the accuracy of solution with lesser DOFs and computational time as compared to conventional methods. Extending the concept in [143], Bouchard et al. [14] proposed an advanced fully-automatic remesher to deal with multiple boundaries and multiple materials in discrete crack approaches (Fig. 2.9). Radial concentric meshes along with evolving refinement were introduced in order to improve the accuracy of computations at each crack tip. Bouchard et al. [47] further utilized the automatic remesher to compare and highlight advantages/disadvantages of different crack growth criteria and their corresponding predictions of crack-path. Rethore et al. [144] and Shahani and Fasakhodi [145] worked on analyzing dynamic crack propagation using remeshing techniques. However, Rethore et al. [144] focused more on developing an appropriate numerically stable strategy for dynamic crack propagation problems, and used varying mesh-sizes to examine the stability of the scheme. The aim of this work, in fact, was not to develop an efficient remeshing procedure with accurate projections, but to deal with the numerical stability of the scheme and the uncontrolled transfer of energy while using projections via so-called *balance recovery method*. On the other hand, the focus of Shahani and Fasakhodi [145] was to perform an FE simulation based on remeshing technique compatible with the actual dynamic fracture process. In [145], a dynamic fracture toughness criterion was used to predict the crack-tip velocity, and a remeshing procedure using ANSYS Parametric Design Language (APDL) was employed at each crack extension step to model the crack-tip singularity.

Since failure in composites involve a large-number of micro-cracking mech-

anisms, modifying the model geometry and mesh to track these micro-cracks becomes a challenging task even for the simplest analyses. As a consequence, remeshing has found very limited application within the context of progressive damage and failure modelling in composites. Rather, the continuum damage approaches that are capable of modelling multiple cracking, crack branching and merging phenomena in a computationally less expensive manner are preferred [142].

2.4.2 Cohesive zone modelling (CZM) and cohesive element (CE) method

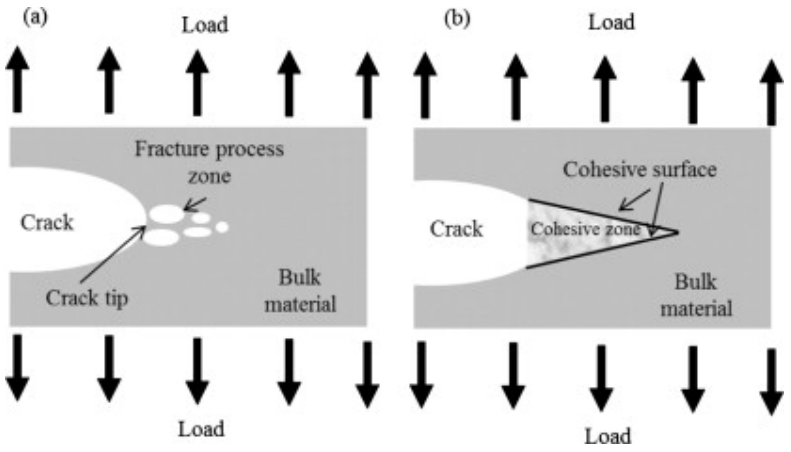

Figure 2.10: Concept of fracture process zone and modelling of damage using cohesive zone method (image reproduced from Jousset and Rachik [15], with permission from Elsevier)

Cohesive zone modelling (CZM) is a class of discrete fracture mechanics approach in which the stress state is redistributed over a finite domain termed as the fracture process zone (FPZ), and involves gradual fracture formation (Fig. 2.10). Many materials such as composites or concrete are not perfectly brittle in the Griffith [146] sense; rather they exhibit some ductility after attaining their critical stress. This is due to the presence of the FPZ in the vicinity of the crack-tip, which is accompanied by small-scale yielding and the initiation and coalescence of micro-cracks. The crack in CZM spreads across extended crack tips and is resisted by cohesive tractions that vary as a function of the crack opening. In particular, the cohesive model defines the strength degra-

dation behaviour starting from the point when the critical fracture strength is reached until the interface stiffness becomes zero, and the substructure is completely separated [42].

The concept of cohesive zone models was originally proposed in the works of [110, 111, 127], which introduced a traction-separation law that governed the material separation across adjoining interfaces. As the crack tip is extended over FPZ, CZM tends to reduce the mesh sensitivity as compared to purely stress based discrete approaches, although marginally. CZM has several advantages over other fracture mechanics approach such as the virtual crack closure technique (VCCT) or other LEFM approaches [147].

In VCCT, the fracture energy released during crack propagation is assumed equal to the energy required to close the crack back to it's original position, and computes the energy release rate based on nodal forces and displacements [148]. VCCT requires the nodal information from the nodes ahead and behind the crack-tip to calculate fracture parameters, which is often cumbersome and requires remeshing. Cohesive zone models overcomes these issues and also predict accurate crack behaviour of uncracked structures, including those with blunt notches [149]. To this point, CZM has been employed within the frameworks of the Finite Element Method [150], Boundary Element Method [151], Partition of Unity approach [152], Smoothed Particle Hydrodynamics [153], Kernel particles [154] and Element-Free Galerkin method [155].

2.4.2.1 Application to composites

The ease of implementing CZM within a discretization scheme, e.g., FEM or BEM and its capability to avoid singularities makes it a preferable method for analyzing composite fracture problems [156]. Both delamination initiation and propagation can be modelled using CZM without the need of pre-existing cracks [157, 158]. Cohesive zone theories have been extensively used to model delamination failures in composites [148, 159–165]. Camacho and Ortiz [166] applied CZM to model discrete crack nucleation and propagation enabling de-

tailed predictions of dynamic fracture and fragmentation progression in brittle materials subjected to impact. This has been successfully used for delamination modelling in both static [167–170] and dynamic [171–175] loading and impact conditions. CZM has also been successfully used to predict anisotropic damage initiation, evolution, prediction of strength and damage zone size in orthotropic composite layups [176, 177].

CZM can be implemented in the form of cohesive elements or cohesive interactions between the adjoining surfaces. Cohesive elements are used when the interface adhesive layer has finite thickness and macroscopic properties, such as the stiffness and strength of adhesive material are available [178]. However, when the thickness of the adhesive layer is negligibly small, it is more appropriate and computationally efficient to use cohesive surface interactions, especially in explicit analysis as it does not penalize the stable time increment. In the cohesive element approach, fictitious elements, also termed as interface elements, are introduced between the finite element mesh at the interface and traction separation laws are defined as their constitutive relations. Cohesive elements are a class of continuum finite elements, added in between the connected substructures as a means of adding a damageable layer for delamination modelling [179].

Cohesive elements combine principles from CFM and CDM and model both delamination and debonding in composite materials [147]. They do not require an a-priori assumption of initial damage size and computationally expensive re-meshing algorithms, which renders it a highly beneficial method over classical fracture mechanics theory [159]. A drawback of using cohesive elements is that they cannot account for an arbitrary crack front shape, which makes it difficult to differentiate between shear damage mode II and III during delamination [180]. This also limits its application primarily to scenarios where the fracture takes place along well-defined interfaces and the placement of cohesive surface is clear, e.g. delamination [112].

For intra-laminar fracture propagation within composite plies or any other bulk material, the crack paths are arbitrary and often unknown, which makes

it difficult to mark clear interfaces. A variant of CZM is the Cohesive Segment Method (CSM) first introduced in [112], in which the crack is modelled as a collection of overlapping cohesive segments that incorporates displacement jumps within partition of unity framework. The method allows for the insertion of these cohesive segments at arbitrary locations and orientations, which facilitates convenient modelling of complex crack initiation and growth at multiple locations. CSM has been effectively used in modelling intra-laminar as well as inter-laminar cracks in composites [181–184].

2.4.3 eXtended finite-element method (XFEM)

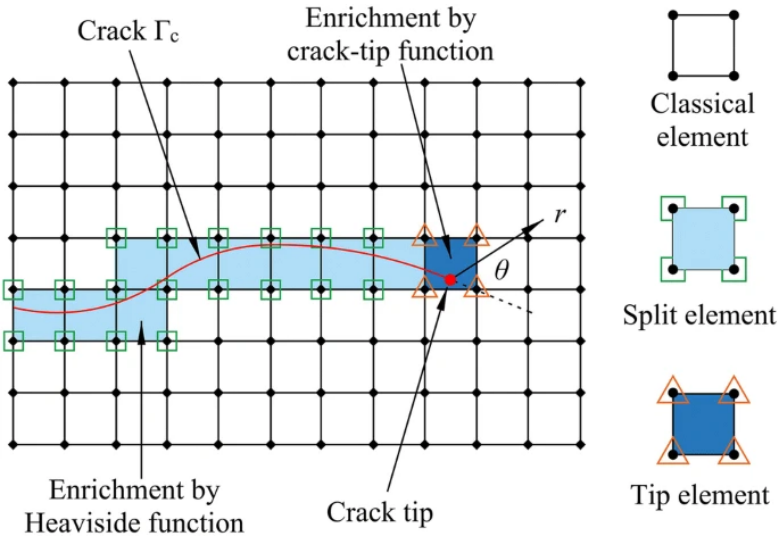

Figure 2.11: Schematic description of damage modelling with eXtended finite-element method (XFEM) (image reproduced from Wu et al. [16]), with permission from Springer Nature)

The main challenge in conventional FEM approaches lies in the fact that the mesh needs to be updated at each crack propagation step [17]. The development of extended [50] and generalized [58] finite element methods based on the concept of the partition of unity (PU) [152, 185, 186] has managed to solve this issue to a great extent. The extended finite element method (XFEM), first developed by Belytschko and Black [49] and Moës et al. [50], models crack propagation by enriching the solution space with a set of additional degrees of freedom and adding discontinuous basis functions to the standard polynomial basis. XFEM disassociates the crack topology from the underlying finite

element mesh and hence, does not rely on expensive mesh-update algorithms to track the crack paths (Fig. 2.11). This makes XFEM highly flexible in resolving crack-tip stress singularities with a much coarser discretization. In contrast to standard FEM, the mesh for XFEM model is completely independent of the location of the grain boundaries [187]. Furthermore, it mitigates the reduced accuracy of the FEM due to the introduction of mesh dependent projection errors. Belytschko et al. [187] presented a thorough review on applications of extended/generalized finite element methods (XFEM/GFEM) to material modelling problems with reference to fracture, dislocations, grain boundaries and phase interfaces. XFEM was further extended to three-dimensional crack modelling by Sukumar et al. [188] using the notion of partition of unity. This was achieved by adding discontinuous functions and functions from two-dimensional asymptotic crack-tip displacement fields to model the interior of crack surface and crack front enrichment respectively.

2.4.3.1 Application to composites

Some of the early works of extending the application of XFEM for fractures in orthotropic media, e.g., composites, can be traced to [189, 190]. The XFEM solutions, applicable for the static case, were extended to analyze dynamic stress intensity factors for fixed cracks [191] and later for the dynamic analysis of moving cracks using time-independent enrichment functions [192] in composites. Several attempts have been made to numerically study matrix cracking, interface debonding and crack propagation in bi-material composite systems with XFEM [193–196].

Dimitri et al. [195] combined the level set method with XFEM to predict the direction of propagation and near crack-tip stress intensity factors for composite fractures under different loading conditions. XFEM has been increasingly used in performing fatigue crack growth simulations and predicting fatigue life of metallic, super-alloys, composite and plastically graded materials, see e.g. [197–202]. The eXtended Iso-Geometric Analysis (XIGA) combines the numerical advantages of XFEM and the meshing flexibility of Isogeomet-

ric Analysis (IGA) and has been used in solving a range of crack discontinuity problems in different materials [203–207]. Very recently, Egger et al. [17] presented a critical review comparing crack-path and strength prediction capabilities of different discrete (XFEM/SBFEM) and diffused (PFM) damage modelling approaches.

As compared to cohesive zone and cohesive element techniques, XFEM does not require the crack to align with the interface between two elements, which makes it highly suitable for analysing complex intra-laminar crack patterns in composites. XFEM has also been increasingly applied in conjunction with Cohesive zone models to study delamination and matrix crack growths in composites. Originally proposed by Moës and Belytschko [208], the combined method results in representation of crack independent of underlying mesh and crack propagation based on CZM. This has been applied to several damage simulations of composite structures including delamination, see e.g. [209–211]. However, XFEM is also prone to some disadvantages that limit its applicability. As the number of crack segments increase, the pair of level set functions required for the definition of their topology also increase, and so does the computational complexity and problem size due to the incorporation of additional DOFs [97]. The numeric implementations of XFEM are not generic and involves significant algorithmic changes to the code to extend them to further types of analysis. Extension of XFEM to simulate 3-D problems is not straightforward and involves complexities in specifying the crack-propagation increment in 3-D. Furthermore, it is not intuitive and requires expert knowledge to assess if a crack has arrested near the obstacles or it's further propagation is limited by XFEM itself, see e.g. [17].

2.4.4 Scaled boundary finite-element method (SBFEM)

SBFEM belongs to the class of semi-analytical methods [55, 59, 212–215], and has been a useful method in providing numerical solutions to diverse physical problems [42], including discrete fracture propagation [216]. The main

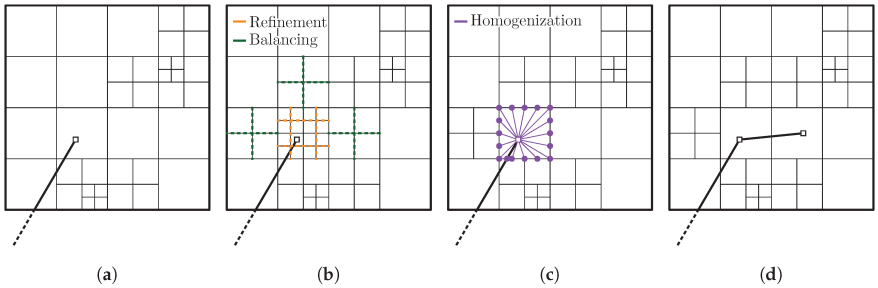

Figure 2.12: Schematic description of damage modelling with scaled-boundary finite-element method (SBFEM) (image reproduced from Egger et al. [17])

advantage of SBFEM over standard FEM approaches is that it only requires the domain boundary to be discretized, and approximates the solution in the interior domains based on the boundary values (Fig. 2.12). The method is an extension to the classical boundary element method, which derives the kernel solution numerically on the basis of finite element approximations. It allows for more accurate quantification of stress intensity factors (SIFs) at material interfaces, and is efficient in modelling singular stress fields in the vicinity of cracks. Yang [217] developed a mixed-mode crack propagation model based on LEFM by exploiting the direct SIF calculation capability of SBFEM, owing to its analytic representation of stress-singularities at crack tips.

SBFEM was originally developed for unbounded domains, but it was later realized that it is more effective in modelling bounded domains, especially within the context of LEFM [218]. This is corroborated by the SBFEM's capability of straightforward extraction of fracture parameters like stress-intensity factors, T-stress and higher order term coefficients from the singular components of stress-field [219, 220]. Wolf and Song [221] adopted a consistent infinitesimal finite-element cell method which they later standardized into SBFEM, by using weighted residual method [215, 222]. Deeks and Wolf [223] further provided a virtual work based formulation that led to broader adoption of SBFEM.

To this point, the method has been effectively used in modelling nonlinear cohesive and dynamic fractures [216, 224–226], crack propagation [227, 228] in concrete, SIFs and singularity order computations in multi-material plates under both static and dynamic loading [218, 229], crack direction prediction

in bi-material notches [230], free-edge stress determination in laminated composites [231], functionally graded materials [232, 233] and non-local damage [234, 235]. Initial attempts to use SBFEM for crack propagation, see e.g. [217] required manual specification of initial meshes [17]. To overcome the issues of laborious meshing procedure, automated meshers were proposed for polygonal elements [236, 237]. Recently, Ooi et al. [238] proposed the use of quadtree decomposition with polygon clipping for accurately discretizing curved geometries with coarse meshes. The primary advantage of this approach is that the computational efficiency can be enhanced significantly, as it results in a limited number of possible element realizations that can be pre-computed [17].

The SBFEM has also been applied within a multiscale setting, see e.g. [239–241] with the aim to improve the computational efficiency of damage simulations. Recently, the principles of SBFEM were combined with Isogeometric Analysis (SBIGA) that reduces error norms per degree of freedom in displacements and energy, providing exact treatment of curved boundaries and delivering additional refinement and continuity adjustment possibilities [242, 243]. SBIGA leads to slightly higher computational costs due to the Non-Uniform Rational B-Splines (NURBS) based integration procedures associated with IGA [244, 245], however the drawback is effectively overcome as only the domain boundary needs to be discretized [17].

2.4.4.1 Application to composites

There have been few attempts to apply SBFEM for numerical modelling of composites [246–251]. Bek et al. [246] applied SBFEM to investigate the elastic properties of Polymer Nano-composite (PNC) materials using an adaptive meshing algorithm. A semi-analytical technique based on SBFEM was presented in [247, 252] to analyze cracks and notches in piezoelectric composites, evaluating the generalized stress and electric displacement intensity factors directly from the semi-analytical solution.

Li et al. [248] evaluated the dynamic stress and electric displacement intensity factors of impermeable and interface cracks in piezoelectric homogeneous and bi-materials respectively. Hell and Becker [249] studied the influence of laminate free-edge effect and 3-D crack configurations in composite laminates involving inter-fiber cracks using SBFEM. Saputra et al. [253] used SBFEM to analyse cement-based piezoelectric ceramic composites and determining its mechanical properties based on actual distribution of piezoelectric particles in cement matrix. Very recently, SBFEM has been applied to analyze interface cracks emanating from the free edges of composite laminates [250] and weakly bonded laminated composite plates including unidirectional and symmetric/anti-symmetric cross ply laminates, subjected to cylindrical bending [251]. However, the method is still in its premature stage to be actually utilized in practical composite damage applications, and the robustness of the method is greatly determined by the numerical stability of underlying eigenvalue problem [254].

Contrary to XFEM that permits the crack propagation analysis using constant mesh, the quadtree mesh in SBFEM needs to updated frequently with each time-increment. Furthermore, the polygon clipping introduces displacement discontinuities in the form of double nodes, which increase the overall number of system DOFs. In some cases, the clipping results in non star-convex elements which cannot be effectively treated by SBFEM, or elements with poor aspect ratios in FEM sense which may lead to erroneous numerical integration [17].

2.5 Smooth Representations of Damage

2.5.1 Continuum Damage Modelling (CDM)

Instead of representing a crack as a discrete geometrical entity, CDM represents damage with an appropriately defined damage variable whose evolution is governed by a phenomenological constitutive relation [115]. CDM fa-

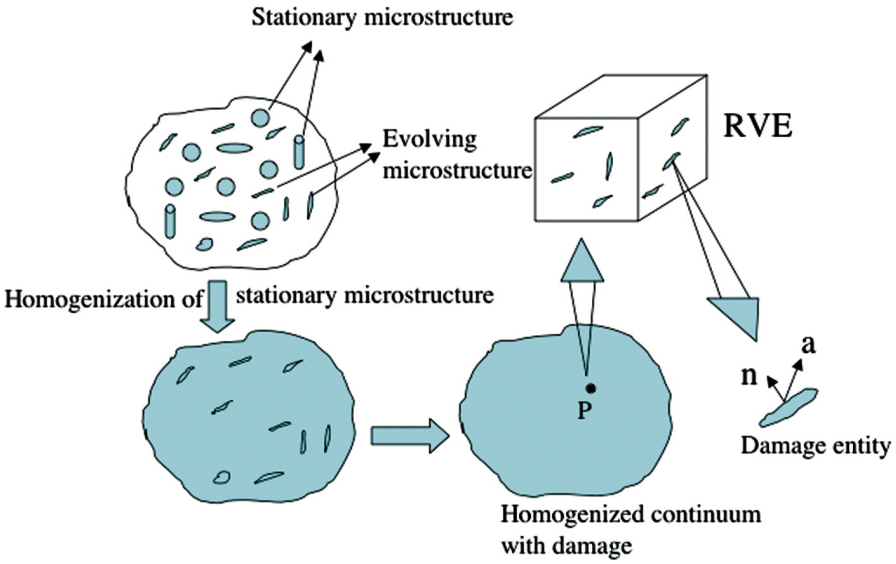

Figure 2.13: Illustration of continuum damage modelling (CDM) using principle of homogenisation (image reproduced from Talreja [18], with permission from Taylor & Francis)

cilitates the modelling of progressive failure in structures and the prediction of their failure strength by characterizing the distributed macroscopic defects and incorporating stiffness degradation effects using the damage variables. Kachanov [115], see also [255], developed the first CDM model for creep rupture of metals popularly known as the Rabotnov-Kachanov equations, which involved the evolution of a creep-strain (ε_c) and a damage parameter (ω) as shown in Eq. (2.1)-(2.2). The variable ω defines the damaged state of the material and ranges from 0 (no damage) to 1 (failure).

$$\dot{\varepsilon}_c = C_1 \frac{\sigma^n}{(1-\omega)^m} \tag{2.1}$$

$$\dot{\omega} = C_2 \frac{\sigma^\nu}{(1-\omega)^\mu} \tag{2.2}$$

where C_1, C_2, n, m, ν, μ are material constants that depend on the temperature. The Rabotnov-Kachanov creep damage model posed problems pertaining to the damage rate becoming excessively large near material failure, i.e., when ω approached unity. Liu and Murakami [116] proposed an improved model involving the constitutive and evolution Eqs. (2.3)-(2.4) of creep and creep-

damage from the micro-mechanical point of view.

$$\dot{\varepsilon}_c = C\sigma^{n_2} \exp\left(\frac{2(n_2+1)}{\pi\sqrt{1+3/n_2}} \cdot \omega^{3/2}\right) \tag{2.3}$$

$$\dot{\omega} = D\left(\frac{1-e^{-q_2}}{q_2}\right)\sigma_r^p e^{q_2\omega} \tag{2.4}$$

with $\{C, n_2, D, q_2, p\}$ representing material constants and σ_r denoting the rupture stress.

2.5.1.1 Application to composites

The prime difference in the fracture mechanism of monolithic metallic structures and composites is that in the former a single dominant crack contributes to the overall material degradation and failure, whereas in the latter, a large number of micro-cracks can be evenly distributed within the overall structure [256] (Fig. 2.13). Due to the uniform distribution of micro-cracks within the material volume, damage in composites is regarded as a homogeneous phenomenon and renders itself naturally for the application of CDM models. Fracture mechanics and micro-damage mechanics approaches model each individual crack and their interaction with other defects which require high amount of computational resources and are practically inefficient for large-scale industrial problems. CDM provides an efficient alternative to model constitutive models for damaged composites by representing the complete damage effect by means of a homogeneous damage field.

Over the past five decades, CDM has proven to be an effective tool for predicting damage initiation and evolution in composite laminates and subsequently the load-bearing capacity. In CDM theory, the damage evolution laws for fibre-reinforced plastics (FRP) are established based on damage tensors and internal state variables, that relate to mechanical aspects of damage mechanisms and the dissipation energy required for damage evolution [42]. To this point, several theories and failure criteria have been established that predict progressive damage and ultimate failure strength of composites based on di-

verse failure mechanisms, e.g. fibre breakage, fibre pullouts/bridging, debonding, matrix cracks, shear failure etc. The most prominent amongst these are the Hashin [257], LaRC [258–261], Rotem [262–264], Puck [265, 266], Tsai-Wu [267], Tsai-Hill [268], maximum stress [269], Hoffman [270], and Yamada-Sun [271] failure criteria. With an exception of the LaRC, a large number of these continuum-based criteria are empirical in nature, and are derived as a relation between the internal stresses and experimental material strength measures at the onset of failure [258].

Chaboche [272] incorporated CDM into a generic thermodynamical framework by accounting for the irreversible nature of damage, and developed it into a systematic branch of mechanics by introducing damage as a state variable. CDM has proved its robustness in variety of cases where computational fracture mechanics becomes difficult to apply, e.g. ductile damage scenarios under large deformations [273] or in composites with brittle matrices and relatively weak inter-facial bond that display extensive debonding behaviour, which makes it difficult to identify the exact point of crack initiation [274]. One of the earliest attempts to apply CDM to composites can be traced back to Talreja [275], who characterized the damage response using a set of vector fields representing different damage modes. This was later extended to predict damage evolution in cross-ply laminates [276], see also [277] for overview of developments in fatigue and damage of composites.

The fundamental assumption of CDM theory is to treat the damaged material as a statically homogeneous continuum so that a macro-scale material constitutive relationship involving elasticity and damage can be used to describe the overall material behaviour. As a result, the concept central to CDM is the homogenization of damage for a representative volume element (RVE) inside the damaged material. For this concept to be legitimate, the size of RVE has to be sufficiently large so that the effective material properties of damaged material do not depend on the locations of micro-cracks [92, 256]. Allix et al. [278] implemented inner failure and delamination initiation of composite laminates accounting for their nonlinear behaviour.

Ladevèze et al. [279] proposed a damage meso-model for composite laminates capable of computing damage mechanism intensities inside the plies as well as interfaces. Maimí et al. [118, 119] introduced a continuum damage model based on anisotropic damage tensor and damage activation function based on LaRC04 failure criteria to predict diverse ply-level failure mechanisms. Camanho et al. [280] compared the strength and size-effect prediction capabilities of CDM model and established its robustness and accuracy over other damage modelling approaches. Thermodynamic models to describe progressive failure and stiffness degradation properties in composite laminates were established for plane-structures in [280–282] and for cylindrical laminates in [283, 284]. Pinho et al. [120, 285] developed a combined 3-D failure criteria for laminated fibre-reinforced composites that derived all damage model properties from physics-backed models. The model was successfully applied to reproduce key failure aspects observed in composites like the inclined fracture plane in matrix compression, $\pm 45^o$ shear failure patterns, kink band formations, crushing of composite column etc [120, 285]. CDM has been extensively used in modelling progressive damage based on anisotropic intralaminar ply-failure mechanisms including fibre/inter-fibre failures, matrix cracks, debonding etc [286–289], fatigue failure [290–295], damage evolution under low-velocity, high-energy and ballistic impact scenarios [2, 296–301]. A detailed review of CDM models has been previously reported in [42, 180].

A downside of CDM models is that they are phenomenological rather than being derived from a robust mathematical/ physics-based framework. Also, when the strain softening behaviour is included within the CDM, the corresponding boundary value problem becomes ill-posed often resulting in numerical instabilities [281, 302, 303]. Consequently, the finite-element solution becomes mesh-dependent and additional energy-based regularization techniques, e.g., the crack-band model, must be employed to prevent spurious damage localization and ensure an admissible mesh-objective solution [118, 128]. Although CDM models have reached at a matured stage and provide good estimate of overall reduction in material strength, using them to

model multiple localized crack paths such as the one observed during crack branching and merging phenomena is a difficult and challenging task.

2.5.2 Phase field modelling (PFM)

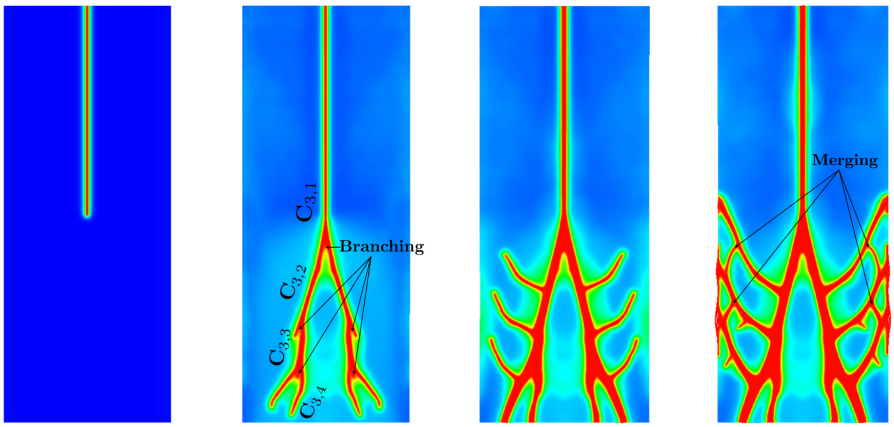

Figure 2.14: Modelling of crack branching/merging using Phase field modelling (PFM) (image reproduced from Kakouris and Triantafyllou [19], with permission from Elsevier)

PFM falls under the broader category of diffused crack approaches and uses the variational theory of fracture [93] as point of departure. In PFM, the crack is diffused into the surrounding domains instead of being modelled as a discrete geometrical entity, and the width of this diffusion zone is controlled via a length-scale parameter l_o.

Contrary to CDM, the damage description in PFM is obtained in terms of a phase field that naturally emerges as the solution of a physics-driven partial differential equation, which minimizes the total potential energy over the entire computational domain. This enables accurate representation of cracks without requiring crack-paths to be defined a priori. Furthermore, the crack nucleation, growth, coalescence and crack-arrest are natural byproducts of PFM [304, 305], which renders it with enormous flexibility to model curvillinear crack patterns involving crack merging and branching without any modification of the underlying finite-element mesh [17]. PFM does not require numerical tracking of the evolving discrete crack topologies, and naturally resolves complex problems like 3-D cracking [see, e.g., 129, 306–308] and dynamic fragmentation [309].

In the regularized phase field model, the sharp crack surface is replaced by a diffusive crack interface that is represented by the scalar phase field variable. The phase field variable $\phi \in [0,1]$ indicates the cracked $(\phi = 1)$ and intact $(\phi = 0)$ states of the material [24]. However, ϕ can also be represented conversely with $\phi = 1$ and $\phi = 0$ indicating the intact and cracked states respectively, see e.g. [129]. Both formulations are physically equivalent, and the correct formulation can be chosen based on the representation of ϕ. Phase field method has garnered much attention during the past 10 years due to its highly generalized crack modelling framework which can be adapted to diverse physical applications. Fig. 2.15 depicts the rise in number of PFM-related publications made over recent few years. In the variational theory of brittle fracture, the total energy potential is expressed as the sum of elastic strain energy and the fracture energy as shown in Eq. (2.5) with $\mathcal{G}_c$ as the crack resistance. The path integral in Eq. (2.5) can be regularized via a length-scale l_o dependent domain integral (Eq. (2.6)), and the total potential energy can be minimized with respect to the displacement and phase field (or damage) variables to obtain their corresponding evolution equations in Eq. (2.7).

$$\Psi(\varepsilon, \Gamma_c) = \int_{\Omega \setminus \Gamma_c} \Psi_{el}(\varepsilon)\, \mathrm{d}\Omega + \int_{\Gamma_c} \mathcal{G}_c\, \mathrm{d}\Gamma_c \tag{2.5}$$

$$\int_{\Gamma_c} \mathcal{G}_c d\Gamma_c \approx \int_{\Omega} \mathcal{G}_c F_{\Gamma_c}(\phi, \nabla\phi)\, d\Omega \tag{2.6}$$

$$\nabla \cdot \sigma = \mathbf{0} \;\; ; \;\; \Big(\frac{\mathcal{G}_c}{l_0} + 2\psi_e^+\Big)\phi - \mathcal{G}_c l_0 \Delta\phi = 2\psi_e^+ \tag{2.7}$$

where ψ_e^+ being the maximum tensile strain energy density, see [24, 310] for more details.

Bourdin et al. [94] extended the variational formulations in [93] to provide a general regularised formulation based on the length-scale parameter, that was considered more suitable for numerical approximations. Significant work was performed by Miehe et al. [307] in the context of establishing the thermodynamic consistency of phase field models and extending them to multi-dimensional, mixed-mode, multi-physics and dynamic brittle fractures

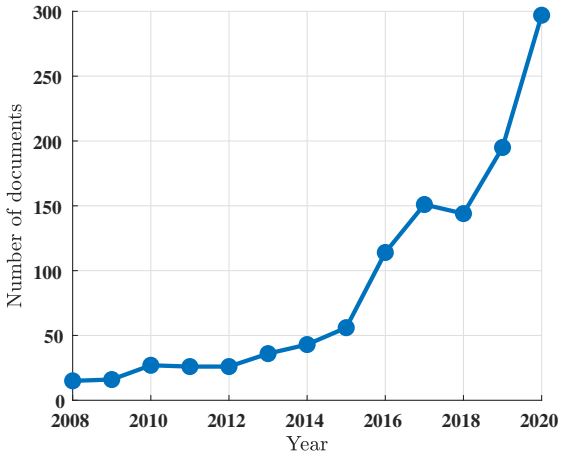

Figure 2.15: An indicative illustration showing rise in the number of articles/ documents related to phase field method published on SCOPUS over the past few years

[24, 311, 312]. Miehe et al. [24] related crack propagation only to tensile strain energy (ψ_e^+) and introduced a local history variable as the crack driving force that controls the evolution of crack phase field. The phase field evolution Eq. (2.7) may yield both homogeneous and non-homogeneous solutions for the phase field parameter.

The extensions of PFM to model ductile fracture were proposed in [129, 313–317] that also included finite strain applications. PFM has been applied to model hydraulic [318–320], chemo-mechanical [321–323], thermo-mechanical [324, 325] and fatigue fracture problems [326–328]. In addition to FEM, phase field method has been incorporated within Material Point Method (MPM) [19, 54, 329], Virtual Element Method (VEM) [330, 331] and Isogeometric Analysis (IGA) [129, 332] frameworks. The PFM has been used in modelling thin-shell fractures based on the Kirchoff-Love (KL) shell theory [333–335]. Kiendl et al. [335] and Ambati and De Lorenzis [314] adopted higher order smooth basis functions (NURBS) for KL and solid-shell elements respectively, whereas Amiri et al. [333] employed maximum entropy meshfree approximations based on C^1 continuous basis functions. Reinoso et al. [336] extended the PFM for brittle fracture in large-deformation solid shell elements based on enhanced assumed strain (EAS) formulations. However, despite significant computational gains offered by shell elements in simulating three dimensional surfaces, there have been very limited efforts to apply PFM in shell damage problems [337].

PFM has been implemented in Abaqus via User element (UEL) [97, 338, 339] and User material (UMAT) [306] subroutines. Liu et al. [306] compared the monolithic and sequentially staggered schemes for coupled phase field models using Abaqus on the basis of their efficiency, accuracy, and sensitivity to mesh sizes. Although the conventional monolithic algorithm provides accurate fracture predictions, it suffers from poor convergence issues due to the non-convexity of the underlying energy functional with respect to both displacement and crack phase field variables [337]. Efforts have been made to alleviate this issue, see e.g., line search assisted monolithic techniques [340], and the more efficient Broyden–Fletcher–Goldfarb–Shanno (BFGS) monolithic algorithm [339, 341] that involves fewer iterations and reformulations of the system matrix in each increment.

It is of interest to note that due to the non-convexity of energy functional that needs to be minimised in the phase field models, the necessary stationarity conditions may admit multiple solutions, see e.g. [342–344]. There doesn't exist a general numerical algorithm that can guarantee global minimisation of such non-convex functionals. Hence, the solution obtained from the coupled phase field equations is non-unique in the sense that it is one of the several local minimisers. Gerasimov et al. [344] proposed a stochastic solution based on random fields, which allows capturing several non-unique crack solutions along with their probability of occurrence.

One of the demerits of conventional phase field models for brittle fracture is that the fracture response and the critical fracture stresses depended on the chosen value of the length-scale parameter l_o which is considered as a numerical parameter [24, 345]. This poses limitations on the fracture prediction capabilities of PFM in real-life scenarios and makes experimental verification of PFM difficult. Borden et al. [129] analytically derived the critical values of stresses, strains and phase field variable for the homogeneous 1-D case Eq. (2.8), and suggested that l_o should not only be considered as a numerical parameter, but as a material property since it influences the critical stress

σ_c.

$$\sigma_c = \frac{9}{16}\sqrt{\frac{E\mathcal{G}_c}{6l_o}} \; ; \; \varepsilon_c = \sqrt{\frac{\mathcal{G}_c}{6l_oE}} \; ; \; \phi_c = \frac{3}{4} \tag{2.8}$$

Tanné et al. [304], see also [346], showed based on 1-D tension problem that l_o must be linked to material's characteristic length and peak strength to make quantitative predictions of crack nucleation; this was verified on 3-point and 4-point bending of geometries containing different types of notches and different brittle materials including steel, Polyvinyl chloride (PVC) foams, Polymethyl methacrylate (PMMA) etc. To this point, many successful attempts have been made to quantitatively validate experimental brittle fracture response of different materials by appropriately choosing l_o based on critical stress [304, 347–350].

The vast majority of PFM related works have focused on the regularization of Griffith [146] type brittle fractures, that consider stress fields at the crack-tip to be singular. However, most materials are not perfectly brittle in the Griffith sense; rather, they exhibit some ductility after reaching the peak fracture stress. This is due to the formation of a fracture process zone (FPZ) ahead of the crack-tip that is characterized by small-scale yielding and micro-crack initiations [351]. The assumption of pure-brittle fracture is valid only as long as the size of the FPZ is considerably small in comparison to the entire structure.

However in the general case, the fracture is quasi-brittle with Griffith's theory being no longer valid, and hence the effect of cohesive forces in the FPZ must be accounted [351]. Wu [352] first implemented a generalized cohesive description of phase field method for treating quasi-brittle fracture scenarios, which could be adapted to calibrate different cohesive softening laws. The primary advantage of the cohesive phase field model is that the critical stresses are inherently independent of the length-scale parameter l_o [353], and the model can be effectively calibrated using the cohesive softening parameters that renders it with enormous flexibility in accurately predicting experimental fracture response [352]. The cohesive PFM has been successfully applied within the context of hydrogen assisted cracking [354], fatigue damage mod-

elling in rubber [355], dynamic fractures [351], macro-meso damage modelling of quasi-brittle materials [356], multi-phase materials [357] and quasi-brittle fractures in concrete [358].

2.5.2.1 Application to composites

Some efforts have been made to apply PFM model for cohesive fractures that were particularly aimed towards modelling composite interface delamination problems, see e.g. [359–361]. In these works, the cohesive zone approach [111] was adapted into an energetic framework and an auxiliary field variable was introduced to represent crack opening across the localization band. The motivation to use an auxiliary field was to define the crack openings as properly defined kinematic quantity, instead of an internal discontinuity as usually done for brittle fracture. However, these approaches require tracking of crack propagation paths similar to the discrete crack methods and lead to spurious numerical oscillations due to the mismatch between cohesive traction and bulk stresses, thereby limiting its application to simpler loading scenarios [352].

Contrary to [359], Nguyen et al. [361] incorporated level-sets to describe diffuse displacement jump at the interfaces and used the phase field variable directly to model both bulk brittle fracture and interface cracking. Roy et al. [362] presented a general phase field augmented peridynamics damage model to model delamination in composite structures, that inherently models cohesive damage evolution and eliminates the need of a traction separation law. It must be highlighted that the application of PFM to model delamination in composites has currently been limited, except few other recent works, see e.g. [121, 363–365].

Despite the significant advantages offered by PFM, there have been only limited applications vis-à-vis the simulation of intra-laminar fracture problems in composites [27, 347, 350, 364]. The primary reason is that the composite intra-laminar fractures are highly anisotropic in not only their elastic but also fracture regime. Although there have been a wide variety of anisotropic phase

field models developed till-date, see, e.g., [25, 366, 367], most of them are based on a unique fracture toughness distribution defined with respect to the crack orientation. This is not in line with the actual fracture behaviour of composites, wherein each intra-laminar failure mode, i.e., fibre breakage under tension, matrix cracking under tension/shear, has different critical stresses and energy release rates associated with them [347]. Moreover, most currently available anisotropic phase field models assume material properties to be isotropic which is in contrast to composites which display highly anisotropic material behaviour corresponding to matrix and fibre directions.

Bleyer and Alessi [27] modelled anisotropic brittle fracture in composites considering distinct phase fields for longitudinal and transverse damage mechanisms. Reinoso et al. [368] predicted the strength of notched thin-ply laminates using a homogeneous isotropic phase field model and compared it to a finite fracture mechanics (FFM) approach. Dean et al. [350] coupled phase field method with a pressure-dependent phenomenological elasto-plastic material model for ductile fracture in short fibre reinforced composites. Natarajan et al. [369] studied the role of fiber-orientations and the inter-fiber spacing on the fracture characteristics of constant/variable stiffness composite laminates using a brittle phase field model.

Reinoso et al. [370], Guillén-Hernández et al. [371] combined phase field and cohesive zone models to investigate failure initiation at composite micro-scales. There have been some efforts to model the interaction between intra-laminar and inter-laminar failures in composites by coupling the brittle phase field model and cohesive zone method in a physically consistent manner, see for e.g. [364, 365, 372]. Quintanas-Corominas et al. [347] developed a novel and robust strategy to simulate intra-laminar and trans-laminar brittle fracture in long-fibre composites by incorporating anisotropy in both the elastic and fracture properties. Their implementation relied on an additive split of the crack-driving forces associated with each individual damage mechanism, and the same phase field variable was associated with all driving forces. It was also highlighted that this approach results in a single stress-degradation function

that triggers the degradation of all elastic properties simultaneously and by the same amount, which eventually may lead to premature triggering of failure in a full laminate analysis. Zhang et al. [373] combined the phase field and cohesive element models to capture complicated progressive mechanisms in composites. Recently, significant efforts have been made in analyzing intra-laminar fractures of long fibre-reinforced (LFRC) [371, 374, 375], short fibre-reinforced (SFRC) [350] and curved fibre [28] composites.

The major advantage of diffuse crack methods such as the PFM specifically lies in their generality. On the contrary, discrete crack methods involve significant algorithmic changes when extended to exhibit similar crack modelling capabilities, as the codes are often custom and not readily extendable to further types of analysis [17]. PFM facilitates use of a robust physics-based fracture modelling framework that is backed by rigorous variational structure. A downside of PFM is that a fine mesh is often required for accurate resolution of the crack-paths that leads to high computational costs. However, this computational burden can be effectively addressed using straightforward utilization of parallel solvers, adaptive mesh refinement [129, 376], multiscale methods [377, 378] and local/global solution technique [379]. In addition, the ease of extending PFM to simulate 3-D fractures, curvillinear crack patterns and multi-physics problems, and their robust connection to both finite fracture and continuum damage mechanics effectively renders them to be worthy of further investigation [337].

2.6 Multiscale Modelling of Composites

Characterization of defects and damage within a multiscale framework and modelling them as a single unified criteria has consistently been a difficult and challenging task. A typical large scale composite structure can be modelled on (at least) three different scales, Fig. 2.16:

- Macro-scale (level of structures)

- Meso-scale (level of plies)
- Micro-scale (level of fibres/matrix)

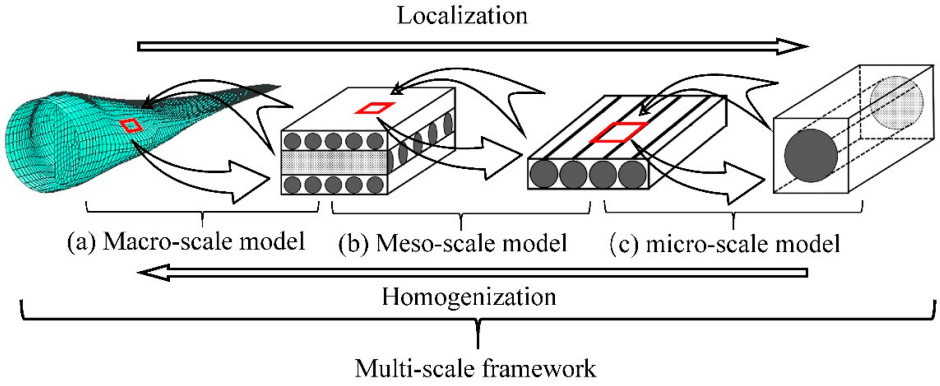

Figure 2.16: Schematic description of different scales of resolution within composite materials (image reproduced from Wang and Huang [20])

When the modelling of composites is performed solely at a macroscopic scale (e.g. in conventional finite element methods), the physics at the microscopic scale is often accounted in the form of empirical constitutive relations. On the contrary, the modelling approaches operating at microscopic levels (like quantum mechanics or molecular dynamics) assume macroscopic material behaviour to be homogeneous at larger scales. This renders macroscopic models not being accurate enough to capture material's physical behaviour, whereas microscopic models are computationally inefficient for solving large-scale industrial problems [380]. In composites, experimental evidence suggests that defects and damage often initiate at the micro-scale (fibre/matrix level) leading to a nonlinear material behaviour. Composites can be categorized as materials exhibiting heterogeneous microstructure, whose specific morphology affects the mechanical behaviour of the final product [44]. They can hence be regarded as multiscale materials which have much lower order scale for its constituents than the scale of the resulting material, and subsequently the complete structure which is an assemblage of mesoscale laminates (Fig. 2.16). From a simulation standpoint, accounting for the nonlinear mechanical behaviour of composites at macro-scale (component/structural level) and accurately predicting the structure's critical load bearing capacity and associated damage thresholds requires significantly fine mesh, rendering the method inefficient.

Multi-scale methods couple the physical models at different scales and offer a reasonable compromise between the overall accuracy and efficiency.

Multiscale modelling has emerged as a robust method for the analysis of structures and characterising their material behaviour at multiple scales. Multiscale methods incorporate different constitutive relations for describing different scales of resolution, and helps achieving efficiency of macroscopic models with the accuracy of microscopic models [381]. Such an approach promises to make the analysis efficient by significantly reducing the computational overheads as compared to standard simulation methods [382]. Multiscale methods extract analysis information from a finer scale and solve an equivalent problem on a coarser scale, often with the aid of finite element methods [383]. The micro-scale in composites usually corresponds to the fibre/matrix level, whereas in metals it corresponds to the atomistic level [384]. Most of the physical phenomena observed at the structural level are a direct consequence of microscale properties, for e.g. the fibre length and orientations in the case of composites or grain sizes/shapes in the case of metals.

Physical problems involving multiple scales can be categorized into two types, i.e., Type A in which multiscale modelling is used to resolve local defects and stress singularities, and Type B in which the multiscale model supplies equivalent constitutive relations at the macro-scale [385, 386] (Fig. 2.17). In type A problems, the computational domain is decomposed into interconnected regions that can be solved using different modelling techniques by incorporating a global-local coupling at their interfaces. The more expensive nonlinear microscopic model is employed only in the region of interest, e.g. near the cracks, dislocations, shocks contact lines etc., whereas a macroscopic model is used in regions far-away from these defects, see e.g. [387–389].

On the other hand, type B problems are solved with homogenization based approaches wherein the meso-scale models are solved independently of the macro-scale simulations, and an equivalent constitutive law is defined at the macro-scale. The meso-scale simulations are performed on a representative volume element (RVE) subjected to macro-scale strains under periodic

boundary conditions. In the case of damage evolution at meso-scale, the final degraded stresses are supplied back to the macro-scale model, thus establishing a direct coupling between the meso- and macro-models.

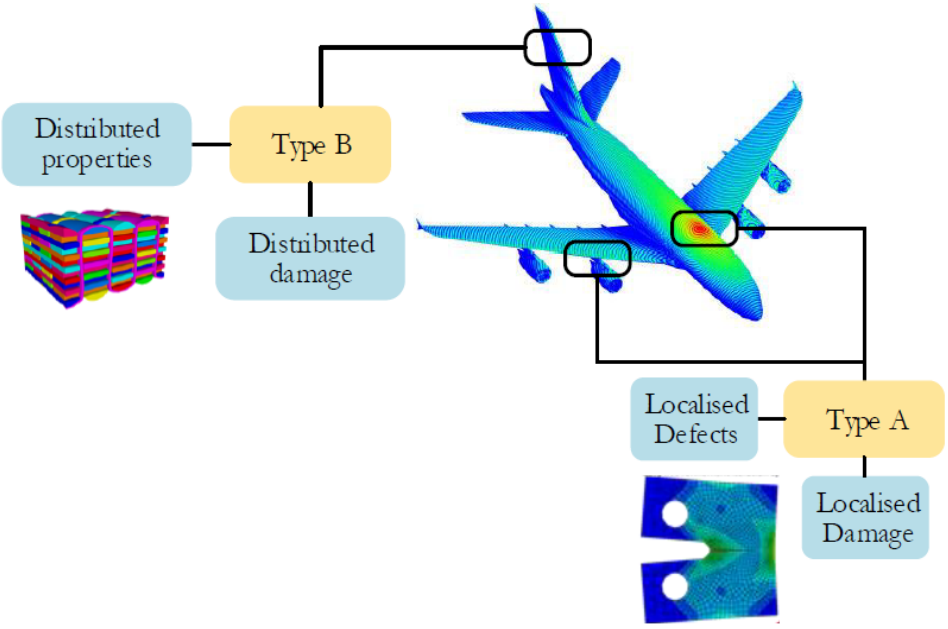

Figure 2.17: Illustration of Type-A and Type-B multiscale physical problems (image reproduced from [21])

One of the important examples of global-local multiscale approach is the Finite Element Tearing and Interconnecting (FETI) [390]. In FETI, the domain is decomposed into disconnected domains that are meshed separately with non-conforming meshes, and Lagrange multipliers are introduced to iteratively enforce the displacement field continuity between different sub-domains [390]. However, FETI relies on stiffness matrices decomposition to uncouple different sub-domains, which poses implementation challenges for problems with nonlinear material behaviour [389].

Another useful technique is to apply non-intrusive global-local formulations iteratively to achieve force and displacement equilibrium at the interface [387]. The advantage of this technique is that the domain could be discretized with a relatively coarse mesh and solved using a linear elastic material model, whereas the nonlinearity can be handled in a separate local model with a fine discretization. The method is non-intrusive in the sense that no modifications or remeshing are required in the original global model; rather the

local model can be analysed independently of the global model. Several works have adopted the global-local technique for damage modelling in composites [389, 391–393]. A limitation of this method is that compatible sub-domain meshes need to be defined with a clear interface between the global and local models, so that the force and displacement equilibrium can be achieved between them. This becomes challenging especially in materials with complex micro-structure where compatible meshes are difficult to define.

Other multiscale techniques used within the context of damage modelling include domain decomposition approaches with interlocked sub-domains and interfaces [394, 395] and model reduction techniques [396, 397] wherein the damage is modelled in the meso-scale model. Multi-scale methods for heterogeneous materials including composites have been reviewed in [44, 398, 399].

Homogenization based techniques are another class of multiscale approaches, in which the homogenized stress response is extracted from the meso-scale model and provided to the macro-scale as a response to applied macro-strains [400, 401]. Meso-scale models comprising RVE that denote the smallest repeating unit of composite material are solved under periodic boundary conditions (PBC) [402, 403]. The averaged RVE stress-strain response can be obtained using asymptotic [404–406], numerical [407, 408] or computational [401, 409, 410] homogenization.

The fundamental assumption in homogenization theory is that the principle of scale separation must hold, i.e. the size of RVE must be considerably smaller than the size of macro-scale structure [411]. Homogenization based methods have been widely used within the FE^2 approach for concurrent analysis of macro and micro/meso models [411–415]. In FE^2 models, each integration point in the macro-mesh comprises an underlying RVE, that is representative of the complex internal structure of composites. During the macro-scale simulations, the macro strain tensor at each of these integration points is transferred on to the RVE as boundary values, which is then analysed under periodic boundary conditions (PBCs). The homogenized stresses obtained from the RVE simulations are transferred back as equivalent constitutive response

to the macro-model.

Overall FE^2 is a robust multiscale technique that models both linear and nonlinear problems accurately. However, due to the need of solving both macro and micro-scale simulations concurrently, it is associated with high computational costs. To alleviate the computational burden, FE^2 analysis has been used in conjunction with surrogate modelling techniques. This eliminates the inefficient procedure of concurrently analysing RVE at each time-increment, and rather provides the homogenized stress-strain response from the micro/meso scale directly using a robust surrogate model [61, 416]. El Said et al. [389] employed a Polynomial Chaos Expansion (PCE) based surrogate model to analyse the multiscale elastic response of thick composites containing internal defects and features. Yan et al. [416] introduced an efficient multiscale framework to model progressive damage behaviour in composites using surrogate model based on Artificial Neural Networks (ANN).

Several other surrogate and reduced order modelling approaches have been used to perform multiscale damage and reliability analysis of composites [417–420]. Multiscale damage modelling in composites has traditionally been performed using CDM models with homogenization based approaches [406, 421, 422]. Significant efforts have also been directed towards applying mean-field homogenization method with gradient enhanced damage models [423, 424], multiscale finite element method (MsFEM) with PFM [377, 378, 425] and XFEM [426, 427], and variationally consistent computational homogenisation (VCH) framework for phase field damage [428]. Surrogate models present a promising alternative to replace computationally expensive RVE feedback loop in FE^2 approaches, however, their usage within the context of multiscale modelling has been fairly limited till date.

2.7 Conclusions from state-of-the art

Based on the literature survey, the main limitations/challenges of different damage modelling methods that are currently applicable for composites have

been identified. Some of these challenges and potential contributions towards overcoming them are highlighted below:

- Most discrete damage modelling approaches face challenges in modelling vast number of mutually interacting intra-laminar composite damage mechanisms. The approaches based on smooth representation of damage (CDM/PFM) display a promising behaviour vis-à-vis composite damage modelling. However, CDM relies on a phenomenological description of damage and cannot accurately reproduce localized curvillinear crack paths. On the other hand, PFM is backed by robust variational framework, and has displayed excellent capabilities in predicting accurate material fracture behaviour as well as modelling complex crack patterns including crack branching and merging. This renders PFM worthy of further investigation for modelling diverse intra-laminar failure modes in composites.

- Thin composite plies are often numerically modelled using Reissner-Mindlin shell elements due to their high computational efficiency. Damage in composite plies occurs under the influence of coupled membrane (in-plane) and bending (out-of-plane) deformations. However, a robust phase field modelling framework that simulates damage evolution in thin plies, whilst simultaneously alleviating both transverse shear and membrane locking effects observed in Mindlin shell elements, is missing in the literature. This is addressed in Chapter 3 by proposing a brittle phase field damage model for thin Mindlin shell elements based on MITC4+ approach.

- Damage in thin-ply composites is accompanied with fibre pullouts that leads to fibre-bridging between crack faces and subsequent formation of fracture process zone. The damage behaviour in such cases is quasi-brittle and is characterized by gradual degradation of material strength post damage-initiation. This effect becomes more prominent in thin-ply composites, where fibre-based failures are influential, and transverse

matrix cracks and subsequent delamination are practically delayed or suppressed. To this end, an anisotropic cohesive phase field model has been proposed in Chapter 4, which simulates the quasi-brittle fracture behaviour and accurately captures the diverse intra-laminar failure modes of composites, e.g. fibre cracking/ pullouts/ bridging and matrix shear cracking. The proposed damage model is validated against experimental results and subsequently extended to simulate damage evolution in full composite laminates.

- Composite damage initiates at the micro-scale (fibre/matrix level) and propagates onto the macro-scale (component level). This progressive damage is manifested at the component and structural level as loss of stiffness, loss of strength and may eventually lead to structural collapse. A multiscale approach is required to efficiently simulate these physics. FE^2 relies on simultaneous numerical modelling of different composites scales, and provides reliable fracture estimates for both linear and non-linear analyses, however, it is associated with high computational costs. A multiscale modelling approach based on PFM and involving surrogate models based on Polynomial Chaos Expansion (PCE) and Artificial Neural Networks (ANN) is proposed in Chapter 5. The approach provides equivalent stress response at the macro-scale corresponding to applied macro-strains using a surrogate model, and avoids simultaneous solving of meso-scale RVE models at each time increment.

3

Phase field modelling of brittle fracture in MITC4+ shell elements

In this chapter, a phase field modelling framework to simulate brittle fracture using MITC4+ Reissner-Mindlin shell elements is developed. These are widely used in numerical modelling of thin-ply composites. As the MITC4+ formulation alleviates the effects of membrane and shear locking, the formulation renders itself naturally to the analysis of not only planar but also curved geometries.

The overall objective is to model damage initiation and evolution in thin-plies under the effect of coupled membrane and bending deformations, that occur in aerospace composites during impact damage scenarios. Mindlin-shell elements suffer from membrane and transverse shear locking issues when they are thin, i.e. they over-predict the membrane/bending stiffness and hence, under-predict the displacements by orders of magnitude lesser than their analytical estimates. In conventional shell element formulations, locking occurs purely as a result of the interpolation scheme chosen to calculate the membrane and transverse shear strains. In particular, the standard displacement-based interpolation functions result in non-zero (parasitic) transverse shear strains within the element, even when a constant bending moment is applied. Hence, although the shell kinematics contain Kirchhoff shell assumptions, the numerical discretization procedure does not well-represent these assumptions [22].

This renders Mindlin shells incapable of modelling thin ply-like structures unless locking alleviation techniques are applied [22]. Similarly, membrane locking may occur when flat shell elements are used in a curved geometry, when the shell element geometry itself is curved (e.g. higher order shell elements), or when nonlinear deformations lead to out of plane distortions in the shell element [23]. Membrane locking leads to spurious coupling between the membrane and transverse shear strains, and hence exclusion of desired bending modes from the element's kinematic response [8].

In the current implementation, locking issues are alleviated using the MITC4+ approach [22, 23], which treats both membrane and transverse shear locking. The implementation is restricted to 4-noded shell elements subjected to small strain deformations; however, the approach is general and can be straight-forwardly extended to higher order MITC shell elements. The proposed formulation is used to examine the post-fracture response of 3-D surfaces. The proposed scheme is validated by comparing against analytically predicted critical fracture loads. The proposed approach forms the foundation of anisotropic intra-laminar damage model for thin-ply composites presented in the subsequent Chapter 4. The research outcomes described in this chapter have been published in [64].

The chapter is structured as follows: In Sec. 3.1, the geometrical and kinematic considerations for the Mindlin shell element are discussed on the basis of the small-strain theory and coupled bending/membrane deformations. This is followed by a brief review of MITC4/MITC4+ formulations in Sec. 3.1.3. In Sec. 3.2 the combined constitutive relations extending brittle phase field theory to MITC4+ shells are proposed, followed by numerical validations in Sec. 3.3.

3.1 The MITC4+ Reissner-Mindlin shell element

3.1.1 Geometrical considerations

Point of departure for the formulation presented herein is the Reissner-Mindlin degenerated 4-node shell element [8]. The element comprises 6 local degrees of freedom (DOF), i.e., 3 translations and 3 rotations, as shown in Fig. 3.1.

The vector of the local nodal DOF at each node i is $\mathbf{d}_i = [u_i, v_i, w_i, \alpha_i, \beta_i, \gamma_i]$ (Fig. 3.1b). The translational DOF, i.e., $[u_i, v_i, w_i]$ are defined with respect to the global coordinate system xyz. However, the rotational DOF, i.e., $[\alpha_i, \beta_i, \gamma_i]$ are aligned with the local shell vectors, i.e., $\mathbf{V}_{1i}$, $\mathbf{V}_{2i}$, and $\mathbf{V}_{3i}$, respectively. The vector $\mathbf{V}_{3i}$ is normal to the shell midsurface; the coplanar vectors $\mathbf{V}_{1i}$, and $\mathbf{V}_{2i}$ are perpendicular to $\mathbf{V}_{3i}$ (see also Fig. 3.1).

The coordinates of any arbitrary point $\mathbf{x}$ within the shell element are expressed in terms of the mid-surface nodal coordinates according to Eq. (3.1)

$$\mathbf{x} = \sum_{i=1}^{4} N_i \mathbf{x}_i + \sum_{i=1}^{4} N_i \zeta \frac{t_i}{2} \mathbf{V}_{3i} \tag{3.1}$$

where, t_i is the shell thickness, and N_i, and $\mathbf{x}_i = [x_i, y_i, z_i]^T$ are the shape functions and coordinate vectors for the mid-surface nodes, respectively. Furthermore, ζ is the parametric coordinate along the thickness direction ($\zeta \in [-1, 1]$), see also Fig. 3.1a.

It becomes evident from the aforementioned that due to the non-planar geometry of a curved shell, the shell kinematics needs to be resolved in shell-specific local coordinate systems. For the sake of convenience, the following coordinate systems as shown in Fig. 3.2 are introduced.

1. A global Cartesian coordinate-system $[x, y, z]$; this is used to define the geometry and the translations of the element in the physical space.

2. A parametric coordinate-system $[\xi, \eta, \zeta]$; this is used to define the parametric space of the element and hence account for non regular quadrilat-

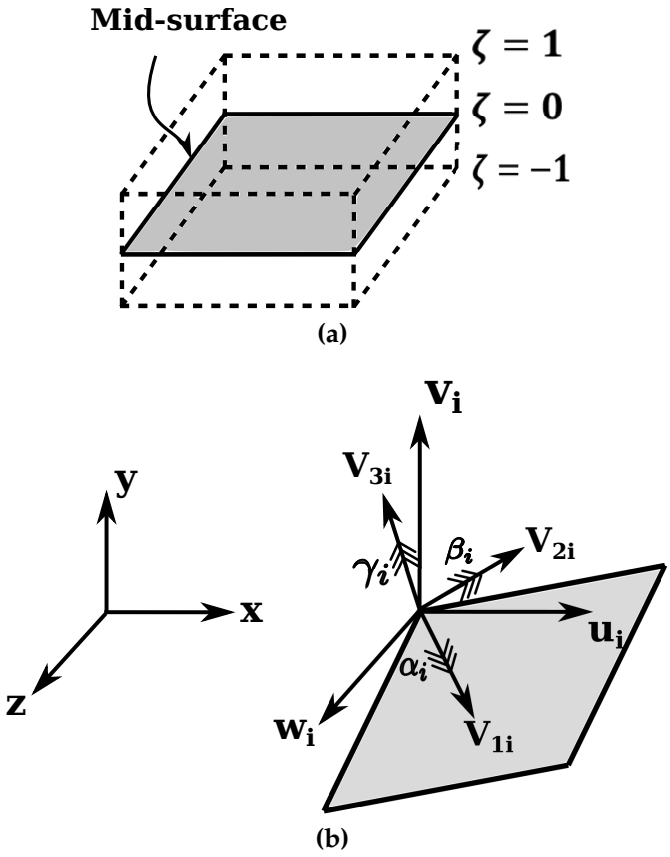

Figure 3.1: A degenerated 4-noded Reissner-Mindlin shell element: (a) shell mid-surface (b) degrees of freedom and local coordinate system

eral geometries.

3. A shell-aligned local coordinate system $[1, 2, 3]$ based on the mid-surface nodal vectors $[\mathbf{V}_1, \mathbf{V}_2, \mathbf{V}_3]$; these are used to define the directions of rotational DOFs $\{\alpha, \beta, \gamma\}$ and account for the surface curvatures.

4. Finally, a convective coordinate system $[r, s, t]$ in which all MITC4+ modifications are performed as discussed in Sec. 3.1.3. This can be given as $r = g_1/|g_1|$, $s = g_2/|g_2|$, $t = g_3/|g_3|$. Here, g_i are the tangent vectors to the shell-surface at any arbitrary point with position vector $\mathbf{x}$. These can be obtained as $g_i = \mathbf{x}_{,\zeta_i}$, wherein $(\cdot)_{,\zeta_i}$ denotes partial derivative with respect to the parametric directions $\zeta_i \in \{\xi, \eta, \zeta\}$ (see Appendix A.1).

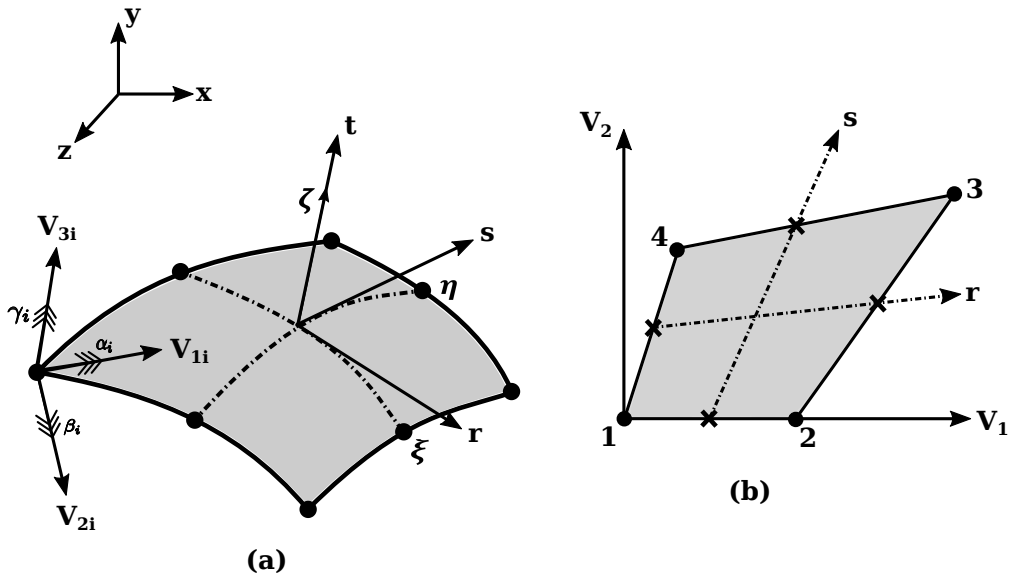

Figure 3.2: (a) Illustration of the different coordinate systems used in the formulation of the Reissner-Mindlin shell element (b) Orientation of $[r,s]$ with respect to $[1,2]$ coordinate system in a flat shell element

3.1.2 Kinematics

The displacement at any point P lying above or below the shell mid-surface (Fig. 3.1a) is expressed with respect to the mid-surface displacements according to Eq. (3.2) [8].

$$\mathbf{u}_P = \begin{bmatrix} u \\ v \\ w \end{bmatrix} = \sum N_i \left(\begin{bmatrix} u_i \\ v_i \\ w_i \end{bmatrix} + \zeta \frac{t_i}{2} [\mu_i] \begin{bmatrix} \alpha_i \\ \beta_i \\ \gamma_i \end{bmatrix} \right) \tag{3.2}$$

where μ_i contains the direction cosines of the shell vectors $\mathbf{V}_{1i}$ and $\mathbf{V}_{2i}$, and assumes the following form (Eq. (3.3))

$$[\boldsymbol{\mu}_i] = \left[-\frac{\mathbf{V}_{2i}}{|\mathbf{V}_{2i}|}, \frac{\mathbf{V}_{1i}}{|\mathbf{V}_{1i}|}, \mathbf{0} \right] = \begin{bmatrix} -l_{2i} & l_{1i} & 0 \\ -m_{2i} & m_{1i} & 0 \\ -n_{2i} & n_{1i} & 0 \end{bmatrix} \tag{3.3}$$

The strain tensor $[\boldsymbol{\varepsilon}]_{xyz}$ in the global cartesian system is defined according

to Eq. (3.4) below.

$$\boldsymbol{\varepsilon}_{xyz} = \begin{bmatrix} \varepsilon_{xx} & \varepsilon_{yy} & \varepsilon_{zz} & \gamma_{xy} & \gamma_{yz} & \gamma_{zx} \end{bmatrix}^T = \sum_{i=1}^{4} [\boldsymbol{B}_i^{\boldsymbol{u}}] d_i \tag{3.4}$$

where $[\boldsymbol{B}_i^{\boldsymbol{u}}]$ is the 6×6 strain-displacement matrix at each shell node i. The detailed definition of matrix $[\boldsymbol{B}_i^{\boldsymbol{u}}]$ is provided in Appendix A.3, see also Cook et al. [8].

Remark 1. The drilling DOF γ_i have no stiffness associated with them. Hence, when all shell elements that share a common structural node are co-planar, the drilling rotation about the shell normal $\mathbf{V}_{3i}$ at that node is not resisted, which makes the system matrix singular. To alleviate this, in flat-shell geometries, the drilling rotation DOFs γ_i can be directly omitted from the list of overall structural DOFs.

Conversely, when some of the elements connected to a structural node are not co-planar, the normal rotation of any element at the shared node has a component, which is resisted by the bending stiffness of adjacent elements. In this case, suppressing γ_i would naturally lead to an over-constrained model and unwarranted stiffening of the structure [8]. Keeping this in view, in this work all 6 DOFs $[u_i, v_i, w_i, \alpha_i, \beta_i, \gamma_i]$ are retained at nodes which are shared by non-coplanar elements; they are however omitted for nodes shared by coplanar elements. Further details about the numerical treatment of the 6^{th} drilling rotational DOF γ_i are provided in Appendix A.4.

3.1.3 MITC4/MITC4+ formulations

In this section, the modified formulations for the transverse shear strain components based on the MITC4+ approach [22, 23] are briefly presented. The 4-noded flat shell element shown in Fig. 3.2 is considered, with it's convected and shell-aligned local coordinate systems represented by $[r, s, t]$ and $[1, 2, 3]$, respectively.

In the original MITC4 formulations [22], the convected transverse shear

strains ε_{st} and ε_{rt} are assumed constant along the edges perpendicular to the r and s axes, respectively (Fig. 3.3a). Furthermore, at any arbitrary point inside the element, these are interpolated based on the strain values at a pre-defined set of tying points $\{A, B, C, D\}$ (Fig. 3.3a) using Eq. (3.5).

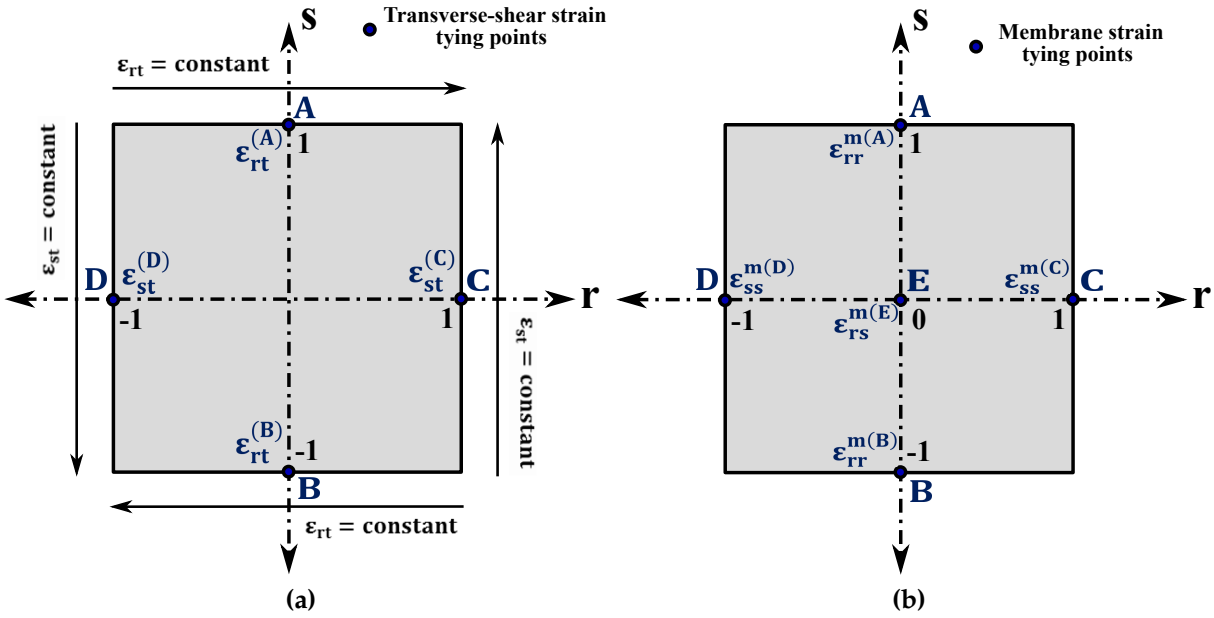

Figure 3.3: Location of tying points used for assumption of (a) transverse-shear strains [22] (b) membrane strains within MITC4+ approach [23]

$$\begin{aligned} \varepsilon_{rt} &= \frac{1}{2}(1+\eta)\varepsilon_{rt}^{(A)} + \frac{1}{2}(1-\eta)\varepsilon_{rt}^{(B)} \\ \varepsilon_{st} &= \frac{1}{2}(1+\xi)\varepsilon_{st}^{(C)} + \frac{1}{2}(1-\xi)\varepsilon_{st}^{(D)} \end{aligned} \tag{3.5}$$

The corresponding transverse shear strains at these tying points, i.e., $\{\varepsilon_{rt}^{(A)}, \varepsilon_{rt}^{(B)}, \varepsilon_{st}^{(C)}, \varepsilon_{st}^{(D)}\}$, are calculated using the standard displacement based interpolation scheme in Eq. (3.4)

$$\begin{aligned} \varepsilon_{rt}^{(TP)} &= (\varepsilon_{rt})_{\text{at TP using DI}} \\ \varepsilon_{st}^{(TP)} &= (\varepsilon_{st})_{\text{at TP using DI}} \end{aligned} \tag{3.6}$$

where $TP \in \{A, B, C, D\}$ denotes the tying points, and DI denotes the direct displacement-based interpolation analogous to Eq. (3.4).

Similarly, in the MITC4+ formulations the membrane strain components $\{\varepsilon_{rr}, \varepsilon_{ss}, \varepsilon_{rs}\}$ are interpolated using separate expressions based on the displacement-based membrane strains at tying points $\{A, B, C, D, E\}$ shown in Fig. 3.3b. The detailed expressions can be referred from [23], and are included in Appendix A.5 for reference.

3.1.4 Coordinate transformations

To formulate the local element matrices, the material orientations have to be accounted for, and hence the constitutive relations have to be defined in their corresponding coordinate system. Therefore, the strain tensor in Eq. (3.4) must be transformed into the shell-aligned local coordinate system $[1, 2, 3]$ using the strain-transformation matrix $\mathcal{T}_\varepsilon$ in Eq. (3.7)

$$\boldsymbol{\varepsilon}_{123} = [\varepsilon_{11}\ \varepsilon_{22}\ \varepsilon_{33}\ \gamma_{12}\ \gamma_{23}\ \gamma_{13}]^T = \mathcal{T}_\varepsilon\ \boldsymbol{\varepsilon}_{xyz} \tag{3.7}$$

A general definition for $\mathcal{T}_\varepsilon$ involving strain-transformation between any two arbitrary coordinate systems is provided in Appendix A.2 for completeness.

The assumed strains introduced in Eq. (3.5) are defined in the convected coordinate system $[r, s, t]$, whereas the strains in Eq. (3.7) are expressed with respect to the shell-aligned local system $[1, 2, 3]$. Hence, to impose the MITC4+ modification, the shell-aligned local strains $\boldsymbol{\varepsilon}_{123}$ must be first transformed into the convective strains $\boldsymbol{\varepsilon}_{rst}$. Due to the planar geometry of the 4-noded Mindlin shell elements, the in-plane directions for both coordinate systems $[r, s]$ and $[1, 2]$ are co-planar, but rotated with respect to each other as shown in Fig. 3.2b. The rotation for transverse shear strains $[\gamma_{13}, \gamma_{23}]^T$ into the convected coordinates $[r, s, t]$ is performed according to Eq. (3.8), see Bathe [74] for details.

$$\begin{aligned} [\gamma_{rt}\ \ \gamma_{st}]^T &= [\mathbf{R}]\ [\gamma_{13}\ \ \gamma_{23}]^T \\ [\mathbf{R}]^{-1}\ [\gamma_{rt}\ \ \gamma_{st}]^T &= [\gamma_{13}\ \ \gamma_{23}]^T \end{aligned} \tag{3.8}$$

where

$$[\mathbf{R}] = \begin{bmatrix} sin\,\beta & -sin\,\alpha \\ -cos\,\beta & cos\,\alpha \end{bmatrix}^{-1} \tag{3.9}$$

In Eq. (3.9), α and β are the angles between the r and V_1 axes and s and V_1 axes respectively, see Fig. 3.2.

The in-plane convective strain components $[\varepsilon_{rr}, \varepsilon_{ss}, \gamma_{rs}]$ are derived according to Eq. (3.10) [74].

$$\begin{aligned} [\varepsilon_{rr}, \varepsilon_{ss}, \gamma_{rs}]^T &= [\mathcal{T}_\varepsilon^{'}]\,[\boldsymbol{\varepsilon}_{123}] \\ [\varepsilon_{11}, \varepsilon_{22}, \gamma_{12}]^T &= [\mathcal{T}_\varepsilon^{'}]^{-1}\,[\boldsymbol{\varepsilon}_{rst}] \end{aligned} \tag{3.10}$$

where $\boldsymbol{\varepsilon}_{123}$ is the 6×1 vector provided in Eq. (3.7). The transformation matrix $\mathcal{T}_\varepsilon^{'}$ with size 3×6 is derived from the full 6×6 $\mathcal{T}_\varepsilon$ matrix shown in Appendix A.2, by extracting its 1^{st}, 2^{nd}, and 4^{th} rows that correspond to the in-plane strain components ε_{rr}, ε_{ss}, and γ_{rs}, respectively.

The MITC4+ modifications are performed on the convected transverse shear strains $\{\gamma_{st}, \gamma_{rt}\}$ and in-plane membrane strains $\{\varepsilon_{rr}, \varepsilon_{ss}, \gamma_{rs}\}$. The total convected strain tensor $\boldsymbol{\varepsilon}_{rst}$ is transformed back into the shell-aligned local coordinate system $\boldsymbol{\varepsilon}_{123}$ by applying the inverse transformations shown in Eq. (3.8)-(3.10).

The complete shell-aligned local strain tensor can then be expressed according to Eq. (3.11).

$$\boldsymbol{\varepsilon}_{123} = \begin{bmatrix} \varepsilon_{11} & \varepsilon_{12} & \varepsilon_{13} \\ \varepsilon_{12} & \varepsilon_{22} & \varepsilon_{23} \\ \varepsilon_{13} & \varepsilon_{23} & \varepsilon_{33} \end{bmatrix} \equiv [\varepsilon_{11}\ \varepsilon_{22}\ \varepsilon_{33}\ \gamma_{12}\ \gamma_{23}\ \gamma_{13}]^T \tag{3.11}$$

In the MITC4+ shell element, plane-stress assumptions hold, i.e., the out-of-plane tensile stress $\sigma_{33} = 0$ in the shell-aligned local coordinate system $[1, 2, 3]$. Hence, the expression for the out-of-plane tensile strain ε_{33} is derived

according to Eq. (3.12)

$$\varepsilon_{33} = -\frac{\nu}{1-\nu}\left(\varepsilon_{11} + \varepsilon_{22}\right) \tag{3.12}$$

where ν is the material Poisson's ratio. The subscript for local strains $\boldsymbol{\varepsilon}_{123}$ is further dropped, and it is denoted as $[\boldsymbol{\varepsilon}]$ in the remainder of this chapter.

As discussed in Sec. 3.1, the translational DOFs $[u_i, v_i, w_i]$ are defined with respect to the the global Cartesian vectors $[x, y, z]$. However, the rotational DOFs $[\alpha_i, \beta_i, \gamma_i]$ are defined in the direction of shell-local vectors $[V_1, V_2, V_3]$. Therefore, the local DOF vector $d_{loc_i} = [u_i, v_i, w_i, \alpha_i, \beta_i, \gamma_i]$ is transformed to the global coordinate system according to Eq. (3.13) below

$$d_{glob} = \left[\mathcal{T}_{rot}\right]^T d_{loc} \tag{3.13}$$

with,

$$\mathcal{T}_{rot} = \begin{bmatrix} 1 & 0 & 0 & 0 & 0 & 0 \\ 0 & 1 & 0 & 0 & 0 & 0 \\ 0 & 0 & 1 & 0 & 0 & 0 \\ 0 & 0 & 0 & l_1 & m_1 & n_1 \\ 0 & 0 & 0 & l_2 & m_2 & n_2 \\ 0 & 0 & 0 & l_3 & m_3 & n_3 \end{bmatrix} \tag{3.14}$$

where $d_{glob} = [u_{xi}, v_{yi}, w_{zi}, \theta_{xi}, \theta_{yi}, \theta_{zi}]$ are the global DOFs in $[x, y, z]$ coordinates, and the expressions for the direction cosines $\{l_i, m_i, n_i\}$ with $i \in \{1, 2, 3\}$ are provided in Eq. (A.9).

3.2 Constitutive phase field model

Griffith's theory of brittle fracture [146] derives from the assumption that the total potential energy of a fractured solid is additively decomposed into bulk strain energy that depends on the elastic deformations, and crack surface en-

ergy as shown in Eq. (3.15).

$$\begin{aligned} \Pi(\boldsymbol{u}, \Gamma_c) &= \int_{\Omega} \psi_e(\boldsymbol{\varepsilon}(\boldsymbol{u}))\, d\Omega + \int_{\Gamma_c} \mathcal{G}_c\, d\Gamma_c - \mathcal{W}_{ext} \\ \text{with,} \quad \mathcal{W}_{ext} &= \int_{\Omega} \boldsymbol{b} \cdot \boldsymbol{u}\, d\Omega + \int_{\partial\Omega} \boldsymbol{t} \cdot \boldsymbol{u}\, d\, \partial\Omega \end{aligned} \tag{3.15}$$

In Eq. (3.15), and also Fig. 3.4, $\boldsymbol{u}$ is the displacement vector at any arbitrary point within the domain Ω, $\boldsymbol{b}$ and $\boldsymbol{t}$ represent the body forces within Ω and surface-traction forces on external boundary $\partial\Omega$ respectively, Γ_c is the internal discontinuous boundary, ψ_e is the elastic energy density and $\mathcal{G}_c$ is the critical energy release rate. The linearised strain tensor $\boldsymbol{\varepsilon}(\boldsymbol{u})$ is given as Eq. (3.16), and can be calculated numerically using Eq. (3.4).

$$\boldsymbol{\varepsilon}(\boldsymbol{u}) = \frac{\nabla \boldsymbol{u} + \nabla^T \boldsymbol{u}}{2} \tag{3.16}$$

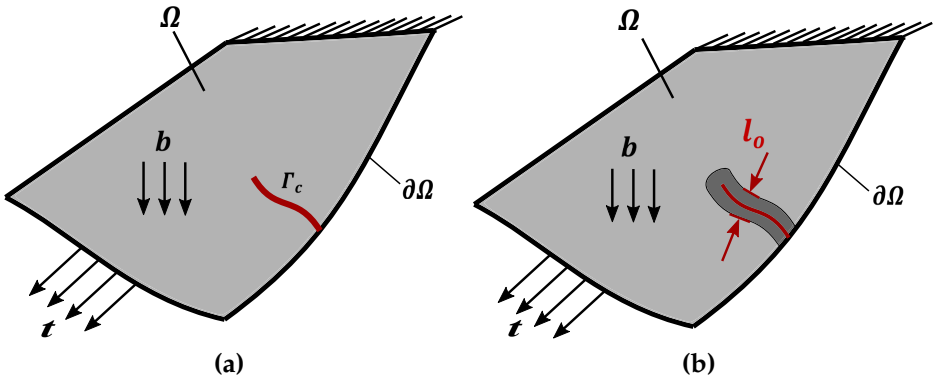

Figure 3.4: Illustration of general shell-domain Ω containing (a) Internal sharp crack, and (b) Diffused crack, and subjected to body force $\boldsymbol{b}$ and surface traction forces $\boldsymbol{t}$

In the variational phase field formulation, the sharp crack surface energy term in Eq. (3.15) is replaced by a volume integral using a phase field regularisation function $F_{\Gamma_c}(\phi, \nabla\phi)$ according to Eq. (3.17); the phase field ϕ becomes a diffused representation of the discrete crack.

$$\int_{\Gamma_c} \mathcal{G}_c d\Gamma_c \approx \int_{\Omega} \mathcal{G}_c F_{\Gamma_c}(\phi, \nabla\phi) d\Omega \tag{3.17}$$

where, $\phi \in [0, 1]$ is the phase field variable. Different variants of phase field

regularisation function F_{Γ_c} can be obtained based on second-order quadratic or linear approximations, or fourth-order quadratic approximation, see e.g. [24, 332, 429, 430]. In the second-order quadratic approximation introduced in Ambrosio and Tortorelli [429, 431], the phase field regularisation function $F_{\Gamma_c}(\phi, \nabla\phi)$ assumes the following form, i.e.,

$$F_{\Gamma_c}(\phi, \nabla\phi) = \left[\frac{(\phi-1)^2}{4l_o} + l_o|\nabla\phi|^2\right] \tag{3.18}$$

where l_o is the length-scale parameter controlling the width of phase field diffusion zone. Using the functional definition of Eq. (3.18), it is straight-forward to show that $\phi = 0$ and $\phi = 1$ correspond to the fully-cracked and fully-intact states of the material, respectively. Fig. 3.5 illustrates the variation of phase field in the direction normal to crack surface using second-order quadratic approximation in Eq. (3.18), as compared to the discrete fracture case.

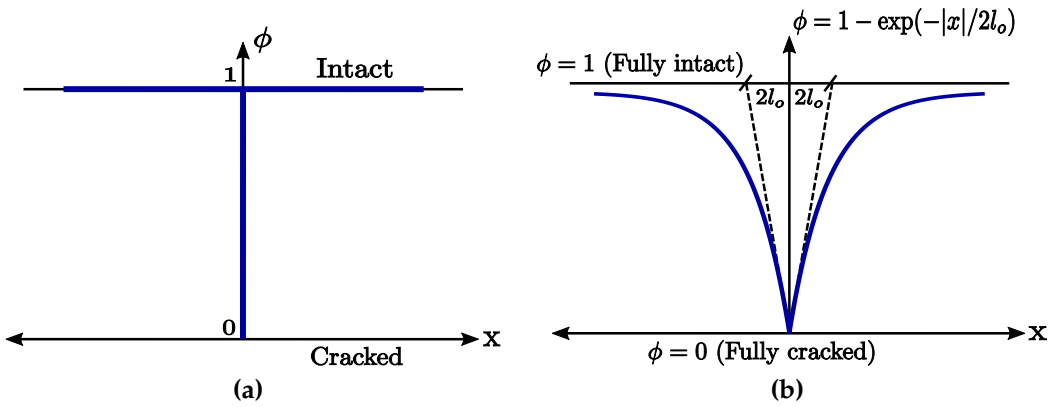

Figure 3.5: 1-D spatial variation of phase field $\phi(x)$ for (a) Discrete (sharp) crack and (b) Diffused crack with second-order quadratic approximation provided in Eq. (3.18) [$\phi = 0$ and $\phi = 1$ represent cracked and intact states of the material respectively]

As the crack evolves, the elastic strain energy and induced stresses of the solid must decrease to compensate for the fracture energy required to generate new crack surfaces. This degradation mechanism is accounted for in the method by means of a degradation function $g(\phi) \in [0, 1]$, so that the elastic strain energy degrades according to Eq. (3.19)

$$\psi_e(\boldsymbol{\varepsilon}, \phi) = g(\phi)\psi_e(\boldsymbol{\varepsilon}) \tag{3.19}$$

Combining Eqs. (3.15)-(3.19), the following expression for the regularized potential energy of a cracked solid is obtained

$$\Pi(\boldsymbol{\varepsilon}, \phi, \nabla\phi) = \int_{\Omega} \left[g(\phi)\psi_e(\boldsymbol{\varepsilon}) + \mathcal{G}_c F_{\Gamma_c}(\phi, \nabla\phi) \right] d\Omega \\ - \int_{\Omega} b_i u_i \, d\Omega - \int_{\partial\Omega} t_i u_i \, d \, \partial\Omega \quad (3.20)$$

with u_i, b_i and t_i as the vector components of displacement $\boldsymbol{u}$, body-force $\boldsymbol{b}$ and surface traction force $\boldsymbol{t}$ respectively. Eq. (3.20) corresponds to the phase field model with an isotropic energy split; this however results in cracks evolving also in regions that are under pure compression.

To address the issue of non-physical crack evolution under pure compression, phase field models based on an anisotropic energy-splitting have been proposed, see, e.g., [24, 345, 432]. Herein, the spectral decomposition of the strain tensor as introduced in Miehe et al. [24] is employed to facilitate comparisons with published results. To effectively impose the plane-stress assumptions and calculate the in-plane and out-of-plane contributions of the strain energy density accurately, an additional 2-D strain tensor $\boldsymbol{\varepsilon}'$ comprising only in-plane strain components $[\varepsilon_{11}, \varepsilon_{22}, \varepsilon_{12}]$ is defined, i.e.,

$$\boldsymbol{\varepsilon}' = \begin{bmatrix} \varepsilon_{11} & \varepsilon_{12} & 0 \\ \varepsilon_{12} & \varepsilon_{22} & 0 \\ 0 & 0 & \varepsilon_{33} \end{bmatrix} \text{ with, } \varepsilon_{33} = \frac{-\nu}{1-\nu}(\varepsilon_{11} + \varepsilon_{22}) \quad (3.21)$$

The effective Cauchy stress vector is defined accordingly as

$$\sigma = [\sigma_{11}, \sigma_{22}, \sigma_{33}, \tau_{12}, \tau_{23}, \tau_{13}]^T \quad (3.22)$$

Remark 2. The plane stress assumption must hold also after damage has initiated. To ensure that this is the case, the in-plane membrane stress components $[\sigma_{11}, \sigma_{22}, \tau_{12}]^T$ and their corresponding contributions to the total strain energy density must be calculated based on the 2-D strain tensor ε' in Eq. (3.21), whereas the out-of-plane stresses $[\tau_{23}, \tau_{13}]^T$ and their strain-energy contribu-

tions must be calculated using the complete 3-D strain tensor ε in Eq. (3.11). In addition, the out-of-plane tensile stress σ_{33} can be explicitly set to zero to achieve optimal convergence characteristics and ensure that the plane-stress assumptions hold even post-initiation of damage.

The tensile and compressive components of the 2-D and 3-D strain tensors $\{\boldsymbol{\varepsilon}', \boldsymbol{\varepsilon}\}$ defined in Eq. (3.21) and (3.11) respectively, can be obtained using Eqs. (3.23) and (3.24) below.

$$\boldsymbol{\varepsilon} = \sum_{i=1}^{3} \lambda_i \boldsymbol{n}_i \otimes \boldsymbol{n}_i \quad ; \quad \boldsymbol{\varepsilon}' = \sum_{i=1}^{3} \lambda_i' \boldsymbol{n}_i' \otimes \boldsymbol{n}_i' \tag{3.23}$$

$$[\boldsymbol{\varepsilon}]_{\pm} = \sum_{i=1}^{3} \langle \lambda_i \rangle_{\pm} \boldsymbol{n}_i \otimes \boldsymbol{n}_i \;\; ; \;\; [\boldsymbol{\varepsilon}']_{\pm} = \sum_{i=1}^{3} \langle \lambda_i' \rangle_{\pm} \boldsymbol{n}_i' \otimes \boldsymbol{n}_i' \tag{3.24}$$

where λ_i / λ_i' are the eigenvalues (principal stretches), $\boldsymbol{n}_i / \boldsymbol{n}_i'$ are eigenvectors (principal stretch directions), and $\{\varepsilon_{\pm}, \varepsilon_{\pm}'\}$ are the tensile/compressive strain components for the strain tensors $\{\boldsymbol{\varepsilon}, \boldsymbol{\varepsilon}'\}$ respectively. $(\cdot) \otimes (\cdot)$ denotes the outer-product of eigenvectors, and the expression $\langle \cdot \rangle_{\pm}$ are the Macaulay brackets, i.e.,

$$\langle \cdot \rangle_{\pm} = [(\cdot) \pm |(\cdot)|]/2 \tag{3.25}$$

where $\langle \lambda_i \rangle_{\pm}$ and $\langle \lambda_i' \rangle_{\pm}$ contain only the positive/negative eigenvalues of the strain tensors $\{\boldsymbol{\varepsilon}, \boldsymbol{\varepsilon}'\}$, respectively.

Based on the spectral strain decomposition for the 2-D strain tensor $[\boldsymbol{\varepsilon}']$ in Eq. (3.24), the in-plane components of the strain energy density ψ^{IP} and its corresponding tensile/ compressive parts $\psi_{\pm}^{IP}$ are defined as shown in Eq. (3.26)

$$\begin{aligned} \psi_e^{IP}(\boldsymbol{\varepsilon}', \phi) &= g(\phi) \psi_+^{IP}(\boldsymbol{\varepsilon}_+') + \psi_-^{IP}(\boldsymbol{\varepsilon}_-') \\ \psi_{\pm}^{IP}(\boldsymbol{\varepsilon}_{\pm}') &= \frac{\lambda}{2} \langle \mathrm{tr}(\boldsymbol{\varepsilon}') \rangle_{\pm}^2 + \mu \mathrm{tr}\left[(\boldsymbol{\varepsilon}_{\pm}')^2 \right] \end{aligned} \tag{3.26}$$

where λ and μ are the Lamé constants and tr denotes the trace of strain tensor. The corresponding definitions of splitted stress tensor $\sigma_{\pm}^{IP}$ are provided in Eq.

(3.27)

$$\begin{aligned}\sigma^{IP} &= \begin{bmatrix}\sigma_{11} & \tau_{12}\\ \tau_{12} & \sigma_{22}\end{bmatrix} = g(\phi)\sigma_{+}^{IP}(\boldsymbol{\varepsilon}'_{+}) + \sigma_{-}^{IP}(\boldsymbol{\varepsilon}'_{-})\\ \sigma_{\pm}^{IP}(\boldsymbol{\varepsilon}'_{\pm}) &= \begin{bmatrix}(\sigma_{11})_{\pm} & (\tau_{12})_{\pm}\\ (\tau_{12})_{\pm} & (\sigma_{22})_{\pm}\end{bmatrix} = \lambda\langle \mathrm{tr}(\boldsymbol{\varepsilon}')\rangle_{\pm}\mathcal{I} + 2\mu\left(\boldsymbol{\varepsilon}'_{\pm}\right)\end{aligned} \tag{3.27}$$

Here $\boldsymbol{\mathcal{I}}$ is 2×2 identity tensor, and the stress tensor σ^{IP} is expressed in Voigt notation as $\sigma^{IP} = [\sigma_{11}, \sigma_{22}, \tau_{12}]^T$.

According to Eqs. (3.26) and (3.27), only the positive tensile parts of the strain energy density and the Cauchy stress tensor, respectively are multiplied by the degradation function $g(\phi)$. In these formulations, the quadratic degradation function originally introduced in Miehe et al. [307], Pham and Marigo [433] has been employed, i.e.,

$$g(\phi) = (1 - \eta_r)\phi^2 + \eta_r \tag{3.28}$$

where the parameter η_r was first defined in [431], and denotes the residual stiffness to prevent ill-conditioning of system matrices when damage has fully propagated.

To obtain the out-of-plane Cauchy stress σ^{OP} and the corresponding strain energy density terms $\{\psi_e^{OP}, \psi_{\pm}^{OP}\}$ in a similar manner, the tensile/ compressive components of full 3-D strain tensor $[\varepsilon]$ provided in Eq. (3.24) are used as shown in Eq. (3.29) and Eq. (3.30), respectively, i.e.,

$$\begin{aligned}\psi_e^{OP}(\boldsymbol{\varepsilon}, \phi) &= g(\phi)\psi_{+}^{OP}(\boldsymbol{\varepsilon}_{+}) + \psi_{-}^{OP}(\boldsymbol{\varepsilon}_{-})\\ \psi_{\pm}^{OP}(\boldsymbol{\varepsilon}_{\pm}) &= 2\mu\left[(\varepsilon_{23})_{\pm}^2 + (\varepsilon_{13})_{\pm}^2\right]\end{aligned} \tag{3.29}$$

$$\begin{aligned}\sigma^{OP} &= \begin{bmatrix}\tau_{23}\\ \tau_{13}\end{bmatrix} = g(\phi)\sigma_{+}^{OP}(\boldsymbol{\varepsilon}_{+}) + \sigma_{-}^{OP}(\boldsymbol{\varepsilon}_{-})\\ \sigma_{\pm}^{OP}(\boldsymbol{\varepsilon}_{\pm}) &= \begin{bmatrix}(\tau_{23})_{\pm}\\ (\tau_{13})_{\pm}\end{bmatrix} = 2\mu \begin{bmatrix}(\varepsilon_{23})_{\pm}\\ (\varepsilon_{13})_{\pm}\end{bmatrix}\end{aligned} \tag{3.30}$$

where $\{(\varepsilon_{23})_{\pm}, (\varepsilon_{13})_{\pm}\}$ are the transverse shear components in the tensile/ compressive 3-D strain tensors $\{\varepsilon_{\pm}\}$ defined previously in Eq. (3.24).

In the standard Mindlin shell theory, the transverse shear stresses are assumed constant along the shell thickness; however in actual 3-D solids, they follow a parabolic distribution. To account for this effect, the transverse shear strains in Eq. (3.30) are typically scaled by a factor of $(5/6)$ [8].

$$\begin{aligned}\tau_{23} &= (5/6)\ \tau_{23}\\ \tau_{13} &= (5/6)\ \tau_{13}\end{aligned} \tag{3.31}$$

Using the in-plane and out-of-plane contributions given in Eq. (3.26) and (3.29), respectively the overall tensile and compressive components of the total strain energy density can be obtained as in Eq. (3.32)

$$\psi_{\pm} = \psi_{\pm}^{IP}(\boldsymbol{\varepsilon}'_{\pm}) + \psi_{\pm}^{OP}(\boldsymbol{\varepsilon}_{\pm}) \tag{3.32}$$

Based on this, the expression for the total potential energy in Eq. (3.20) can be modified to naturally suppress crack growth in the regions under pure compression

$$\begin{aligned}\Pi(\boldsymbol{\varepsilon}, \phi, \nabla\phi) = \int_{\Omega} \big[g(\phi)\psi_{+}(\boldsymbol{\varepsilon}^{+}) + \psi_{-}(\boldsymbol{\varepsilon}^{-}) + \\ \mathcal{G}_c F_{\Gamma_c}(\phi, \nabla\phi)\big]\, d\Omega - \int_{\Omega} b_i u_i\, d\Omega + \int_{\partial\Omega} t_i u_i\, d\, \partial\Omega\end{aligned} \tag{3.33}$$

The strong form of the governing linear momentum and phase field evo-

lution equations are henceforth obtained by minimizing the total potential energy in Eq. (3.33) with respect to the displacement and phase field variables $\{u, \phi\}$.

$$\begin{aligned} &\nabla\boldsymbol{\sigma} + \boldsymbol{b} = 0, \text{ on } \Omega \\ &\left(\frac{4l_o\left(1-\eta_r\right)\psi_+}{\mathcal{G}_c} + 1\right)\phi - 4l_0^2\Delta\phi = 1, \text{ on } \Omega \end{aligned} \tag{3.34}$$

where the boundary conditions satisfy,

$$\begin{aligned} &\mathbf{u} = \bar{\boldsymbol{u}}, \text{ on } \partial\Omega_u \\ &\frac{\partial\phi}{\partial x_i} n_i = 0, \text{ on } \partial\Omega_\phi \end{aligned} \tag{3.35}$$

with n_i, $i \in \{1, 2, 3, ...r\}$ being the outward pointing normal vectors at the crack boundary.

To facilitate crack-irreversibility, a history variable (also referred to as crack-driving force $\mathcal{D}$) proposed by [24], based on maximum strain energy density throughout the deformation history is adopted in the current formulations. The expression for $\mathcal{D}$ can be given as:

$$\boldsymbol{\mathcal{D}} = \max_{(t>t_0)} \psi_+ \tag{3.36}$$

where t_0 is the initial time. The second of Eqs. (3.34) can be re-written as

$$\left(\frac{4l_o\left(1-k\right)\boldsymbol{\mathcal{D}}}{\mathcal{G}_c} + 1\right)\phi - 4l_0^2\Delta\phi = 1, \text{ on } \Omega \tag{3.37}$$

Using the history variable to impose crack irreversibility produces acceptable and accurate results in cyclic loading scenarios [24]. It must be emphasized however, that it also disrupts the original variational formulation [94]. Alternative techniques to impose crack irreversibility can be found in [351, 434].

Remark 3. It is noted for the sake of clarity that different notations of the length-scale parameter l_o are adopted in the literature, e.g. the l_o used by

Miehe et al. [24] is twice the size of l_o in [129]. This implies that the formulation detailed in [24] requires the minimum value of l_o to be at-least twice the mesh-size h_e ($l_o \geq 2h_e$), whereas on the other hand, the minimum value of l_o should be $l_o \geq h_e$ for the formulations provided in [129].

Indeed both the definitions of l_o are equivalent, and one must be careful while appropriately choosing the value of l_o when comparing results from the two formulations. The formulations presented in Eq. (3.37) use the definition from [129], and hence the condition $l_o \geq h_e$ consistently holds for all the numerical simulations performed in this chapter.

3.2.1 Effective material tangent operator

The undamaged material elastic constitutive law for homogeneous materials is expressed in the local shell-aligned coordinate system $[1, 2, 3]$ as

$$\boldsymbol{\sigma} = \boldsymbol{C_o}\, \boldsymbol{\varepsilon}$$

$$\Rightarrow \begin{bmatrix} \sigma_{11} \\ \sigma_{22} \\ \sigma_{33} \\ \tau_{12} \\ \tau_{23} \\ \tau_{13} \end{bmatrix} = \begin{bmatrix} E' & \nu E' & 0 & 0 & 0 & 0 \\ \nu E' & E' & 0 & 0 & 0 & 0 \\ 0 & 0 & 0 & 0 & 0 & 0 \\ 0 & 0 & 0 & G & 0 & 0 \\ 0 & 0 & 0 & 0 & 5G/6 & 0 \\ 0 & 0 & 0 & 0 & 0 & 5G/6 \end{bmatrix} \begin{bmatrix} \varepsilon_{11} \\ \varepsilon_{22} \\ \varepsilon_{33} \\ \gamma_{12} \\ \gamma_{23} \\ \gamma_{13} \end{bmatrix} \tag{3.38}$$

where $E' = E/(1-\nu^2)$ with E and ν as Young's modulus and Poisson's ratio respectively, and $G = E/[2(1+\nu)]$ is the shear modulus of the material [8].

Eq. (3.38) is derived on the basis of a plane-stress assumption and indicates that the in-plane components of the elastic Cauchy stresses $[\sigma_{11}, \sigma_{22}, \tau_{12}]^T$ are obtained only using the corresponding in-plane components of undamaged material tangent $\mathbf{C_o}$, whereas the transverse shear stress components $[\tau_{23}, \tau_{13}]^T$ are obtained using only out-of-plane shear components of $\mathbf{C_o}$.

To achieve optimal convergence rates even with the modified stress defi-

nitions in Eq. (3.27) and (3.30), plane-stress assumptions must hold even when the material is undergoing damage. To achieve this, a split of the damaged tangent stiffness matrix $\mathcal{C}_d$ into its corresponding components as shown in Eq. (3.39) and (3.42) is considered, which are based on in-plane $\{\sigma^{IP}, \varepsilon'\}$ and out-of-plane $\{\sigma^{OP}, \varepsilon\}$ stresses and strains, respectively.

$$[\mathcal{C}_d]^{IP} = \frac{\partial \sigma^{IP}}{\partial \boldsymbol{\varepsilon}'} = g(\phi)[\mathcal{C}_d]^{IP}_{+} + [\mathcal{C}_d]^{IP}_{-} \tag{3.39}$$

where $[\mathcal{C}_d]^{IP}_{\pm}$ is

$$[\mathcal{C}_d]^{IP}_{\pm} = \frac{\partial \sigma^{IP}_{\pm}}{\partial \boldsymbol{\varepsilon}'} \tag{3.40}$$

The in-plane material tangent operator $[\mathcal{C}_d]^{IP}$ can also be represented as the 4×4 tensor shown in Eq. (3.41).

$$[\mathcal{C}_d]^{IP} = \begin{bmatrix} \mathcal{C}_d^{1111} & \mathcal{C}_d^{1122} & 0 & \mathcal{C}_d^{1112} \\ \mathcal{C}_d^{2211} & \mathcal{C}_d^{2222} & 0 & \mathcal{C}_d^{2212} \\ 0 & 0 & 0 & 0 \\ \mathcal{C}_d^{1211} & \mathcal{C}_d^{1222} & 0 & \mathcal{C}_d^{1212} \end{bmatrix} \; ; \; \mathcal{C}_d^{ijkl} = \frac{\partial \sigma_{ij}^{IP}}{\partial \boldsymbol{\varepsilon}'_{kl}} \tag{3.41}$$

The out-of-plane component of the material tangent operator are derived in a similar fashion and are provided in Eqs. (3.42) and (3.43), i.e.,

$$[\mathcal{C}_d]^{OP} = \begin{bmatrix} \mathcal{C}_d^{2323} & 0 \\ 0 & \mathcal{C}_d^{1313} \end{bmatrix} = g(\phi)[\mathcal{C}_d]^{OP}_{+} + [\mathcal{C}_d]^{OP}_{-} \tag{3.42}$$

and

$$[\mathcal{C}_d]^{OP}_{\pm} = \begin{bmatrix} \dfrac{\partial (\tau_{23})_{\pm}}{\partial (\varepsilon_{23})_{\pm}} & 0 \\ 0 & \dfrac{\partial (\tau_{13})_{\pm}}{\partial (\varepsilon_{13})_{\pm}} \end{bmatrix} \tag{3.43}$$

respectively where $\{(\tau_{23})_{\pm}, (\tau_{13})_{\pm}\}$ and $\{(\varepsilon_{23})_{\pm}, (\varepsilon_{13})_{\pm}\}$ are the tensile/ compressive components of the 3-D transverse shear stresses and strains defined in Eq. (3.30) and (3.24), respectively.

Collecting the in- and out-of-plane components, the combined damaged material tangent tensor $[\mathcal{C}_d]$ is eventually expressed as

$$[\mathcal{C}_d]_{6\times 6} = \begin{bmatrix} [\mathcal{C}_d]^{IP} & \mathbf{0} \\ \\ \mathbf{0}^T & [\mathcal{C}_d]^{OP} \end{bmatrix} \tag{3.44}$$

where $\mathbf{0}$ corresponds to the 4×2 null tensor.

3.2.2 Crack driving force variation along the shell-thickness

As discussed in Sec. 3.1.2, the 3-D kinematics of Mindlin shell elements are defined with respect to the kinematics of the mid-surface. Furthermore, damage evolution as manifested by the evolution of the phase field is obtained only at the mid-surface nodes as a 2-D field. Hence, achieving an accurate and realistic stress degradation along the thickness becomes a challenging task [see, e.g., 335].

Driven by the observation that, especially in thin shells, crack propagation through all thickness layers is often sudden and brutal, a maximum through-thickness driving force rule to control the evolution of the phase field is employed. Within this setting, the crack driving forces are evaluated at each through the thickness integration point according to Eq. (3.45) as

$$\boldsymbol{\mathcal{D}'}_{ij} = \max_{(t>t_0)} (\psi_{+,ij}) \tag{3.45}$$

where $i = 1 \dots n_{thick}$ and $j = 1 \dots n_{GP}$ with n_{thick} denoting the number of thickness layers and n_{GP} the number of integration points per layer, respectively. Hence, the crack-driving force is evaluated based on the 3-D stress state at each individual integration point of the shell element.

The crack-driving force at all thickness integration points corresponding to a particular mid-surface location is then set equal to the maximum of driving forces prevalent at those integration points as shown in Eq. (3.46).

$$\mathcal{D}_{ij} = \max_{(i)} \left(\mathcal{D}'_{ij}\right) \tag{3.46}$$

The phase field evolution Eq. (3.37) is integrated at each Gauss-point over the entire shell-element volume, thus causing phase field (or damage) to evolve based on the max crack-driving force description in Eq. (3.46). The procedure is schematically illustrated in Fig. 3.6 for the case of $n_{thick} = 3$ thickness layers and $n_{GP} = 4$ integration points per layer.

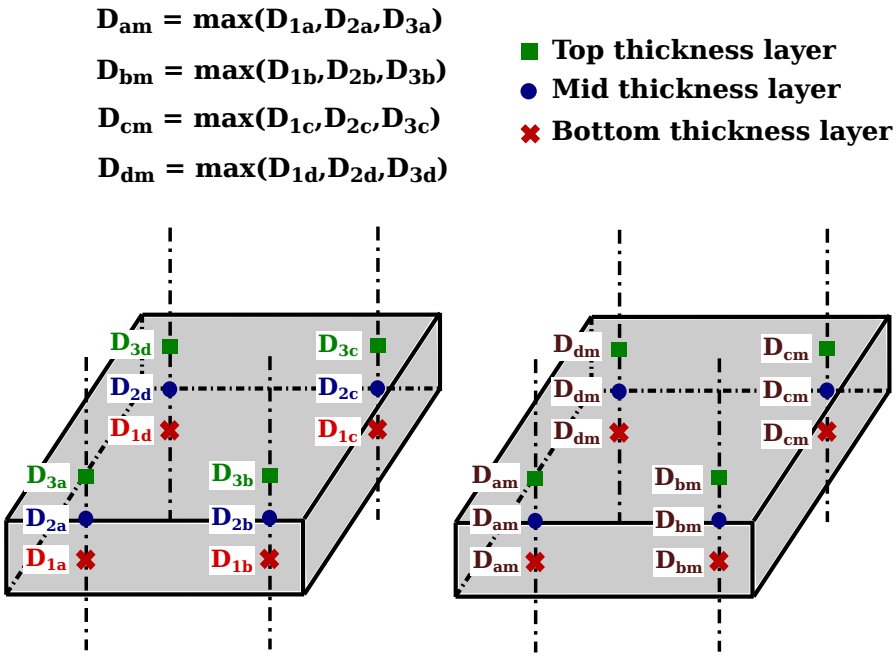

Figure 3.6: Schematic illustration of the procedure employed to evaluate the crack-driving force $\mathcal{D}$ based on the maximum through the thickness rule employed. The case of 3 thickness layers and 4 integration point per thickness layer is considered.

It is of interest to note that in realistic bending dominated deformations, different stress states would occur along the shell thickness, i.e. the outermost and innermost shell surfaces will develop tensile and compressive stresses respectively. In a physical sense, this should also result in varying phase field solution along the thickness, wherein the crack initiates at the outermost shell surface under tension, and gradually propagates towards the inner thickness

layers. However, since Reissner-Mindlin shell theory uses 2-D shape functions to interpolate the solution, it becomes challenging to obtain a 3-D through-the-thickness phase field variation.

In the current formulation, the phase field initiates and evolves based on the maximum crack driving force, effectively the maximum positive elastic energy density along the thickness of the shell. This approach ensures that a crack always initiates and evolves under tensile strains only. Since the outermost thickness layer is under pure tension, it cracks first. Following this, the penultimate (next to outermost) thickness layer develops the maximum tensile stresses, and hence it cracks next, and so on. The physical motivation for the assumption stated herein comes from the fact that such layer-by-layer cracking phenomena through-the-thickness will often occur suddenly and simultaneously in the case of thin shells. Hence, the stress degradation must start as soon as the critical energy release rate is reached in any one of these thickness layers.

The extensive numerical experiments conducted towards the end of this chapter have shown that this assumption captures the physical cracking phenomena through the shell thickness and leads to highly accurate critical fracture strength predictions. A disadvantage of this formulation however is that once initiated, it results in abrupt evolution of crack across the shell thickness, which may not be realistic in the case of thick-shells.

Remark 4. To accurately capture the phase field variation through the thickness, e.g., in the case of thick-shells or multi-layered composite laminates [368], where a significant variation of the fracture toughness is expected, one could stack a number of shell elements along the thickness (see, e.g., [2, 65, 435]).

3.2.3 Discretization and solution procedure

The coupled strong-form evolution Eqs. (3.34) are discretized via a Galerkin approximation. The test $\mathcal{S}$ and weighting $\mathcal{W}$ function spaces for the displace-

ment field are defined as

$$\mathcal{S}_{\boldsymbol{u}} = \left\{ \boldsymbol{u} \in \left(\mathcal{H}^1(\Omega) \right)^d \,\middle|\, \boldsymbol{u} = \bar{\boldsymbol{u}} \text{ on } \partial\Omega \right\} \tag{3.47}$$

$$\mathcal{W}_{\boldsymbol{u}} = \left\{ \delta\boldsymbol{u} \in \left(\mathcal{H}^1(\Omega) \right)^d \,\middle|\, \delta\boldsymbol{u} = \bar{\delta\boldsymbol{u}} \text{ on } \partial\Omega \right\} \tag{3.48}$$

The corresponding spaces for the phase field are

$$\mathcal{S}_{\phi} = \left\{ \phi \in \left(\mathcal{H}^1(\Omega) \right) \right\} \tag{3.49}$$

$$\mathcal{W}_{\phi} = \left\{ \delta\phi \in \left(\mathcal{H}^1(\Omega) \right) \right\} \tag{3.50}$$

Multiplying the strong form Eqs. (3.34), integrating by parts and performing the necessary algebraic manipulations eventually leads to the the following convenient nodal residual form for the equilibrium equation at node i,

$$\begin{aligned} \mathcal{R}_i^{\boldsymbol{u}} &= \mathcal{F}_{ext}^{\boldsymbol{u}} - \mathcal{F}_{int}^{\boldsymbol{u}} \\ &= \int_V N_i b_i \, dV - [\mathcal{T}_{rot}]^T \int_V [\mathcal{T}_{\boldsymbol{\varepsilon}} \, \boldsymbol{B}_i^{\boldsymbol{u}}]^T \, \boldsymbol{\sigma} \, dV \end{aligned} \tag{3.51}$$

and the phase field evolution equation at node i

$$\begin{aligned} \mathcal{R}_i^{\phi} = -\mathcal{F}_{int}^{\phi} = \int_V \left(\frac{4 l_o \, (1 - \eta_r) \, \mathcal{D}}{\mathcal{G}_c} + 1 \right) N_i \phi \, dV \\ + \int_V 4 l_0^2 \left[\boldsymbol{B}_i^{\phi} \right]^T \left[\boldsymbol{B}_j^{\phi} \right] \phi_j \, dV - \int_V N_i \, dV \end{aligned} \tag{3.52}$$

respectively. In Eqs. (3.51) and (3.52), V is the element volume, N_i is the 2-D shape function and $[\boldsymbol{B}_i^{\boldsymbol{u}}]$ is the strain-displacement matrix as expressed in Eq. (3.4), and $[\mathcal{T}_{rot}]$, $[\mathcal{T}_{\boldsymbol{\varepsilon}}]$ are the rotation and strain-transformation tensors defined in Eqs. (3.13) and (3.7), respectively, which facilitate the calculation of the internal forces $\mathcal{F}_{int}^{\boldsymbol{u}}$ in the local shell coordinate system $[1, 2, 3]$ and their subsequent rotation into global $[x, y, z]$ system.

Similarly, the corresponding stiffness matrices for linear momentum and

phase field evolution equations is given by Eq. (3.53) and Eq. (3.54).

$$\begin{aligned}[\mathcal{K}^{\boldsymbol{u}}_{loc}] &= \int_V [\mathcal{T}_{\boldsymbol{\varepsilon}}\ \boldsymbol{B}^{\boldsymbol{u}}_i]^T\ [\mathcal{C}_d]\ [\mathcal{T}_{\boldsymbol{\varepsilon}}\ \boldsymbol{B}^{\boldsymbol{u}}_i]\ dV \\ \mathcal{K}^{\boldsymbol{u}}_i &= [\mathcal{T}_{rot}]^T\ [\mathcal{K}^{\boldsymbol{u}}_{loc}]\ [\mathcal{T}_{rot}]\end{aligned} \tag{3.53}$$

$$\mathcal{K}^{\phi}_i = \int_V \left(\frac{4l_o\,(1-\eta_r)\,\mathcal{D}}{\mathcal{G}_c} + 1\right) N_i N_j\ dV + \int_V 4l_0^2 \left[\boldsymbol{B}^{\phi}_i\right]^T \left[\boldsymbol{B}^{\phi}_j\right]\ dV \tag{3.54}$$

where $[\mathcal{C}_d]$ is the damaged material tangent tensor in Eq. (3.44). The explicit expressions for N_i and $[\boldsymbol{B}^{\boldsymbol{u}}_i]$ can be obtained from [8], and are shown in Appendix A.1 and A.3 for reference. Furthermore, $\left[\boldsymbol{B}^{\phi}_i\right]$ is defined with respect to shell-local system $[1, 2, 3]$ as shown in Eq. (3.55).

$$\left[\boldsymbol{B}^{\phi}_i\right] = [N_{i,1},\ N_{i,2},\ N_{i,3}]^T \tag{3.55}$$

The complete solution algorithm for modelling brittle fracture in MITC4+ Mindlin shell elements is provided in Algorithm A.1.

Remark 5. In practice, the components of $\left[\boldsymbol{B}^{\phi}_i\right]$ can be effectively obtained by choosing the relevant components of the locally transformed strain-displacement tensor $[\mathcal{T}_{\boldsymbol{\varepsilon}}\ \boldsymbol{B}^{\boldsymbol{u}}_i]$. Since in Mindlin shell theory, the kinematics of the shell-element is represented using 2-D shape functions at the mid-surface, $N_{i,3}$ can be effectively set as zero.

Assembling the contributions from each element shown in Eqs. (3.51) and (3.52) into the overall residual vectors $\mathcal{R}^u$ and $\mathcal{R}^{\phi}$, the solution $\{\boldsymbol{u}, \phi\}$ to the combined system of equations (3.34) can be obtained by setting $\mathcal{R}^{\boldsymbol{u}} \to \mathbf{0}$ and $\mathcal{R}^{\phi} \to \mathbf{0}$.

In the current work, the solution is obtained using the one-pass staggered (alternating minimization) approach based on [24]. To ensure accuracy of the obtained solution, either both equations must be solved using staggered iterations [313] or the analysis must be solved using small incremental steps [24].

3.2.4 Integration procedure

For the MITC4+ shell element analyzed in the current work, a full-integration technique is employed with 4 Gauss integration points defined at each parametric thickness layer within the element. The integral expressions in Eqs. (3.51) and (3.52) are expressed in terms of parametric coordinates $[\xi, \eta, \zeta]$ according to Eq. (3.56)

$$\int_V (\mathcal{I})\, dV = \int_{-1}^{1}\int_{-1}^{1}\int_{-1}^{1} (\mathcal{I})\ \det[\mathrm{J}]\, d\xi d\eta d\zeta \tag{3.56}$$

where $\mathcal{I}$ is evaluated at each integration point through the shell-volume and the definition for Jacobian $[J]$ is provided in Appendix A.1. The in-plane integration over $\{\xi, \eta\}$ within each thickness layer ζ is performed using the Gauss-integration rule,

$$\int_{-1}^{1}\int_{-1}^{1} (\mathcal{I})\ \det[\mathrm{J}]\, d\xi d\eta = \sum_{i=1}^{4} (\mathcal{I}_i)\ \det[J]_i w_i \tag{3.57}$$

where $i \in \{1, 2, 3, 4\}$ are the in-plane integration points and $w_i \in \{1, 1, 1, 1\}$ are the weights associated with each of these points. The out-of-plane integration along thickness layers is performed using the Simpson's rule, which can be expressed as in Eq. (3.58) for any integrand $\mathcal{I}'$.

$$\int_{-1}^{1} \mathcal{I}' d\zeta = \frac{\Delta h}{3}\left(\mathcal{I}'_0 + 2\mathcal{I}'_1 + 4\mathcal{I}'_2 + 2\mathcal{I}'_3 + ... + ... + \mathcal{I}'_n\right) \tag{3.58}$$

where $\Delta h = 2/n$, and $\{\mathcal{I}'_0, \mathcal{I}'_1, ..., \mathcal{I}'_n\}$ are the values of the integrand $\mathcal{I}'$ evaluated at the different shell-thickness layers $\zeta \in [-1, 1]$ starting with the value of $\mathcal{I}'_0$ at the bottom-most layer $\zeta = -1$.

While performing the through-thickness integration of the phase field evolution equation (3.52), the value of crack-driving force $\mathcal{D}$ at any Gauss-point within a specific thickness layer is obtained based on the maximum crack-

driving force rule detailed in Sec. 3.2.2 and Fig. 3.6.

3.3 Numerical examples

In all the test cases examined in this section, a displacement controlled analysis has been employed. Unless explicitly stated, a one-pass staggered (alternating minimization) approach with a very small time-increment size ($1.e^{-06} - 1.e^{-05}$) has been used for the solution of the coupled displacement- phase field problem, and the residual stiffness η_r is set to 0 for all examples.

3.3.1 Notched square plate subjected to in-plane tension

The standard benchmark of the notched square plate shown in Fig. 3.7 under tension is examined herein. The material properties considered are $E = 210$ GPa, $\nu = 0.3$, and $\mathcal{G}_c = 0.0027$ kN/mm. The mesh-size is $h_e = 0.0025$ mm in the central strip where the crack is expected to propagate and the length scale parameter is $l_o = 0.0075$ mm. A displacement control analysis is performed with an equilibrium tolerance of $tol_u = 10^{-8}$.

The resulting crack-path and load-displacement response are shown in Fig. 3.8 and Fig. 3.9, respectively. The crack initiates at the notch-tip due to stress concentrations, and propagates horizontally towards the right boundary causing complete rupture of the plate. The crack initiation occurs at a critical fracture force $\mathcal{F}_{crit} = 0.7052\,kN$, followed by sharp degradation of structural stiffness which is typically observed in the case of brittle fractures. The crack-path matches exactly and the predicted fracture force is within $\sim 0.12\%$ of the results reported in the literature [see, e.g., 24, 307].

3.3.2 Notched square plate subjected to in-plane shear

The square plate specimen examined in Sec. 3.3.1 is subjected to horizontal in-plane traction as shown in Fig. 3.10. The bottom edge is pinned in all DOFs,

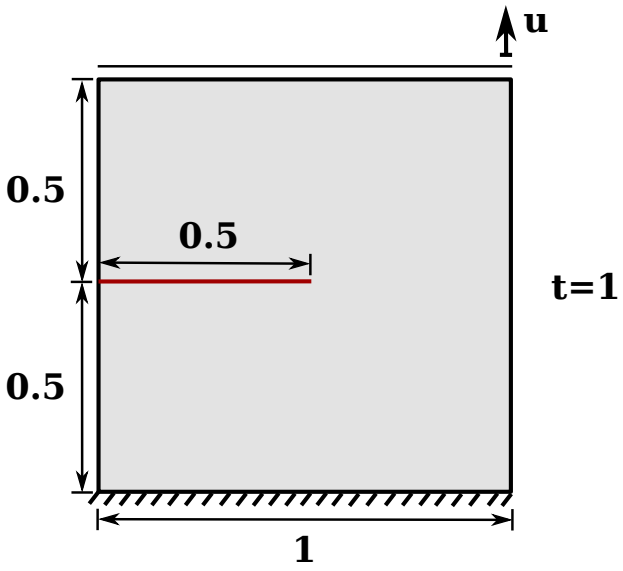

Figure 3.7: Geometry and boundary conditions for square plate with horizontal notch subjected to in-plane tension (All dimensions in mm)

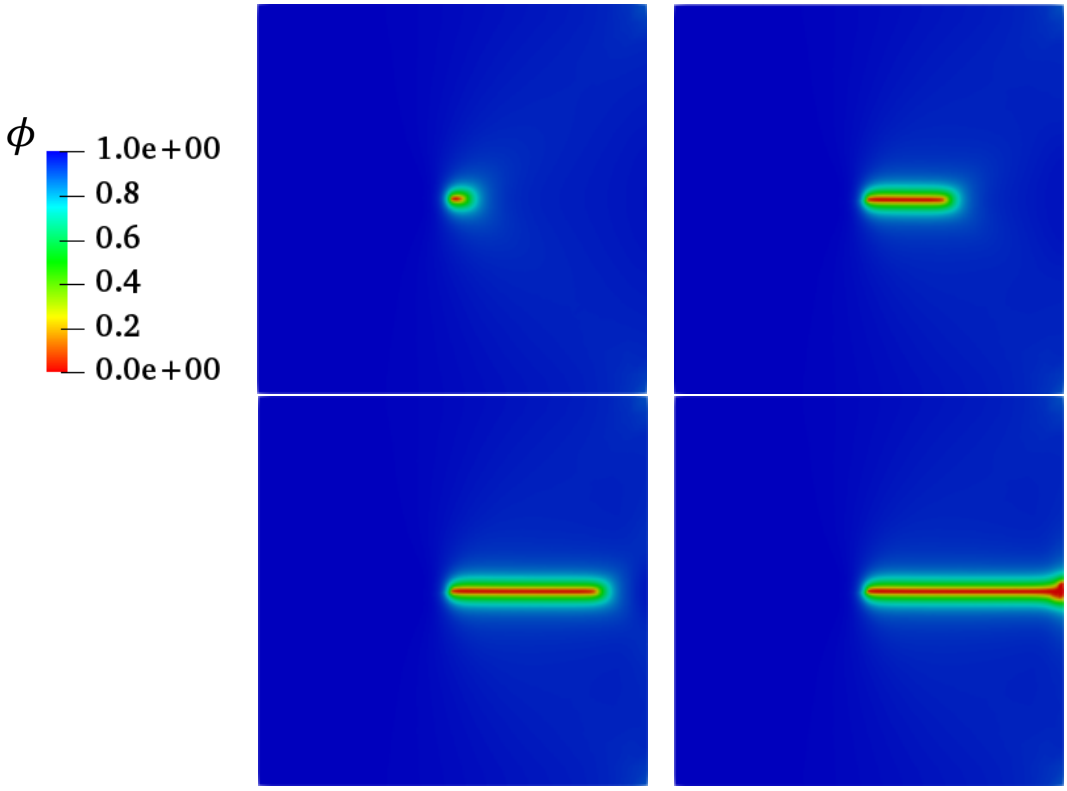

Figure 3.8: Notched plate under in-plane tension: phase field evolution with increasing load-increments [$\phi = 1$ and $\phi = 0$ intact and cracked states of the material]

the left and right edges are constrained to move in vertical directions and the horizontal traction is applied on the top-edge. Due to the nature of loading and boundary conditions in this case, the specimen attains a bi-axial strain state which leads to the propagation of crack at an angle of 45^o to the hor-

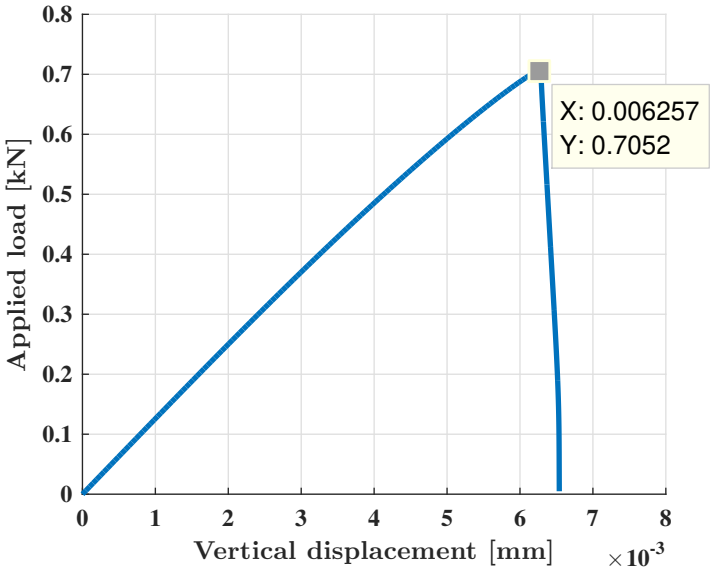

Figure 3.9: Notched plate under in-plane tension: Load-displacement response

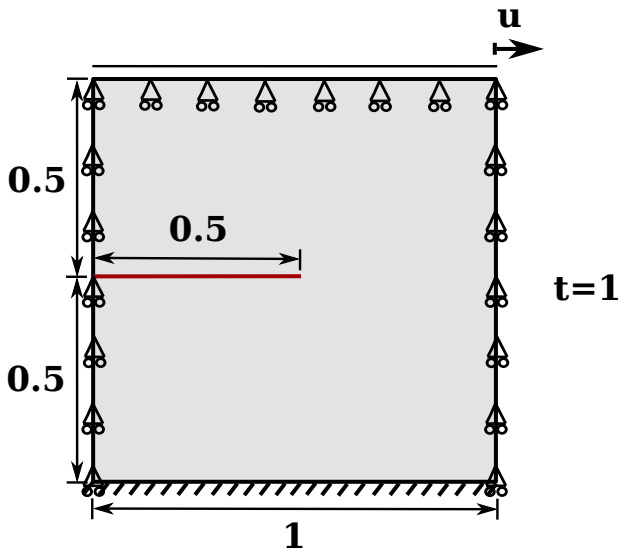

Figure 3.10: Geometry and boundary conditions for square plate with horizontal notch subjected to in-plane shear (All dimensions in mm)

izontal direction. An equilibrium tolerance of $tol_u = 1.e^{-06}$ is used for the displacement controlled analysis. Fig. 3.11 and Fig. 3.12 display the development of crack with each subsequent load-increment and the load-displacement response, respectively. The predicted crack-path matches closely and the critical fracture load $\mathcal{F}_{crit} = 0.5248\,kN$ is within $\sim 1.5\%$ of the results reported in [24]. Both examples (Sec. 3.3.1 and 3.3.2) demonstrate that the proposed phase field model is capable of predicting accurate fracture response and crack paths in membrane-dominated loading scenarios.

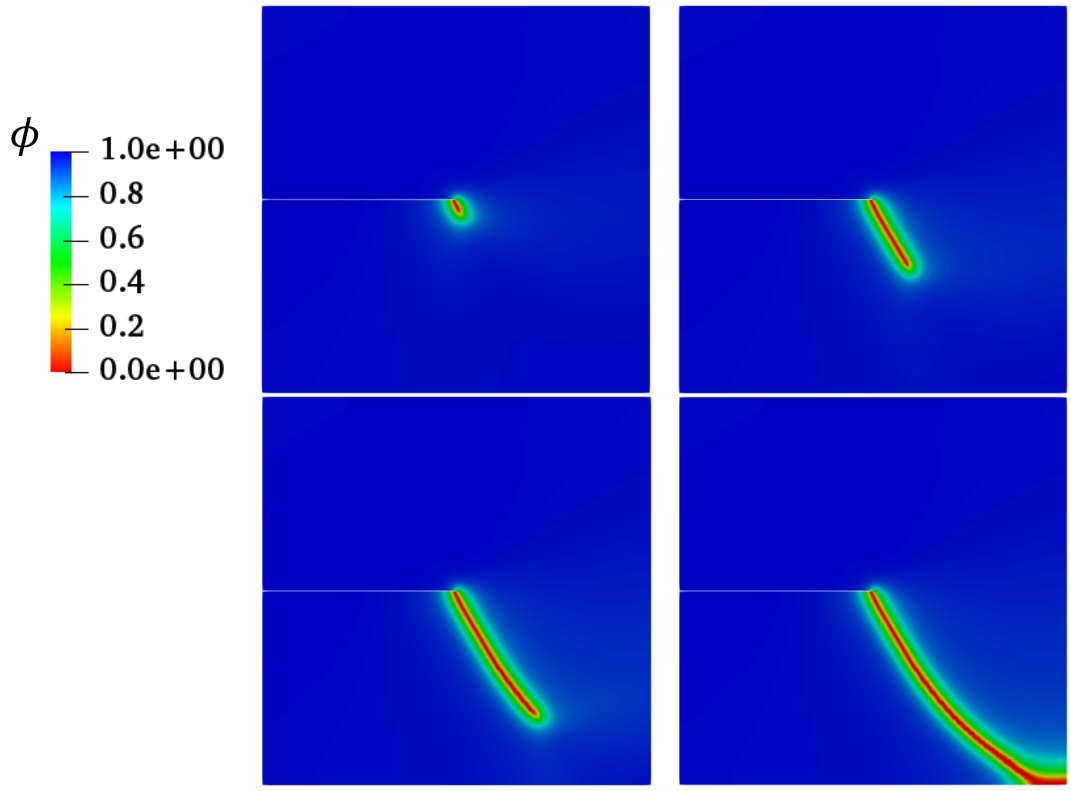

Figure 3.11: Notched plate under in-plane shear: phase field evolution with increasing load-increments [ϕ=1 and ϕ=0 represent intact and cracked states of the material]

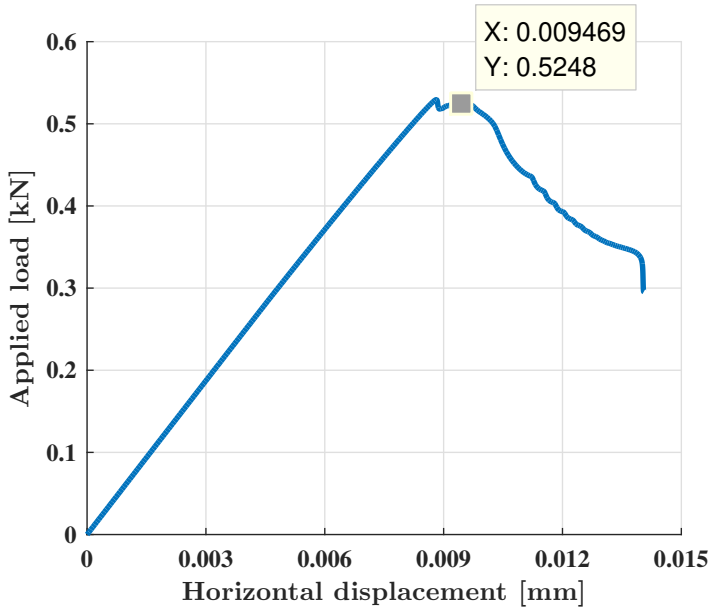

Figure 3.12: Notched plate under in-plane shear: Load-displacement response

3.3.3 1-D beam subjected to transverse bending

A simply-supported rectangular plate subjected to a uniformly distributed pressure over the entire top face as shown in Fig. 3.13 is considered. The

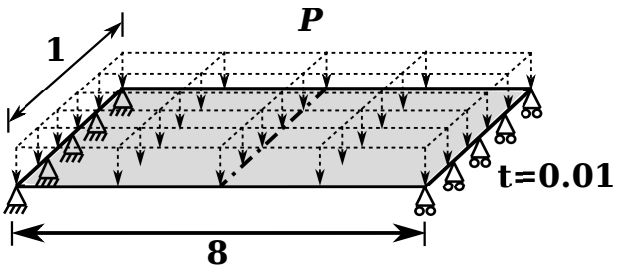

Figure 3.13: Geometry and boundary conditions for rectangular 1-D beam subjected to transverse unidirectional bending under uniformly distributed pressure load P (All dimensions in mm)

aim of this example is to verify the accuracy of proposed formulation predictions under bending-dominated fracture scenarios. The material and fracture properties are $E = 1.e10$ MPa, $\nu = 0$, $\mathcal{G}_c = 3$ N/mm, and $l_o = 0.01$ mm. The mesh is refined with $h_e = 0.003$ mm in the entire mid-span of the plate where the crack propagation is expected. The thickness of the beam $t = 0.01$ mm is very small in comparison to the other two plate-dimensions ($l = 8$ mm and $w = 1$ mm) so that the effects of transverse shear and membrane locking on the critical fracture characteristics can be monitored.

The vertical displacement is monitored at the centre-node of the plate, and the total applied distributed load is analysed with $tol_u = 1.e^{-06}$. The crack initiates at the plate's mid-span which is also the location of maximum transverse deformation u_z, as shown in Fig. 3.14. The load-displacement response is shown in Fig. 3.15 where a brittle fracture response under pure bending is indeed recovered.

Since the Poisson's ratio is null, the transverse bending stiffness and the critical fracture loads should be identical to those predicted by the classical Euler/ Bernoulli beam theory. According to the Euler/ Bernoulli beam theory, the analytical elastic stiffness/length of the beam is established in Eq. (3.59) as

$$k = P/\delta = \frac{384EI}{5\,l^4} \tag{3.59}$$

where δ is the maximum transverse deformation obtained at the centre-span, E is the Young's modulus, $I = wt^3/12$ is the area moment of inertia for the beam, and $P = F/l$ is the total distributed applied load/length on the beam

with units in N/mm, wherein F is the total applied load in N.

For the current case, the analytical elastic stiffness of the beam can be calculated using Eq. (3.59) as $k = P/\delta \approx 15.625\ N/mm^2$. The relative error between this analytical estimate and the slope of the predicted elastic load-displacement response in Fig. 3.15b ($k' = 0.06249/0.004 = 15.6225\ N/mm^2$) is approximately 0.016%. This confirms the correctness of implemented MITC4+ shell formulations [23] which produce a locking-free bending response.

Considering the case of isotropic phase field fracture, i.e., fracture initiating both at tension and compression, the critical fracture load of the beam can be evaluated as

$$P_{cr} = 8M_{cr}/l^2 \tag{3.60}$$

where, M_{cr} is the critical bending moment required for crack initiation

$$M_{cr} = \sigma_{cr} w t^2/6 \tag{3.61}$$

and σ_{cr} is the critical fracture stress. Based on derivations in [129], the critical fracture stress can be analytically evaluated as Eq.(3.62).

$$\sigma_{cr} = \frac{9}{16}\sqrt{\frac{E\mathcal{G}_c}{6l_o}} \tag{3.62}$$

For the given material and fracture properties, the critical stress in Eq. (3.62) is evaluated as $\sigma_{cr} = 3.9775 \cdot 10^5$ N/mm^2. This can be inserted into Eq. (3.60) to obtain the analytical critical fracture load $P_{cr} = 0.8286$ N/mm.

Comparing this with the critical fracture load predicted in Fig. 3.15a, the relative error is $\sim 0.65\%$. Hence, it is evident that the maximum crack-driving force description through thickness detailed in Sec. 3.2.2 predicts the fracture force as accurate as the analytical value P_{cr} estimated by Eq. (3.60) for the isotropic phase field model. This reinstates the validity of the assumption that for brittle fracture in thin shells, all transverse thickness layers at a given

location would fracture simultaneously as soon as the crack is initiated in any one of these layers. Hence to incorporate this effect, the material stiffness degradation in all thickness layers at that shell location must start as soon as the crack-driving force in any one of the associated layers attains a critical limit. Such a description of crack-driving force $\mathcal{D}$ enables a 3-D description of crack topology and stress-degradation effects, albeit using a 2-D phase field, refer to Sec. 3.2.2 for details.

Solving the phase field evolution Eq. (3.34) using the spectral split proposed in [24] and with the same crack-driving force definition (Fig. 3.6) results in the load-displacement response in Fig. 3.15b. The corresponding critical fracture load is higher than the one provided by the isotropic model as in this case the material degradation occurs only on the part of the shell undergoing tension. For the spectral strain-decomposition case [24], the accuracy of predicted critical force is verified against the analytical estimates and XFEM results in next Sec. 3.3.4.

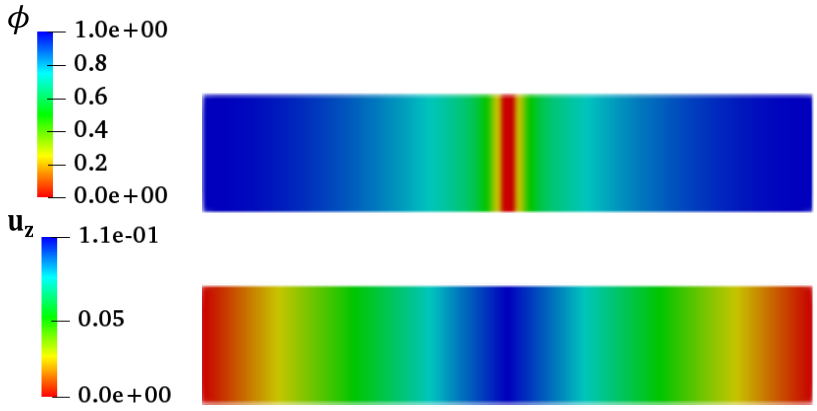

Figure 3.14: 1-D beam under transverse unidirectional bending: Plan-view of (a) Crack-path ϕ and, (b) Vertical displacement u_z represented at the shell mid-surface [ϕ=1 and ϕ=0 represent intact and cracked states of the material]

3.3.4 Rectangular plate with a through crack subjected to pure bending moments

The rectangular plate specimen with a through crack as shown in Fig. 3.16 is subjected to pure bending moments on its opposite edges. The accuracy of

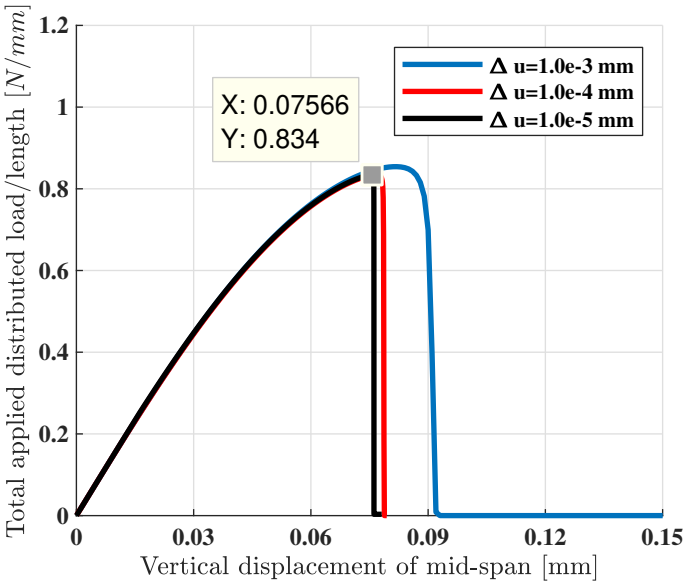

(a)

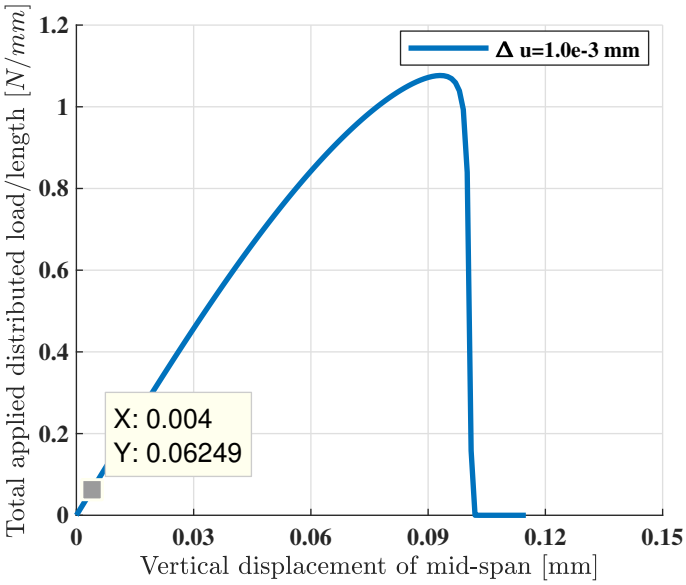

(b)

Figure 3.15: 1-D beam under transverse unidirectional bending: Load-displacement response at beam's centre-node for a) Isotropic phase field formulations b) Anisotropic phase field formulations with spectral decomposition [24]

predicted peak moments are compared with the corresponding analytical values obtained using the stress-intensity factors (SIFs) in [436]. This example has been examined previously in Rouzegar and Mirzaei [437], where a comparison between SIFs obtained with XFEM and the analytical SIFs was performed. Herein, in this example, the critical fracture load predicted by the proposed phase field model with spectral strain decomposition is compared against the

analytical formulations provided in Sih et al. [436]. The material properties are $E = 210,000$ MPa and $\nu = 0.33$.

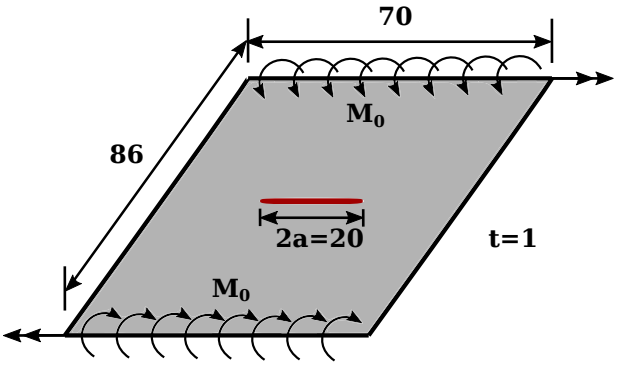

Figure 3.16: Geometry and boundary conditions for the rectangular plate subjected to pure bending moments (All dimensions in mm)

The rotational increment $\Delta\theta_X$ is monitored at the top-right corner node, and the plate is analysed with respect to varying magnitudes of $\Delta\theta_X$ until the peak critical bending-moment is reached. An equilibrium tolerance of $tol_u = 1.e^{-06}$ is used in each case. According to [436], the analytical expression for the critical SIF for a centrally-cracked plate with infinite width and subjected to remotely applied pure bending moment as the one shown in Fig. 3.16, is evaluated as

$$\begin{aligned} K_{1c} &= \frac{6M_{0,crit}}{t^2}\sqrt{a} \;\; ; \;\; K_{2c} = 0 \\ \Rightarrow K_c &= \sqrt{K_{1c}^2 + K_{2c}^2} \end{aligned} \tag{3.63}$$

where K_c is the equivalent critical SIF, t is the plate thickness, $M_{0,crit}$ is the critical bending moment and a is half-length of the central crack. The analytical value of critical SIF for this example is provided in [437] as

$$K_{1c} = 189.74 \text{ MPa mm}^{-1/2} \tag{3.64}$$

Assuming plane-stress conditions, the corresponding critical energy release rate $\mathcal{G}_c$ is

$$\mathcal{G}_c = \frac{K_c^2}{E} = 0.171435 \text{ N/mm} \tag{3.65}$$

Substituting the value of K_{1c} from Eq. (3.64) into (3.63) and considering the edge length $l = 70$ mm, the critical bending moment/edge-length is derived as

$$M_{0,crit} = \frac{K_{1c}\, t^2}{6l\sqrt{a}} = 10.0002 \text{ N-mm/mm} \tag{3.66}$$

For the phase field simulations, the mesh is refined in the central region with the element size $h_e = 0.25$ mm where the crack is expected to propagate. The length-scale parameter and residual stiffness are chosen as $l_o = 0.25$ mm and $\eta_r = 1.0e^{-3}$, respectively. In the original variational formulation proposed by Bourdin et al. [94], it was shown that the fracture energy is overestimated depending on the size of finite element discretization. To compensate for this amplification, an effective critical energy release rate was proposed for the purpose of phase field simulations [349], see also [347] for alternative definition. The down-scaling of amplified fracture energy is important for the phase field results to be comparable with XFEM or experimental response, as also previously shown in [17].

$$\mathcal{G}_c^{eff} = \frac{\mathcal{G}_c}{1 + (h_e/4l_o)} \tag{3.67}$$

Considering $\mathcal{G}_c = 0.171435$ N/mm, $h_e = 0.25$ mm and $l_o = 0.25$ mm, the effective critical energy release rate $\mathcal{G}_c^{eff}$ for the current analysis is $\mathcal{G}_c^{eff} = 0.13715$ N/mm.

The resulting crack topology is shown in Fig. 3.18. The crack originates simultaneously at both notch-tips and propagates horizontally towards the ends of the plate. The moment versus edge rotation response is illustrated in Fig. 3.17.

Furthermore, to demonstrate that the obtained results are independent of the magnitude of chosen time-increments, a comparison of moment-rotation responses is performed in Fig. 3.17 for varying magnitudes of moment-increments ΔM_0. The converged value for the critical moment/length in Fig. 3.17 is $M_{0,PFM} = 10.83$ N-mm/mm, which is within $\sim 7.5\%$ of the analytical bending moment/length $M_{0,crit}$ derived in Eq. (3.66). Herein, l_o is regarded as a numerical parameter, so that the Γ-convergence property is retained in the

limit of vanishing length-scale $l_o \to 0$, which forms the foundation of brittle phase field models [94, 307]. Within this setting, more accurate predictions of predicted critical moments can be obtained with decreasing mesh-sizes and length-scale parameter [17, 307]. It must be emphasized that l_o may also be chosen as material parameter based on 1-D homogeneous solution [304, 438], however, it requires accurate estimation of critical fracture stress σ_{cr} which was not available in this case. Moreover with this approach, the phase field model loses its Γ-convergence property, and may predict erroneous fracture behaviour in the case when the calculated l_o is too large with respect to the problem dimensions, see e.g. [353, 438]. This example further validates the assumptions made in Sec. 3.2.2 also for the phase field model based on anisotropic spectral strain decomposition [24], and verifies the accuracy of proposed phase field formulations in characterising realistic bending-dominated fracture scenarios.

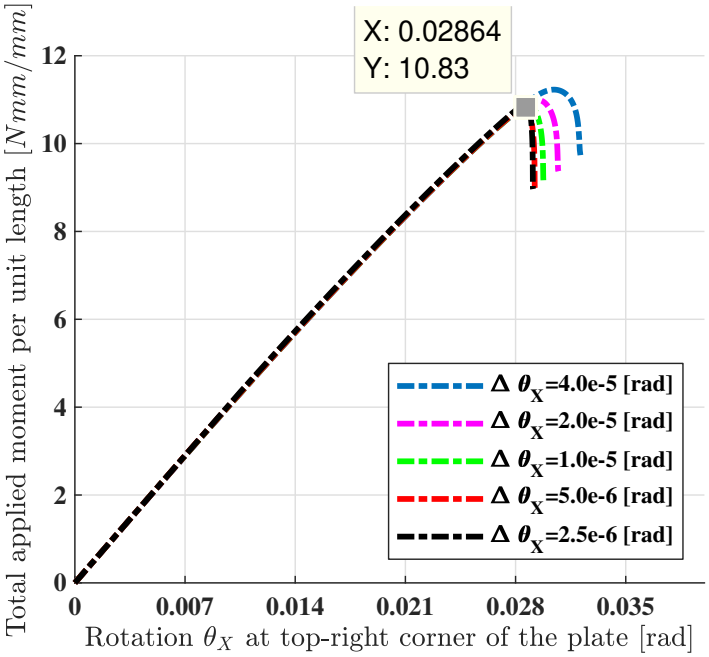

Figure 3.17: Rectangular plate under pure-bending moments: Moment vs edge-rotation response

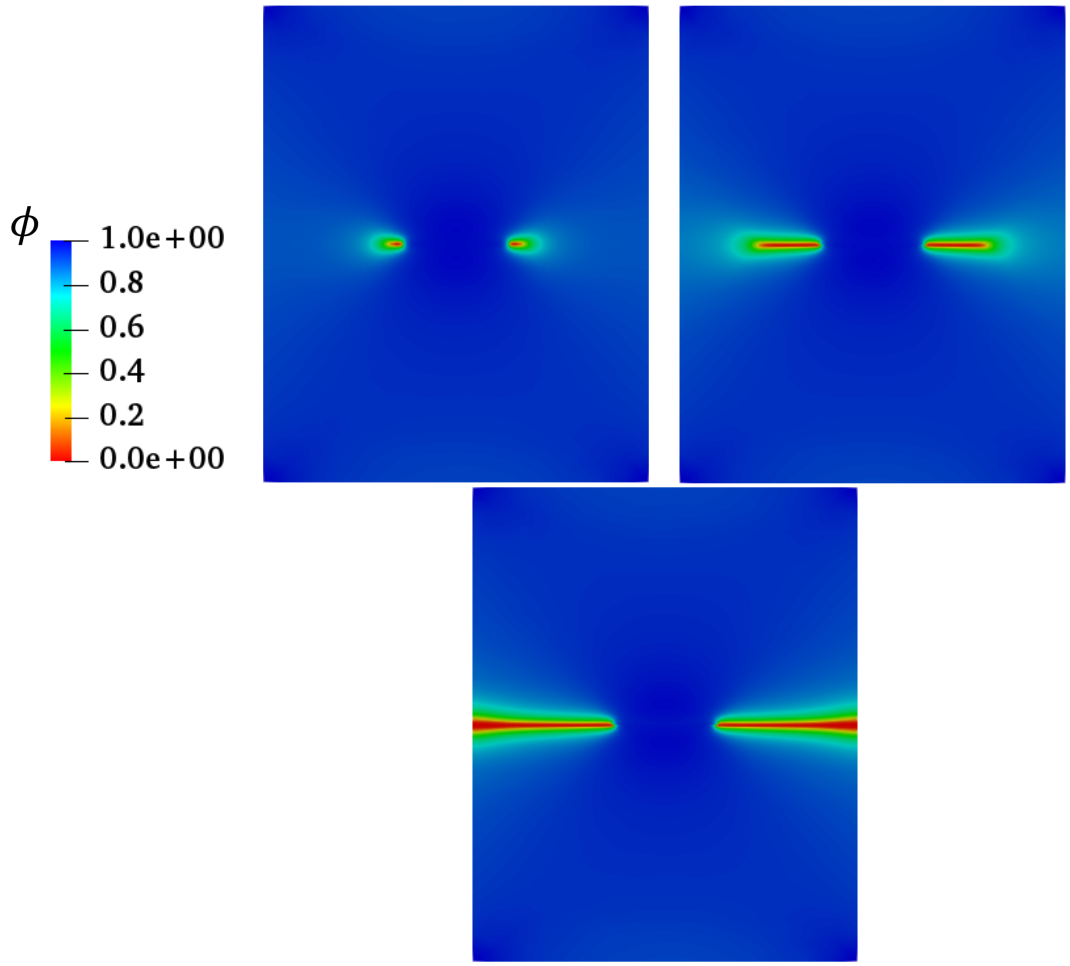

Figure 3.18: Rectangular plate under pure-bending moments: phase field evolution with increasing load-increments [ϕ=1 and ϕ=0 represent intact and cracked states of the material]

3.3.5 Simply supported plate subjected to bi-directional bending under uniformly distributed loads

To demonstrate cracking phenomena under bi-directional bending loads, a simply supported plate with a uniformly distributed surface load is examined. The material and fracture properties are $E = 1.9e^5$ MPa, $\nu = 0.3$, $l_o = 0.01$ mm, $\mathcal{G}_c = 0.295$ N/mm, and the boundary conditions are as shown in Fig. 3.19. The mesh is refined along the plate's diagonal with $h_e = 0.005$ mm. Only a quarter section of the plate is analyzed owing to symmetry. The quarter-section is simply supported on the outer edges of the plate, whereas the internal shared edges are subjected to symmetric boundary conditions. A uniformly distributed load is applied over the entire top face until complete fracture of

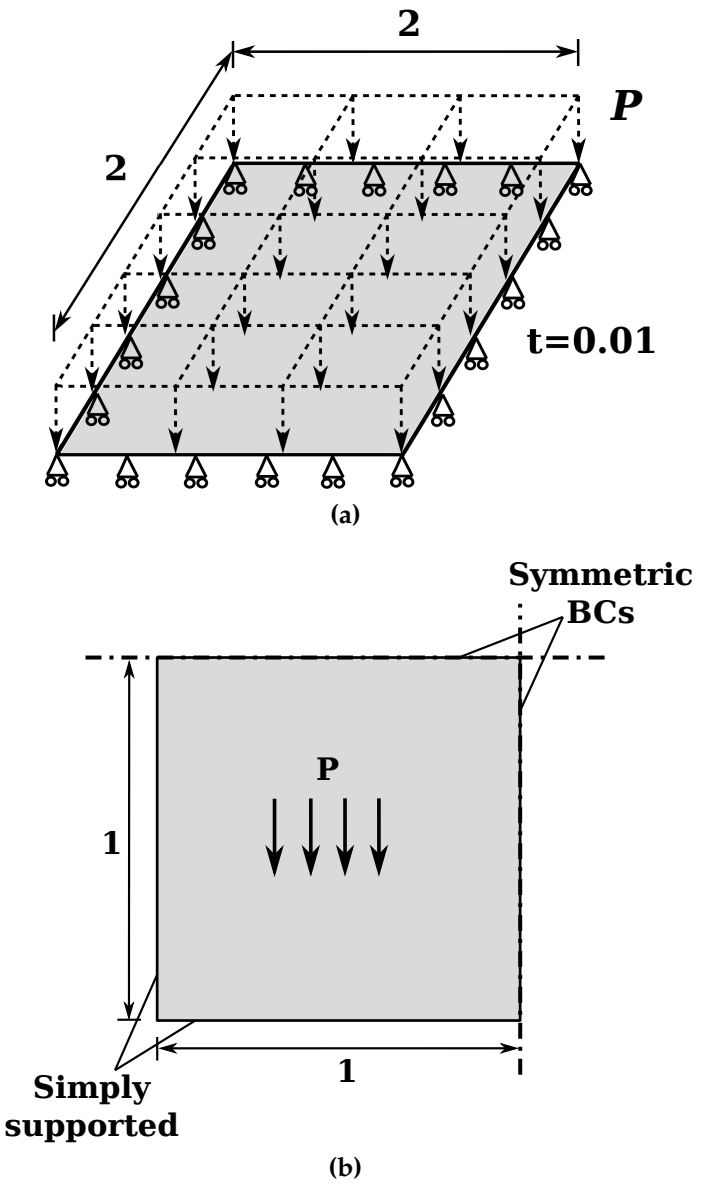

Figure 3.19: (a) Geometry and boundary conditions of simply-supported plate subjected to bidirectional bending under uniformly distributed pressure load P (b) Quarter-part of the plate (All dimensions in mm)

the plate, and the vertical displacement is monitored at the centre node of the plate. The analysis is run until a convergence tolerance of $tol_u = 1.e^{-06}$ is reached.

The crack originates at the centre and the individual crack-branches propagate simultaneously towards the 4 corners of the plate. The crack-path is illustrated on the full plate in Fig. 3.20, which is consistent with the results reported previously in [335, 439]. The load-displacement curve is shown in Fig. 3.21.

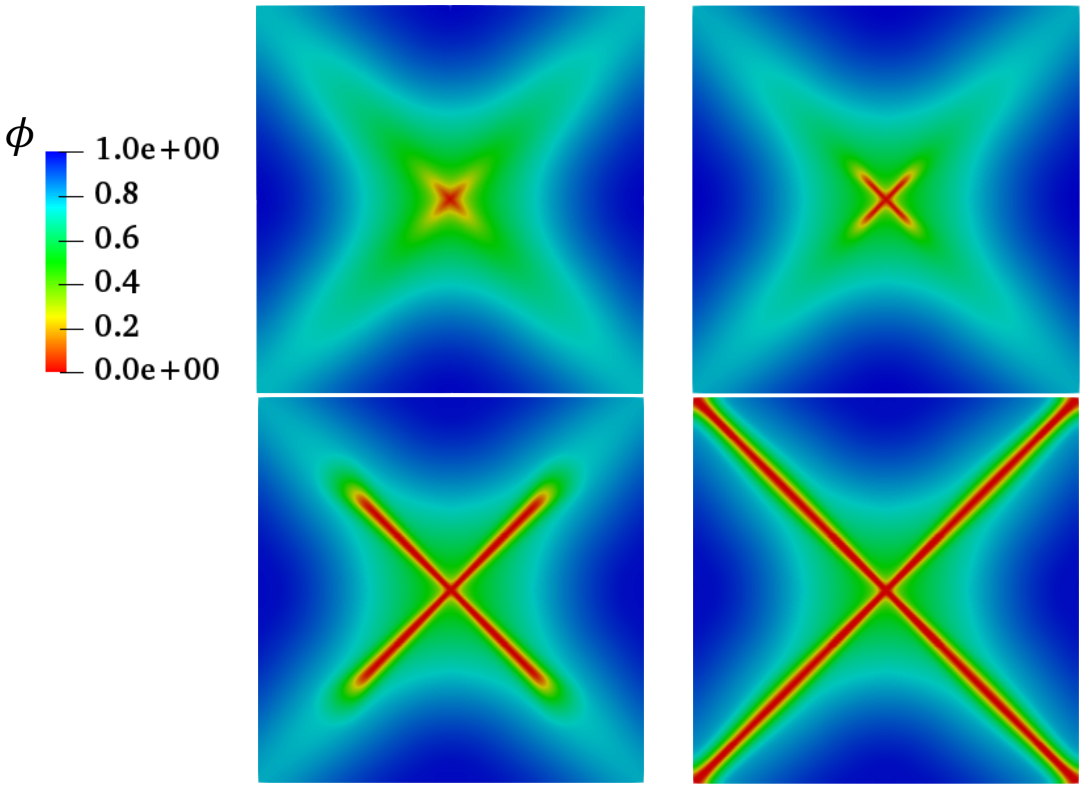

Figure 3.20: Simply-supported plate under bidirectional bending: phase field evolution with increasing load-increments [ϕ=1 and ϕ=0 represent intact and cracked states of the material] (Full-plate assembled for better visualization)

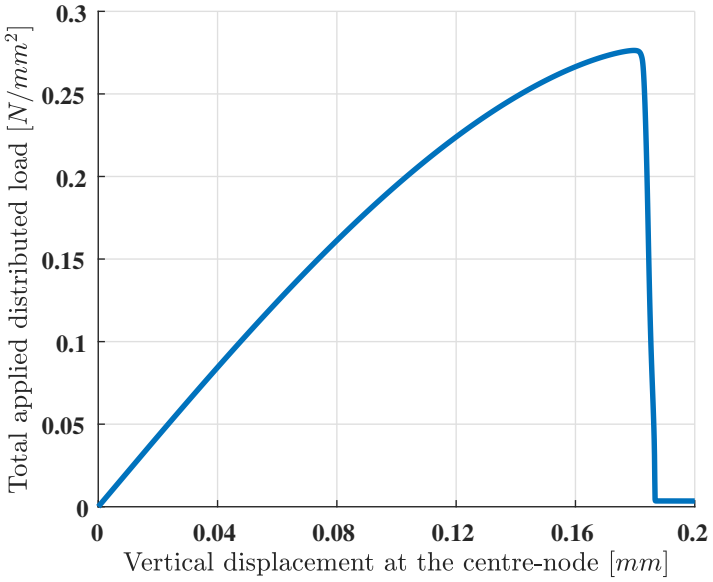

Figure 3.21: Simply-supported plate under bidirectional bending: Load-displacement response at the centre node of the plate

3.3.6 Cylinder with/without spherical closing cap subjected to uniform pressure loads

A cylindrical shell geometry with small axial notches placed on diametrically opposite ends and uniformly applied pressure load on its inner surface is con-

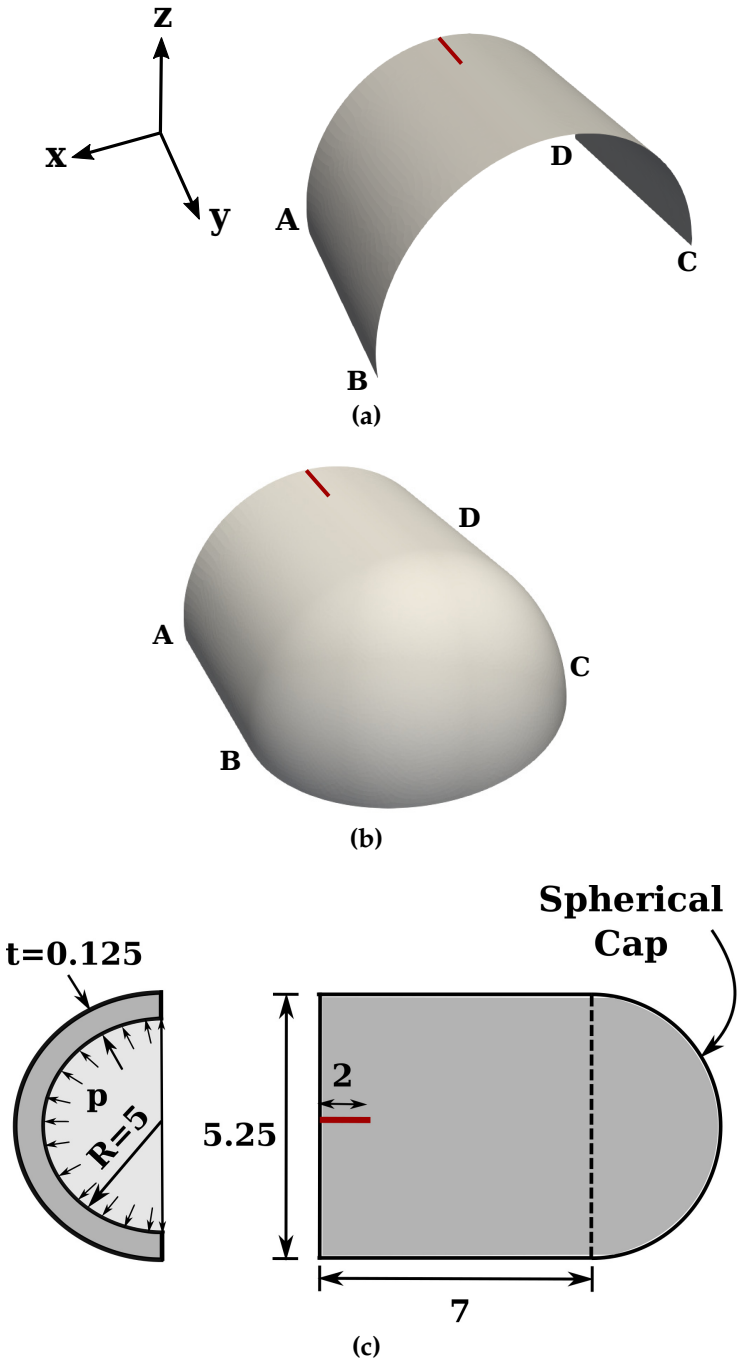

Figure 3.22: Geometry and boundary conditions of cylindrical shell with notch (a) without (b) with spherical cap at the end, and subjected to uniform internal pressure p (All dimensions in mm)

sidered. Owing to the problem symmetry across the xy and xz planes, only the quarter part of the full cylinder is analyzed as shown in Fig. 3.22.

To examine the robustness of the approach, two different cases are examined, i.e. with and without a spherical cap at the two ends of the cylindrical shell. The latter is expected to give rise to crack branching at the spherical cap.

The material and fracture properties are $E = 7.0e^4$ MPa, $\nu = 0.3$, $l_o = 0.125$ mm, $\mathcal{G}_c = 1.5$ N/mm. The mesh is refined with the size $h_e = 0.1$ mm in all the cylindrical and spherical cap regions where the crack is expected to propagate. A displacement controlled analysis is performed with an equilibrium tolerance of $tol_u = 1.e^{-05}$. For the cylinder specimen without spherical cap (Fig. 3.22a), the vertical circular arc BC is fixed along the x and z directions, whereas symmetric boundary conditions are imposed on horizontal edges AB, CD, and AD. The specimen with spherical closing cap (Fig. 3.22b) is subjected to symmetric boundary conditions on all free edges, i.e. the vertical circular arc AD towards the notch is subjected to y-symmetric and horizontal edges AB, BC and CD are subjected to z-symmetric boundary conditions. The example demonstrates the capability of proposed phase field formulations in simulating damage for thin curved geometries which display significant membrane as well as transverse shear locking effects.

The responses between the total applied pressure load and the displacement-norm measured at the notch-tip are compared in Fig. 3.23 for both the uncapped and capped specimens.

The crack-path at increasing load-increments for the uncapped and capped cylinders are shown in Figs. 3.24 and 3.25, respectively. In the former case, the crack initiates at the notch-tip and propagates along the axial direction of the cylinder. In the latter, the specimen demonstrates a similar response (Fig. 3.25), however, in this case the crack initiates at a slightly lower critical fracture load (Fig. 3.23). Over the spherical cap region, the crack first propagates linearly, but subsequently splits into two symmetric crack branches; these further evolve simultaneously.

3.3.7 Assymetric hyperboloid structure subjected to uniform internal pressure

To further demonstrate the robustness of proposed formulations in analysing curved shell problems, an assymetric hyperboloid geometry is considered which

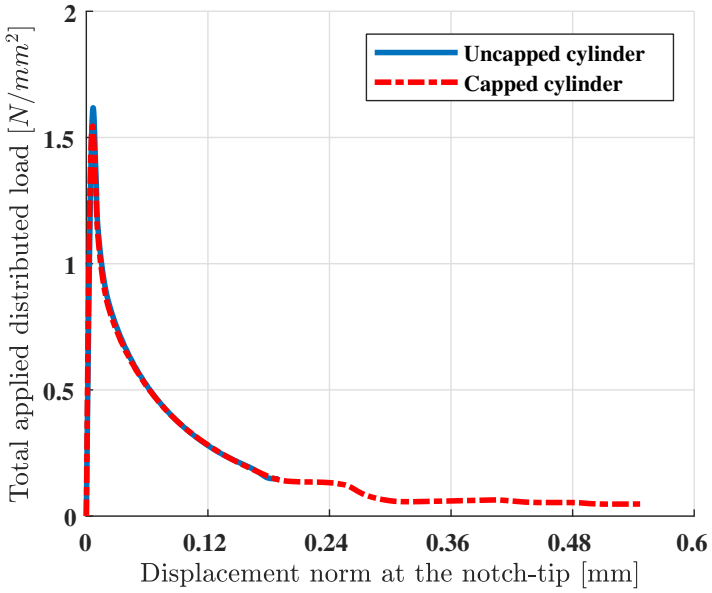

Figure 3.23: Notched cylinder with/without spherical cap under uniform internal pressure: Applied pressure load vs norm of the displacement $\mathbf{u}_{norm} = \sqrt{u_x^2 + u_y^2 + u_z^2}$ measured at the notch-tip

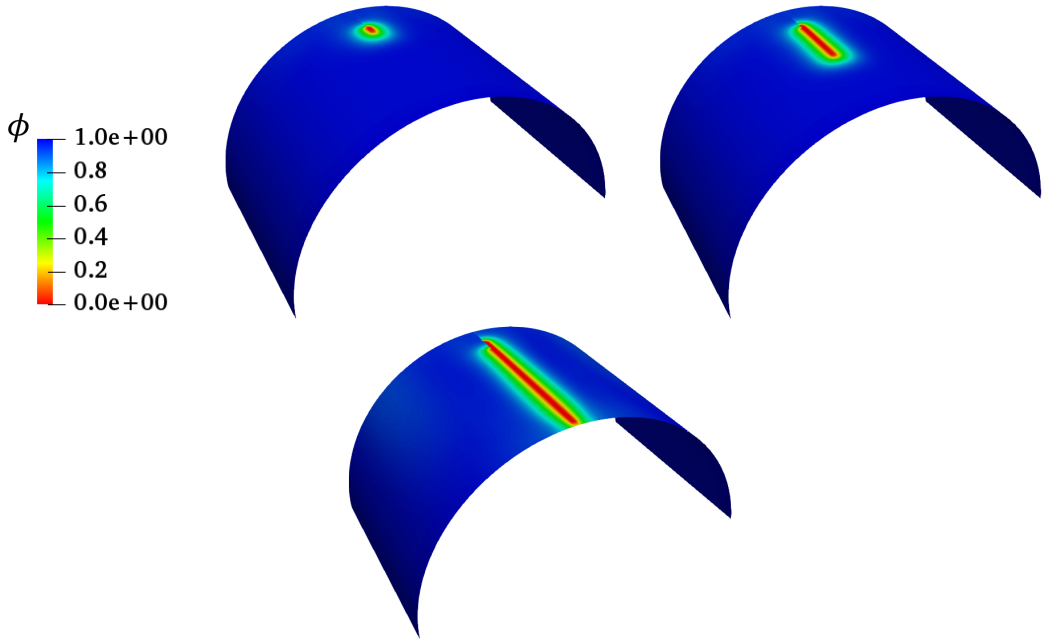

Figure 3.24: Notched cylinder under uniform internal pressure: phase field evolution with increasing load-increments [ϕ=1 and ϕ=0 represent intact and cracked states of the material]

is subjected to a uniform internal pressure applied in the direction normal to its surface. The thin-shell assumptions apply as the thickness of the geometry $t = 0.1$ mm is significantly smaller than the other dimensions of the hyperboloid. A notch is introduced at the mid-height along the longitudinal di-

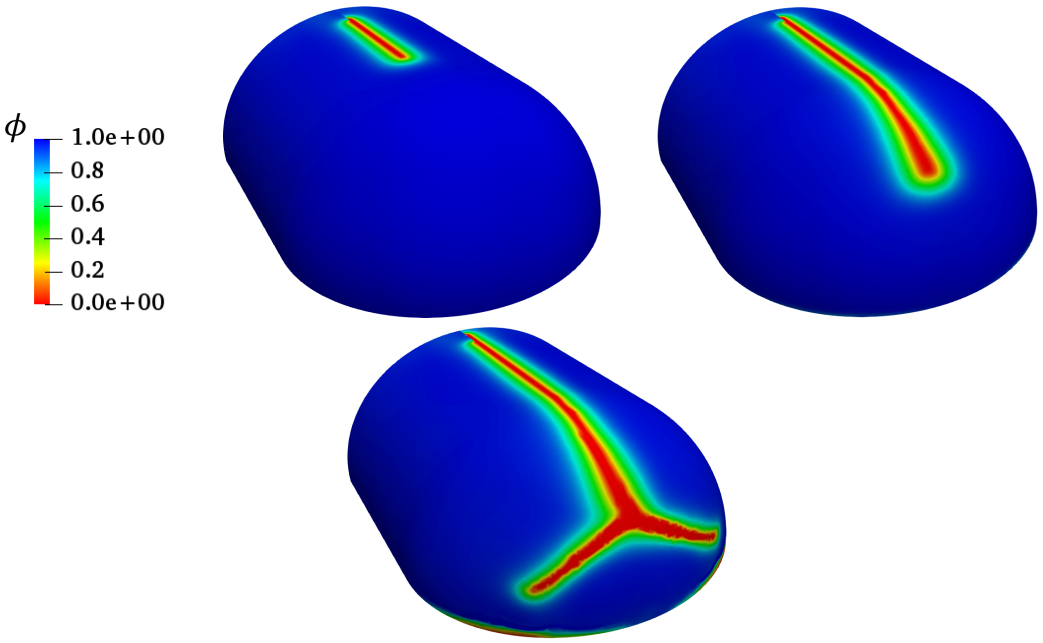

Figure 3.25: Notched cylinder with spherical cap under uniform internal pressure: phase field evolution with increasing load-increments [ϕ=1 and ϕ=0 represent intact and cracked states of the material]

rection. Due to the model symmetry only half part of the complete model as shown in Fig. 3.26 is analysed. To reduce the effect of bending at the boundary, the hyperboloid geometry is supported by an elastic shell structure, displayed as ABFE in Fig. 3.26 in which the evolution of phase field (or damage) is restricted.

The material and fracture parameters for the hyperboloid are $E = 210$ GPa, $\nu = 0.3$, $\mathcal{G}_c = 0.0027$ kN/mm, $l_o = 0.75$ mm, and a uniform mesh size with $h_e = 0.5$ mm is used. The material properties for the elastic base-support is $E = 21000$ GPa, $\nu = 0.3$ with the Young's modulus chosen as 100 times higher than the hyperboloid.

Furthermore, the translational DOFs at the bottom-most part of the elastic base-support is completely fixed ($u_x = u_y = u_z = 0$) while the rotational DOFs are kept free. For the curved side-edges BC and AD, z-symmetric boundary conditions are imposed whereas the top-edge CD is unrestrained. The internal distributed load is applied only on the hyperboloid region EFCD in the direction of outward-pointing normals to its surface. The complete elastic base-support ABFE is unloaded. The radial displacement is monitored at

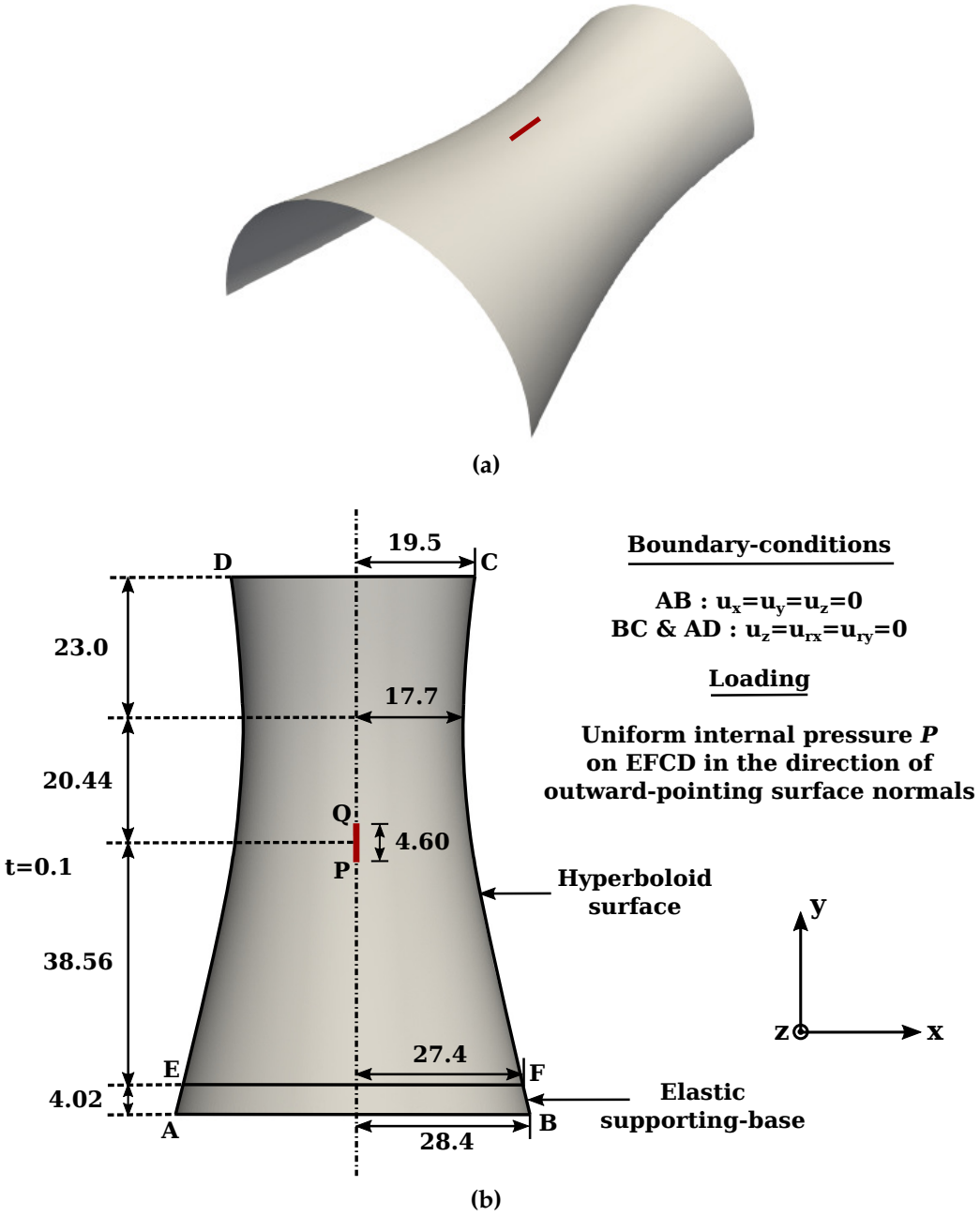

Figure 3.26: Geometry, boundary conditions and loading on the assymetric hyperboloid tower with central notch subjected to uniform internal surface-pressure P (All dimensions in mm)

the bottom notch-tip shown by P in Fig. 3.26, and $tol_u = 1.e^{-05}$. The crack initiates at the bottom notch-tip P as shown in Fig. 3.27, and propagates vertically downwards followed by a second branch that initiates at the top notch-tip Q. The two cracks propagate simultaneously and crack-branching is eventually observed at the bottom crack due to the shell-curvature at which point the shell loses all bearing capacity. The response between the vertical z-displacement at

the bottom notch-tip P and the total applied load is shown in Fig. 3.28.

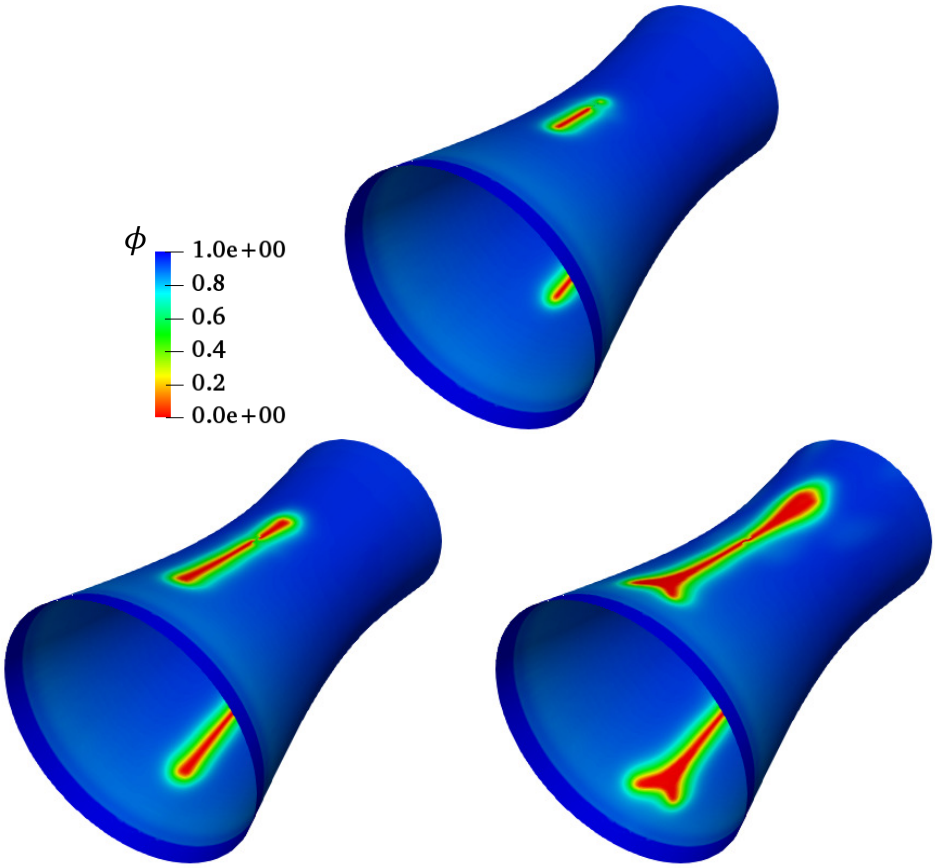

Figure 3.27: Assymetric hyperboloid tower under uniform internal pressure: phase field evolution with increasing load-increments [ϕ=1 and ϕ=0 represent intact and cracked states of the material] (Full geometry assembled for better visualization)

3.4 Concluding Remarks

In this chapter, a phase field enhanced shell element formulation is presented to simulate brittle fracture in Reissner-Mindlin shells. An MITC4+ approach is employed to alleviate transverse-shear and membrane locking. The method is based on the assumption of a maximum through-the-thickness crack driving force rule definition. Considering an anisotropic split for damage evolution, the plane stress assumptions are imposed directly on the tangent constitutive matrix. This approach has been found to provide accurate results and optimum convergence rates.

The accuracy of the proposed model is demonstrated by a set of illustra-

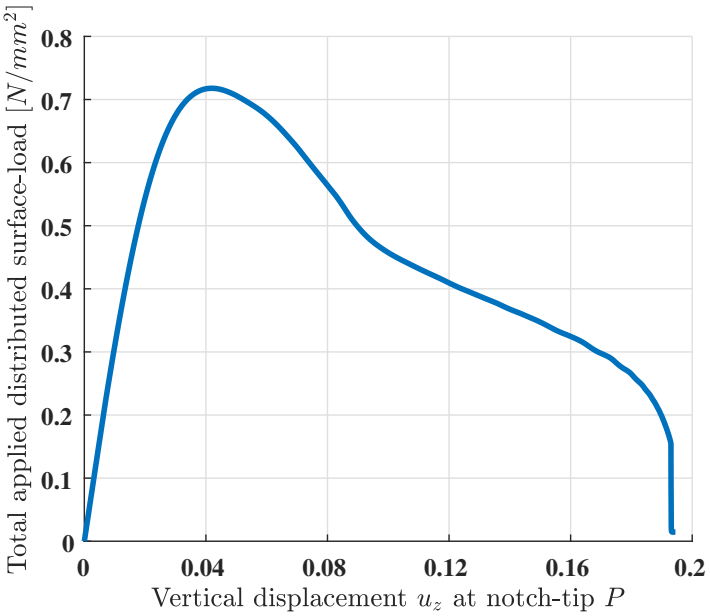

Figure 3.28: Assymetric hyperboloid tower under uniform internal pressure: Applied pressure load vs vertical displacement u_z measured at the bottom notch-tip P

tive numerical examples. The damage results are verified against the analytical estimates both in the case of isotropic and anisotropic phase field models. The validity of the proposed model is further established by obtaining realistic and accurate fracture predictions in curved shell geometries, which display significant membrane and transverse shear locking due to the coupling of membrane and bending deformations.

It must be highlighted that phase field modelling of brittle fracture that simultaneously also alleviates both transverse shear and membrane locking issues in Reissner-Mindlin shell elements has not been addressed in the literature yet [314, 333–336, 440]. Hence in the current study, analytical results are used to compare the accuracy of the bending dominated fracture response, which is considered to be more accurate and reliable approach with regards to characterisation of material's fracture behaviour. Analytical validations have been performed for both the elastic stiffness prior to damage initiation as well as the critical fracture stresses, which proves the efficacy of the proposed model in predicting accurate locking-free brittle fracture response.

Furthermore, despite the non-convex nature of the phase field functional, the predicted solution for all benchmark examples in this chapter are physi-

cally realistic and unique. However, non-unique solutions may emerge in the presence of complex loading or multiple geometric singularities, in which case a stochastic analysis may be performed to predict the probability of each solution [344]. Such an analysis is beyond the scope of the current work.

The phase field model proposed in this chapter presents a robust alternative for intra-laminar damage modelling of thin-ply composites, which fail due to combined membrane and bending deformations. It must be highlighted that the inclusion of rotational degrees of freedom in the MITC4+ formulation would naturally raise implementational challenges vis-à-vis the modelling of multi-layered composite profiles where delamination is a possible failure mode [364, 365]. In this case, coupling with, e.g., a cohesive zone model would require the evaluation of displacements at the interface based on the Reissner-Mindlin kinematical assumptions and the definition of multi-point constraints to couple the degrees of freedom associated with the shell and cohesive elements at the interface [441–443].

4

Robust damage modelling of fibre-reinforced composite laminates

Thin spread-tow unidirectional and woven-fabric reinforced composites are widely utilized in the aerospace and automotive industries due to their enhanced fatigue life and damage resistance. Providing high-fidelity simulations of intra-laminar damage in such laminates is a challenging task both from a physics and a computational standpoint, due to their complex and largely quasi-brittle fracture response. This is manifested by matrix cracking and fibre breakage, which result in a sudden loss of strength with minimum crack separation; subsequent fibre pull-outs result in a further, although gradual, strength loss. In such cases, the crack-tip extends over larger fracture-process zones (FPZ), and hence it becomes necessary to account for cohesive forces evolving within FPZ to model this damage response effectively. Furthermore, the interaction of the failure mechanisms pertinent to both the fibres and the matrix necessitate the definition of anisotropic damage models. Till date, a phase field model that simulates such quasi-brittle fracture behaviour along with the complex anisotropic cracking mechanisms in thin spread-tow composites has been missing from the literature. Furthermore, there have been very limited efforts to effectively calibrate the phase field models to perform realistic experimental validation for composites.

In this chapter, an anisotropic 3-parameter cohesive phase field model is

proposed to simulate intra-laminar fracture in fibre reinforced composites. To capture damage anisotropy, distinct energetic crack driving forces are defined for each pertinent composite damage mode together with a structural tensor that accounts for material orientation dependent fracture properties. The material degradation is governed by a 3-parameter quasi-quadratic degradation function, which can be calibrated to experimentally derived strain softening curves. The numerical implementation procedure for the proposed damage model in commercial FEM software Abaqus is discussed in detail. Furthermore, a strategy to obtain material softening law by calibrating the values of cohesive-shape parameters with respect to the experimental response corresponding to different damage modes is proposed, based on isotropic formulations in Lorentz [444]. The proposed model is further extended to dynamic explicit case and combined with the cohesive zone model to perform full composite-laminate analysis involving both intra-laminar and inter-laminar damage. Benchmark numerical examples are presented towards the end, along with experimental validations performed on spread-tow composite laminates, followed by conclusions. The results presented in this chapter have been published in [445].

The point of departure is the isotropic cohesive phase field model proposed in [351, 352] for simulating quasi-brittle fractures, which is briefly revisited in Sec. 4.1.

4.1 Isotropic cohesive phase field model

In this chapter, the phase field regularisation function F_{Γ_c} is obtained using a second-order linear approximation according to Eq. (4.2), contrary to the quadratic approximation used in Eq. (3.18) of the previous Chapter 3.

$$\int_{\Gamma_c} \mathcal{G}_c \, d\Gamma_c \approx \int_{\Omega} \mathcal{G}_c F_{\Gamma_c}(\phi, \nabla \phi) \, d\Omega \tag{4.1}$$

$$F_{\Gamma_c}(\phi, \nabla\phi) = \frac{3}{4l_o}\left[\phi + \frac{l_o^2}{4}\nabla\phi \cdot \nabla\phi\right] \tag{4.2}$$

with l_o being the length-scale parameter that controls the width of the diffusion zone.

The linear description of the fracture surface energy in Eq. (4.2) results in cracks with a finite diffusion width and plays an important role in obtaining a purely elastic material response prior to crack-initiation. This is central to the phase field description of cohesive fracture [351], and alleviates one of the main drawbacks of the brittle fracture phase field models discussed in Chapter 3, in which the damage evolution starts as soon as the material is loaded. The 1-D variation of phase field parameter ϕ in the direction normal to crack surface using a second order linear approximation [430] is shown in Fig. 4.1. It can be noticed that in this case, $(\phi = 1)$ correspond to the fully-cracked and $(\phi = 0)$ to the fully-intact states of the material, as opposed to the previous representation of ϕ in Chapter 3. Both the former and the latter representations are equivalent, and have no effect on the overall phase field formulations.

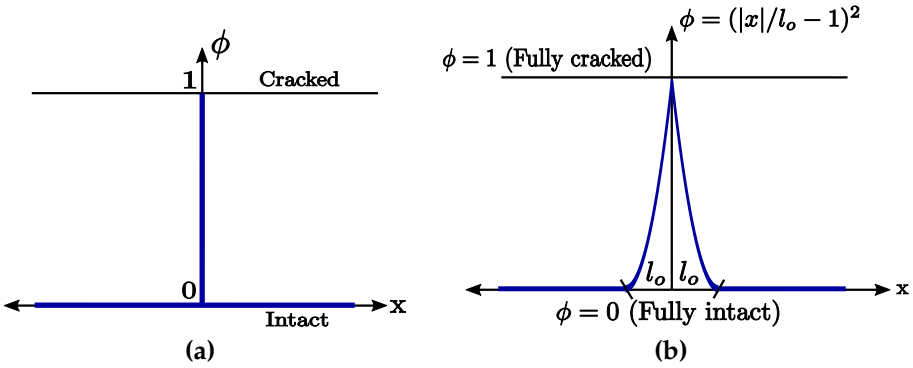

Figure 4.1: 1-D spatial variation of phase field $\phi(x)$ for (a) Discrete (sharp) crack and (b) Diffused crack with second-order linear approximation provided in Eq. (4.2) [$\phi = 0$ and $\phi = 1$ represent intact and cracked states of the material respectively]

The regularized potential energy of the solid assumes the following form, analogous to Eq. (3.20).

$$\Pi\left(\boldsymbol{u}, \phi, \nabla\phi\right) = \int_{\Omega} \psi[\boldsymbol{\varepsilon}(\boldsymbol{u}), \phi]\, d\Omega + \int_{\Omega} \mathcal{G}_c F_{\Gamma_c}(\phi, \nabla\phi)\, d\Omega$$

$$-\int_{\Omega} \boldsymbol{b} \cdot \boldsymbol{u}\, d\Omega - \int_{\partial\Omega_b} \bar{\boldsymbol{t}} \cdot \boldsymbol{u}\, d\partial\Omega_b \quad (4.3)$$

where $\boldsymbol{b}$ and $\bar{\boldsymbol{t}}$ are externally applied body and traction forces, respectively and $\psi[\boldsymbol{\varepsilon}(\boldsymbol{u}), \phi]$ is the degraded elastic strain energy density which accounts for the fact that the stored elastic strain energy of the solid must decrease as the crack evolves and the amount of dissipated fracture energy increases. The expression for linearized strain tensor $\boldsymbol{\varepsilon}(\boldsymbol{u})$ is given by Eq. (3.16).

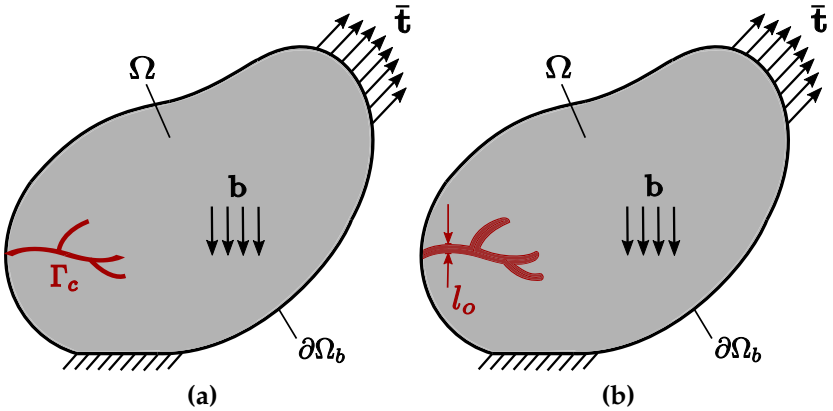

Figure 4.2: General domain Ω containing (a) Internal sharp crack Γ_c, and (b) Diffused crack with length-scale l_o, and subjected to body force $\boldsymbol{b}$ and surface traction forces $\bar{\boldsymbol{t}}$

As explained previously in Chapter 3, the elastic strain energy density $\psi[\boldsymbol{\varepsilon}(\mathbf{u})]$ includes contributions from both tensile and compressive deformation modes. However, the un-physical evolution of crack must be suppressed in regions under pure compression [24, 345, 432]. The isotropic cohesive phase field model in [351] follows the approach described in [24], wherein the elastic strain energy $\psi[\boldsymbol{\varepsilon}(\boldsymbol{u})]$ is split into a tensile and a compressive part, and only the active part is responsible for driving the crack evolution process. This is accomplished via a spectral decomposition of the strain tensor into its tensile and compressive components as shown in Eq. (4.4)

$$\begin{aligned} \boldsymbol{\varepsilon} &= \boldsymbol{\varepsilon}^{+} + \boldsymbol{\varepsilon}^{-} \\ \boldsymbol{\varepsilon}^{\pm} &= \langle \lambda_i \rangle^{\pm} \boldsymbol{n}_i \otimes \boldsymbol{n}_i \end{aligned} \quad (4.4)$$

where the Macaulay brackets imply $\langle x \rangle^{\pm} = (x \pm |x|)/2$ and λ_i, $\boldsymbol{n}_i$ are the eigenvalues and eigenvectors of the strain tensor $\boldsymbol{\varepsilon}$. Based on Eq. (4.4), the degraded

elastic strain energy $\psi[\boldsymbol{\varepsilon}(\boldsymbol{u}), \phi]$ is additively decomposed into a tensile ψ^+ and a compressive ψ^- component. To account for the fracture induced material degradation, a degradation function $g(\phi)$ is imposed on the tensile part of the elastic energy density so that

$$\psi[\boldsymbol{\varepsilon}(\boldsymbol{u}), \phi] = g(\phi)\psi^+(\boldsymbol{\varepsilon}^+) + \psi^-(\boldsymbol{\varepsilon}^-) \tag{4.5}$$

where

$$\psi^\pm = \frac{1}{2}\lambda_s \left[\langle \mathrm{tr}(\boldsymbol{\varepsilon})\rangle^\pm\right]^2 + \mu_s \boldsymbol{\varepsilon}^\pm : \boldsymbol{\varepsilon}^\pm \tag{4.6}$$

and λ_s, μ_s are the Lamé constants. Based on the work of Lorentz [444] on isotropic gradient damage model, the degradation function $g(\phi)$ is defined as

$$\begin{aligned} g(\phi) &= \frac{(1-\phi)^2}{(1-\phi)^2 + m\phi A(\phi)} \;\; ; \;\; p \geq 1 \\ \text{with, } ; \;\; m &= \frac{3\mathcal{G}_c E}{2 l_o \sigma_c^2} \;\; ; \;\; l_o < \frac{3E\mathcal{G}_c}{2(p+2)\sigma_c^2} \end{aligned} \tag{4.7}$$

In Eq. (4.7), $A(\phi)$ is a continuously differentiable function expressed as $A(\phi) = 1 + p\phi$ or $A(\phi) = 1 + p\phi\left[\exp(q^2\phi^2)\right]$, E is the Young's modulus, σ_c is the critical fracture stress, and p and q are model parameters. The detailed derivation can be referred from [444].

The governing equations of the cohesive phase field model emerge from the minimisation problem

$$\{\boldsymbol{u}, \phi\} = \mathrm{Argmin}\{\Pi(\boldsymbol{u}, \phi)\} \tag{4.8}$$

that gives rise to the following coupled strong form

$$\begin{aligned} \nabla \cdot \boldsymbol{\sigma} + \boldsymbol{b} &= \boldsymbol{0} \\ \delta_\phi \gamma(\phi, \nabla\phi) = \frac{-g'(\phi)\psi^+}{\mathcal{G}_c} &= \tilde{\mathcal{D}}_{iso} \\ \text{with,} \quad \delta_\phi \gamma = \frac{3}{4 l_o}\left[1 - \frac{l_o^2}{2}\nabla\cdot\nabla\phi\right] \quad &\text{and} \quad \dot{\phi} \geq 0 \end{aligned} \tag{4.9}$$

where $\tilde{\mathcal{D}}_{iso}$ is the isotropic crack-driving force term and $\boldsymbol{\sigma}$ is the Cauchy stress

tensor.

Remark 6. Lorentz [444] proposed closed-form parametric expressions for separation displacement (δ) and stress (σ), and established their convergence to asymptotic cohesive law by obtaining cohesive limit ($\delta_{czm}, \sigma_{czm}$) for vanishing values of length scale parameter l_o. It was also highlighted that the obtained σ-δ response exhibits all important properties of a cohesive law, such as perfect adhesion below initial stress threshold, decreasing stresses with increasing separation displacement as damage evolves, and finally, the material failure with zero stresses and finite critical separation displacement. The initial softening slope and final separation are calculated as Eq. (4.10).

$$\begin{aligned} \left.\frac{d\sigma_{czm}}{d\delta_{czm}}\right|_{\phi=0} &= \frac{2}{3\pi}\left(A'(0)+2\right)^{3/2}\frac{\sigma_c^2}{\mathcal{G}_c} \\ \delta_c &= \frac{3\pi}{4}\sqrt{A(1)}\frac{\mathcal{G}_c}{\sigma_c} \end{aligned} \tag{4.10}$$

The choice of the functions $g(\phi)$ and $A(\phi)$ in Eq. (4.7) is restricted by the constraints that they must ensure convexity, an increasing damage band width, and decreasing stresses to maintain the objectivity of the cohesive law [446]. To fulfil these constraints, Lorentz [444] derived an upper bound for the length scale parameter in Eq. (4.7) based on the cohesive length $E\mathcal{G}_c/\sigma_c^2$ corresponding to fracture process zone.

$$l_o < \frac{3E\mathcal{G}_c}{2(A'(0)+2)\sigma_c^2} \tag{4.11}$$

4.2 The anisotropic cohesive phase field model for fibre-reinforced composites

Composites are highly anisotropic materials that fail under diverse modes of failure that can be primarily classified into fibre fracture and pullouts/bridging and matrix rupture. Often, the fracture behaviour displayed by different composite damage mechanisms is quasi-brittle in nature and a fracture-process

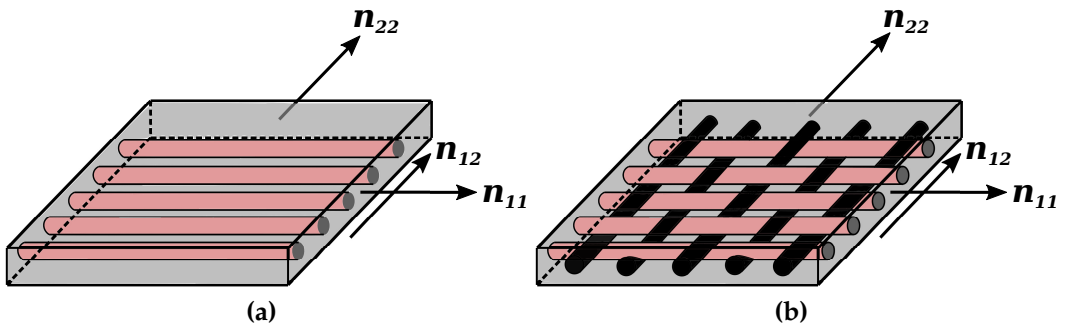

Figure 4.3: Illustration of directions n_{11}, n_{22} and n_{12} in thin spread-tow (a) unidirectional and (b) woven-fabric composite plies

zone evolves due to the presence of fibre pullout/bridging effects as shown in Fig. 4.4.

Each mechanism not only differs in the driving force which triggers crack initiation, but is also associated with a different value of fracture stress and corresponding critical energy release rate. This necessitates the extension of the cohesive phase field model discussed in Sec. 4.1 to incorporate anisotropic effects, which can accurately capture the fracture response pertaining to each composite damage mechanism.

The formulations presented herein, are motivated primarily from the work of Lorentz [444] on nonlocal gradient damage model for cohesive fractures. Aspects pertinent to the numerical implementation are drawn from the isotropic cohesive phase field method described in Sec. 4.1.

Contrary to the work introduced in [27], the proposed model relies on the definition of a single phase field variable that describes each composite failure mode. This significantly reduces the underlying computational costs, see also [28, 347]. Conversely, the stresses and elastic properties in each direction are degraded using distinct degradation functions that depend on the critical energy release rate and the fracture stress along that direction. The crack driving state functions and stress-degradation functions corresponding to each individual damage mechanism, e.g., in-plane longitudinal/transverse cracks in the fibres and shear cracks in the matrix, are determined separately.

4.2.1 Anisotropic Damage considerations

An anisotropic structural tensor is defined to orient the crack-path in the direction associated with the lower fracture strength and critical energy release rate. Furthermore, a 3-parameter cohesive phase field model is introduced that provides higher flexibility in controlling the shape of the cohesive softening law. This is important because the damage models in which the initial and the final stages of the cohesive softening curve cannot be controlled independently have only limited capability in accurately predicting the post-fracture material response [444, 447].

Driven by the derivations provided in [366, 448] and also in [28, 347, 369] for composite materials, a structural tensor $\mathcal{A}$ is first introduced in the definition of the functional $\gamma(\phi, \nabla\phi)$ (see, Eq. (4.2))

$$\gamma(\phi, \mathcal{A}, \nabla\,\phi) = \frac{3}{4l_o}\left[\phi + \frac{l_o^2}{4}\nabla\phi \cdot \mathcal{A}\,\nabla\phi\right] \tag{4.12}$$

The generalised functional definition of Eq. (4.12) enables the model to drive the crack along the directions with the lower fracture toughness σ_c and critical energy release rate $\mathcal{G}_c$.

In unidirectional composites, the fracture properties in the direction normal to the fibre orientation are substantially weaker when compared to the fibre directions. This implies that it is comparatively much more difficult to crack the fibres, and experimental evidence suggests that the crack propagates in the direction parallel to fibres [449]. In thin woven fabric composites, for e.g. in plies with fibre orientations $(0^o/90^o)$, cracking in either direction would involve fibre failure, but the crack might still have a preferred orientation based on the values of fracture strength and toughness in different directions. Hence, in the current work the structural tensor $\mathcal{A}$ is defined according to Eq. (4.13) in line with the definition in [347].

$$\mathcal{A} = \alpha_1 n_{11} \otimes n_{11} + \alpha_2 n_{22} \otimes n_{22} \tag{4.13}$$

In the case of UD composites, n_{11} and n_{22} correspond to the fibre and matrix directions, respectively (Fig. 4.3a). In the case of woven-fabric composites, both n_{11} and n_{22} correspond to the fibre directions as shown in Fig. 4.3b.

Furthermore, $\alpha_n = \{\alpha_1, \alpha_2\}$ are parameters that penalize crack propagation along the material directions which are manifested with a higher fracture toughness and strength. These parameters assume a value as $\alpha_n = 1$ along the stronger material direction. Conversely, a very low value is considered for the weaker direction (typically $\alpha_n \approx 0.02 - 0.05$). Specific values can also be obtained on the basis of the ratio of critical energy release rates $G_{c(s)}$ and $G_{c(w)}$ along the stronger and weaker directions, respectively, as discussed in [27, 28].

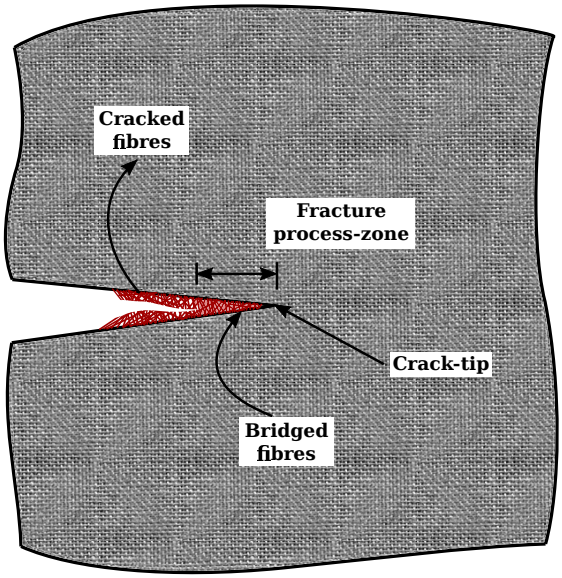

Figure 4.4: Illustration of fracture-process zone (FPZ) in fibre-reinforced composite plies due to combined fibre breakage and fibre pullout/bridging effect

4.2.2 Constitutive assumptions

The decomposition of the strain energy density ψ and the corresponding crack-driving force $\tilde{\mathcal{D}}_{iso}$ defined in Eqs. (4.6) and (4.9), respectively are valid as long as the material is isotropic in its elastic and post-fracture response. To this point, anisotropic phase field models have been developed, see, e.g. [25, 366, 367] that rely on the assumption of elastic isotropy and consider an anisotropic definition of the critical energy release-rate $\mathcal{G}_c$ depending on the crack orien-

tation. However, in composites preferential directions emerge due to the fibre orientations that result in anisotropic elastic properties. This implies that the deformation modes in each direction contribute to specific components of the strain energy density, which then trigger individual failure mechanisms.

Typically, in thin spread-tow fabric and UD plies these failure mechanisms can be classified into the following categories (see, also Fig. 4.3).

1. Fibre fracture and pullouts in both woven-fabric and UD-tape plies due to tensile deformations along the n_{11} direction
2. In-plane matrix cracking in UD-tape or fibre fracture and pullouts in woven-fabric plies due to tensile deformations along the n_{22} direction
3. In-plane matrix cracking in both woven-fabric and UD-tape plies, due to shear deformation along the n_{12} direction

In the subsequent sections, the above damage mechanisms are denoted by a subscript $i \in \{11, 22, 12\}$. The subscripts $\{11\}$, and $\{22\}$ correspond to the tensile failure modes in the material directions n_{11} and n_{22}, respectively whereas $\{12\}$ corresponds to the shear failure mode in direction n_{12}.

Remark 7. The transverse damage mechanisms such as matrix cracking under transverse shear deformations and subsequent delamination are practically suppressed in thin spread-tow composites [38], and hence are not accounted for in this work.

Based on the above analysis, it becomes important to individually characterize the active strain energy density components ψ_i which are responsible for triggering each corresponding damage mechanism. Similar to [28, 347], the current study considers that each damage mechanism is associated with a distinct critical energy release rate $\mathcal{G}_{ci}$ and a critical fracture strength σ_{ci} that can be experimentally identified.

Within this setting, Eq. (4.9) is reformulated and the following coupled strong form for the anisotropic cohesive phase field model is defined according

to Eq. (4.15).

$$\nabla \cdot \boldsymbol{\sigma} + \boldsymbol{b} = \boldsymbol{0} \tag{4.14}$$

$$\delta_\phi \gamma(\phi, \mathcal{A}, \nabla\phi) = \tilde{\mathcal{D}} \tag{4.15}$$

where

$$\delta_\phi \gamma = \frac{3}{4 l_o} \left[1 - \frac{l_o^2}{2} \nabla \cdot \mathcal{A} \nabla \phi \right] \tag{4.16}$$

The explicit expressions for the Cauchy stress $\boldsymbol{\sigma}$ and the anisotropic crack-driving force $\tilde{\mathcal{D}}$ are discussed in Sec. 4.2.3 and Sec. 4.4, respectively.

To ensure that the coupled strong form gives rise to evolving damage only, hence non-healing, the following irreversibility constraint is imposed on the phase field evolution Eq. (4.15).

$$\dot{\phi} \geq 0 \tag{4.17}$$

This irreversibility constraint has been traditionally imposed via a history variable [see, e.g., 24, 54]. In this work, the Augmented Lagrange Method (ALM) [351] is used to impose crack-irreversibility, as discussed in the algorithmic implementation of the proposed model in Sec. 4.7.

4.2.3 Elastic strain energy density

Based on the preferential material directions in composites and the classification of different damage mechanisms provided in Sec. 4.2.2, the following split for the strain tensor naturally emerges (see, also [27])

$$\boldsymbol{\varepsilon} = \boldsymbol{\varepsilon}^+ + \boldsymbol{\varepsilon}^- \tag{4.18}$$

where

$$\boldsymbol{\varepsilon}^+ = \begin{bmatrix} \langle \varepsilon_{11} \rangle^+ \\ \langle \varepsilon_{22} \rangle^+ \\ \gamma_{12} \end{bmatrix} \tag{4.19}$$

is the active part and

$$\boldsymbol{\varepsilon}^{-} = \begin{bmatrix} \langle \varepsilon_{11} \rangle^{-} \\ \langle \varepsilon_{22} \rangle^{-} \\ 0 \end{bmatrix} \tag{4.20}$$

is the passive part, respectively. In Eqs. (4.19) and (4.20), $\langle x \rangle_{\pm} = (x \pm |x|)/2$ are the Macaulay brackets.

It is of interest to note that when using the strain-decomposition method shown in Eqs. (4.19) and (4.20), the positive/negative components of stresses and strains are not always orthogonal, i.e. the cross-components ($\langle \sigma_{ij} \rangle^{+} \cdot \langle \varepsilon_{ij} \rangle^{-}$) in the original strain energy density expression do not necessarily vanish. This aspect has been addressed in the recent work of Wu et al. [450] wherein a positive/negative projection in the energy norm is employed leading to a well-defined energy functional and a thermodynamically consistent framework.

Despite this potential inconsistency, the split shown in Eqs. (4.19) and (4.20) [27] provides a natural and intuitive framework vis-à-vis the failure response of composites, since the material properties are anisotropic and the distinct failure mechanisms are primarily driven by the prevalent mode-specific components of stresses and strain-energy densities. The extensive experimental validations performed as part of this study (see, also, Sec. 4.10) demonstrate that such an assumption is valid and of practical use for the case of composites. Further extending the method provided in Wu et al. [450] for the case of anisotropic fractures would also lend the methodology described herein to a thermodynamically consistent framework. However, such an extension for the case of composites is non-trivial, and hence, beyond the scope of the present work.

The effective stress tensor $\bar{\boldsymbol{\sigma}}$ at each material point within each ply is defined accordingly based on Classical Lamination Theory (CLT) as Eq. (4.21).

$$\bar{\boldsymbol{\sigma}} = \boldsymbol{C}_o : \boldsymbol{\varepsilon} \tag{4.21}$$

$$\boldsymbol{C}_o = \begin{bmatrix} \dfrac{E_{11}}{1-\nu_{12}\nu_{21}} & \dfrac{\nu_{12}E_{22}}{1-\nu_{12}\nu_{21}} & 0 \\ \dfrac{\nu_{21}E_{11}}{1-\nu_{12}\nu_{21}} & \dfrac{E_{22}}{1-\nu_{12}\nu_{21}} & 0 \\ 0 & 0 & G_{12} \end{bmatrix} \text{ and, } \boldsymbol{\varepsilon} = \begin{bmatrix} \varepsilon_{11} \\ \varepsilon_{22} \\ \gamma_{12} \end{bmatrix} \tag{4.22}$$

where $\boldsymbol{C}_o$ is the elastic material stiffness matrix; plane-stress conditions are considered. In Eq. (4.22), E_{11} and E_{22} are the elastic Young's moduli, G_{12} is the in-plane shear modulus, and ν_{12} and ν_{21} are the in-plane Poisson's ratios defined for each ply of the composite laminate, where the relation $\nu_{21}E_{11} = \nu_{12}E_{22}$ holds.

The effective stress $\bar{\boldsymbol{\sigma}}$ in Eq. (4.21) can be similarly split into an active and passive part, i.e.,

$$\bar{\boldsymbol{\sigma}} = \bar{\boldsymbol{\sigma}}^{+} + \bar{\boldsymbol{\sigma}}^{-} \tag{4.23}$$

with

$$\bar{\boldsymbol{\sigma}}^{+} = \begin{bmatrix} \langle \bar{\sigma}_{11} \rangle^{+} \\ \langle \bar{\sigma}_{22} \rangle^{+} \\ \bar{\tau}_{12} \end{bmatrix} \tag{4.24}$$

and

$$\bar{\boldsymbol{\sigma}}^{-} = \begin{bmatrix} \langle \bar{\sigma}_{11} \rangle^{-} \\ \langle \bar{\sigma}_{22} \rangle^{-} \\ 0 \end{bmatrix} \tag{4.25}$$

as active and passive parts respectively.

Based on Eqs. (4.18)-(4.20) and (4.23)-(4.25), the components of the elastic strain energy density ψ, which are responsible for driving different composite failure mechanisms emerge as

$$\begin{aligned} \psi_{11}^{+} &= \frac{1}{2}\langle \bar{\sigma} \rangle_{11}^{+} \langle \varepsilon \rangle_{11}^{+} & \psi_{11}^{-} &= \frac{1}{2}\langle \bar{\sigma} \rangle_{11}^{-} \langle \varepsilon \rangle_{11}^{-} \\ \psi_{22}^{+} &= \frac{1}{2}\langle \bar{\sigma} \rangle_{22}^{+} \langle \varepsilon \rangle_{22}^{+} & \psi_{22}^{-} &= \frac{1}{2}\langle \bar{\sigma} \rangle_{22}^{-} \langle \varepsilon \rangle_{22}^{-} \\ \psi_{12}^{+} &= \frac{1}{2}\bar{\tau}_{12}\gamma_{12} & \psi_{12}^{-} &= 0 \end{aligned} \tag{4.26}$$

In this work, each active energy term ψ_{11}^{+}, ψ_{22}^{+} and ψ_{12}^{+} contributes to specific damage mechanisms, i.e., $\{11\}$, $\{22\}$, and $\{12\}$, respectively and are hence evaluated separately. The isotropic formulations can be obtained by summing up the corresponding active and passive components of strain energy density, i.e.,

$$\psi^{+} = \psi_{11}^{+} + \psi_{22}^{+} + \psi_{12}^{+} \tag{4.27}$$

$$\psi^{-} = \psi_{11}^{-} + \psi_{22}^{-} + \psi_{12}^{-} \tag{4.28}$$

4.3 Energetic degradation function

In this section, the explicit definitions of the damage mechanism specific degradation functions are provided. Each function operates on specific strain energy components, pertinent to the corresponding damage mechanism. A key aspect of the proposed definitions is that contrary to the methods proposed in [28, 347], the premature and simultaneous initiation of failure in all modes is delayed or avoided to significant extent, thus closely resembling the actual physical behaviour of composites.

Following the derivations presented in [444] [see, also Eq. (4.7)] for the case of an isotropic medium, a 3-parameter quasi-quadratic degradation function $g_i(\phi)$ is introduced for each anisotropic damage mechanism $i \in \{11, 22, 12\}$, which depends on the critical fracture stress, critical energy release rate and the cohesive law shape corresponding to that mechanism. The degradation functions $g_{11}(\phi)$, $g_{22}(\phi)$ and $g_{12}(\phi)$ are expressed as

$$g_{11}(\phi) = \frac{(1-\phi)^2}{(1-\phi)^2 + m_{11}\phi A_{11}(\phi)} \tag{4.29}$$

$$g_{22}(\phi) = \frac{(1-\phi)^2}{(1-\phi)^2 + m_{22}\phi A_{22}(\phi)} \tag{4.30}$$

$$g_{12}(\phi) = \frac{(1-\phi)^2}{(1-\phi)^2 + m_{12}\phi A_{12}(\phi)} \tag{4.31}$$

where the parameters $m_{11} = -g'_{11}(0)$, $m_{22} = -g'_{22}(0)$ and $m_{12} = -g'_{12}(0)$

correspond to the initial slope of the corresponding degradation functions and are defined as

$$m_{11} = \frac{3\mathcal{G}_{c11}E_{11}}{2l_o\sigma_{c11}^2} \tag{4.32}$$

$$m_{22} = \frac{3\mathcal{G}_{c22}E_{22}}{2l_o\sigma_{c22}^2} \tag{4.33}$$

$$m_{12} = \frac{3\mathcal{G}_{c12}G_{12}}{2l_o\sigma_{c12}^2} \tag{4.34}$$

Furthermore A_{11}, A_{22}, A_{12} assume the following form

$$A_{11}(\phi) = 1 + p_{11}\phi\left[\exp(q_{11}^2\phi^2)\right] \tag{4.35}$$

$$A_{22}(\phi) = 1 + p_{22}\phi\left[\exp(q_{22}^2\phi^2)\right] \tag{4.36}$$

$$A_{12}(\phi) = 1 + p_{12}\phi\left[\exp(q_{12}^2\phi^2)\right] \tag{4.37}$$

where q_i, and $p_i \geq 1$ are model parameters.

The degradation functions $g_i(\phi)$ defined in Eqs. (4.29)-(4.31) are imposed on the active tensile strain energy densities ψ_i^+ in Eq. (4.26), hence resulting in the following equation

$$\psi = g_{11}\psi_{11}^+ + g_{22}\psi_{22}^+ + g_{12}\psi_{12}^+ + \psi_{11}^- + \psi_{22}^- + \psi_{12}^- \tag{4.38}$$

Hence, contrary to the isotropic case of Eq. (4.5), in the anisotropic case each failure mode specific degradation function $g_i(\phi)$ acts only on its respective active energy term ψ_i^+. This ensures that once the damage is triggered, the material compliance in each direction is penalised by different amounts of degradation based on mode-specific elastic and fracture properties.

Remark 8. The 3-parameter degradation function chosen in this work allows for a versatile and accurate simulation of damage evolution in composites. Cohesive laws in which the initial and the final stages of softening cannot be controlled independently have been shown to offer limited capabilities in high-fidelity damage simulations [444, 447]. The model can be further extended by introducing additional parameters and higher-order polynomials in the degra-

dation function definition, see e.g., [352], to obtain more diverse softening behaviour.

The model parameters $\{m_i, p_i, q_i\}$ control the shape of the cohesive softening law for each individual failure mode $i \in \{11, 22, 12\}$. Their effect on the degradation functions $g_i(\phi)$ are shown in Fig. 4.5. In particular, parameter p_i controls the initial slope of the degradation function only (Fig. 4.5a). Higher values of p_i result in faster material degradation hence reducing the predicted peak fracture stresses. Conversely, q_i controls the final stage of the degradation function only (Fig. 4.5b). Thus, it affects the final crack-separation displacement in the cohesive-law.

The third parameter m_i, see Eq. (4.32)-(4.34), depends on the material and fracture properties $(E_i, \sigma_{ci}, \mathcal{G}_{ci})$ which are constants for any given material and affect the shape of the softening branch. Smaller values give rise to near-linear descending branches (Fig. 4.5c). The fact that m_i depends also on the length scale l_o, which is common for all failure modes, implies that $\{m_{11}, m_{22}, m_{12}\}$ cannot be calibrated independently of each other. However, it is now well-accepted that the fracture response of cohesive phase field models is *length scale independent* [351–353], and l_o only needs to assume a small enough value so that the diffusion zone becomes bounded. In the limit $l_o \to 0$, the cohesive phase field model converges to an asymptotic cohesive zone model, as demonstrated in [444]. It is worth noting that in the current model, the estimated peak fracture force and the final crack-separation displacement are insensitive to variations in the parameters m_i and the length-scale l_o, as would be demonstrated with the numerical examples.

Furthermore, it can be observed that due to the specific formulations adopted for $g_i(\phi)$ in Eq. (4.29), the stresses σ_i in each direction are naturally subjected to different amounts of degradation, which is controlled by the anisotropic fracture parameters $\{\mathcal{G}_{ci}, \sigma_{ci}\}$; these correspond to specific composite failure modes $i \in \{11, 22, 12\}$.

Remark 9. Similar to Eq. (4.11), an equivalent upper bound definition for the

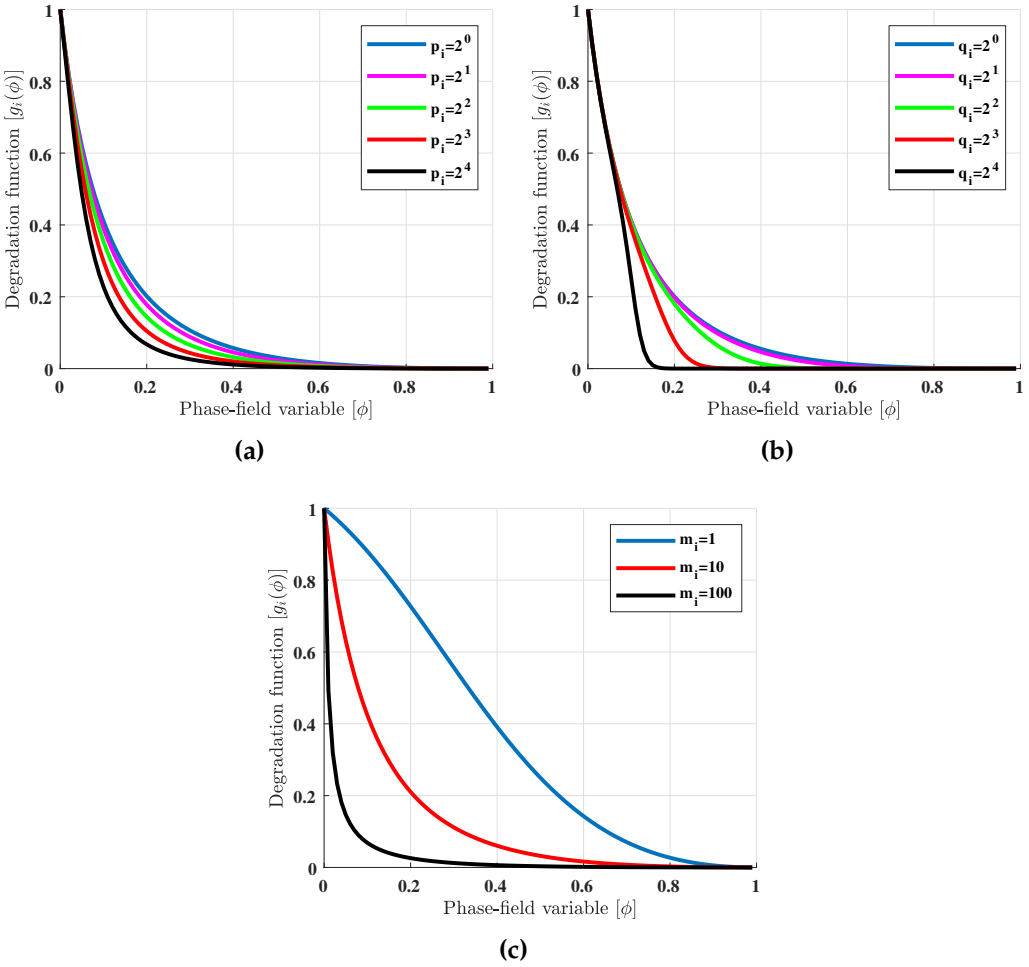

Figure 4.5: Variation of stiffness degradation function $g_i(\phi)$ for any composite damage mechanism i with respect to phase field variable ϕ for different values of cohesive shape parameters $\{m_i, p_i, q_i\}$

length-scale must be incorporated within the proposed anisotropic cohesive phase field model to obtain a well-conditioned system with optimal convergence rate. This is defined herein based on the material and fracture properties in two principal, viz. warp and weft, directions of the spread-tow woven-fabric and spread-tow unidirectional composites,

$$l_o < l_{o(UB)} = \min\left(\frac{3E_{11}\mathcal{G}_{c11}}{2(A_1'(0)+2)\sigma_{c11}^2}, \frac{3E_{22}\mathcal{G}_{c22}}{2(A_2'(0)+2)\sigma_{c22}^2}\right) \tag{4.39}$$

where $\mathcal{G}_{ci}$ are the critical energy release rates, σ_{ci} are the critical fracture stresses and l_o is the length scale parameter with its upper-bound defined by $l_{o(UB)}$. The expression in Eq. (4.39) is closely related to the characteristic length of the

fracture process zone, which is given as $l_{FPZ_i} = E_i \mathcal{G}_{ci} / \sigma_{ci}^2$.

4.4 Anisotropic crack-driving force

The definition of failure-mode specific degradation functions ensures that these degrade only the corresponding active part of the elastic energy density Eq. (4.27), with the degradation rates governed by respective material and fracture properties. This ensures that despite using a single damage variable in the current formulations, a slower damage evolution rate in stronger material directions post damage initiation is maintained. This anisotropic degradation effect must also be manifested within the definitions of the crack-driving forces responsible for triggering each failure mode. To ensure independent crack evolution in each direction, (see Fig. 4.6 for a woven-fabric composite ply), the crack-driving force $\tilde{\mathcal{D}}$ in Eq. (4.15) is additively decomposed into failure mode specific components, i.e.,

$$\tilde{\mathcal{D}} = \tilde{\mathcal{D}}_{11} + \tilde{\mathcal{D}}_{22} + \tilde{\mathcal{D}}_{12} \tag{4.40}$$

where

$$\tilde{\mathcal{D}}_{11} = -\frac{g'_{11} \psi_{11}^+}{\mathcal{G}_{c11}} \tag{4.41}$$

$$\tilde{\mathcal{D}}_{22} = -\frac{g'_{22} \psi_{22}^+}{\mathcal{G}_{c22}} \tag{4.42}$$

and

$$\tilde{\mathcal{D}}_{12} = -\frac{g'_{12} \psi_{12}^+}{\mathcal{G}_{c12}} \tag{4.43}$$

respectively.

In Eqs. (4.41)-(4.43), the mode specific crack driving force terms depend on the mode specific critical energy release rates $\mathcal{G}_{ci}$, the tensile strain energy densities ψ_i^+, and the degradation functions $g_i(\phi)$. Hence, the coupling between the governing Eqs. (4.14) and (4.15) is naturally achieved in a failure mode-wise manner.

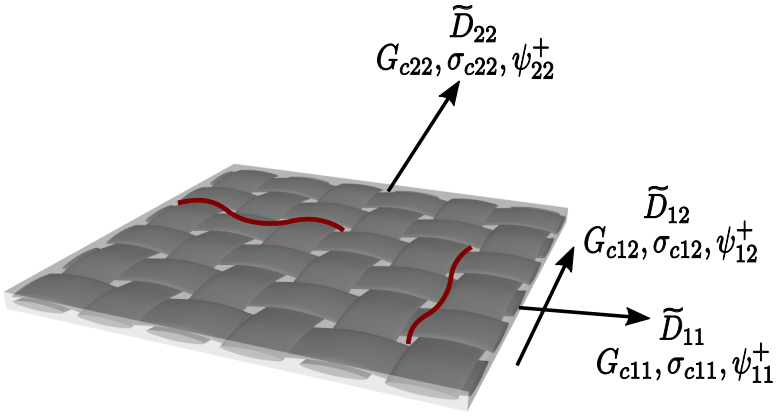

Figure 4.6: Illustration of different crack-driving forces $\tilde{\mathcal{D}}_i$, critical energy release rates $\mathcal{G}_{ci}$, critical fracture stresses σ_{ci} and strain energy density contribution ψ_i^+, responsible for initiating each damage mechanism i in spread-tow fabric composites. Each $\tilde{\mathcal{D}}_i$ is degraded using distinct degradation function $g_i(\phi)$

Remark 10. The isotropic case can be recovered by setting,

$$\begin{aligned} \sigma_c &= \sigma_{c11} = \sigma_{c22} = \sigma_{c12} \\ \mathcal{G}_c &= \mathcal{G}_{c11} = \mathcal{G}_{c22} = \mathcal{G}_{c12} \end{aligned} \tag{4.44}$$

which also eventually leads to,

$$g(\phi) = g_{11}(\phi) = g_{22}(\phi) = g_{12}(\phi) \tag{4.45}$$

4.5 Effective critical energy release-rate

Bourdin et al. [94] in their original variational formulation showed that the fracture energy is slightly overestimated during phase field simulations. The amplitude of this overestimation depends on the characteristic mesh size in the overall finite-element discretization. To alleviate this effect, the critical energy release rate obtained from the experiments must be scaled to an effective $\mathcal{G}_c^{eff}$ for the purpose of phase field simulations, see also Egger et al. [17] for a comparative review. In this work, the scaling procedure provided in [347] for the case of anisotropic composite fracture is closely followed for each mode-

specific $\mathcal{G}_{ci}$

$$\mathcal{G}_{ci}^{eff} = \mathcal{G}_{ci}\left(1 - \frac{h_e}{l_o}\right) \tag{4.46}$$

where h_e is the characteristic element length, l_o is the length-scale parameter, and $\mathcal{G}_{ci}$ and $\mathcal{G}_{ci}^{eff}$ are the actual and effective critical energy release rates, respectively. For an effective comparison between the experimental results and the fracture estimations provided by phase field simulations, it is important to use $\mathcal{G}_{ci}^{eff}$ in the formulations [347]. It can be noted that Eq. (4.46) from [347] is fundamentally similar to Eq. (3.67) from [349] presented in the previous Chapter 3, except for the fact, that binomial theorem as shown in Eq. (4.47) is applied to obtain Eq. (4.46), where $h_e \ll l_o$ has been assumed. This is consistently followed, and discussed in detail in the numerical examples presented in this chapter.

$$\left(1 + \frac{h_e}{l_o}\right)^{-1} \approx \left(1 - \frac{h_e}{l_o}\right) \tag{4.47}$$

4.6 Shear isotropic hardening in woven fabric-reinforced composites

In woven-fabric reinforced composites, the shear response is primarily dominated by the material properties of the matrix. This involves nonlinear plastic deformations of the matrix followed by strength degradation due to the initiation of matrix micro-cracks [2, 5]. To account for the plasticity and subsequent strength reduction, the anisotropic cohesive phase field model is combined with an elastic-plastic constitutive model with isotropic hardening for the in-plane shear behaviour. The plastic evolution of shear stresses is controlled using a threshold function proposed in [5], also shown in Eq. (4.48), which governs the onset and evolution of plastic shear behaviour.

$$\bar{\tau}_{12} = S_{LP} + \zeta_E\left[1 - e^{-|\zeta_E^T \varepsilon_{12}^p|}\right] + \zeta_L \varepsilon_{12}^p \tag{4.48}$$

where $\bar{\tau}_{12}$ is the in-plane shear stress, ε^p_{12} is the plastic shear strain, and S_{LP} is the shear yield stress. The constants $\{\zeta_E, \zeta^T_E, \zeta_L\}$ are material parameters that can be obtained through calibration to experimental results obtained from pure shear tests of woven fabric-reinforced composites, see, e.g. [2]. Fig. 4.7 schematically illustrates the shear stress-strain response for any typical fabric-reinforced composite, based on the elastic-plastic cohesive phase field model proposed in this work.

The corresponding plastic strain evolution law is defined as Eq. (4.49)

$$\dot{\varepsilon}^p_{12} = \dot{\varepsilon}^i_{12}\text{sign}(\varepsilon^e_{12}) \tag{4.49}$$

where ε^e_{12} is the elastic shear strain and ε^i_{12} is isotropic hardening variable [5].

Based on this, the active shear strain energy density ψ^+_{12} in Eq. (4.26) and (4.43) must be modified for the case of fabric-reinforced composites, to include only the elastic part of the shear strains as shown in Eq. (4.50).

$$\psi^+_{12} = \frac{1}{2}\bar{\tau}_{12}\gamma^e_{12} \tag{4.50}$$

where γ^e_{12} is the engineering elastic shear strain given by Eq. (4.51).

$$\begin{aligned} \gamma^e_{12} &= 2\varepsilon^e_{12} \\ \varepsilon^e_{12} &= \varepsilon_{12} - \varepsilon^p_{12} \end{aligned} \tag{4.51}$$

Once the critical shear stress S_L is reached, the post-peak shear stress-degradation is controlled using the cohesive phase field model with appropriate softening parameters.

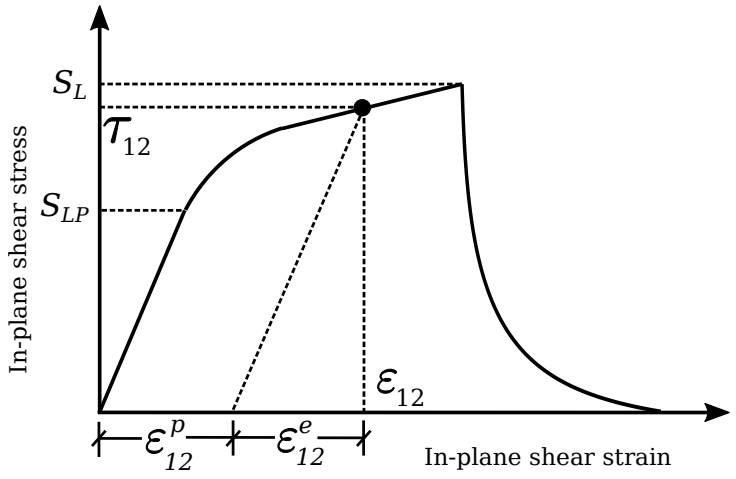

Figure 4.7: Illustration of characteristic in-plane shear behaviour for a typical spread-tow fabric (STF) reinforced composite

4.7 Solution scheme and Abaqus implementation

4.7.1 Augmented Lagrangian form of the governing equations

Eq. (4.17) imposes the necessary irreversibility constraint to the phase field, i.e., a crack should not be allowed to heal. Similar to [351], this constraint is introduced by means of an augmented Lagrangian expression and Eq. (4.15) is re-written as

$$\frac{3}{4l_o}\left[1-\frac{l_o^2}{2}\nabla\cdot\mathcal{A}\nabla\phi\right]-\langle\lambda+\gamma(\phi_{n-1}-\phi)\rangle_+-\langle\lambda+\gamma(1-\phi)\rangle_-=\tilde{\mathcal{D}} \quad (4.52)$$

where λ and γ are augmented Lagrange and penalty parameters respectively, and $\{\phi_{n-1}\}$ is the phase field variable values obtained at time $t = t_{n-1}$. The penalty γ is imposed whenever the value of the phase field decreases during subsequent time-increments i.e. $\phi < \phi_{n-1}$, or when it exceeds unity i.e. $\phi > 1$. The Lagrange multiplier is updated iteratively until convergence. It is of interest to note that although the original objective function is minimally distorted in the augmented Lagrange method due to iterative updating of the Lagrange multiplier, more accurate values of γ can be obtained based on the lower-bound analytical limit presented in [434]. In line with the recommended values in [351], the extensive numerical experiments conducted in this study

also confirm that the penalty parameter $\gamma = 1.e4$ and the corresponding convergence tolerance $\mathcal{R}_\gamma = 1.0e^{-4}$ provide robust and accurate fracture predictions.

4.7.2 Galerkin approximation

To obtain the displacement and phase field solutions from the strong form linear momentum balance in Eq. $(4.14)_1$ and the modified phase field evolution Eq. (4.52) using finite element approximation, the following trial solution spaces can be defined.

$$\begin{aligned} \mathcal{S}_{\boldsymbol{u}} &= \left\{ \boldsymbol{u} \in \left(\mathcal{H}^1(\Omega) \right)^d \,\middle|\, \boldsymbol{u} = \bar{\boldsymbol{u}} \text{ on } \partial\Omega_b \right\} \\ \mathcal{S}_{\phi} &= \left\{ \phi \in \left(\mathcal{H}^1(\Omega) \right) \right\} \end{aligned} \tag{4.53}$$

with the corresponding weighting or test function spaces as defined in Eq. (4.54).

$$\begin{aligned} \mathcal{W}_{\boldsymbol{u}} &= \left\{ \delta\boldsymbol{u} \in \left(\mathcal{H}^1(\Omega) \right)^d \,\middle|\, \delta\boldsymbol{u} = \bar{\delta\boldsymbol{u}} \text{ on } \partial\Omega_b \right\} \\ \mathcal{W}_{\phi} &= \left\{ \delta\phi \in \left(\mathcal{H}^1(\Omega) \right) \right\} \end{aligned} \tag{4.54}$$

Multiplying the strong form equations (4.14) with the above test functions $\boldsymbol{\delta u}$ and $\delta\phi$, and performing integration by parts leads to the following weak form of governing equilibrium equations (4.55).

$$\begin{aligned} \mathcal{R}_{\boldsymbol{u}} &= \int_\Omega \boldsymbol{\sigma} \cdot \nabla \delta\boldsymbol{u} \, d\Omega - \int_\Omega \boldsymbol{b} \cdot \delta\boldsymbol{u} \, d\Omega - \int_{\partial\Omega_b} \boldsymbol{t} \cdot \delta\boldsymbol{u} \, d\partial\Omega_b \approx \boldsymbol{0} \\ \mathcal{R}_{\phi} &= -\int_\Omega \tilde{\mathcal{D}} \, \delta\phi \, d\Omega + \int_\Omega \frac{3}{4l_o} \left[\delta\phi + \frac{l_o^2}{2} \nabla\delta\phi \cdot \mathcal{A} \nabla\phi \right] \, d\Omega \\ &\quad - \int_\Omega \left(\langle \lambda + \gamma(\phi_{n-1} - \phi) \rangle_+ + \langle \lambda + \gamma(1 - \phi) \rangle_- \right) \delta\phi \, d\Omega \approx 0 \end{aligned} \tag{4.55}$$

The matrix form for the phase field residual and stiffness matrix is shown

in Eq. (4.56).

$$
\begin{aligned}
\mathcal{R}_i^{\phi} &= -\int_{\Omega} N_i\, \tilde{\mathcal{D}}\, d\Omega + \int_{\Omega} \frac{3}{4l_o}\left[N_i + \frac{l_o^2}{2}[B_i^{\phi}]^T\, [\mathcal{A}]\, [B_j^{\phi}]\, \phi_j\right]\, d\Omega \\
&\quad - \int_{\Omega} N_i\, \left(\langle \lambda + \gamma(\phi_{n-1} - N_j\, \phi_j)\rangle_+ + \langle \lambda + \gamma(1 - N_j\, \phi_j)\rangle_-\right)\, d\Omega \\
\mathcal{K}_i^{\phi} &= \int_{\Omega} N_i N_j \frac{\partial \tilde{\mathcal{D}}(\phi_j)}{\partial \phi_j}\, d\Omega - \int_{\Omega} \frac{3l_o}{8}\, [B_i^{\phi}]^T\, [\mathcal{A}]\, [B_j^{\phi}]\, d\Omega \\
&\quad - \int_{\Omega} \gamma N_i N_j \left(\frac{\langle \lambda + \gamma(\phi_{n-1} - N_j\, \phi_j)\rangle_+}{\lambda + \gamma(\phi_{n-1} - N_j\, \phi_j)} + \frac{\langle \lambda + \gamma(1 - N_j\, \phi_j)\rangle_-}{\lambda + \gamma(1 - N_j\, \phi_j)}\right)\, d\Omega
\end{aligned}
\tag{4.56}
$$

where, N_i and B_i^{ϕ} are the shape functions and their derivative matrix given in Eq. (A.3) and Eq. (3.55) respectively. The solution to the combined set of Eqs. (4.55) is obtained using either monolithic or staggered algorithms which are based on simultaneous and alternating minimization respectively, of residuals $\mathcal{R}_{\mathbf{u}}$ and $\mathcal{R}_{\phi}$. The conventional monolithic algorithm although provides accurate fracture predictions, but suffers from poor convergence issues due to non-convexity of the underlying energy functional [337]. However, this can be alleviated by using the more efficient BFGS monolithic algorithm recently proposed in [339, 341], which involves lesser iterations and reformulations of the system matrix in each increment.

In contrast to monolithic approaches, the staggered (alternating minimisation) algorithm relies on decoupling the linear momentum and phase field equations and solving them separately within each increment. This is achieved by freezing one solution variable at a constant value and solving for another variable, and vice-versa. This retains the convexity of the energy functional and hence, displays excellent convergence characteristics.

Wu et al. [339], in their recent work showed that the BFGS monolithic algorithm performs considerably faster than the staggered schemes. The solution strategy based on BFGS algorithm is both robust and efficient, and is implemented in Abaqus using user-element (UEL) subroutine. One of the drawbacks with Abaqus UEL is that the post-processing and visualization of

results is not straightforward, and this requires defining a duplicate fictitious mesh that shares common nodes with the original mesh and doubles the size of system matrix. In this implementation and for the sake of brevity, a one-pass staggered (alternating minimisation) solution scheme presented in [451] is used, see also [351]. At every time-increment, the displacement solution is updated using Abaqus UMAT, whereas the phase field solution is updated using an external MKL PARDISO solver as shown in Fig. 7. Such an implementation guarantees direct visualization of solution results in Abaqus/Viewer without requiring a fictitious mesh, which would considerably increase the computational costs. Furthermore, it allows for a straightforward and efficient utilization of Abaqus parallel solving capabilities.

4.7.3 Hybrid phase field formulation

In the current work, a hybrid-type formulation has been employed, in which the stress and the phase fields are derived using distinct energy functionals $\bar{\psi}$ and ψ respectively. For the phase field evolution equations $(4.55)_2$, the crack-driving force term $\tilde{\mathcal{D}}$ is still defined based on the active (tensile) strain energy density expressions ψ_i^+ in Eq. (4.40). However, the evolution of Cauchy stress within the linear momentum balance Eq. $(4.55)_1$ is governed by the energy functional $\bar{\psi}$ in Eq. (4.57) below.

$$\bar{\psi} = \boldsymbol{\varepsilon}^T : \boldsymbol{C}_o : \boldsymbol{\varepsilon} \tag{4.57}$$

where $\boldsymbol{C}_o$ and $\boldsymbol{\varepsilon}$ are taken from Eq. (4.22). The derivative of $\bar{\psi}$ with respect to $\boldsymbol{\varepsilon}$ provides the effective stresses $\bar{\boldsymbol{\sigma}}$ in Eq. (4.58), which is similar to the definition previously given in Eq. (4.21)

$$\bar{\boldsymbol{\sigma}} = \frac{\partial \bar{\psi}}{\partial \boldsymbol{\varepsilon}} = \begin{bmatrix} \bar{\sigma}_{11} & \bar{\sigma}_{22} & \bar{\tau}_{12} \end{bmatrix}^T = \boldsymbol{C}_o : \boldsymbol{\varepsilon} \tag{4.58}$$

Furthermore, the degraded (σ) Cauchy stress tensor can be obtained as

shown in Eq. (4.59) below.

$$\boldsymbol{\sigma} = \begin{bmatrix} \sigma_{11} \\ \sigma_{22} \\ \tau_{12} \end{bmatrix} = \begin{bmatrix} g_{11}(\phi) & 0 & 0 \\ 0 & g_{22}(\phi) & 0 \\ 0 & 0 & g_{12}(\phi) \end{bmatrix} \begin{bmatrix} \bar{\sigma}_{11} \\ \bar{\sigma}_{22} \\ \bar{\tau}_{12} \end{bmatrix} \tag{4.59}$$

Such a hybrid split based on separate energy functionals $\bar{\psi}$ and ψ has been investigated previously for brittle fractures in [312, 432, 452], quasi-brittle fractures in [352, 453–456] and recently for composite brittle fractures in [28]. The hybrid split conceptually resembles gradient-enhanced continuum damage mechanics models and has proved to reduce the computational effort by atleast an order of magnitude, as the resulting linear momentum and phase field equations get rid of their severe non-linear characteristics. The hybrid damage model is no more variationally consistent, but such a variational crime doesn't violate the second law of thermodynamics and the energy dissipation inequality as established in [455, 456], see also [337, 352, 454]. Moreover, the asymmetric nature of fracture under tensile/compressive deformation modes can be very accurately captured using hybrid split while significantly enhancing the computational efficiency [337, 432, 456].

4.7.4 Implementation within an Abaqus UMAT subroutine

The solution algorithm is implemented within commercial software Abaqus using a user-material (UMAT) subroutine as illustrated in Fig. 4.8, see also Algorithm A.2. The choice of UMAT is justified in the sense that one gains access to complete Abaqus in-built functionality; e.g., defining composite ply layups and fibre orientations can be directly utilized. Moreover, no additional visualization modules are needed and the post-processed final results can be directly visualized in Abaqus CAE/Viewer as opposed to the user-element (UEL) subroutine, see for e.g. [97, 306, 320, 338]. Since no additional DOFs are introduced when using the UMAT subroutine, the Abaqus solver can only be used to solve those DOFs which are inherent to the Abaqus standard library [178], for e.g.

displacement DOFs in this case. To solve the phase field equations, an external linear system solver such as Intel's Math-Kernel Library (MKL) PARDISO [457] is used in the current work. To facilitate sequential solving of linear momentum and phase field equations within the staggered solution scheme, the UEXTERNALDB subroutine available in Abaqus is used to call both Abaqus and PARDISO solvers alternately in subsequent time-steps. The common variables which are required to solve both equations, for e.g. the crack driving force $\tilde{\mathcal{D}}$ and the phase field variable ϕ, are exchanged via an external Fortran module. The damage results obtained at the end of each time-step are stored in the form of state-dependent variables (STATEV) in Abaqus, to be used in the subsequent iterations.

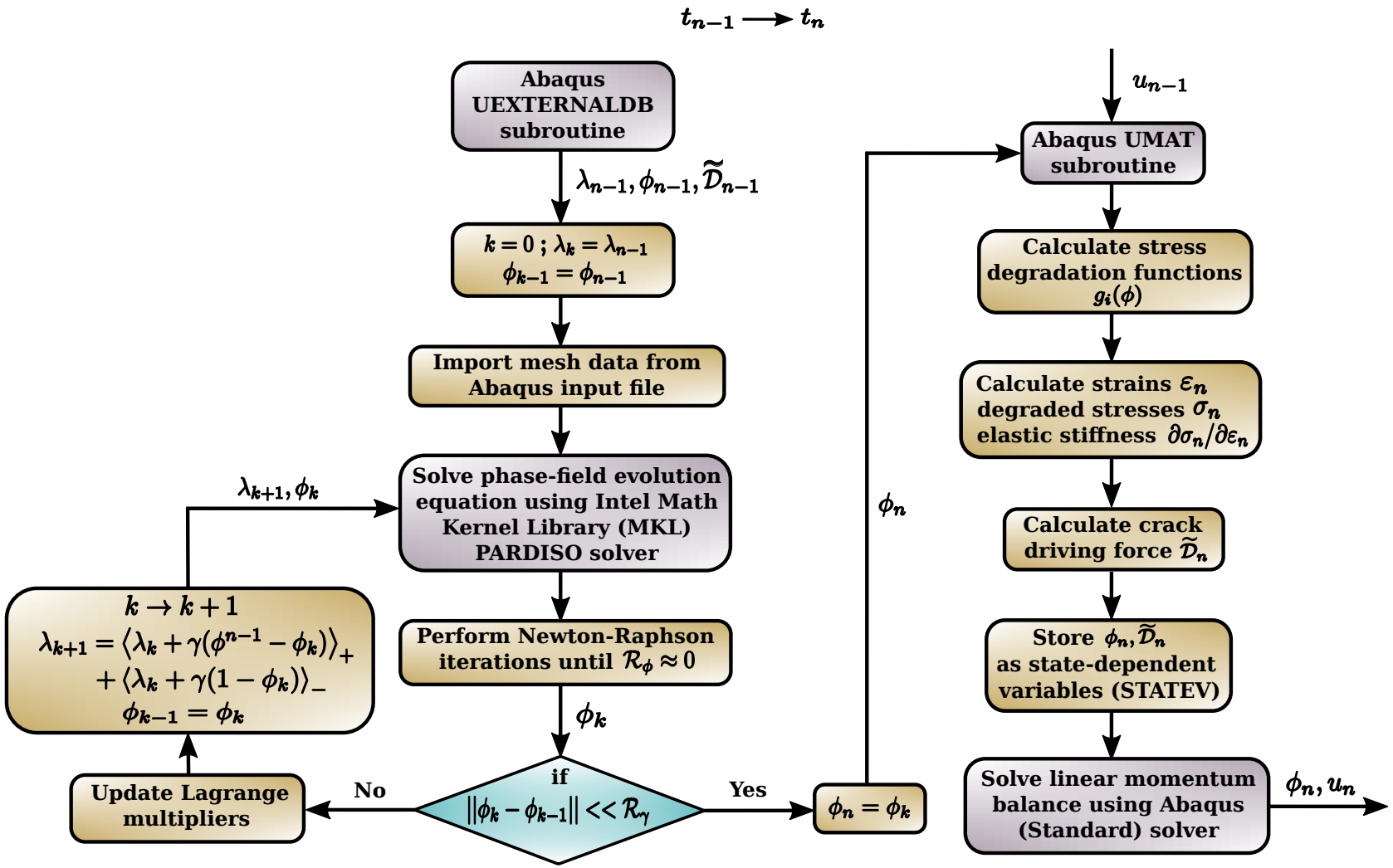

Figure 4.8: Flowchart illustrating solution procedure and algorithm implementation within Abaqus subroutines for time-increment $t_{n-1} \to t_n$

4.8 Experimental calibration

The proposed anisotropic cohesive phase field model relies on the definition of the degradation functions defined in Eqs. (4.29)-(4.31). Hence, a proper calibration of all pertinent material parameters based on experimental measurements is required for the model to provide high-fidelity estimates. In particular, to fully define the degradation functions, the following parameters have to be identified (see also Fig. 4.9)

1. The critical fracture stresses σ_{ci} corresponding to each damage mechanism $i \in \{11, 22, 12\}$ which defines the point of damage initiation;
2. The critical energy release rates $\mathcal{G}_{ci}$ which defines the total area under the cohesive traction-separation curve;
3. The shape of the cohesive softening curve, which is controlled by the parameters $\{m_i, p_i, q_i\}$ and;
4. The displacement at crack separation δ_{ci}.

In practice, the model parameters $\{p_i, q_i\}$ for each damage mechanism $i \in \{11, 22, 12\}$ can be calibrated using two independent experiments. For the case of woven-fabric reinforced laminates, the value of the tensile parameters $\{p_{11}, q_{11}, p_{22}, q_{22}\}$ can be obtained from either an open-hole tension or a compact tension test of $(0^o/90^o)$ laminates. The shear parameters $\{p_{12}, q_{12}\}$ can be obtained from a tensile test on $(-45^o/45^o)$ laminates or a pure shear test on $(0^o/90^o)$ laminates of the same material, see [2, 5] for more details.

Using the parametric definition of the traction separation law provided in Lorentz [444], within the context of a gradient enhanced continuum damage model, the following relations are defined for each individual composite damage mechanism $i \in \{11, 22, 12\}$, i.e.,

$$\frac{\sigma_i(\phi)}{\sigma_{ci}} = \tilde{\sigma}_i(\phi) \tag{4.60}$$

where

$$\tilde{\sigma}_i(\phi) = \frac{1-\phi}{\sqrt{A_i(\phi)}} \tag{4.61}$$

and

$$\frac{\sigma_{ci}}{\mathcal{G}_{ci}}\left[\delta_i(\phi) - l_o\frac{2\sigma_{ci}}{E_i}\tilde{\sigma}_i(\phi)\right] = \tilde{\delta}_i(\phi) \tag{4.62}$$

where

$$\tilde{\delta}_i(\phi) = \frac{3}{2}\tilde{\sigma}_i(\phi)\int_0^{\phi}\frac{\sqrt{\phi'}A_i(\phi')}{(1-\phi')^2}\left[1-\frac{A_i(\phi')(1-\phi)^2}{A_i(\phi)(1-\phi')^2}\right]^{-1/2}d\phi' \tag{4.63}$$

The analytical expressions Eqs. (4.60)-(4.63) can be fitted to experimentally derived softening curves hence identifying the anisotropic mode-specific material parameters for the cohesive phase field model.

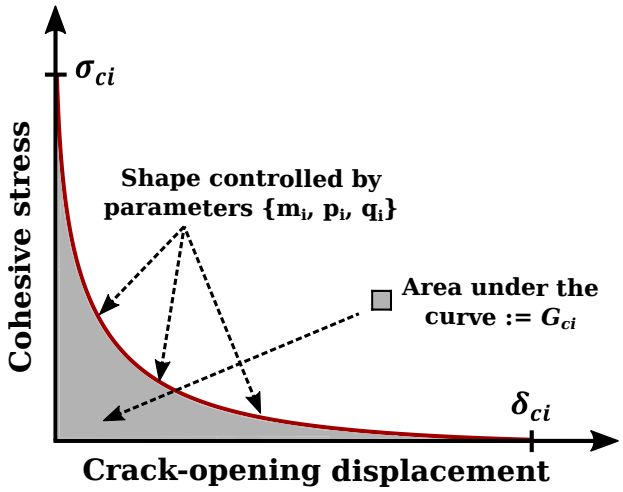

Figure 4.9: Illustration of cohesive softening law with associated material and fracture parameters for any specific composite damage mechanism i

4.9 Extension to full composite-laminate analysis

In this section, the proposed anisotropic cohesive phase field model is extended to perform full composite-laminate simulations. The laminate is constructed by stacking multiple layers of thin-plies separated by adhesive layers, wherein each ply is modelled using conventional fully-integrated S4 shell elements in Abaqus. Since shell elements represent the mid-surface of de-

generated 3-D solids, the top and bottom surfaces of each ply are modelled explicitly using Abaqus surface elements (SFM3D4R) to correctly define the adhesive interactions at ply-interfaces. The mesh-discretization for top and bottom surfaces matches that of the mid-surface, and all three surfaces are tied together in all degrees of freedom using **TIE* constraints in Abaqus. This results in strong coupling between the kinematics of surface and shell elements, wherein the former represents a dummy mesh without an underlying constitutive model, which moves according to the deformations of shell mid-surface. Similar stacked-shell approaches (SSA) have been employed previously in [2, 65, 435], and provide reasonable prediction of complex failure behaviour pertinent to laminated composites. Fig. 4.10 provides a schematic illustration of the through-thickness layup of thin-ply composite laminate model used in this study.

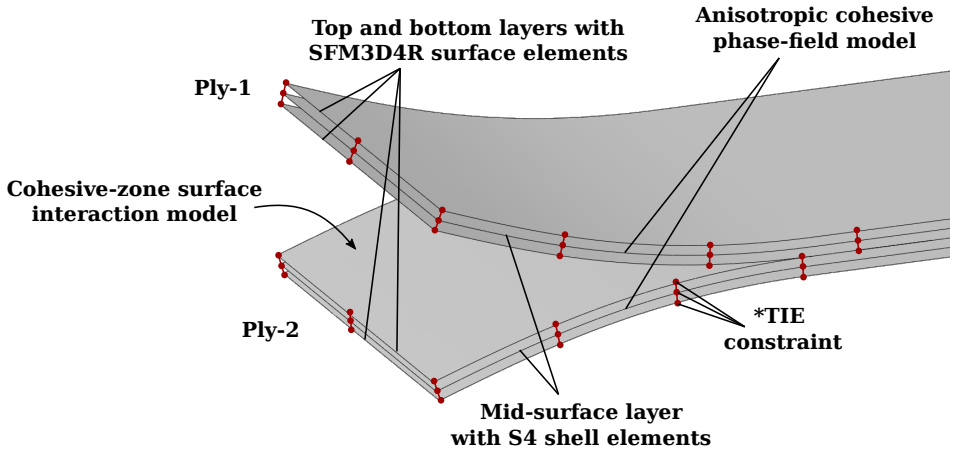

Figure 4.10: Schematic illustration of thin-ply composite laminate modelled with stacked shell approach using tied shell/surface element layers, and phase field and cohesive zone models for intra-laminar and inter-laminar damage respectively

The intra-laminar damage within each ply mid-surface is modelled using the anisotropic cohesive phase field model proposed in Sec. 4.2, whereas the modelling of inter-laminar damage (delamination) between adjacent plies is performed using the cohesive-zone surface interaction model available in Abaqus. The thickness of adhesive layers between the plies is assumed to be negligible, thus motivating the use of cohesive surface interactions over cohesive elements with finite thickness.

4.9.1 Dynamic explicit simulations using Abaqus VUMAT

Until this point in the current chapter, the cohesive phase field model was implemented using UMAT subroutine within a static implicit analysis in Abaqus. Implicit schemes are unconditionally stable and highly accurate, however, they are known to cause severe convergence issues in highly nonlinear damage simulations, e.g. during impact. Especially due to the rapid crack propagation and catastrophic failure behaviour associated with delamination, the underlying numerical scheme may converge very slowly or even diverge depending upon the degree of non-linearity. In such cases, using a dynamic explicit scheme provides significant advantages, although at a cost of using smaller stable time-increments, which depends directly on the minimum element size in the mesh. An advantage of using conventional shell elements in explicit solution scheme is that it does not penalize the stable time-increment size due to smaller through-the-thickness dimension of thin plies.

To alleviate these convergence issues, especially during impact driven nonlinear damage scenarios, the anisotropic cohesive phase field model in Eq. (4.52) is extended to perform dynamic simulations using an explicit time integration scheme. The implementation is done using Abaqus VUMAT subroutine and is based on the approach presented earlier in [458]. In particular, the following dynamic phase field evolution Eq. (4.64) is solved (see also [458]).

$$\eta\dot{\phi} = \langle \mathcal{R}_{\phi}(\phi_n) \rangle_{+} \tag{4.64}$$

where η is the viscous dissipation parameter for crack evolution, $\mathcal{R}_{\phi}$ is the phase field residual in Eq. (4.52) and $\langle \cdot \rangle_{+}$ is the Macaulay bracket shown in Eq. (3.25). The left-hand side of Eq. (4.64) is discretized using an explicit forward difference method, and the phase field variable ϕ_{n+1} at each time-increment t_{n+1} is updated using Eq. (4.65) shown below.

$$\phi_{n+1} = \phi_n + \frac{\Delta t_{n+1}}{\eta} \langle R_{\phi} \rangle_{+} \tag{4.65}$$

Similarly, the displacement field u is simulated by performing an explicit time-integration of linear momentum balance internally by Abaqus [178] using a central-difference scheme as shown in Eq. (4.66).

$$\begin{aligned} \dot{u}_{(n+1/2)} &= \dot{u}_{(n-1/2)} + \frac{\Delta t_{(n+1)} + \Delta t_n}{2} \ddot{u}_n \\ u_{(n+1)} &= u_n + \Delta t_{(n+1)} \dot{u}_{(n+1/2)} \end{aligned} \tag{4.66}$$

To boost the computational efficiency of the overall explicit procedure, diagonal (lumped) element mass matrices are used, which are straightforward to invert and requires a simple matrix-vector multiplication for each update of displacement field u [178].

$$\ddot{u}_n = (M)^{-1}(\mathcal{F}_{ext} - \mathcal{F}_{int}) \tag{4.67}$$

wherein, M is the lumped mass matrix, and $\mathcal{F}_{ext}$ and $\mathcal{F}_{int}$ are the external and internal force vectors respectively. It is worth noting that the time-increment size used within explicit schemes must be lesser than the stable time-increment limit, to obtain reasonable and accurate results. The stability limit is given by the smallest time taken by the dilatational wave to travel across any element in the mesh, and is given by Eq. (4.68).

$$\Delta t_{stable} \approx \frac{L_{min}}{c_d} \tag{4.68}$$

with L_{min} and c_d being the dimension of smallest element dilatational wave speed respectively. In this work, the fully-automatic time-incrementation control in Abaqus is used, which chooses the stable time increment on its own based on the wave speeds in each element or globally, and does not require any external intervention.

All remaining formulations as previously discussed in Sec. 4.2-4.7 are kept intact vis-à-vis implementation of dynamic explicit scheme.

4.9.2 Modelling of inter-laminar damage (delamination)

In impact-driven damage simulations of full composite laminates, delamination becomes one of the major failure mechanism in addition to fibre/matrix based failures. The delamination between top/bottom surface elements layers of adjacent plies is modelled using cohesive zone surface interaction model from Abaqus library. The damage (delamination) initiation is modelled using the quadratic stress (QUADS) criterion (Eq. (4.69)), which is based on the ratio of induced stresses (σ_i) with respect to peak nominal stresses (σ_{ic}) in normal or shear directions [178].

$$\left[\frac{\sigma_1}{\sigma_{1c}}\right]^2 + \left[\frac{\sigma_2}{\sigma_{2c}}\right]^2 = 1 \tag{4.69}$$

The damage evolution is simulated using Benzeggagh-Kenane (B-K) criterion [459] as shown in Eq. (4.70), which is one of the most widespread criterion used for capturing mixed-mode delamination propagation.

$$\mathcal{G}_c = \mathcal{G}_{1c} + (\mathcal{G}_{2c} - \mathcal{G}_{1c}) \left(\frac{\mathcal{G}_{2c}}{\mathcal{G}_{1c} + \mathcal{G}_{2c}}\right)^{\eta} \tag{4.70}$$

where $\mathcal{G}_c$ is the mixed-mode critical energy release rate for delamination, $\mathcal{G}_{1c}$ and $\mathcal{G}_{2c}$ are critical energy release rates in normal and shear modes, and η is a model parameter determined by calibrating the experimental inter-laminar fracture toughness tests. Furthermore, the penalty stiffness coefficients used in the traction-separation law for modelling normal and shear cohesive behaviour are set to large values, so that the global compliance matrix remains unaffected.

4.10 Numerical Experiments

In this section, extensive numerical experiments are performed to validate the proposed damage modelling framework. The numerical examples presented in Sec. 4.10.1-4.10.5 simulate anisotropic intra-laminar fracture based on the implicit method discussed in Sec. 4.2-4.7. However, the examples in Sec. 4.10.6-4.10.7 involve combined intra-laminar and inter-laminar fracture of full

composite laminates, and are based on the dynamic explicit method presented in Sec. 4.9.

4.10.1 Square plate with varying fibre orientation subjected to pure-tension

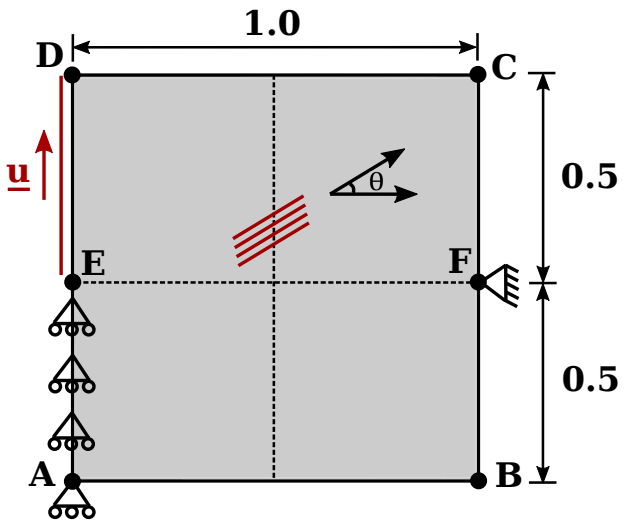

Figure 4.11: Anisotropic square plate under tensile loads: Geometry and boundary condition of square plate with an arbitrary fibre orientation θ [25]

Type	Property	Value	Unit
Elastic properties	E_{11}	171000	MPa
	E_{22}	9080	MPa
	G_{12}	5290	MPa
	ν_{12}	0.32	-
Fracture strength	σ_{c11}	2325	MPa
	σ_{c22}	62.3	MPa
	σ_{c12}	89.6	MPa
Critical energy release rate	$\mathcal{G}_{c11}$	97.8	N/mm
	$\mathcal{G}_{c22}$	0.277	N/mm
	$\mathcal{G}_{c12}$	0.788	N/mm
Cohesive softening parameters	(p_{11}, q_{11})	$(1,0)$	-
	(p_{22}, q_{22})	$(1,0)$	-
	(p_{12}, q_{12})	$(1,0)$	-

Table 4.1: Elastic and fracture properties of IM7/8552 unidirectional ply taken from [1]

A square plate under tensile loading is considered in this example. The geometry and boundary conditions are shown in Fig. 4.11. Node F is constrained

in all translational and rotational DOFs. Only the vertical displacements off all the nodes on the edge AE are constrained. A uniform vertical displacement is imposed along the edge ED. This set of boundary conditions results in stress-concentration at E, where the crack is expected to initiate. The material properties considered are shown in Table 4.1 and correspond to Hexcel IM7/8552 unidirectional ply [347].

To examine the effect of the fibre orientation on the crack path, a set of simulations is performed for varying fibre angles, i.e., $\theta = 0^o, 30^o, 45^o, 60^o$. To avoid the effect of mesh-bias, the mesh is uniformly refined in the entire plate with total 15750 elements and element size $h_e = 0.008$ mm. The length-scale parameter is $l_o = 0.025$ mm. As shown in Fig. 4.12, the crack initiates at E and consistently propagates along the fibre directions for all orientations. This is consistent with experimental observations that in unidirectional composites, matrix cracking often becomes the primary mode of failure resulting in crack propagation parallel to fibres [449]. This is due to the fact that the matrix-strength is considerably lower than the fibre-strength, and the fracture energy required to crack the fibres (characterized by σ_{c11} and $\mathcal{G}_{c11}$) is much higher than the fracture energy required to crack the matrix (characterized by σ_{c22} and $\mathcal{G}_{c22}$).

4.10.2 Compact-tension (CT) test for Textreme-80g/m^2 spread-tow fabric composite

Compact-tension tests are typically performed to characterize the fibre tensile fracture toughness. In this example, the tensile fracture strength of a widely used spread-tow woven-fabric reinforced composite material, i.e., Textreme® 80 g/m^2 is analysed, which is manufactured by Oxeon [460]. An extensive experimental campaign was conducted on Textreme® [3, 26, 461], and the results obtained from Compact-Tension tests have been previously reported in [2]. In this example, the experimentally derived fracture response is used to validate the proposed anisotropic cohesive phase field model.

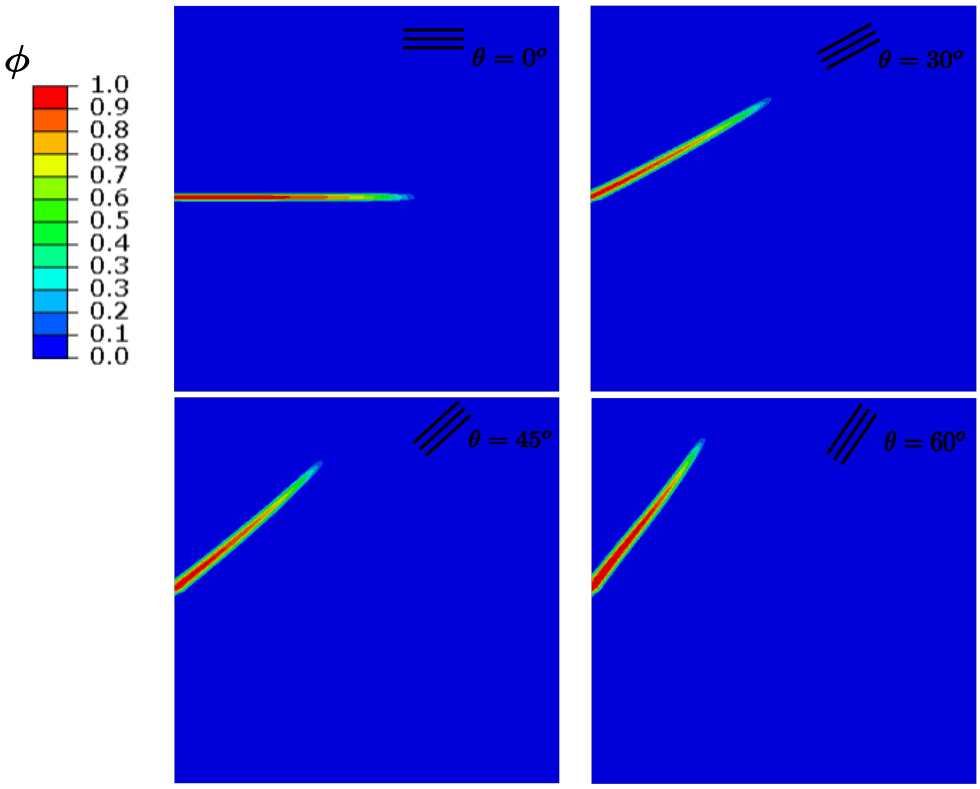

Figure 4.12: Anisotropic square plate under tensile loads: Crack propagation pattern with increasing time-increments for different fibre orientation angles $\theta = 0^o, 30^o, 45^o, 60^o$. The values of phase field variable ϕ where ϕ=0 and ϕ=1 represent intact and cracked states of the material

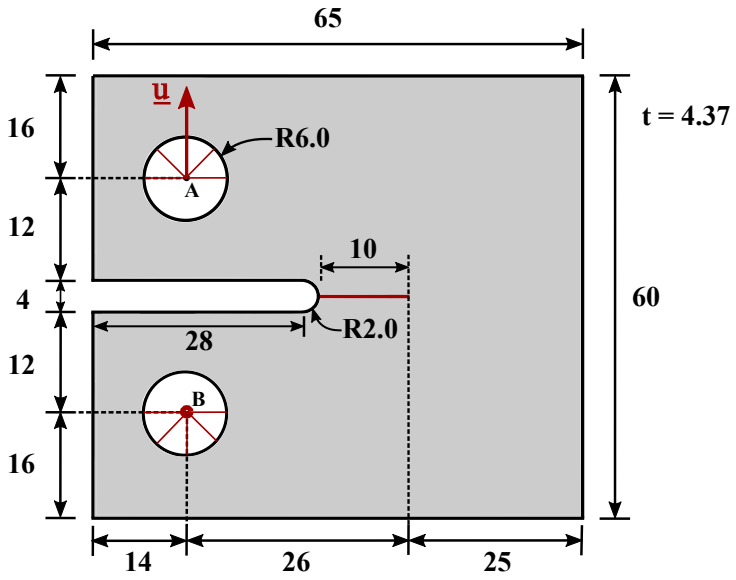

Figure 4.13: Compact Tension (CT) test: Geometry and boundary conditions for Textreme® 80 g/m^2 spread-tow fabric composite laminate [All dimensions in mm]

The experiments detailed in [2] were conducted on laminates each with a $[0^o/90^o]$ stacking sequence containing 56 plies. The average laminate thickness

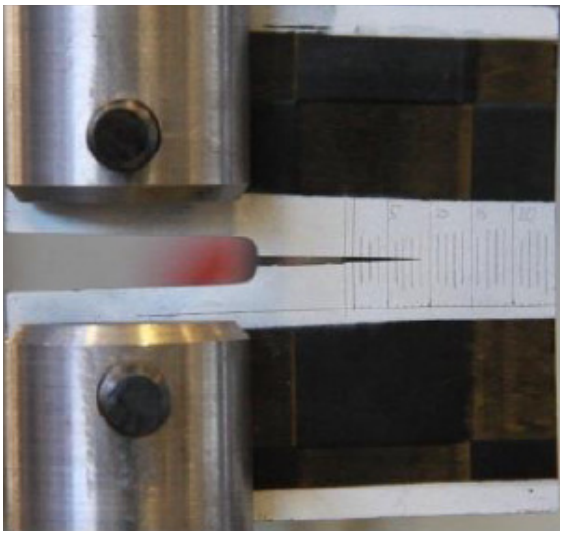

Figure 4.14: Compact Tension (CT) test: Experimental set-up and load application on Textreme® 80 g/m^2 spread-tow fabric composite laminate [3]

was 4.37 mm. A thin sharp crack with a radius of 250 μm and a length of 10 mm was machined using a diamond coated wire. The loading was applied using a hydraulic universal testing machine MTS-858 which is equipped with a 25 kN load cell, see Fig. 4.14. During the experiments, very little buckling was observed with the crack being confined in the desired crack path. In addition, no delamination was observed in the C-scan inspections which indicated the validity of these tests [3]. More details about the experimental procedure can be found in [2].

The geometry and boundary conditions employed in the simulation are shown in Fig. 4.13. The material properties are taken from [2] and shown in Table 4.2. Since the shear critical energy release rate $\mathcal{G}_{c12}$ has not been provided in [2], it is assumed herein to be 1.5 times the tensile $\mathcal{G}_{c11}$ and $\mathcal{G}_{c22}$ owing to negligible shear cracking observed in Textreme® 80 g/m^2.

Remark 11. It of interest to note that the in-plane shear behaviour of fabric-reinforced composites is predominantly governed by the matrix properties [5]. However, due to the very small ply thickness and the fabric structure within Textreme® 80 g/m^2 laminate, there was negligible matrix cracking under in-plane shear observed during the experiments [2]. A similar behaviour was also reported by Wagih et al. [462], where fiber-based failures were the primary

Type	Property	Value	Unit
Elastic properties	E_{11}	61400	MPa
	E_{22}	61400	MPa
	G_{12}	3782	MPa
	ν_{12}	0.042	-
Fracture strength	σ_{c11}	975.4	MPa
	σ_{c22}	975.4	MPa
	σ_{c12}	85.9	MPa
Critical energy release rate	$\mathcal{G}_{c11}$	65.4	N/mm
	$\mathcal{G}_{c22}$	65.4	N/mm
	$\mathcal{G}_{c12}$	98.1	N/mm
Shear plasticity parameters	S_{LP}	30	MPa
	ζ_E	34.5	MPa
	ζ_E^T	141.5	-
	ζ_L	335.1	MPa
Cohesive softening parameters	(p_{11}, q_{11})	$(5.5, 1.1)$	-
	(p_{22}, q_{22})	$(5.5, 1.1)$	-
	(p_{12}, q_{12})	$(5.5, 1.1)$	-

Table 4.2: Elastic and fracture properties of Textreme® 80 g/m^2 taken from [2]

modes of intra-laminar damage in Textreme® 80 g/m^2. Hence, the influence of the shear fracture properties is practically negligible on the overall fracture response.

Since there was no interlaminar damage observed in the experiments, the phase field simulations are performed using a single layer of fully-integrated S4 shell elements available within the Abaqus standard library. The mesh consists of total 20320 elements and is refined with $h_e = 0.1$ mm in the central region where the crack is expected to propagate. The length-scale parameter is taken as $l_o = 0.6$ mm. Based on the chosen values of h_e and l_o, the critical energy release rates provided in Table 4.2 are scaled to their effective values $\mathcal{G}_{c11} = \mathcal{G}_{c22} = 54.5$ N/mm and $\mathcal{G}_{c12} = 81.75$ N/mm based on Eq. (4.46). The evolution of the crack path with increasing load increments is shown in Fig. 4.15. The crack-path obtained from the cohesive phase field model is compared with the experimentally obtained crack and C-Scan inspections in Fig. 4.16; the two crack paths match.

The influence of the cohesive parameters p_i and q_i on the critical fracture load and the post-fracture softening response for a fixed length-scale l_o is il-

lustrated in Fig. 4.17. It is evident that by choosing appropriate values of p_i and q_i, a very accurate prediction of the experimental fracture response can be obtained, which also coincides with the prediction made by Soto et al. [2] using a Continuum Damage Mechanics (CDM) model, see Fig. 4.18.

Remark 12. The third set of cohesive parameters m_i cannot be controlled independently for each individual composite damage mechanisms $i \in \{11, 22, 12\}$ as it inherently depends on the anisotropic material and fracture properties. Although different combinations of $m_i \in \{m_{11}, m_{22}, m_{12}\}$ can be obtained by varying the length-scale parameter l_o, each of these combinations would lead to strong interference of the anisotropic stress-degradation mechanisms. To objectively assess the influence of l_o and m_i on the overall fracture response, an isotropic case with $m_i = m_{11} = m_{22} = m_{12} = 3\mathcal{G}_c E/2l_o\sigma_c^2$ is considered. The CT simulations are then performed with different values of m_i by modifying l_o, but fixing the values of $p_i = 1$ and $q_i = 0$.

The material and fracture properties for the isotropic case are taken as $E = 61400$ MPa, $\mathcal{G}_c = \mathcal{G}_{c11} = \mathcal{G}_{c22} = \mathcal{G}_{c12} = 54.5$ N/mm, and $\sigma_c = \sigma_{c11} = \sigma_{c22} = \sigma_{c12} = 975.4$ MPa. All other input parameters are kept unchanged. The resulting crack-paths for different values of $[l_o, m_i]$ are shown in Fig. 4.20. The width of phase field diffusion zone increases with increasing l_o as expected. Furthermore, the influence of $[l_o, m_i]$ on the overall load-displacement response is illustrated in Fig. 4.19. It can be observed that the variations in either the length-scale l_o or m_i do not affect the resulting critical fracture loads and final crack separation, i.e., the initial and final stages of the softening curve; rather they only control its intermediate shape.

In the current analysis, $p_i = 5.5$, $q_i = 1.1$ and $l_o = 0.6$ mm have been found to provide a reasonably good approximation of the fracture response for Textreme® 80 g/m^2 composite. In the next example, these calibrated values of $\{p_i, q_i\}$ and l_o will be used to validate the experimental fracture response of Textreme® using a double-edge notched tension (DENT) test.

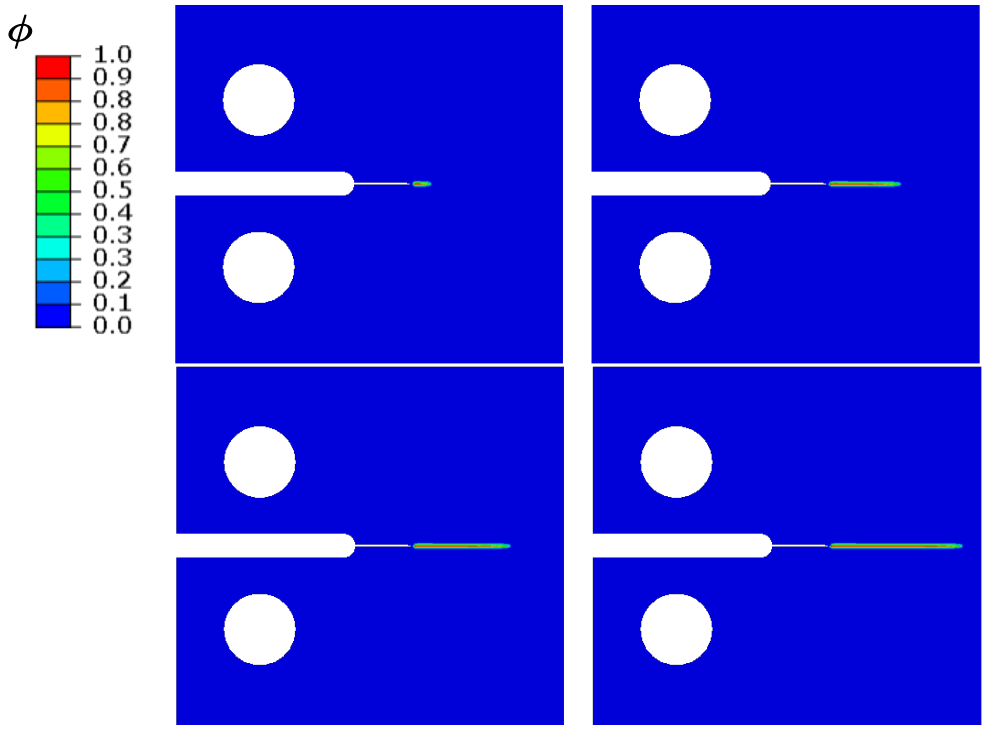

Figure 4.15: Compact-tension (CT) test on Textreme® 80 g/m^2 : Crack propagation pattern for increasing time-increments with cohesive phase field parameters $p_i = 5.5$, $q_i = 1.1$, $l_o = 0.6$ mm. The values of phase field variable ϕ=0 and ϕ=1 represent intact and cracked states of the material

4.10.3 Double-edge notched tension (DENT) test for Textreme-80g/m^2 spread-tow fabric composite

To assess the accuracy and predictive capabilities of the proposed phase field model, a double-edge notched tension (DENT) experiment is simulated on a Textreme® 80 g/m^2 specimen using the calibrated material parameters of the previous example. The simulation results are compared against the experimental data [3].

DENT tests are typically performed on laminates to measure the crack resistance curve (R-curve) associated with their tensile fracture toughness. However for a cross-ply laminate like Textreme®, DENT tests yield tensile fracture toughness corresponding to the fibers. The schematic of the DENT experiment is illustrated in Fig. 4.21. The experiments were performed on a total 5 samples with different widths (W) and initial notch lengths (a_0), however the ratio $2a_0/W$ was kept constant at a value (≈ 0.6) for all samples [3]. The actual

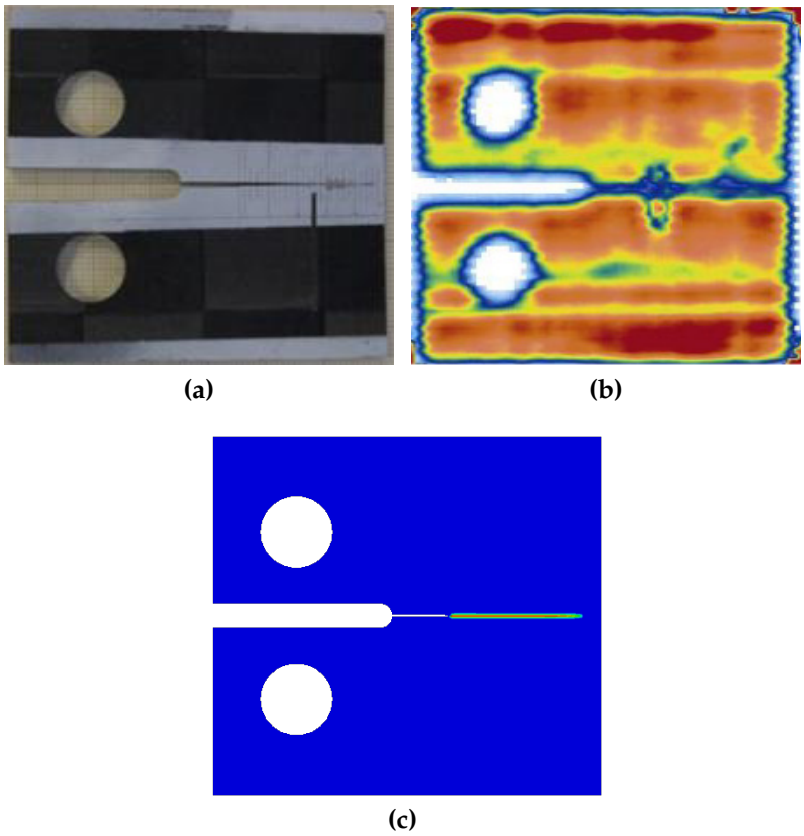

Figure 4.16: Compact-tension (CT) test on Textreme® 80 g/m^2 : Comparison of crack-paths obtained from (a) Experiments [3, 26] (b) C-Scan inspection [26] (c) Cohesive phase field model

sizes of W and a_0 used in the experiments are shown in Table 4.3, and the length of all samples is taken constant as $L = 250$ mm. The laminate stacking sequence is $[0^o/90^o]$ for all specimens with the total effective thicknesses as shown in Table 4.3. Similar to the CT specimens, a diamond coated wire was used to machine thin initial cracks on both left and right edges. The tests were performed with a hydraulic universal tester MTS-810 equipped with a 250 kN load cell, and no tabs were used [3].

For the phase field simulations, the material properties shown in Table 4.2 are used with the previously calibrated values of $\{p_i, q_i\}$ and l_o from Compact-Tension test. The mesh is refined in the central region with $h_e = 0.1$ mm. The total number of elements are 7044, 9422, 11815 and 14151 for specimens S-1, S-2, S-3 and S-4 respectively. The crack path and the representative load-displacement responses for the DENT specimens with varying widths and ini-

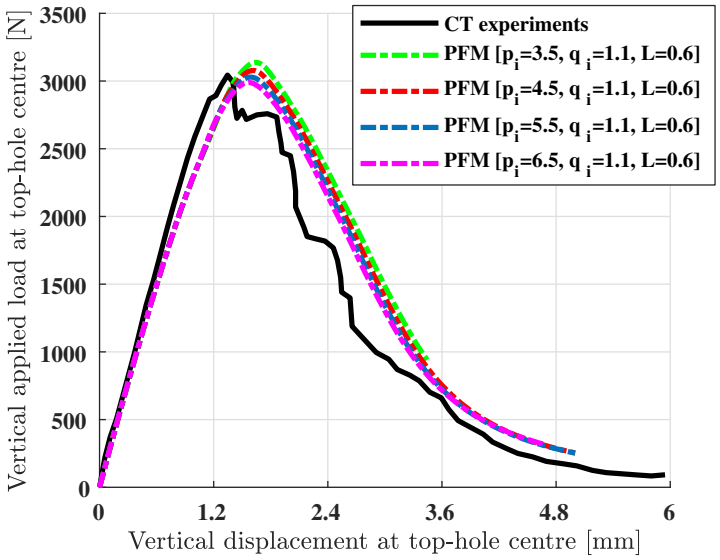

(a)

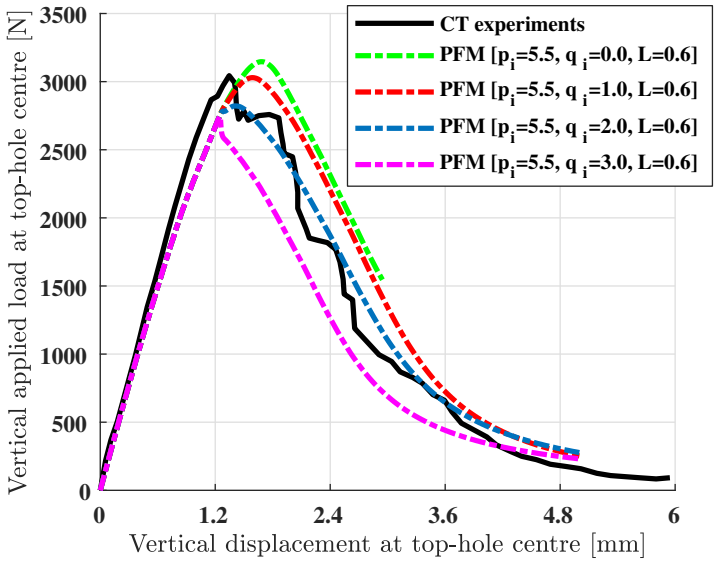

(b)

Figure 4.17: Compact-tension (CT) test on Textreme® 80 g/m^2 : Effect of parameters (a) p_i, and (b) q_i on the overall load-displacement response, with fixed $l_o = 0.6$ mm

tial crack-lengths are shown in Fig. 4.22 and Fig. 4.23, respectively. The predicted fracture strength are compared against the experimentally measured maximum loads in Table 4.3. It is evident from Table 4.3 that the proposed phase field model makes a very accurate prediction of the laminate fracture strength. It is worth noting that the values of $\{p_i, q_i, l_o\}$ can likewise be obtained for any other composite material, and are capable of accurately describing their quasi-brittle intralaminar fracture behaviour under different load-

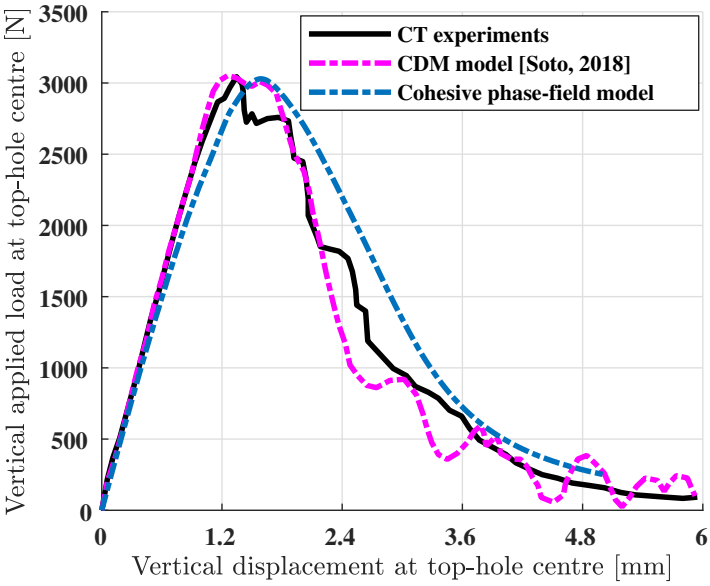

Figure 4.18: Compact-tension (CT) test on Textreme® 80 g/m^2 : Load-displacement response obtained from the cohesive phase field model with parameters $[p_i = 5.5, q_i = 1.1, l_o = 0.6]$. Also shown is its comparison with CT experimental response and the prediction made using continuum damage mechanics (CDM) model in [2]

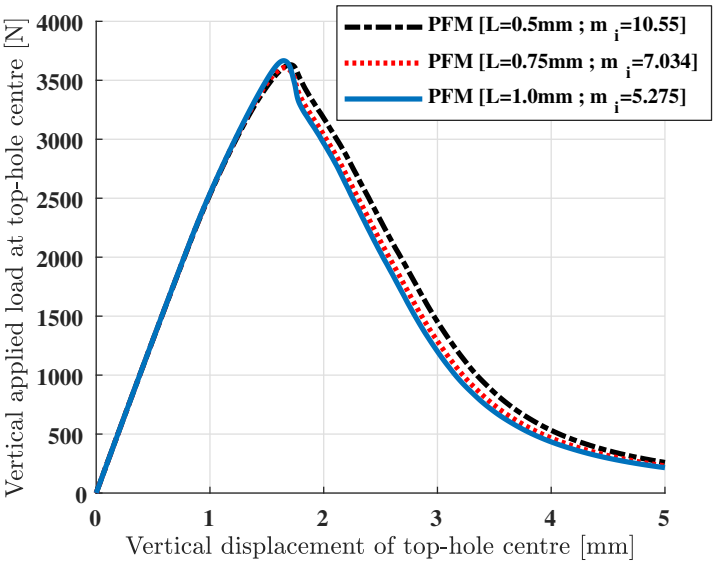

Figure 4.19: Compact-tension (CT) test on Textreme® 80 g/m^2 : Effect of parameters $[l_o, m_i]$ on the overall load-displacement response with (a) $l_o = 0.5$mm ; $m_i = 10.55$ (black) (b) $l_o = 0.75$mm ; $m_i = 7.034$ (red) (c) $l_o = 1.0$mm ; $m_i = 5.275$ (blue). The comparison is made assuming an ideal isotropic case with $m_i = m_{11} = m_{22} = m_{12}$ and $[p_i = 1; q_i = 0]$

ing scenarios. Fig. 4.24 illustrates the size-effect law typically observed in woven-fabric reinforced composites. This occurs due to the presence of fracture process zone during quasi-brittle fractures, and the nominal and effective strengths of the laminate keep reducing with increasing specimen widths [463].

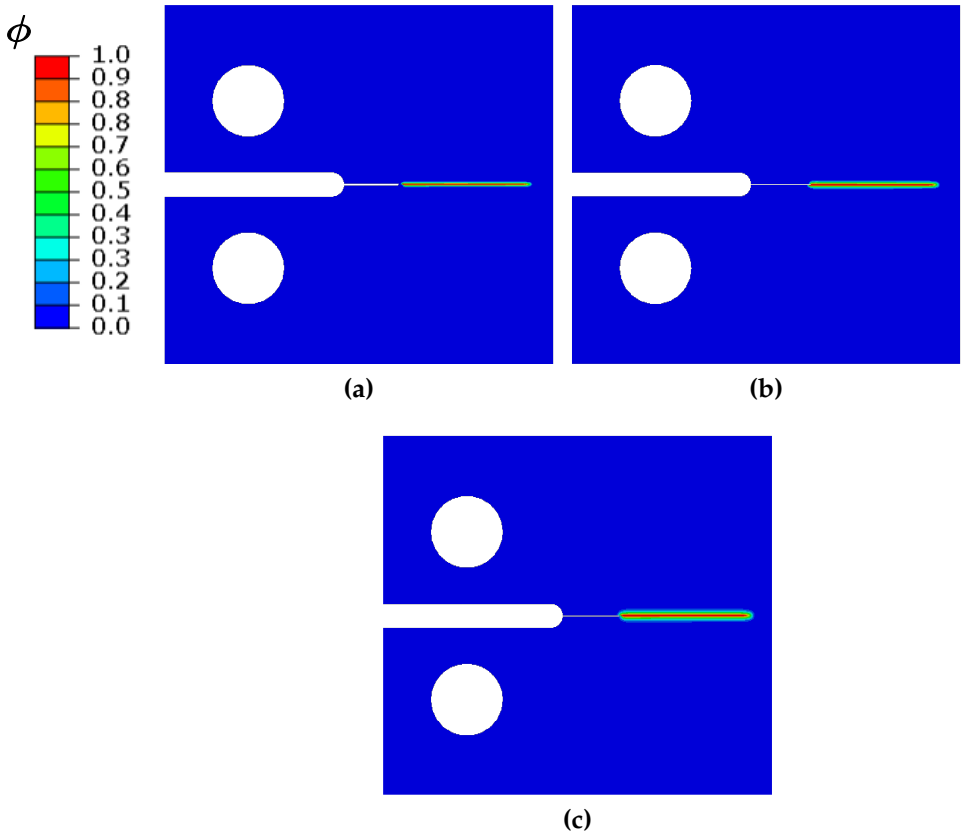

Figure 4.20: Compact-tension (CT) test on Textreme® 80 g/m^2 : Influence of length-scale parameter $[l_o, m_i]$ on the phase field diffusion width for (a) $l_o = 0.5$mm ; $m_i = 10.55$ (b) $l_o = 0.75$mm ; $m_i = 7.034$ (c) $l_o = 1.0$mm ; $m_i = 5.275$. The values of phase field variable ϕ=0 and ϕ=1 represent intact and cracked states of the material. Also, the comparison is made assuming an ideal isotropic case with $m_i = m_{11} = m_{22} = m_{12}$ and $[p_i = 1; q_i = 0]$

4.10.4 Open-hole tension test on glass woven-fabric reinforced composite laminate

An open-hole specimen with the geometry and boundary conditions shown in Fig. 4.25 is considered. The example models a plain woven glass-reinforced fabric $[0^o/90^o]$ embedded in an epoxy matrix with a fibre volume of 62%, which was experimentally tested by Kim et al. [4] for a set of open-hole specimens. Martín-Santos et al. [5] compared the nominal strength predictions for this fabric composite with respect to experimental results using linear and bi-linear Continuum Damage Mechanics (CDM) models, whereas Ahmad [464] used an XFEM model to analyze the nominal strength. It was observed in [5] that the fabric exhibits a quasi-brittle fracture response with a large decrease

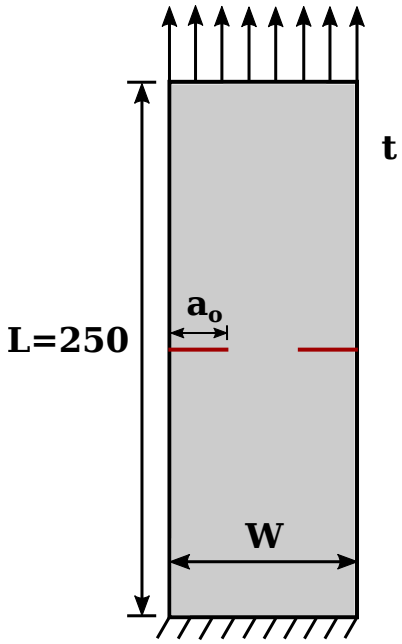

Figure 4.21: Double-edge notched tension (DENT) test: Geometry and boundary conditions for Textreme® 80 g/m^2 spread-tow fabric composite laminate [All dimensions in mm]

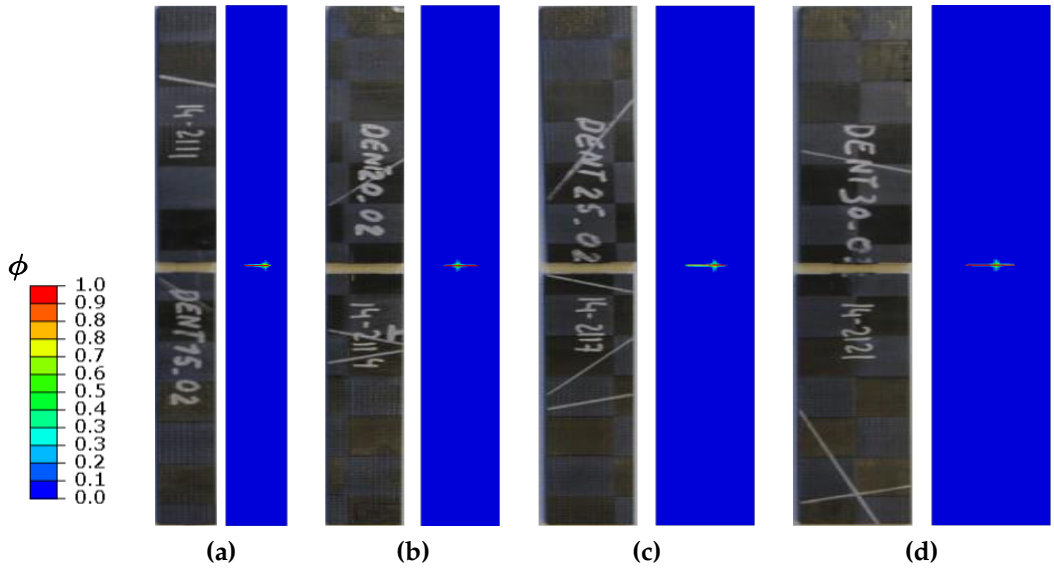

Figure 4.22: Double edge notched tension (DENT) test on Textreme® 80 g/m^2 : Crack paths obtained from experiments [3] and the cohesive phase field model with parameters $p_i = 5.5$,$q_i = 1.1$,$l_o = 0.6$ mm for specimens with (a) Specimen S-1 [$W = 15$mm ; $2a_0 = 9.1$mm] (b) Specimen S-2 [$W = 20.1$mm ; $2a_0 = 12.2$mm] (c) Specimen S-3 [$W = 24.9$mm ; $2a_0 = 15.1$mm] (d) Specimen S-4 [$W = 30.1$mm ; $2a_0 = 18.2$mm]. The values of phase field variable ϕ=0 and ϕ=1 represent intact and cracked states of the material

in stresses but minimal crack-opening post-initiation, followed by a zone defined by a smaller decrease in stresses but large crack opening displacements.

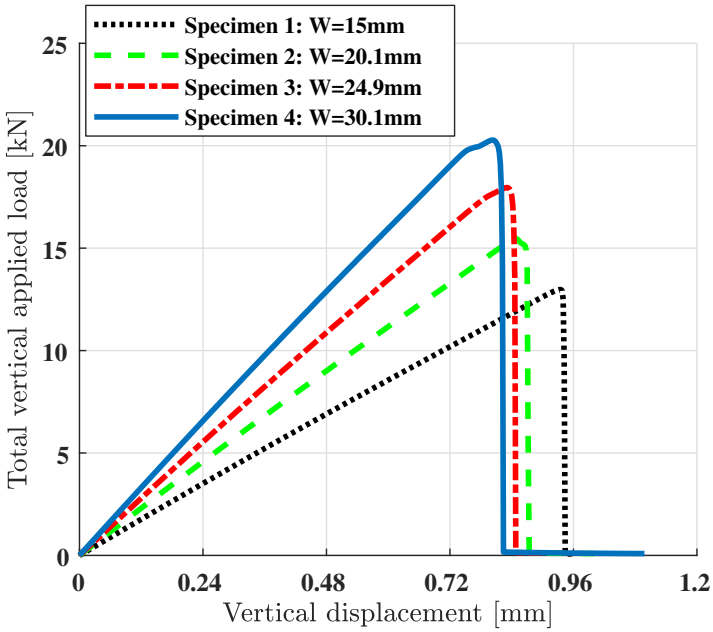

Figure 4.23: Double edge notched tension (DENT) test on Textreme® 80 g/m^2 : Load-displacement responses for varying specimen widths obtained from the cohesive phase field model with parameters $[p_i = 5.5, q_i = 1.1, l_o = 0.6]$

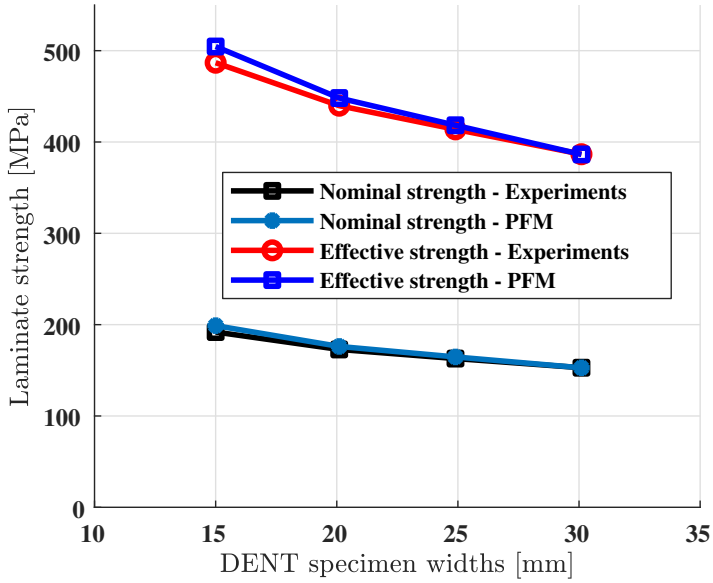

Figure 4.24: Double edge notched tension (DENT) test on Textreme® 80 g/m^2 : Strength vs specimen widths obtained from experiments [3] and the cohesive phase field model illustrating the size-effect law in fabric-reinforced composites. Nominal and effective strengths have been calculated based on the total and effective laminate widths respectively

Hence, a bilinear CDM model was found to be most suitable for capturing the quasi-brittle behaviour and predicting the nominal strength of the fabric accurately. In the current work, the open-hole tension test is performed on

Specimen number	**S-1**	**S-2**	**S-3**	**S-4**
Mean nominal width W [mm]	15	20.1	24.9	30.1
Mean crack-length $2a_0$ [mm]	9.1	12.2	15.1	18.2
Mean effective width [mm]	5.9	7.9	9.8	11.9
Laminate thickness t [mm]	4.36	4.37	4.38	4.41
Critical load (Experiments [3]) [N]	12522.9	15181.7	17763	20288.5
Critical load (Cohesive PFM) [N]	12979	15471.3	17955.7	20277.2
Laminate strength (Experiments) [MPa]	191.92	172.84	162.87	152.84
Laminate strength (Cohesive PFM) [MPa]	198.91	176.14	164.64	152.76
Absolute prediction error [%]	3.6	1.9	1.08	0.05

Table 4.3: Double-edge notched tension (DENT) test on Textreme® 80 g/m^2: Summary of specimen sizes used for the experiments [3], and comparison between critical fracture loads and strengths obtained from the experiments and the proposed cohesive phase field model (PFM) with parameters $p_i = 5.5, q_i = 1.1$ and length-scale $l_o = 0.6$ mm

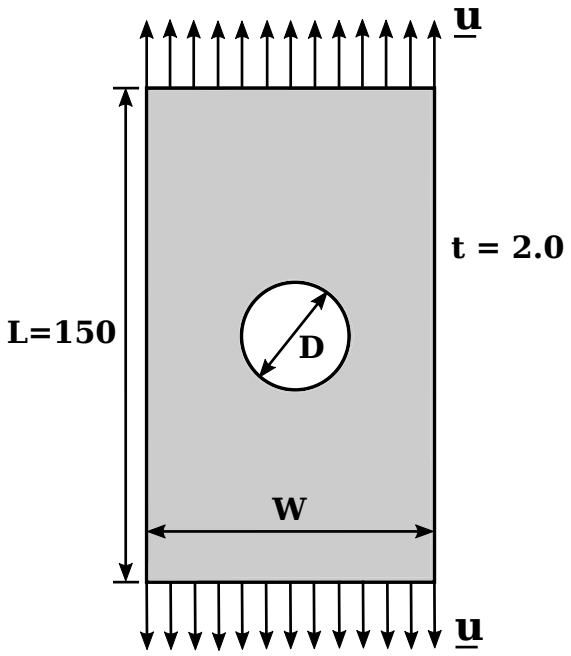

Figure 4.25: Open-hole tension (OHT) test: Geometry and boundary conditions for a plain woven glass-reinforced fabric composite [4, 5] [All dimensions in mm]

specimens of varying width W and hole-diameter D using the proposed cohesive phase field model and compare the nominal strength predictions with results from experiments in [4] and bilinear CDM model in [5].

The material properties are taken from [4, 5] and are also shown in Table 4.4 for reference. The ply lay-up is $[0^o/90^o]$, and the mesh is refined in

Type	Property	Value	Unit
Elastic properties	E_{11}	23600	MPa
	E_{22}	23600	MPa
	G_{12}	4000	MPa
	ν_{12}	0.11	-
Fracture strength	σ_{c11}	351.4	MPa
	σ_{c22}	351.4	MPa
	σ_{c12}	351.4	MPa
Critical energy release rate	$\mathcal{G}_{c11}$	57.5	N/mm
	$\mathcal{G}_{c22}$	57.5	N/mm
	$\mathcal{G}_{c12}$	86.25	N/mm
Shear plasticity parameters	S_{LP}	121	MPa
	ζ_E	5	MPa
	ζ_E^T	500	-
	ζ_L	10	MPa
Cohesive softening parameters	(p_{11}, q_{11})	$(1, 0)$	-
	(p_{22}, q_{22})	$(1, 0)$	-
	(p_{12}, q_{12})	$(1, 0)$	-

Table 4.4: Elastic and fracture properties of glass woven glass-reinforced fabric embedded in an epoxy matrix obtained from [4, 5] for Open-Hole Tension (OHT) test

the central zone with $h_e = 0.2$ mm. The length-scale parameter is chosen as $l_o = 1.2$ mm. The mesh for specimens S-1, S-2, S-3 and S-4 comprise 3480, 2621, 6780 and 4527 fully-integrated S4 shell elements respectively. Based on these values, the critical energy release rates in [4] can be scaled to their effective values $\mathcal{G}_{c11} = \mathcal{G}_{c22} = 47.92$ N/mm and $\mathcal{G}_{c12} = 71.875$ N/mm as described in Eq. (4.46). The specimen with $W = 20$mm and $D = 8$mm is used to calibrate the softening parameters $\{p_i, q_i\}$ required by the cohesive phase field model as shown in Fig. 4.26 and Table 4.5. These are then used to predict and validate the experimentally obtained nominal strengths for remaining specimens.

It can be deduced from Fig. 4.26 and Table 4.5 that the parameters $p_i = 1$ and $q_i = 0$ provide the most accurate match with the experimental laminate fracture strength. The crack-paths for all tested samples are shown in Fig. 4.27, wherein two crack-branches initiate simultaneously at diametrically opposite ends of the hole and propagate horizontally towards the side-edges. This is consistent with experimental results in the literature [45, 368]. The load-displacement response for specimens with different combinations of widths W and hole diameters D is shown in Fig. 4.28.

The nominal strengths predicted by the cohesive phase field model are compared with the experimental data [4] and CDM bilinear model [5] in Table 4.6. The calibrated cohesive phase field model provides a very good prediction of the nominal strengths for all specimens with percentage errors lying within $3-4\%$, which highlights the robust predictive capability of the proposed model.

4.10.4.1 Mesh convergence study

To investigate the sensitivity of the resulting critical fracture loads and the corresponding crack patterns on the mesh-size h_e and the length-scale parameter l_o, a mesh-convergence study is performed on the specimen with dimensions $W = 20$mm and $D = 4$mm. Three different mesh-sizes are considered, i.e., $h_e = 0.1$mm, $h_e = 0.15$mm and $h_e = 0.2$mm. The length-scales are chosen as $l_o = 0.6$mm, $l_o = 0.9$mm and $l_o = 1.2$mm respectively, thus retaining a constant ratio $h_e/l_o = 1/6$ to ensure that the effective critical energy release rates $\mathcal{G}_{ci}$ in Eq. (4.46) are scaled by the same amount.

The resulting load-displacement plots are shown in Fig. 4.30 and demonstrate that the critical fracture force and the overall load-displacement response remain identical in all cases. The corresponding crack-paths are shown in Fig. 4.29. As the length scale increases, the diffusion width of the crack increases although without affecting the load bearing capacity of the simulated specimen. This reaffirms that the critical stresses predicted by the proposed model remains independent of the length-scale parameter l_o.

4.10.5 Open-hole tension test on unidirectional (UD) flax-ply composite laminate

The case of a unidirectional (UD) composite material is examined herein. An open-hole tension test on a quasi-UD flax fiber/epoxy matrix composite FlaxPly-UD180 is considered. The geometry and loading conditions are shown in Fig. 4.31. The areal density of the composite is $180 g/m^2$ [465]. The mate-

p_i	q_i	l_o	**Laminate strength (Experiments) [MPa]**	**Predicted numerical strength [MPa]**	**Absolute prediction error [%]**
1	0	1.2	138	139.67	1.21%
2	0	1.2	138	131.9	4.42%
3	0	1.2	138	126	8.7%

Table 4.5: Open-hole tension (OHT) test on woven glass-reinforced fabric composite: Laminate strengths predicted using different combinations of cohesive phase field parameters for specimen with width $W = 20$mm and hole-diameter $D = 8$mm, and their comparison with experimental laminate strength [4, 5].The most accurate numerical response is obtained using parameters $[p_i = 1, q_i = 0, l_o = 1.2mm]$

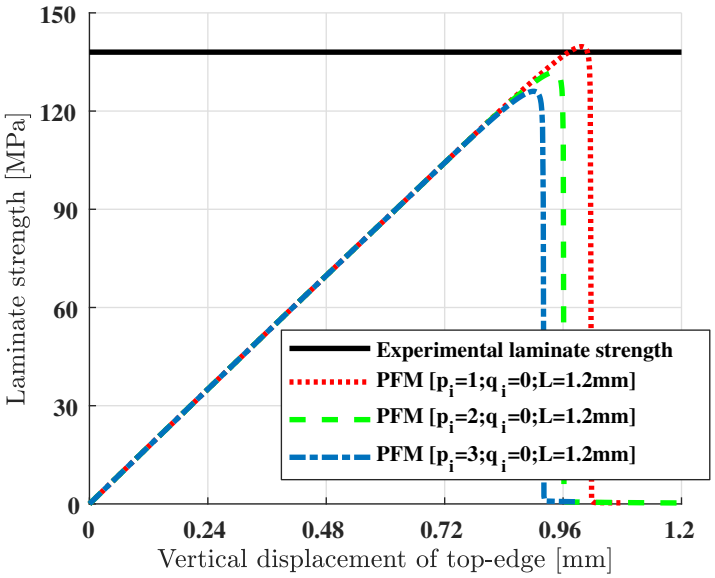

Figure 4.26: Open-hole tension (OHT) test on woven glass-reinforced fabric composite: Calibration of cohesive phase field parameters with respect to the experimental laminate strength in [4, 5] for specimen with width $W = 20$mm and hole-diameter $D = 8$mm. The most accurate numerical response is obtained using parameters $[p_i = 1, q_i = 0]$. The length scale is $l_o = 1.2$ mm in all cases.

rial properties are taken from [6, 7] and are provided in Table 4.7 for reference. A refined mesh is employed with $h_e = 0.2$mm, and the length-scale parameter is assumed $l_o = 1.2$ mm.

The critical energy release rates ($\mathcal{G}_{c22}$ and $\mathcal{G}_{c12}$) for transverse tensile and shear matrix cracking are provided in [6, 7], however $\mathcal{G}_{c11}$ responsible for tensile fibre-failure is not provided. Hence, $\mathcal{G}_{c11}$ is assumed to be 50 times the magnitude of $\mathcal{G}_{c22}$ to prevent fibre-failure in accordance with the assumption in [28]. Similarly, the transverse shear σ_{c12} and longitudinal tensile strengths

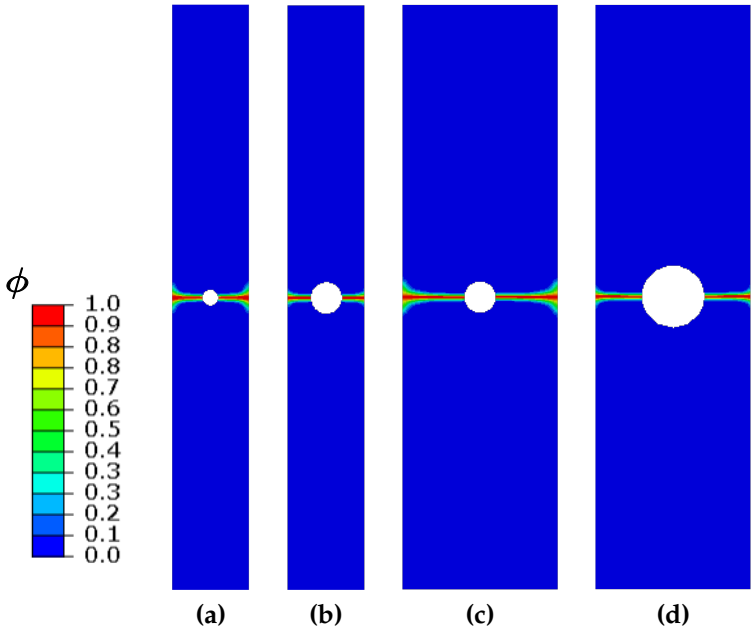

Figure 4.27: Open-hole tension (OHT) test on woven glass-reinforced fabric composite: Crack paths obtained from the cohesive phase field model with parameters $p_i = 1.0$,$q_i = 0.0$,$l_o = 1.2$ mm for specimens with (a) Specimen S-1 [$W = 20$mm, $D = 4$mm] (b) Specimen S-2 [$W = 20$mm, $D = 8$mm] (c) Specimen S-3 [$W = 40$mm, $D = 8$mm] and (d) Specimen S-4 [$W = 40$mm, $D = 16$mm]. The values of phase field variable ϕ=0 and ϕ=1 represent intact and cracked states of the material

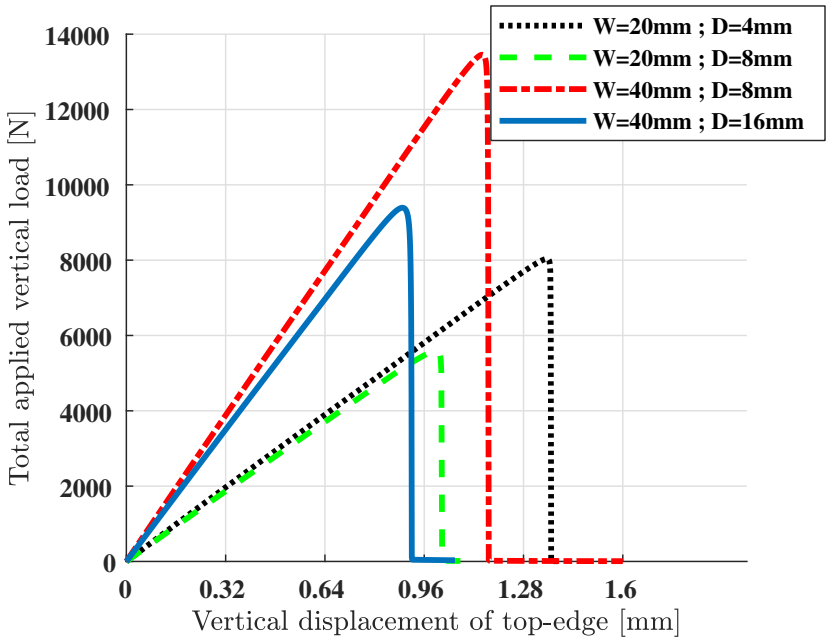

Figure 4.28: Open-hole tension (OHT) test on woven glass-reinforced fabric composite: Load-displacement responses for varying specimen widths W and hole-diameters D obtained from the cohesive phase field model with parameters $[p_i = 1.0, q_i = 0.0, l_o = 1.2]$

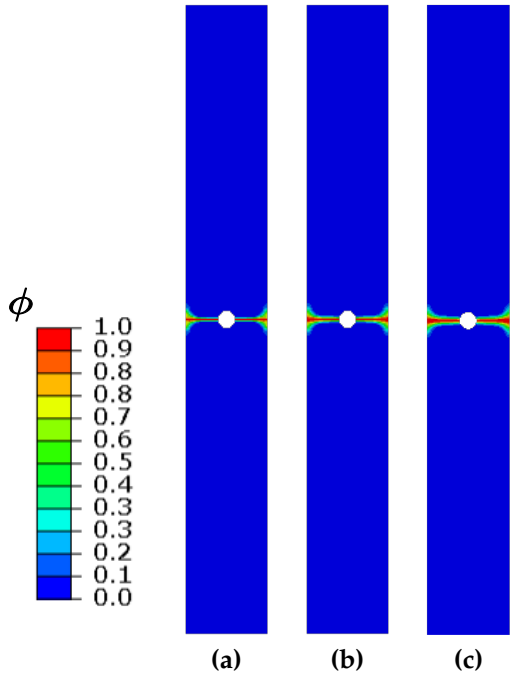

Figure 4.29: Open-hole tension (OHT) test on woven glass-reinforced fabric composite: Crack paths obtained for the mesh-convergence study on specimen with $W = 20$mm and $D = 4$mm. The mesh-sizes and corresponding length-scale parameter considered are: (a) $h_e = 0.1$mm; $l_o = 0.6$mm, (b) $h_e = 0.15$mm; $l_o = 0.9$mm, (c) $h_e = 0.2$mm; $l_o = 1.2$mm. The values of phase field variable ϕ=0 and ϕ=1 represent intact and cracked states of the material

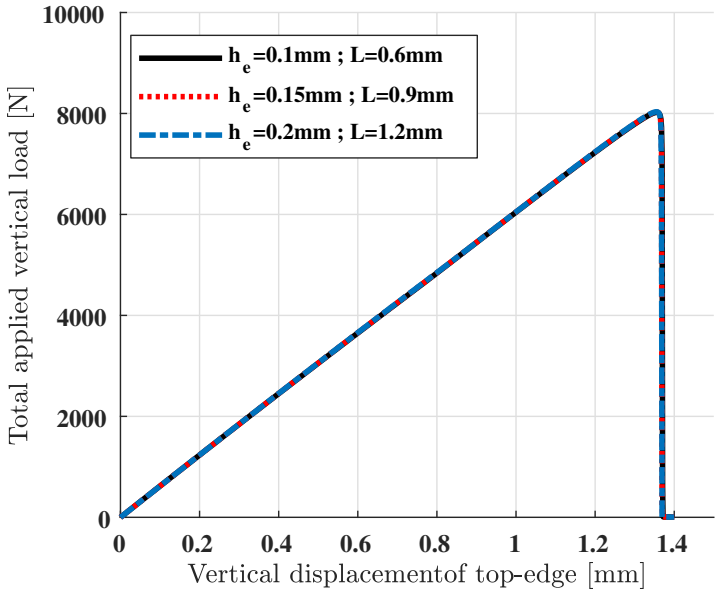

Figure 4.30: Open-hole tension (OHT) test on woven glass-reinforced fabric composite: Comparison of force-displacement plots obtained from the mesh-convergence study on specimen with $W = 20$mm and $D = 4$mm. The mesh-sizes and corresponding length-scale parameter considered are: (a) $h_e = 0.1$mm; $l_o = 0.6$mm, (b) $h_e = 0.15$mm; $l_o = 0.9$mm, (c) $h_e = 0.2$mm; $l_o = 1.2$mm.

Specimen number	**S-1**	**S-2**	**S-3**	**S-4**
Mean width W [mm]	20	20	40	40
Hole diameter D [mm]	4	8	8	16
Laminate thickness [mm]	2	2	2	2
Laminate strength (Experiments [4]) [MPa]	192.9	138	167.5	121.6
Laminate strength (CDM [5]) [MPa]	193.65	136.85	169.94	123.78
Critical load (Cohesive PFM) [N]	8034	5587	13450	9391
Laminate strength (Cohesive PFM) [MPa]	200.85	139.675	168.125	117.3875
Absolute prediction error [%]	4.12	1.21	0.37	3.46

Table 4.6: Open-hole tension (OHT) test on woven glass-reinforced fabric composite: Summary of experimental specimen sizes as obtained from [4, 5], and comparison between critical fracture strengths obtained from the experiments and the proposed cohesive phase field model (PFM) with parameters $p_i = 1.0, q_i = 0$ and length-scale $l_o = 1.2$ mm

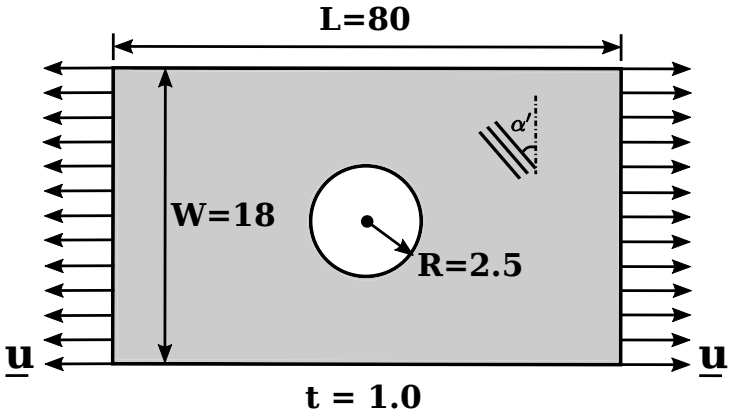

Figure 4.31: Open-hole tension (OHT) test on unidirectional composite laminate: Geometry and boundary conditions for quasi-UD flax fiber/epoxy matrix composite FlaxPly-UD180 with varying fibre-orientation angle α' [6, 7] [All dimensions in mm]

σ_{c11} are assumed based on the transverse tensile strength $\sigma_{c22} = 20.25$MPa provided in [7] using the expressions below:

$$\sigma_{c11} = \sqrt{\sigma_{c22}^2 \frac{\mathcal{G}_{c11}}{\mathcal{G}_{c22}}} = 143.19\text{MPa} \tag{4.71}$$

$$\sigma_{c12} = \sqrt{\sigma_{c22}^2 \frac{\mathcal{G}_{c12}}{\mathcal{G}_{c22}}} = 17.64\text{MPa} \tag{4.72}$$

Considering $h_e = 0.2$mm and $l_o = 1.2$mm, the critical energy release rates are scaled to their effective values based on Eq. (4.46) as $\mathcal{G}_{c11} = 25.9167$N/mm,

Type	Property	Value	Unit
Elastic properties	E_{11}	26500	MPa
	E_{22}	2600	MPa
	G_{12}	1300	MPa
	ν_{12}	0.35	-
Fracture strength	σ_{c11}	143.19 (assumed)	MPa
	σ_{c22}	20.25	MPa
	σ_{c12}	17.64 (assumed)	MPa
Critical energy release rate	$\mathcal{G}_{c11}$	31.1 (assumed)	N/mm
	$\mathcal{G}_{c22}$	0.622	N/mm
	$\mathcal{G}_{c12}$	0.472	N/mm
Cohesive softening parameters	(p_{11}, q_{11})	$(1.0, 0.0)$	-
	(p_{22}, q_{22})	$(1.0, 0.0)$	-
	(p_{12}, q_{12})	$(1.0, 0.0)$	-

Table 4.7: Elastic and fracture properties for Open-Hole Tension (OHT) test on quasi-unidirectional (UD) flax fiber/epoxy matrix composite FlaxPly-UD180 obtained from [6, 7]

$\mathcal{G}_{c22} = 0.5183$N/mm and $\mathcal{G}_{c12} = 0.393$N/mm. Since unidirectional composites do not typically display plasticity in their shear behaviour, the shear plasticity parameters are omitted in this case.

A series of analyses is performed considering different fibre-orientation angles, i.e., $\alpha' = \{0^o, 30^o, 45^o, 60^o\}$. The corresponding crack-paths are shown in Fig. 4.32. The crack deflection angles match closely with the experimental observations [6, 7] with the crack aligning consistently along the fibre-directions as is usually observed in UD composites that have large difference in their fracture properties of fibre and matrix, see e.g. [347, 449].

The force-displacement plots for each case are shown in Fig. 4.33. The effective laminate strengths [Fig. 4.34] are compared to the experimental results provided in [6], and simulation results derived from a finite-fracture mechanics (FFM) approach [7] and brittle phase field models [27, 28]. Although the proposed model slightly under-predicts the effective laminate strengths for the 0^o case by 10%, the predictions for higher orientation angles 45^o and 60^o closely match the experimental results. The difference in the 0^o is attributed to the purely brittle failure mode that this UD composite demonstrated, which cannot be accurately captured by the proposed cohesive implementation.

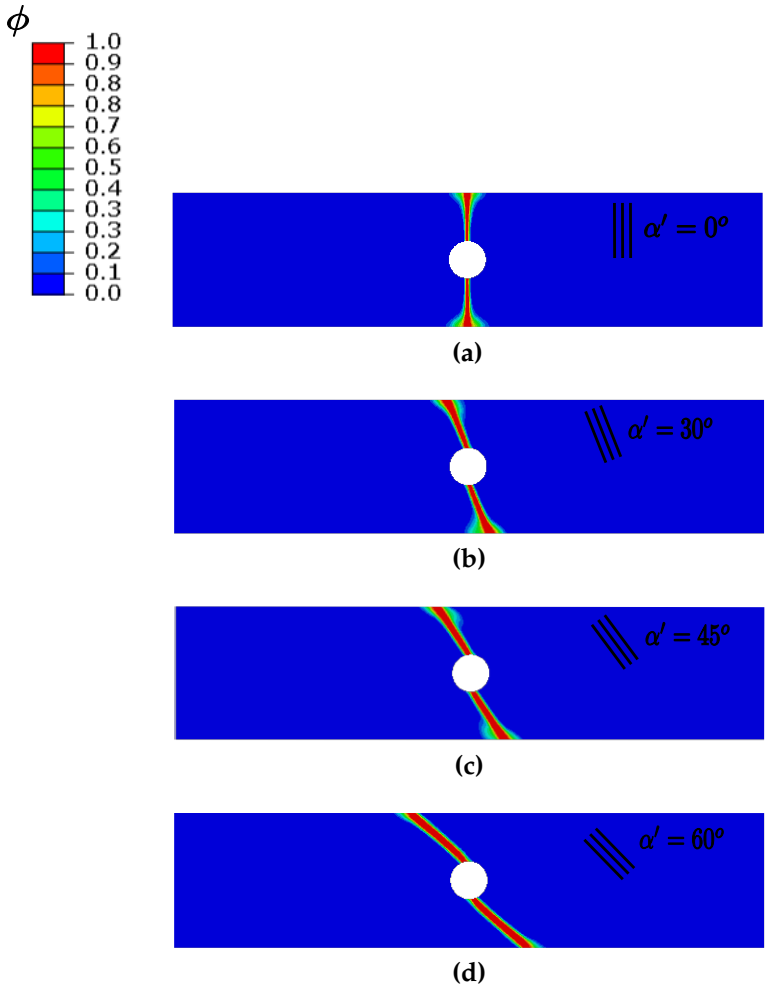

Figure 4.32: Open-hole tension (OHT) test on unidirectional composite laminate: Crack paths for varying fibre-orientation angles $\alpha' = \{0^o, 30^o, 45^o, 60^o\}$. The values of phase field variable ϕ=0 and ϕ=1 represent intact and cracked states of the material

4.10.6 Quasi-static indentation (QSI) test on full Textreme® 80 g/m^2 composite laminate

In this section, quasi-static indentation is performed on a full composite laminate using the dynamic explicit model presented in Sec. 4.9. The geometry and boundary conditions, and the impactor dimensions are illustrated in Fig. 4.35 and Fig. 4.36a respectively. The laminate comprises 4 plies of spread-tow woven fabric-reinforced Textreme® 80 g/m^2 composite with 0.08 mm thickness each. The material properties for Textreme are obtained from Table 4.2, and all pairs of adjacent plies are bonded with HexFlow® RTM 6 mono-component epoxy matrix supplied by Hexcel. Both intra-laminar and inter-laminar frac-

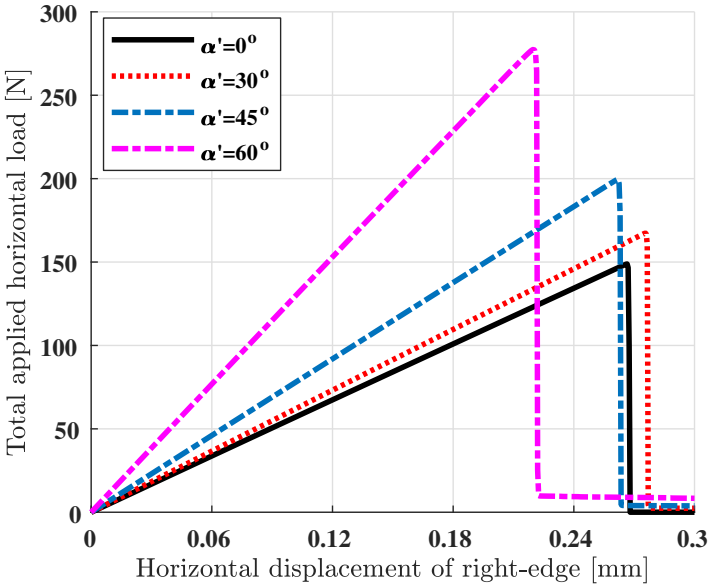

Figure 4.33: Open-hole tension (OHT) test on unidirectional composite laminate: Load-displacement responses for varying fibre-orientation angles $\alpha' = \{0^o, 30^o, 45^o, 60^o\}$

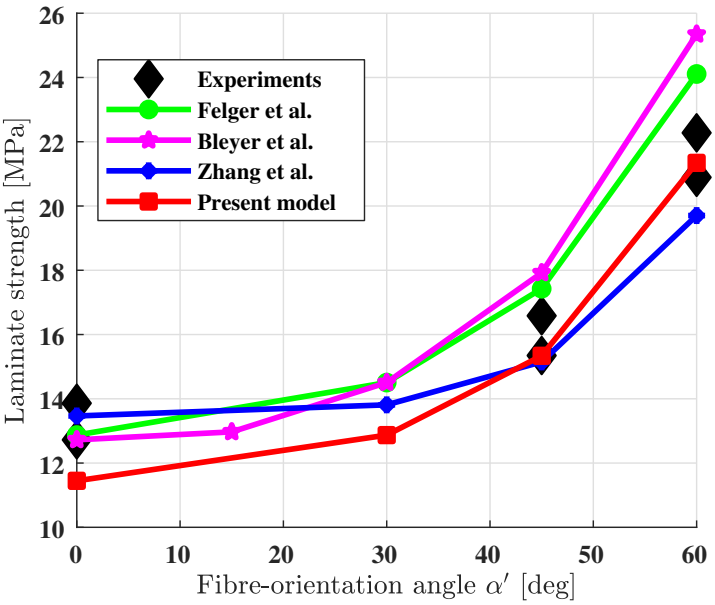

Figure 4.34: Open-hole tension (OHT) test on unidirectional composite laminate: Comparison of laminate strengths for different fibre orientations obtained from a) Experiments b) Finite Fracture Mechanics model in [7] c) LTD phase field model in [27] d) Anisotropic brittle phase field model in [28], and e) Present anisotropic cohesive phase field model

ture are modelled in this example using the dynamic explicit phase field and cohesive zone surface interaction models respectively, as discussed in Sec. 4.9. The experimental material and fracture properties for the ply-interface are obtained from [2] and provided in Table 4.8 for reference. The material densi-

ties of shell element layer at ply-midsurface, surface element layer at ply top and bottom surfaces, and the impactor is taken as $1.5e^{-9}$, $7.5e^{-6}$ and $9.9e^{-10}$ tonne/mm^3 respectively. The impactor is modelled using pure-elastic material model with Young's modulus $E = 210$ GPa and Poisson's ratio $\nu = 0.3$.

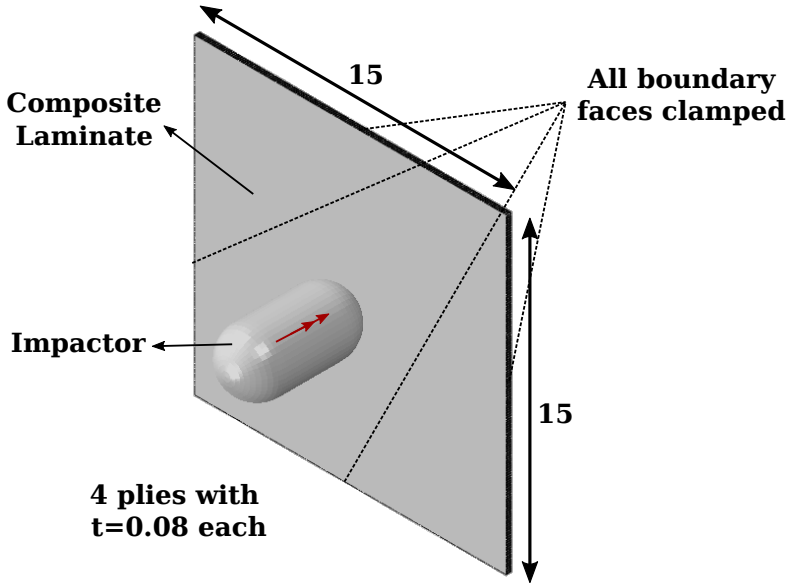

Figure 4.35: Geometry and boundary conditions for quasi-static indentation (QSI) and low-velocity impact (LVI) tests performed on full composite laminate. All dimensions in mm

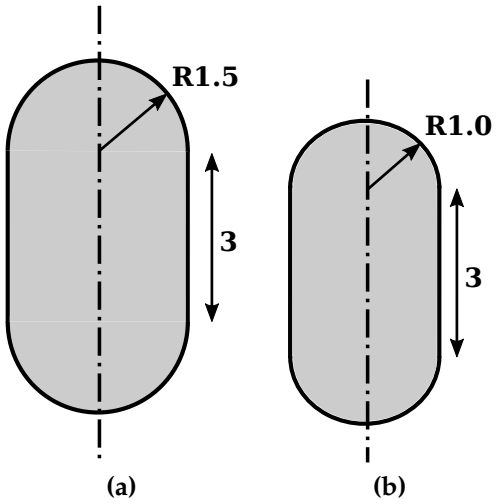

Figure 4.36: Dimensions of impactors used for (a) quasi-static indentation and (b) low-velocity impact tests. All dimensions in mm

The penalty stiffness coefficients for the cohesive traction-separation law are set to $1.0e^5$ N/mm^3 for both normal and shear directions. Furthermore, a penalty-based tangential contact with friction coefficient $\mu = 0.5$ is defined for

Type	Property	Value	Unit
Peak strength	σ_{c1}	58.76	MPa
	σ_{c2}	76.5	MPa
Critical energy release rate	$\mathcal{G}_{c1}$	0.59	N/mm
	$\mathcal{G}_{c2}$	1	N/mm
B-K model parameter	η	3.1	-

Table 4.8: Interface material and fracture properties used for modelling delamination using cohesive zone surface interaction model taken from [2]

all ply-interfaces. The viscous dissipation parameter for the explicit cohesive phase field model is assumed as $\eta = 1.0e^{-5}$.

The explicit solution algorithm is employed with a maximum imposed displacement of 0.25 mm for the impactor in vertically downward direction. The analysis is run for 0.0001 seconds using an automatic time-incrementation control scheme to allow Abaqus to internally calculate the stable time-increment size. All other remaining contacts, e.g. between the impactor and plies is defined using the general contact definition available in Abaqus/Explicit with friction coefficient $\mu = 0.2$.

The 3-D damage evolution through the laminate's thickness is illustrated in Fig. 4.37, wherein both ply fracture and delamination damages occur. Fig. 4.38 shows the intra-laminar damage contours obtained using the anisotropic cohesive phase field model, for all 4 plies in the laminate starting from the top-most ply. It can be noticed that the bottom-most ply is subjected to pure-tensile stresses during the indentation, and hence undergoes maximum amount of failure due to cracking of fibre/matrix under tension. Similarly, the delamination contours modelled using cohesive zone surface interaction model are shown in Fig. 4.39, starting from the top-most to bottom-most ply interface. Delamination is observed at all ply-interfaces with a significantly large failure area in the laminate's centre.

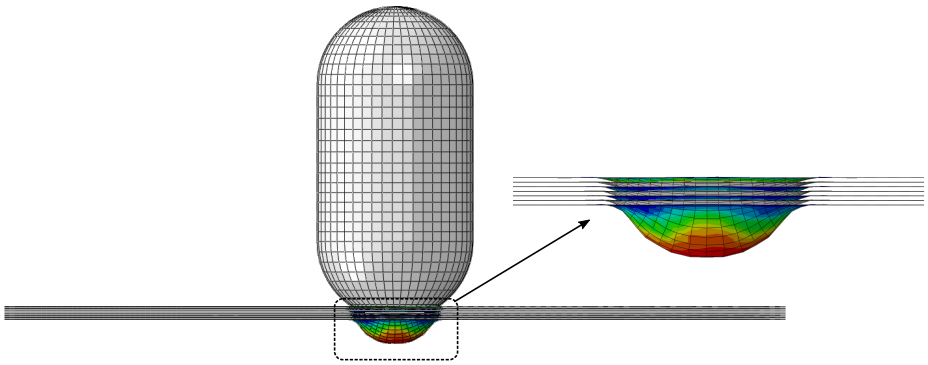

(a)

Figure 4.37: Quasi-static indentation test : Evolution of intra-laminar and inter-laminar damage through the composite laminate's thickness

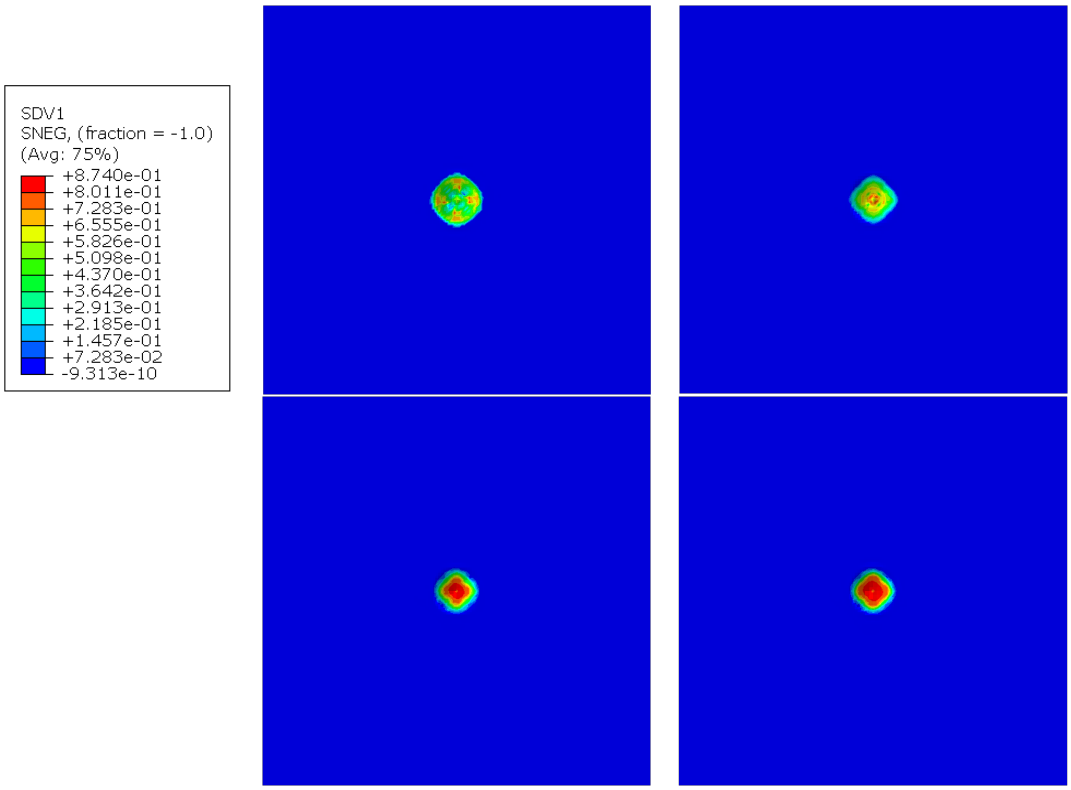

Figure 4.38: Quasi-static indentation : Intra-laminar damage evolution in (a) Ply-1 (b) Ply-2 (c) Ply-3 and (d) Ply-4 modelled using anisotropic cohesive explicit phase field model. Here, Ply-1 is the topmost ply in the composite laminate that faces the impactor, and the values of phase field variable $\phi = 0$ and $\phi = 1$ (SDV1) represent intact and cracked states of the material

4.10.7 Low-velocity impact (LVI) test on full Textreme® 80 g/m^2 composite laminate

A low-velocity impact scenario typically witnessed during bird-strike on aerospace structures is simulated herein on a full Textreme® 80 g/m^2 composite laminate.

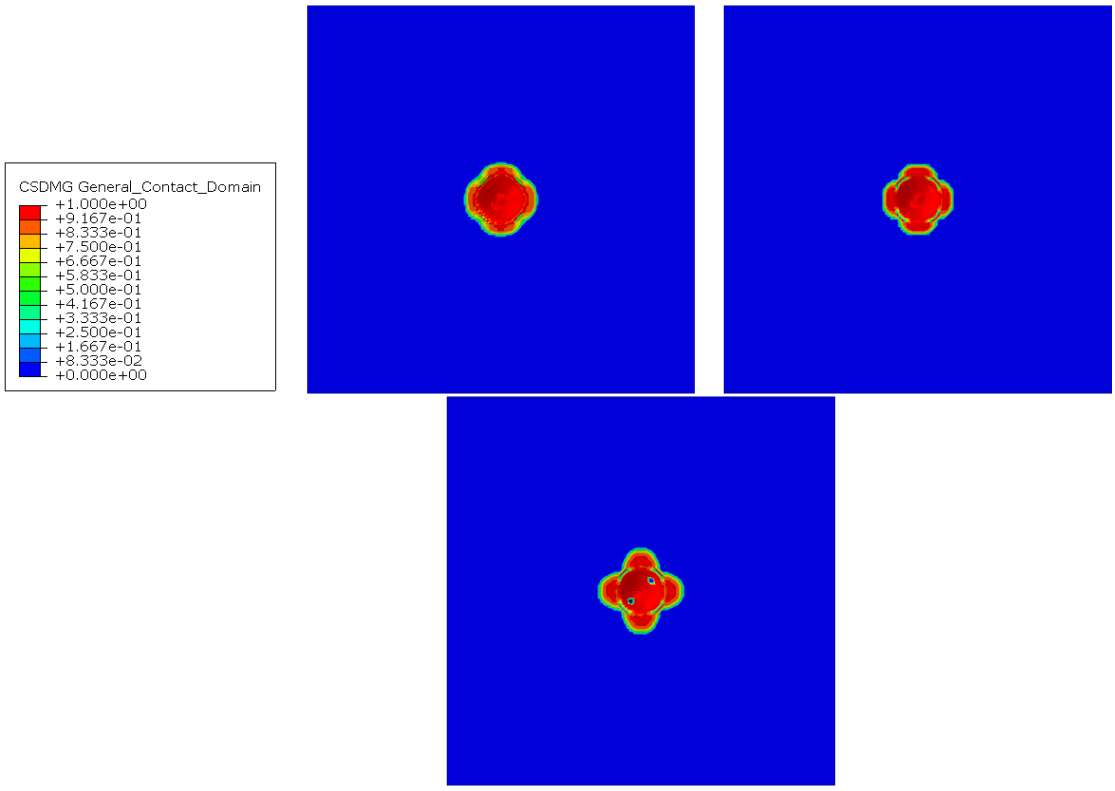

Figure 4.39: Quasi-static indentation : Inter-laminar damage evolution at the interfaces of (a) Ply-1 and Ply-2 (b) Ply-2 and Ply-3 (c) Ply-3 and Ply-4 modelled using cohesive zone surface interaction model. Here, Ply-1 is the topmost ply in the composite laminate that faces the impactor, and CSDMG is the damage variable for cohesive surfaces in Abaqus general contact. CSDMG=0 and CSDMG=1 represents intact and fully-delaminated ply interfaces respectively

The impactor dimensions are shown in Fig. 4.36b. An initial velocity of $2.0e^5$ mm/s is imposed for the impactor. All other parameters including the model geometry, boundary conditions and material/fracture properties, remain similar to the ones used in Sec. 4.10.6 and shown in Fig. 4.35. To realistically reproduce the damage evolution behaviour during bird-strike impact on aerospace composite structures, the impactor is modelled using the Smoothed particle hydrodynamics (SPH) toolbox [466] that is available in Abaqus [178].

SPH belongs to broader meshless or mesh-free methods which represents solids using a collection of discrete points, commonly referred to as particles. SPH relies on full Lagrangian description of solids, but discretizes the continuum partial differential equations based on an evolving interpolation scheme to approximate stress fields directly on discrete particles without needing a fixed spatial mesh as conventional FEM. Such a scheme has been extensively

used for modelling mechanical behaviour that involves extensive deformations like fluid sloshing, paint spraying, ballistics, bird-strike impact etc., see e.g. [467]. The material used for impactor is gelatin with the properties as shown in Table 4.9, which is often used as a bird's substitute material [468]. The hydrodynamic response of gelatin material is incorporated via equation of state **EOS* that provides relation between the current material density ρ and pressure stress p as shown in Eq. (4.73) (more details can be found in [178]).

$$p = f_1(\varepsilon_{vol}) + \rho_0 f_2(\varepsilon_{vol}) E_m \tag{4.73}$$

where f_1 and f_2 are functions of logarithmic volumetric strain $\varepsilon_{vol} = ln(\rho_0/\rho)$ with ρ_0 as the reference density, and E_m is the internal energy per unit mass. The values of f_1, f_2 and ε_{vol} are provided to Abaqus in tabular format as shown in Table 4.10.

The dynamic explicit analysis is performed until 0.0006 seconds using automatic time-incrementation control scheme. Fig. 4.40 illustrates the impact of gelatin SPH particles on the composite laminate from different viewing directions. The final contours for intra-laminar and inter-laminar (delamination) damage in all plies and ply-interfaces, obtained using phase field and cohesive zone methods, are shown in Fig. 4.41 and Fig. 4.42 respectively. The maximum phase field evolution occurs in the bottom-most ply due to large bending stresses, and the delamination is observed at all ply-interfaces with large projected delamination area in the centre of the laminate. These observations are in-line with the experimental and numerical results reported in [2, 462], which predicted delamination at several ply interfaces throughout the laminate thickness without any significant shear matrix cracks.

4.11 Concluding Remarks

In this chapter, an anisotropic 3-parameter cohesive phase field model is proposed for simulating quasi-brittle intralaminar damage in thin spread-tow uni-

Type	Property	Value	Unit
Density	ρ	$9.9e^{-10}$	tonne/mm^3
Elastic/plastic properties			
Shear modulus	G	10	MPa
Yield stress	σ_y	0.1	MPa
Plastic strain at σ_y	ε_{p0}	0	-
Ductile damage initiation			
Fracture strain	ε_f	4	-
Stress triaxiality	η	0	-
Strain rate	$\dot{\varepsilon}$	0	-
Ductile damage evolution			
Displacement at failure (Linear softening)	δ	0	mm
Equation of state (*EOS)	see Table 4.10		

Table 4.9: Material properties taken for gelatin material used as impactor in low-velocity impact simulation

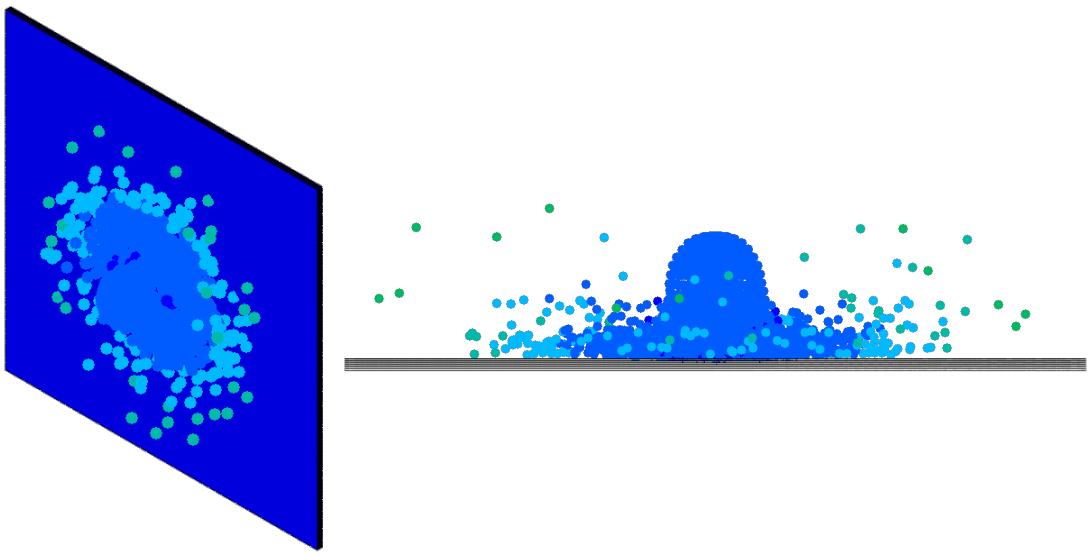

Figure 4.40: Illustration of low-velocity impact (LVI) on full composite laminate using a gelatin impactor discretized using smooth particle hydrodynamics (SPH) method

directional and woven fabric-reinforced composites. The evolving damage is represented using a single scalar phase field variable. However, failure mode specific crack-driving force terms and corresponding degradation functions are defined, thus allowing for a robust and versatile simulation tool custom fit for materials with strong anisotropies both in their elastic and fracture properties.

The stress-degradation functions are established on the basis of 3 parameters that fully describe the post-peak softening response in each failure mecha-

f_1	f_2	ε_{vol}
0	0	0
17.06789813	0	-0.007
34.95050691	0	-0.014
53.64620231	0	-0.021
73.15336604	0	-0.028
93.47038569	0	-0.035
114.5956547	0	-0.042
136.5275725	0	-0.049
159.2645443	0	-0.056
182.8049814	0	-0.063
207.1473014	0	-0.07
232.2899275	0	-0.077
258.2312895	0	-0.084
284.969823	0	-0.091
312.5039701	0	-0.098
340.8321789	0	-0.105
369.952904	0	-0.112
399.8646063	0	-0.119
430.5657531	0	-0.126
462.054818	0	-0.133
494.3302813	0	-0.14
527.3906296	0	-0.147
561.2343564	0	-0.154
595.8599614	0	-0.161
631.2659513	0	-0.168

Table 4.10: Tabular equation of state (*EOS) used for gelatin material in Abaqus

nism. For the case of UD and woven-fabric composites, these can be calibrated based on three experiments, i.e., two tensile tests in two orthogonal directions and a pure shear test. A strategy to accurately calibrate the cohesive softening parameters using experimental softening curves is discussed.

Modified expressions are also provided to account for the case of shear induced plastic deformations; these have been observed to be of relevance in the case of spread-tow woven fabric-reinforced composites. Within this setting, the anisotropic cohesive phase field formulations are modified to incorporate elasto-plasticity with isotropic hardening for the in-plane shear behaviour.

The solution procedure for the coupled system of governing equations is solved in a staggered manner using a hybrid strategy; the crack-driving forces are evaluated based on a direct decomposition of the strain tensor but the

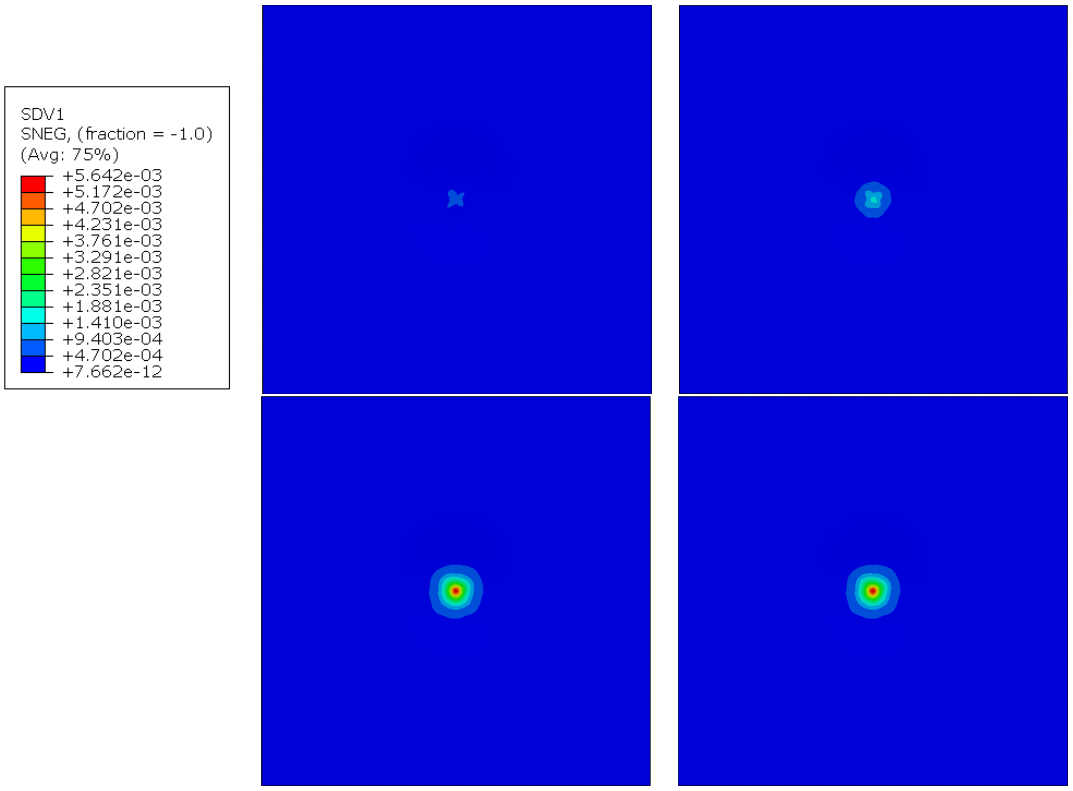

Figure 4.41: Low-velocity impact : Intra-laminar damage evolution in (a) Ply-1 (b) Ply-2 (c) Ply-3 and (d) Ply-4 modelled using anisotropic cohesive explicit phase field model. Here, Ply-1 is the topmost ply in the composite laminate that faces the impactor, and the values of phase field variable $\phi = 0$ and $\phi = 1$ (SDV1) represent intact and cracked states of the material

stresses are degraded uniformly. The overall framework is implemented in the commercial software Abaqus via a user-material (UMAT) subroutine.

The benchmark tests demonstrate the effectiveness of the proposed method in accurately capturing damage evolution due to diverse intra-laminar composite damage mechanisms, namely fibre fracture, fibre pull-outs/bridging, and matrix shear cracking. The proposed method is validated against two sets of experiments, i.e., CT and DENT tests performed on a Textreme® 80 g/m^2 composite. The CT tests were used to calibrate the cohesive parameters. This set of parameters accurately reproduced the DENT experimental results both in terms of the predicted crack path and the overall load deflection response of the specimen. Further validation is performed for the case of unidirectional flax ply and glass-reinforced fabric composites where the proposed model is also shown to provide accurate estimates.

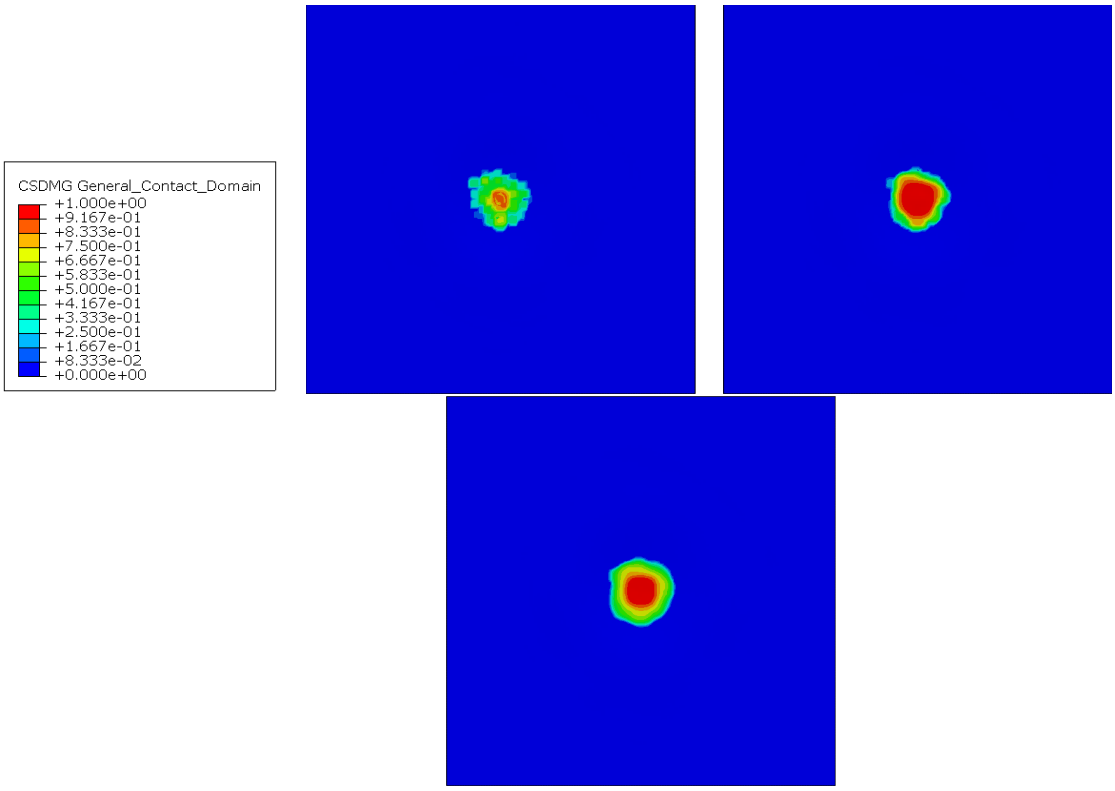

Figure 4.42: Low-velocity impact : Inter-laminar damage evolution at the interfaces of (a) Ply-1 and Ply-2 (b) Ply-2 and Ply-3 (c) Ply-3 and Ply-4 modelled using cohesive zone surface interaction model. Here, Ply-1 is the topmost ply in the composite laminate that faces the impactor, and CSDMG is the damage variable for cohesive surfaces in general contact. CSDMG=0 and CSDMG=1 represents intact and fully-delaminated ply interfaces respectively

The proposed cohesive phase field model is further extended to perform full composite laminate analysis by combining it with cohesive-zone surface interaction model to capture delamination. An explicit cohesive phase field model is proposed to effectively simulate the highly nonlinear damage evolution behaviour pertinent to composite laminates; this is implemented in Abaqus using a VUMAT subroutine. A strategy to perform ply-by-ply modelling using a stacked shell approach is presented, wherein each shell element layer is tied to surface element layers used for defining cohesive interfaces. The combined phase field and cohesive zone model is used to perform robust dynamic-explicit simulations for low-velocity impact and quasi-static indentation on Textreme® 80 g/m^2 composite laminate structure, and capture the complex intra-laminar and inter-laminar damage evolution behaviour.

5

Multi-scale modelling of damage evolution in composites

5.1 Introduction

In this chapter, a multi-scale approach based on surrogate-models is presented to simulate damage evolution in composites. The point of departure is the concurrent FE^2 multiscale method based on computational homogenisation, which has found widespread application in composites. The standard FE^2 method employs an FE-RVE approach in which the strains at the macro-scale are imposed on a meso-scale representative volume element (RVE) model; this is analysed under periodic, displacement or stress boundary conditions at each time increment [469]. The homogenized stress-strain response from the RVE simulation is then provided as an equivalent macro-scale constitutive law for imposed macro-scale strains. In general, FE^2 is an effective multiscale technique for capturing physical behaviour at different inherent scales of composite, however, it is associated with high computational costs due to simultaneous solving of both macro- and meso-scale models.

In the proposed strategy, the FE-RVE approach is replaced by a surrogate model as shown in Fig. 5.1, which is interrogated by the macro-scale model at each time-increment. Two different surrogate models based on Polynomial Chaos Expansion (PCE) and Artificial Neural Network (ANN) are explored,

and their accuracy in predicting the nonlinear damage response of composites is compared against the fine resolution cohesive phase field damage model. The main objective of this surrogate model is to perform fast progressive damage analysis of large composite structures.

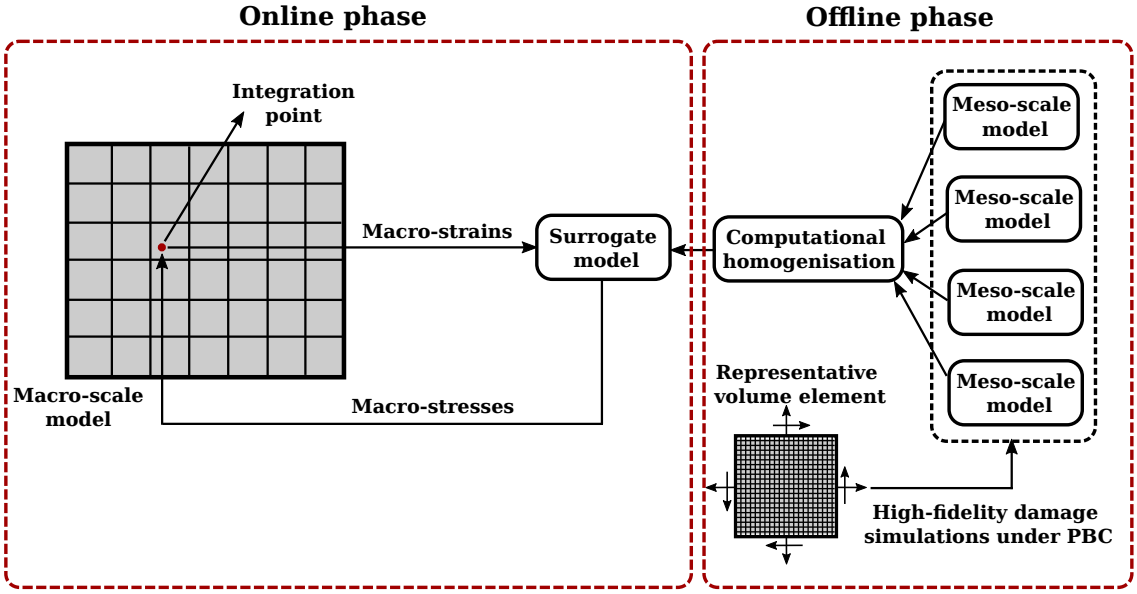

Figure 5.1: Schematic illustration of FE^2 multiscale method for damage modelling in composites using a surrogate model

The surrogate model provides reasonably accurate estimates for the failure initiation stresses and post-peak damage behaviour of composites with respect to any mixed-mode loading case, whilst significantly reducing the computational costs associated with the phase field method. To accurately predict the material failure behaviour, the surrogate model needs to be trained with a database containing large amount of stress-strain data involving damage evolution under different mixed-mode loading conditions. The training data-set could be either obtained from extensive experimental testing, or by simulating meso-scale unit cell models [402] under multi-axial load combinations applied with periodic boundary conditions. Although a surrogate model trained using experimental data-set could provide more accurate approximation of the actual material failure behaviour, it is practically infeasible to conduct such large number of experiments for each of these load-cases. Hence in the context of the current work, an RVE unit cell based approach has been adopted to generate diverse meso-scale responses for different composite failure modes. The

proposed method is demonstrated for 2-D RVE models subjected to in-plane strains, however the approach is generic and can be extended to any complex 3-D case as long as the damage physics at the meso-scale is accurately resolved.

5.2 Computational homogenisation

In composite structures, the cracks initiate at micro-scale (fibres/matrix level) and propagate on to macro-scale (component/structural level) causing full rupture and complete loss of structural stiffness. However in large industrial models, it becomes expensive and impractical to simulate all micro-scale cracks from a computational standpoint. In such cases, effective or homogenized material properties are often used to obtain a global failure indicator and stiffness degradation, instead of modelling local micro-cracks [44]. In concurrent multiscale approach such as FE^2, each integration point in the macro-scale model is assigned with an underlying RVE model as shown in Fig. 5.1. The macro-scale strains at the integration points are then imposed on these RVE models as periodic boundary conditions (PBC), and a meso-scale simulation is performed simultaneously to capture the complex physics of damage evolution at the micro or meso scales. The local stresses in RVE are homogenized and transferred back to the macro-scale model via a FE-RVE feedback loop, as an equivalent response to strains applied at the given integration point. To calculate the equivalent RVE response, a link needs to be established through energy equivalence between the macro and micro/meso-scales, i.e.,

$$\langle \sigma(x,y)\, \varepsilon(x,y) \rangle_{RVE} = \bar{\sigma}(X,Y)\, \bar{\varepsilon}(X,Y) \tag{5.1}$$

where $\{x, y\}$ and $\{X, Y\}$ are meso and macro-scale coordinates, and $\{\sigma, \varepsilon\}$ and $\{\bar{\sigma}, \bar{\varepsilon}\}$ are meso and macro-scale stresses/strains respectively. The averaged macroscopic stresses and strains can be obtained using the Bishop-Hill rela-

tions [470]:

$$\begin{aligned} \bar{\sigma} &= \frac{1}{V}\int_{V} \sigma \, \mathrm{dV} \\ \bar{\varepsilon} &= \frac{1}{V}\int_{V} \varepsilon \, \mathrm{dV} \end{aligned} \tag{5.2}$$

with V as the RVE volume. The homogenization is performed at each time increment, and the complete equivalent stress-strain responses corresponding to different composite failure modes are extracted from each RVE simulation. The homogenized stress-strain curve contains information about the constitutive damage response of given composite including the critical stresses and post-peak fracture behaviour pertaining to each failure mode.

The proposed surrogate modelling approach falls within the remit of concurrent FE^2 multiscale methods. Within this setting, the objective is to analyse the macro-scale structure using the surrogate model over a coarser mesh, whilst simulating the nonlinear damage behaviour occurring at the micro/meso scales (ply level) using high-fidelity phase field model over a fine mesh. To boost the computational efficiency of FE^2 approach during real-time damage simulation of large composite structures, numerous meso-scale RVE models are analysed in an offline phase under diverse multi-axial load combinations. Since, it is impractical to analyse all possible combinations, RVE simulations are performed at specific sample points, and the homogenised fracture response is stored in the form of a database, which is used to train the surrogate model. Once the surrogate model is accurately trained, it is used to replace the FE-RVE concurrent feedback loop in the FE^2 analysis.

5.3 Meso-scale simulations

Meso-scale simulations are performed on the RVE unit cell model in an offline phase, subjected to arbitrary combinations of macro-scale strains applied with periodic boundary conditions (PBC). To obtain a well-sampled dataset, a Latin

Hyper Cube (LHC) approach has been used, which generates different possible combinations of macro-scale strains; these are uniformly distributed and randomly permuted against each other to avoid any correlation between them. The three macro-scale strains $\{\varepsilon_{11}, \varepsilon_{22}, \gamma_{12}\}$ are later used as an input database for training the surrogate model. In LHC sampling, the cumulative density function (CDF) of the input strain distribution is divided into n equally probable intervals and one sample value is extracted from each of these intervals. An illustration of LHC is provided in Fig. 5.2.

LHC sampling spreads the sample values more evenly across the sampling space, and drastically reduces the number of runs as compared to a crude Monte-Carlo, whilst still achieving reasonably accurate results [61]. The macro-strain combinations $\{\varepsilon_{11}, \varepsilon_{22}, \gamma_{12}\}$ obtained via LHC are shown as sampling points in Fig. 5.3a; these are imposed on the RVE using displacement control in Abaqus coupled with PBC defined as equation constraints. The following section provides a description of the RVE unit cell model which has been used for meso-scale simulations.

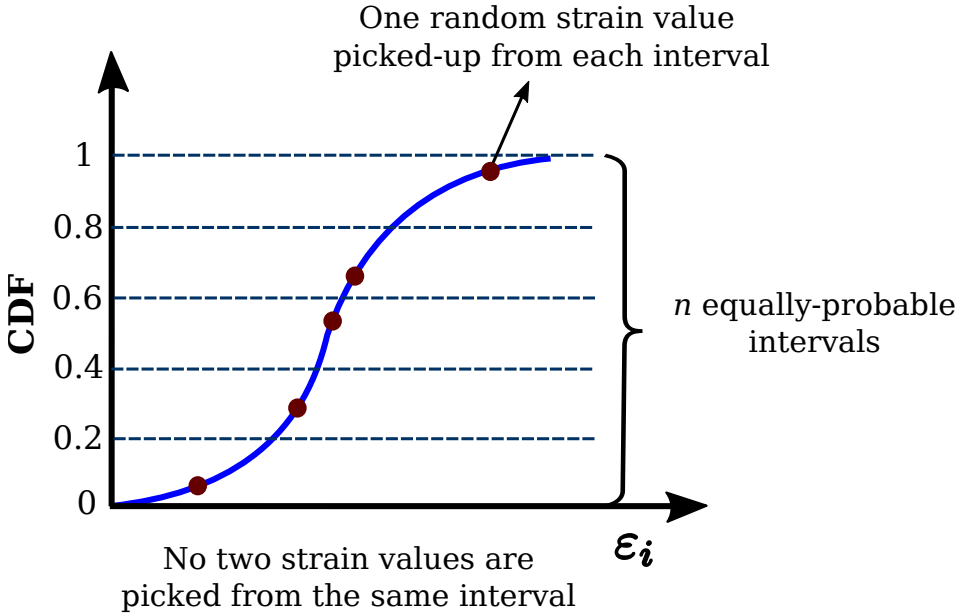

Figure 5.2: Illustration of the Latin HyperCube sampling (LHC) method to extract n random strain samples from evenly partitioned intervals

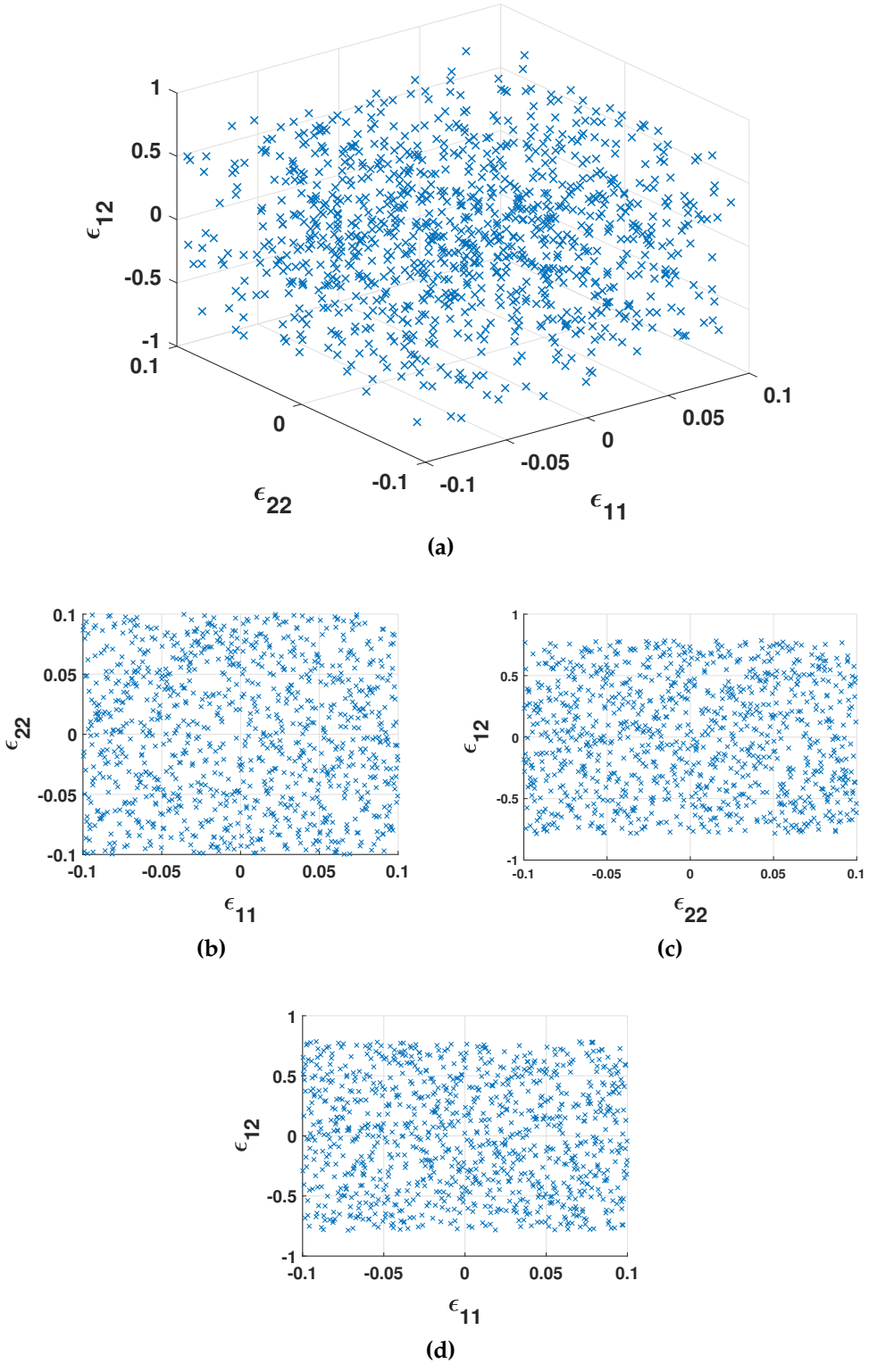

Figure 5.3: (a) Input macro-strain combinations with $\varepsilon_{11} \in [-0.1, 0.1]$, $\varepsilon_{22} \in [-0.1, 0.1]$ and $\varepsilon_{12} \in [-\pi/4, \pi/4]$ generated using LHC. Each strain is uniformly distributed and randomly permuted against each other. Sectional cut views as seen along the (b) ε_{12} axis (c) ε_{11} axis, and (d) ε_{22} axis

5.3.1 Representative volume element (RVE)

The RVE unit cell model represents the smallest periodically repeating unit of an infinite material volume. Unit cell models have been widely applied in the literature to obtain effective material properties and meso-scale damage information for composites. In the current study, the RVE model comprises a single square-shaped plate shown in Fig. 5.4, which is discretized using fully-integrated S4 shell elements in Abaqus, and can represent either unidirectional or woven composite plies.

The material considered herein is the Textreme-80 gsm woven fabric reinforced composite. Its mechanical properties are shown in Table 4.2. The anisotropic cohesive phase field damage model presented in Chapter 4 is used to model intra-laminar ply based failure in the RVE model, which involves fibre cracking, fibre pullouts/bridging, and matrix plastic deformation and cracking under tensile and shear loads. To establish the accuracy of the damage model considered for RVE meso-scale analysis, a pure-tensile and a pure-shear loading case are simulated initially, and their predicted failure responses are compared against the experimental results in Sec. 5.3.2, see e.g. Fig. 5.8.

Periodic boundary conditions (PBC) are applied on the unit cell in accordance with the strategy presented in [402]. The advantage of this approach is that it allows for the imposition of any arbitrary combination of stresses or strains as generalised loads, without requiring a different set of boundary conditions to be derived for each case. Let the RVE model be a regular square unit-cell shown in Fig. 5.4, with 3 translational symmetries in x, y and z directions with periods $b_x = L$, $b_y = L$, and $b_z = t$, respectively. In addition, let's assume that there exists a cell as the region highlighted in Fig. 5.4b that represents the entire domain when translated with defined periods in the respective directions.

The PBCs are generated on this unit-cell RVE model using Abaqus **Equation* keyword, which applies multi-point constraints (MPCs) for the appropriate degrees-of-freedom corresponding to any two nodes present on opposite

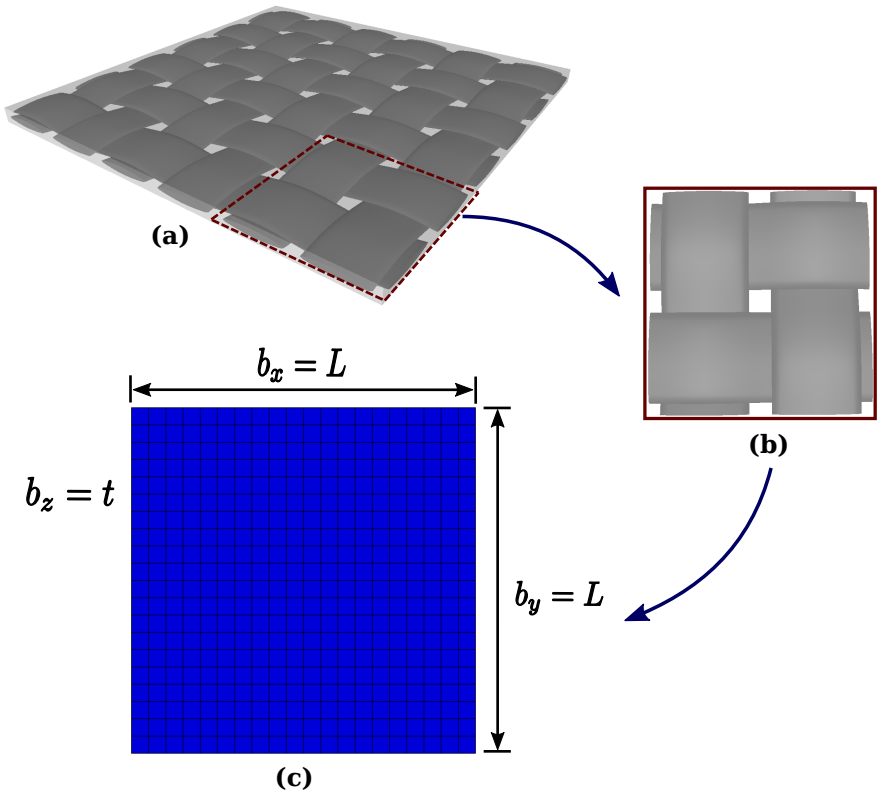

Figure 5.4: (a) Illustration of woven spread-tow fabric-reinforced composite ply (b) Representation Volume Element (RVE) definition, and (c) Square unit-cell RVE model in Abaqus comprising single layer of S4 shell elements

faces or edges. Naturally, the corner nodes of the unit cell are a part of two adjacent edges, and would be constrained by both edges with distinct boundary conditions (B.C.). It is of interest to note that although the presence of dependent B.C. equations do not introduce any problems in the mathematical sense, a commercial software like Abaqus detects it as a source of error and expects the user to render these constraints independent of each other [402]. Hence, the corner nodes must be placed in separate node-sets, and subjected to equation constraints that are independent from those imposed on the RVE edges. Similarly for a 3-D RVE model, separate sets must be formed for RVE corners, edges and faces [402]. Owing to translational symmetry between all corner nodes of the RVE, any corner node (e.g. node A in Fig. 5.6) can be chosen arbitrarily without loss of generality, and the remaining corner nodes can be constrained with respect to it.

To impose **Equation* constraints in Abaqus, the RVE boundary nodes are grouped into corner $\{A, B, C, D\}$ and edge-based $\{AB, BC, DC, AD\}$ node sets.

The edge node-sets can contain multiple nodes, however, they exclude the corner nodes $\{A, B, C, D\}$ to eliminate dependent constraints. The nodes on edges AB and AD (excluding corners) are linked in all DOFs to corresponding nodes situated on the opposite edges DC and BC, respectively.

Similarly, all DOFs of the corner node A are linked to the DOFs of other corner nodes B, C and D. The macro-strains are applied on the RVE as imposed displacements on the reference points, which are included in the **Equation* constraints defined for each pair of linked node-sets. The reference points act as a single point of imposed displacement on the linked nodes, and are disconnected from the actual RVE model. The node linkages with corresponding reference points are illustrated on an example mesh with 4×4 shell elements in Fig. 5.6. The **Equation* constraints imposed on the edge/corner nodes are as follows:

Edges:

$$
\begin{aligned}
u^{BC} - u^{AD} &= L\varepsilon_x \hat{u}^o_{r1} & \qquad u^{DC} - u^{AB} &= L\varepsilon_{yx}\, \hat{u}^o_{r2} \\
v^{BC} - v^{AD} &= L\varepsilon_{xy} \hat{v}^o_{r1} & \qquad v^{DC} - v^{AB} &= L\varepsilon_y\, \hat{v}^o_{r2} \\
w^{BC} - w^{AD} &= 0 & \qquad w^{DC} - w^{AB} &= 0 \\
\theta_x^{BC} - \theta_x^{AD} &= 0 & \qquad \theta_x^{DC} - \theta_x^{AB} &= 0 \\
\theta_y^{BC} - \theta_y^{AD} &= 0 & \qquad \theta_y^{DC} - \theta_y^{AB} &= 0 \\
\theta_z^{BC} - \theta_z^{AD} &= 0 & \qquad \theta_z^{DC} - \theta_z^{AB} &= 0
\end{aligned}
$$

Corners:

$$
\begin{aligned}
u^B - u^A &= L\varepsilon_x\, \hat{u}^o_{r1} & \quad u^C - u^A &= (L\varepsilon_x + L\varepsilon_{yx})\, \hat{u}^o_{r3} & \quad u^D - u^A &= L\varepsilon_{yx}\, \hat{u}^o_{r2} \\
v^B - v^A &= L\varepsilon_{xy}\, \hat{v}^o_{r1} & \quad v^C - v^A &= (L\varepsilon_{xy} + L\varepsilon_y)\, \hat{v}^o_{r3} & \quad v^D - v^A &= L\varepsilon_y\, \hat{v}^o_{r2} \\
w^B - w^A &= 0 & \quad w^C - w^A &= 0 & \quad w^D - w^A &= 0 \\
\theta_x^B - \theta_x^A &= 0 & \quad \theta_x^C - \theta_x^A &= 0 & \quad \theta_x^D - \theta_x^A &= 0 \\
\theta_y^B - \theta_y^A &= 0 & \quad \theta_y^C - \theta_y^A &= 0 & \quad \theta_y^D - \theta_y^A &= 0 \\
\theta_z^B - \theta_z^A &= 0 & \quad \theta_z^C - \theta_z^A &= 0 & \quad \theta_z^D - \theta_z^A &= 0
\end{aligned}
$$

where, $\varepsilon_{xy} = \gamma_{xy}/2$ is the shear strain, and $\{\hat{u}^o_{r1}, \hat{v}^o_{r1}, 0, 0, 0, 0\}$, $\{\hat{u}^o_{r2}, \hat{v}^o_{r2}, 0, 0, 0, 0\}$ and $\{\hat{u}^o_{r3}, \hat{v}^o_{r3}, 0, 0, 0, 0\}$ are the imposed displacements on the reference points $r1$, $r2$, and $r3$, respectively. In addition, all DOFs of the corner-node A are constrained to zero to avoid rigid body modes. The quantities on the right-hand side (RHS) of each equation are applied as imposed displacements to the corresponding DOF of the reference points, which makes the RVE to deform under the given macro-strain combination $\{\varepsilon_x, \varepsilon_y, \gamma_{xy}\}$ as shown in Fig. 5.5. The RVE is then simulated using the cohesive phase field damage model from Chapter 4 subjected to different strain combinations described in Sec. 5.3, and the meso-scale damage response involving fibre and matrix-based failures is obtained. The step-by-step procedure of generating the RVE input models in Abaqus, and the complete multiscale approach including meso and macro-scale simulation is illustrated in the flowchart Fig. 5.9, and the solution algorithm is described in Algorithm A.3.

Remark 13. It is important to note that the periodicity assumptions presented herein, apply to both linear and nonlinear behaviour, including damage. Hence, the damage propagation must also remain periodic, i.e. damage in any element lying at the RVE boundary surface must continue propagating at the opposite surface. Due to the strictly conformal mesh and direct node-to-node coupling, the displacements on each node-pair on opposite RVE surfaces are directly linked to each other. This results in periodic stresses and strains in the RVE, and hence also guarantees the periodicity of induced damage, see e.g. [471].

Periodic homogenization based methods are backed by a robust mathematical background, and have been extensively applied throughout the literature vis-à-vis damage modelling of composites [471–475]. These methods provide accurate damage estimates, however, imposition of PBC also poses restriction on the damage to be essentially periodic, which may lead to unrealistic crack propagation patterns. Although the aim of the current work was to exploit the computational advantages of surrogate models for developing an initial multi-scale damage modelling framework, future work may be directed towards exploring the application of generalized displacement boundary con-

ditions within this context, see e.g. [378, 425].

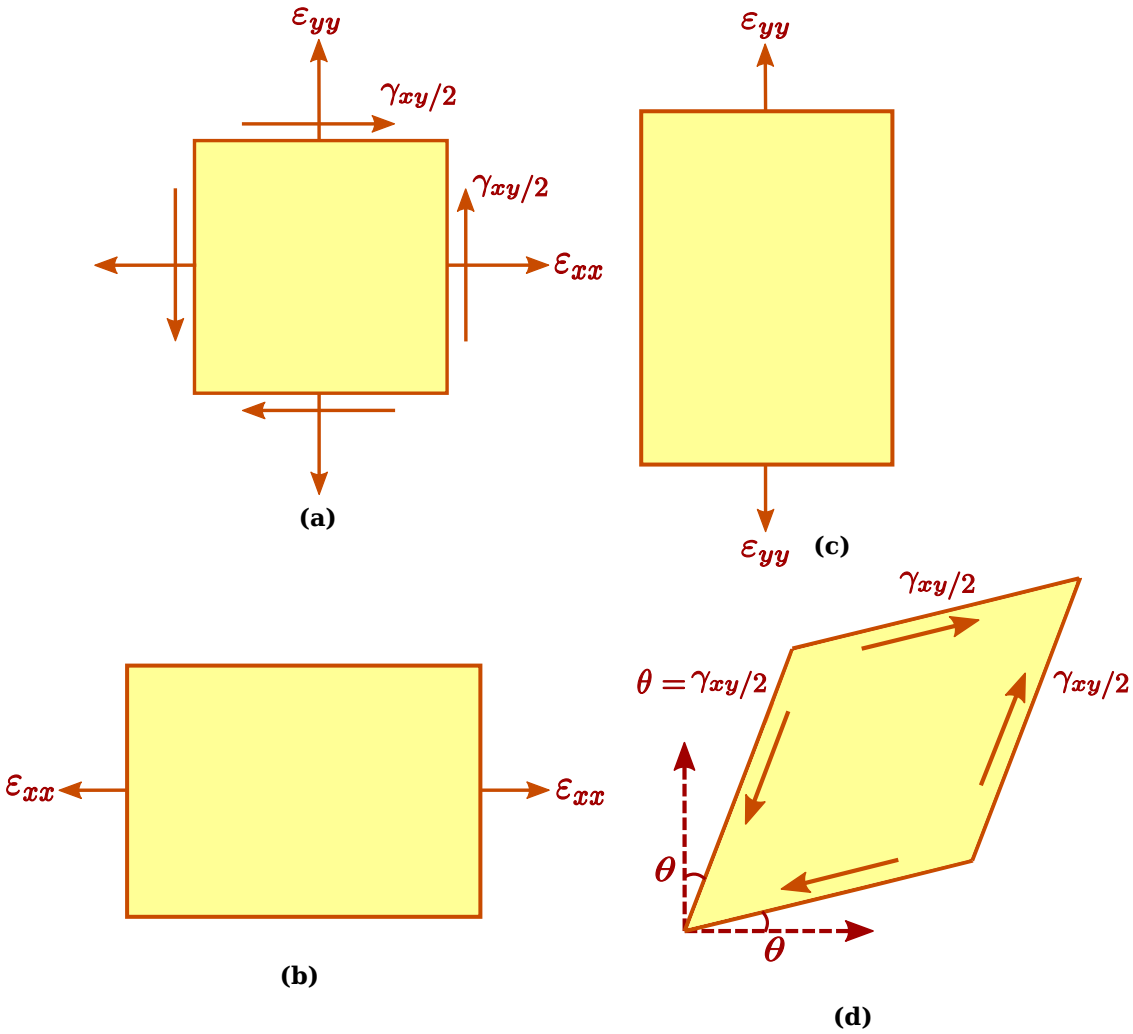

Figure 5.5: (a) Unit-cell square RVE subjected to multi-axial macro-strains, and deformed RVE shapes under (b) longitudinal tensile strain ε_{xx} (c) transverse tensile strain ε_{yy} (d) in-plane shear strain γ_{xy}

5.3.2 RVE database with homogenised meso-scale responses

For each meso-scale RVE simulation, the homogenised stress-strain response is generated based on the approach described in Sec. 5.2. Example responses for pure-tensile and pure-shear modes are illustrated in Fig. 5.8a and Fig. 5.8b respectively, and their critical strengths are compared against the experiments. In the pure tensile mode, the RVE is subjected to a macro-strain combination of $[\varepsilon_{11} = 0.1, \varepsilon_{22} = 0, \gamma_{12} = 0]$, whereas the strain-combination applied in pure shear mode is $[\varepsilon_{11} = 0, \varepsilon_{22} = 0, \gamma_{12} = \pi/4]$. Due to the symmetry of fibre

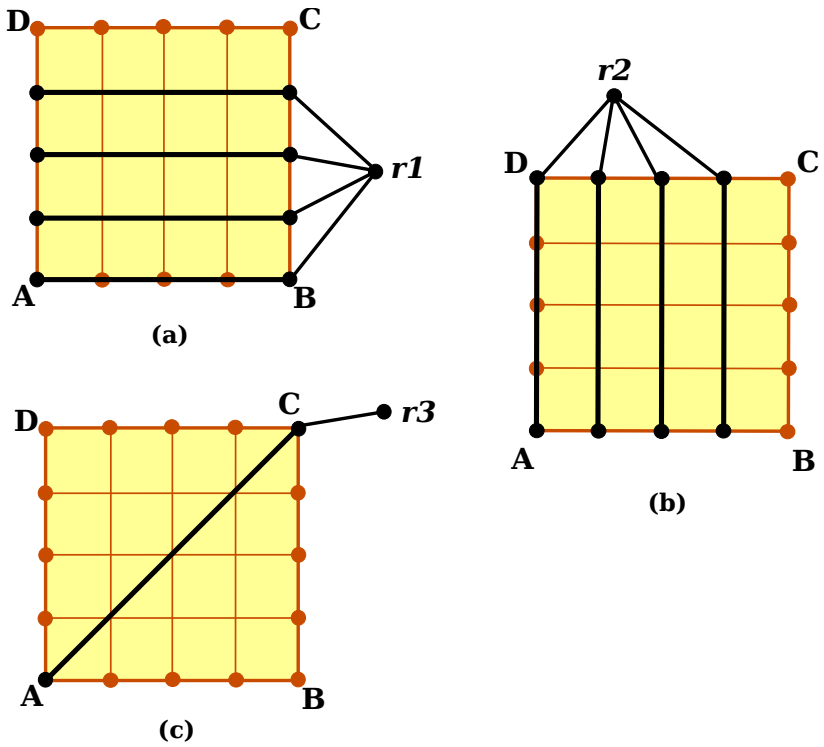

Figure 5.6: Linked degrees of freedom at opposite edge/corner nodes with the reference points (a) $r1$ (b) $r2$ (c) $r3$ for applying periodic boundary conditions (PBC)

orientation in n_{11} and n_{22} directions of Textreme-80gsm with $[0^o, 90^o]$ layup, the homogenized responses for pure-tensile strains applied in warp n_{11} $[\varepsilon_{11} = 0.1, \varepsilon_{22} = 0, \gamma_{12} = 0]$ and weft n_{22} $[\varepsilon_{11} = 0, \varepsilon_{22} = 0.1, \gamma_{12} = 0]$ directions are similar, and hence only the former is illustrated in Fig. 5.8a. It can be noticed that the critical fracture stresses predicted in both Fig. 5.8a and Fig. 5.8b, by the cohesive phase field model as well as the experiments, are within $\sim 5.8\%$ and $\sim 4.2\%$ of each other, respectively. Moreover, the elastic-plastic shear fracture response typically observed in woven fabric-reinforced composites, due to matrix-dominated plastic shear deformation and subsequent cracking, is captured well by the model, as seen in Fig. 5.8b.

The next step is to populate a RVE database that can be used to train the surrogate model. The RVE database contains the macro-scale strains $\{\varepsilon_{11}, \varepsilon_{22}, \gamma_{12}\}$ as the input data-set, and the corresponding homogenized final stresses $\{\sigma_{11}, \sigma_{22}, \sigma_{12}\}$ and critical fracture stresses $\{\sigma_{c11}, \sigma_{c22}, \sigma_{c12}\}$ as the output data-set.

An example of the i^{th} entry in the RVE database corresponding to the meso-scale simulation under i^{th} multi-axial loading combination is shown in

Fig. 5.7. In addition to the macro-scale strain combinations generated with LHC sampling and their respective final stresses post-damage, the input and output data-sets are expanded by adding more sampling points from the stress-stain response at intermediate time-increments of each meso-scale RVE simulation. The number of intermediate points to extract depends on the non-linearity of the response that needs to be captured by the surrogate model. If the stress-strain results are extracted at k equidistant time-increments from each of n RVE simulations, the size of the original data-set effectively expands to $k \times n$.

It must be emphasized that each of these $k \times n$ points in the expanded data-set are unique with respect to each other in the overall sample space. However, the input macro-strain combinations $\{\varepsilon_{11}, \varepsilon_{22}, \gamma_{12}\}$ no longer have a uniform probability distribution that was earlier obtained with LHC, as would be shown in subsequent Sec. 5.6.1. The critical stresses in each failure mode obtained from different RVE simulations are plotted in the 3-D sample space and a convex hull is constructed from these points. The convex hull acts as the 3-D fracture surface that determines the failure initiation points for a given composite. In the macro-scale simulations, this is used to trigger and activate the surrogate model as soon as the stress-state of the material crosses this fracture surface, as will be demonstrated in Sec. 5.6.1.

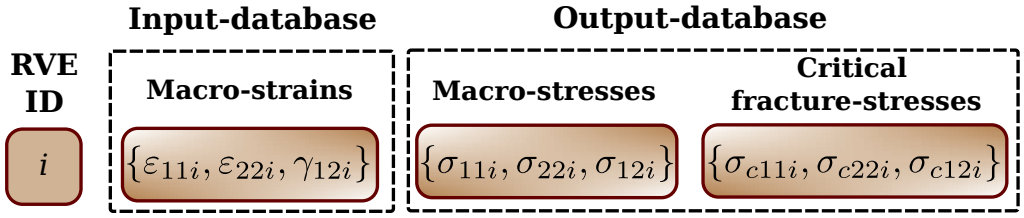

Figure 5.7: An example RVE-database entry showing input and output parameters obtained from the meso-scale damage simulation of RVE subjected to i^{th} multi-axial loading combination

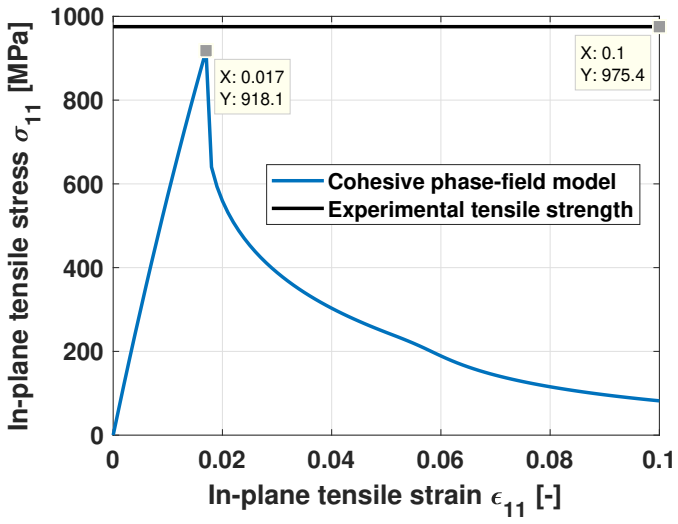

(a)

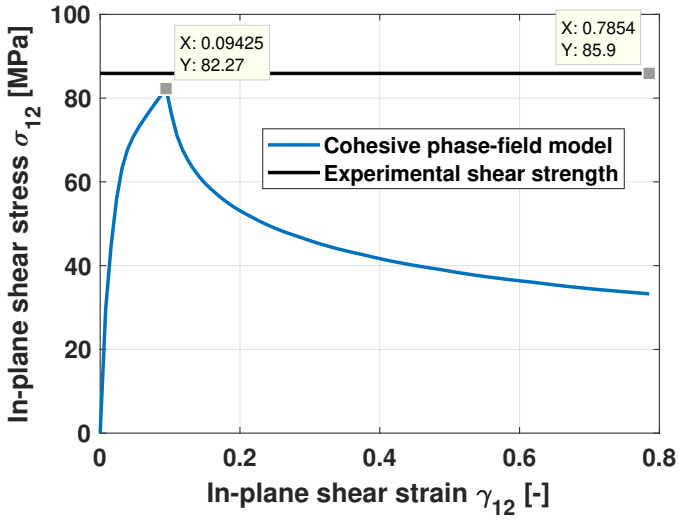

(b)

Figure 5.8: Homogenized stress-strain plots obtained from meso-scale RVE simulations of Textreme-80gsm using anisotropic cohesive phase field model subjected to (a) Pure tensile strain state $[\varepsilon_{11} = 0.1, \varepsilon_{22} = 0, \gamma_{12} = 0]$ (b) Pure shear strain state $[\varepsilon_{11} = 0, \varepsilon_{22} = 0, \gamma_{12} = \pi/4]$. The predicted critical fracture stresses are compared against corresponding experimental laminate strengths of Textreme-80gsm

5.4 Surrogate model

The RVE database obtained in Sec. 5.3.2 is used to train the Polynomial Chaos Expansion (PCE) and the Artificial Neural Network (ANN) based surrogate models.

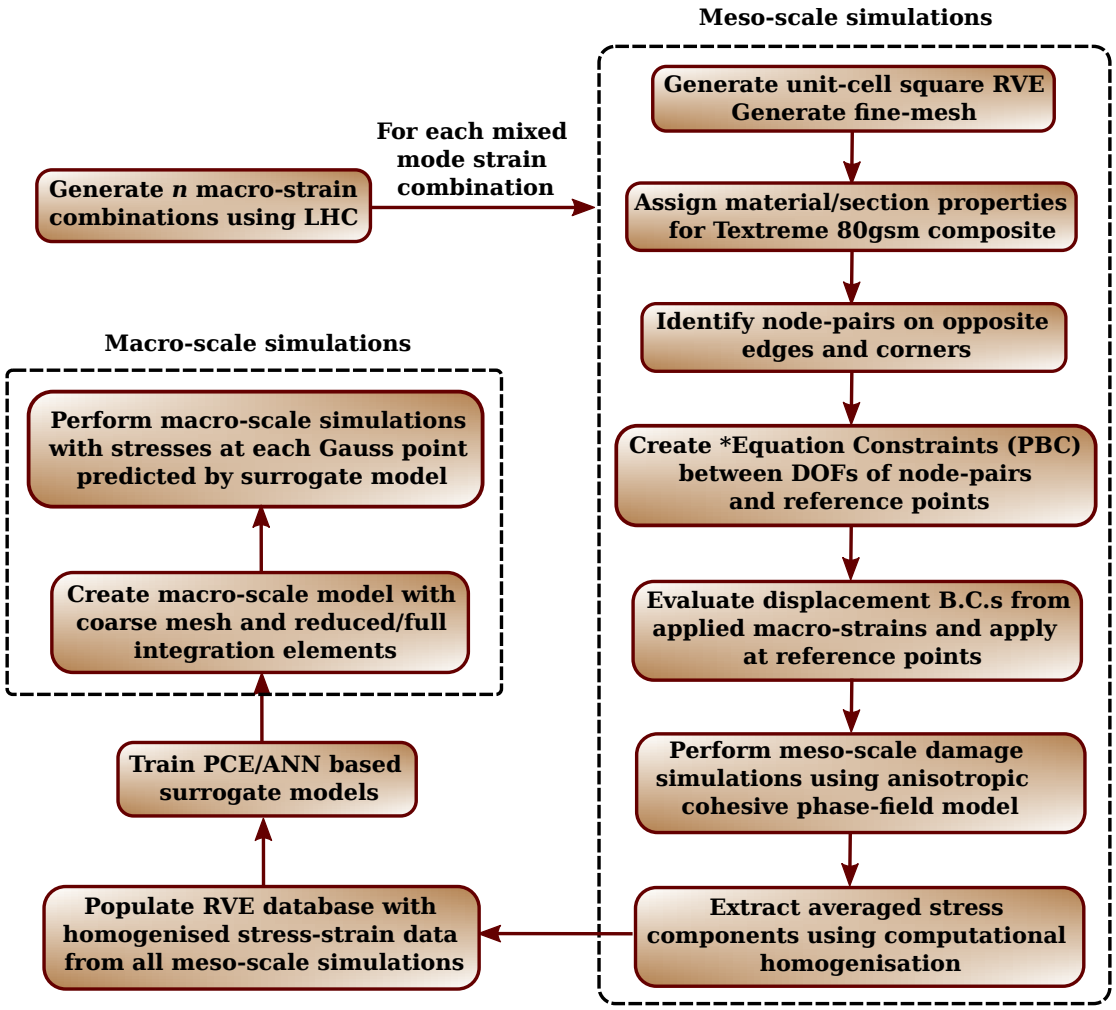

Figure 5.9: Flowchart depicting the steps involved in performing multiscale damage simulation of composites using surrogate models. Each step is automated using Abaqus Python scripting interface.

5.4.1 Polynomial Chaos Expansion (PCE)

PCE initially originated from the work of Wiener [476], has found extensive application in uncertainity quantification over the past 15 years. PCE is a stochastic method that captures uncertainty in the model input and output distributions via polynomial basis functions within a probablistic framework. [477]. It uses orthogonal polynomials to fit a response surface to an output data-set which has been generated with experiments/simulations of an input data-set sampled with a specific probability distribution.

Considering the trivial case of a two-dimensional probability space, let (ζ_1, ζ_2) be two random variables that expand the input-data space, and are

sampled with a given probability distribution p. Each sample-set (ζ_1, ζ_2) yields a discrete point z_i in the output-data space. The main objective of the PCE is to identify a suitable polynomial function $F(\zeta_1, \zeta_2)$, which can accurately calibrate a response surface to the output values z_i such that,

$$z_i \approx F(\zeta_1, \zeta_2) \tag{5.3}$$

with $i \in [1, n]$, where n is the number of sample points in input and output data-sets. The polynomial function $F(\zeta_1, \zeta_2)$ is expanded in terms of orthogonal polynomials $\phi_k(\zeta_1, \zeta_2)$ as shown in Eq. (5.4).

$$F(\zeta_1, \zeta_2) \approx a_0 + \sum_{i=1}^{2} a_i \, \phi_1(\zeta_i) + \sum_{i=1}^{2} \sum_{j=1}^{i} a_{ij} \, \phi_2(\zeta_i, \zeta_j) + ... \tag{5.4}$$

Since the polynomials $\phi_k(\zeta_1, \zeta_2)$ are orthogonal, any arbitrary point within the output-data space can be conveniently represented as their linear expansion. This allows the PCE to require a reduced number of simulations for quantifying uncertainty as compared to brute force Monte-Carlo simulations [477].

The polynomial function $F(\zeta_1, \zeta_2)$ is obtained by choosing appropriate orthogonal polynomials $\phi_k(\zeta_1, \zeta_2)$, and evaluating their corresponding coefficients a_k. The orthogonality of polynomials $\phi_k(\zeta_1, \zeta_2)$ implies that the expected value of their products must be zero [477], i.e. they must satisfy Eq. (5.5).

$$\mathbb{E}(\phi_i \, \phi_j) = \int \phi_i(\varepsilon) \, \phi_j(\varepsilon) \, p(\varepsilon) \, d\varepsilon = 0 \quad \forall \quad i \neq j \tag{5.5}$$

where p is the probability density function for any random variable ε. The coefficients a_k are evaluated using Eq. (5.6)

$$a_k = \frac{\mathbb{E}(\phi_k \, X)}{\mathbb{E}(\phi_k \, \phi_k)} = \frac{\int \phi_k(\varepsilon) \, X(\varepsilon) \, p(\varepsilon) \, d\varepsilon}{\int \phi_k(\varepsilon) \, \phi_k(\varepsilon) \, p(\varepsilon) \, d\varepsilon} \tag{5.6}$$

Remark 14. It is of interest to note that the type of polynomials $\phi_k(\zeta_1, \zeta_2)$ depends on the probability distribution p assumed for the input data ζ_i, e.g. Hermite, Legendre and Laguerre polynomials are used for Normal (Gaussian),

Uniform and Exponential distributions, respectively.

In the methodology established herein, the three macro-strains $\{\varepsilon_{11}, \varepsilon_{22}, \gamma_{12}\}$ are defined as input random variables. As discussed in Sec. 5.3.2, these were initially generated with uniform probability distribution via LHC sampling. However, their probability distribution changes as a result of the data-set expansion procedure described in Sec. 5.3.2. The distribution of this new expanded data-set needs to be identified to chose appropriate orthogonal polynomials for the PCE model. In this work, an open-source library ChaosPy [478] has been used, which integrates a range of different polynomial types and orders into a common Python-based framework, and is a robust numerical tool for performing PCE-based uncertainty quantification. One of the advantages of using ChaosPy is that it automatically picks up the appropriate polynomial-type $\phi_k(x_i, y_i)$ for a given input distribution, evaluates coefficients a_k, and allows straightforward extension to higher-order PCE models.

Using ChaosPy, each macro-stress component $\{\sigma_{11}, \sigma_{22}, \sigma_{12}\}$ is defined as separate PCE-based function of input macro-strains $\{\varepsilon_{11}, \varepsilon_{22}, \gamma_{12}\}$, i.e.

$$\sigma_M(\varepsilon_{11}, \varepsilon_{22}, \gamma_{12}) \approx a_0^M + \sum_{i=1}^{3} a_i^M \, \phi_1(\varepsilon_i) + \sum_{i=1}^{3} \sum_{j=1}^{i} a_{ij}^M \, \phi_2(\varepsilon_i, \varepsilon_j) + ... \tag{5.7}$$

where σ_M represents 3 macro-scale stress components $\{\sigma_{11}, \sigma_{22}, \sigma_{12}\}$. Each of the components σ_M can be fitted with polynomials of different orders depending on their non-linearity and the magnitude of their uncertainty.

5.4.2 Artificial Neural Networks (ANN)

Similar to PCE, Artificial Neural Networks (ANN) can be used as surrogate models to describe the relationship between macro-strains (input) and macro-stress (output) datasets [416]. ANN models are trained using the discrete stress-strain data obtained from meso-scale unit-cell RVE simulations; these are then used to represent complete stress-strain behaviour under any arbitrary mixed-mode loading conditions.

ANN is inspired by biological neural networks that comprise a large number of neurons, which pass information to/from the brain via so-called synapses [479]. Similarly, the ANN architecture consists of hidden layers of artificial neurons that are connected between the input and output data-sets as shown in Fig. 5.10a. Each neuron receives a mixed-set of signals from multiple input links, which are then processed by an activation function and further transmitted to other neurons. The computed values by ANN are propagated between input and output neurons, and the learning of network happens by updating its weights and biases iteratively until the overall error is minimized within a specific tolerance or the maximum number of iterations is reached [416, 480].

The neuron activation functions are crucial components of ANN which determine the network's output, its ability to converge and the convergence speed. The schematic of a neuron along with its activation function is illustrated in Fig. 5.10b. Mathematically, the input-output relationship of an activation function is defined as Eq. (5.8).

$$a^l = \phi\left(\sum_i w_i^l \, a_i^{l-1} + b^l\right) \tag{5.8}$$

where a_i^{l-1} and w_i^l are the i^{th} signal and its corresponding weight, respectively arriving as input to the neuron from the previous layer, b^l is the bias, $\phi(.)$ is the activation function, and a^l is the output transmitted to the next layer. The output of activation functions from each neuron is usually normalized between 0 and 1 or between -1 and 1. Activation functions can be of various types, e.g. sigmoid [481], tanH [482], ReLU [483], Softmax [484], Swish [485], etc. Recently, nonlinear activation functions have been increasingly used in neural networks as they enable learning of much complex data and predict outputs with considerably higher accuracy.

ANN can be classified into various types such as feed-forward, recurrent (Long Short Term Memory) [486, 487], convolutional [488], Kohonen self-organizing [489, 490], radial basis function [491] and Modular neural networks [492, 493]. The most commonly used type in engineering problems is the feed-

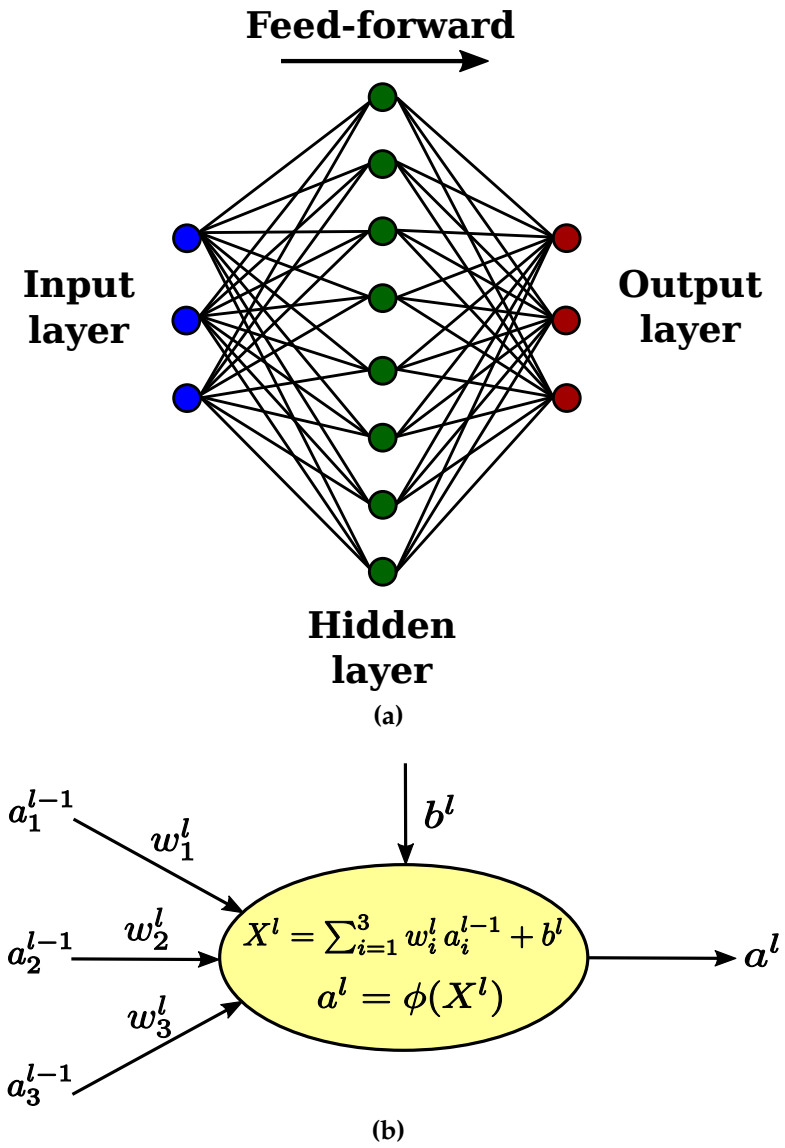

Figure 5.10: (a) Architecture of a feed-forward artificial neural network (ANN) with single-hidden layer (b) Schematic illustration of a neuron in ANN models

forward network which contains 1 input layer, 1 output layer, and a single or multiple hidden layers [416]. In the current work, the neural net fitting tool (*nftool*) available in commercial software MATLAB [29] (Fig. 5.11) has been utilised, which uses a two-layer feed-forward network, with the hidden and output layers governed by sigmoid and linear activation functions, respectively. It is worth emphasizing that more complex deep neural networks could be utilised for better accuracy. However, the choice of MATLAB's *nftool* is primarily driven by the fact that it generates parameters of the trained neural network in the form of simple matrices, that could be easily translated into

Abaqus Fortran subroutine codes later. Moreover, the MATLAB's two-layer feed-forward network provides sufficiently accurate results for the purpose of the current analysis.

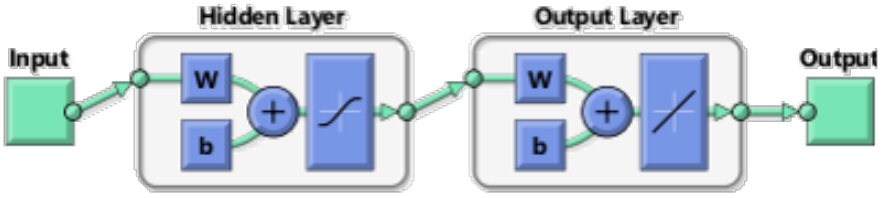

Figure 5.11: Architecture of two-layer feed-forward neural network in MATLAB [29]

Similar to PCE, the input and output data-sets for the ANN model are the macro-strain combinations $\{\varepsilon_{11}, \varepsilon_{22}, \gamma_{12}\}$ and the homogenised macro-scale stresses $\{\sigma_{11}, \sigma_{22}, \sigma_{12}\}$, respectively. These are stored in the RVE database as described in Sec. 5.3.2. The ANN architecture in MATLAB's *nftool* allows for the definition of 1 hidden layer between the input and output layers with multiple neurons. Training is performed for each of the macro-stress components separately, and the model parameters of each trained network is written into a separate text file which can be imported into Abaqus Fortran subroutines.

The training process uses a Bayesian regularization backpropagation function (*trainbr*), which updates the network weights and biases based on the Levenberg-Marquardt (LM) optimization algorithm by minimizing the combination of squared errors and weights. Although *trainbr* requires more time to converge than the standard LM algorithm available in MATLAB, it results in a well-generalized network which has been found to provide better solutions especially for small but noisy data-sets [29].

The input and output data-sets are randomly divided into 3 sets by default, i.e. 70% of total samples are used for training, 15% are used for validation to avoid overfitting, and the remaining 15% are used as independent testing set to generalize the network. The training is performed until the validation error fails to decrease for six consecutive iterations, however for *trainbr*, the training continues until an optimal combination of error/weigths has been found.

The *trainbr* algorithm can be used for any network in which the deriva-

tive functions exist for the network's weight, input and transfer functions. The Bayesian regularization uses Levenberg-Marquadt (LM) algorithm in background and minimizes the linear combination of biases and weights [29]. The network is trained via a supervised learning process with an objective to minimize either the mean (MSE) or sum (SSE) of squared errors [494] shown in Eq. (5.9).

$$e_d = \sum_{i=1}^{n} (t_i - a_i)^2 \tag{5.9}$$

where a_i is the network-predicted output, e_d is the network-error, and t_i is the target output. The MSE/SSE is used as the performance index to produce regularized networks with better generalization and obtain smoother underlying functions. The regularization is added to the objective function as an additional term in the form of sum of squares of network weights (e_w)

$$F = p_1 \, e_d + p_2 \, e_w \tag{5.10}$$

where p_1 and p_2 are network parameters and F is the objective function. When $p_1 >> p_2$, the training reduces the network errors, whereas when $p_2 >> p_1$, the training leads to weight size reduction at the expense of network errors, thereby producing smoother responses [494]. The Jacobian of the network performance with respect to combined network weights and biases is calculated using the backpropagation algorithm, and the parameters are updated such that it results in minimization of the objective function.

It is important to monitor the reduction in network's performance (errors), i.e. overall errors in training, validation and testing data-sets with each iteration to avoid over-fitting of data. Over-fitting can be monitored by checking if the model performs considerably well for the training data, but shows abrupt jumps in the performance (errors) for the validation or testing data-sets. Similarly, error histograms can be assessed to obtain information about the range in which the network errors fall, and indicate the outlier points where the fit is significantly worse than majority of other data points. A network is said to be accurately trained if all network outputs attain equal or very close values to

the target outputs.

Once trained, the network parameters are exported into MATLAB's matrix-only functions, which are then written into external files as tables. These are later imported into a surrogate model within Abaqus Fortran subroutines, to perform macro-scale simulations of the given composite material for which the ANN model has been trained.

5.5 Macro-scale simulations

The PCE and ANN-based surrogate models developed in Sec. 5.4.1 and 5.4.2, respectively are used to obtain an equivalent constitutive law for the macro-scale simulations. The macro-scale simulations are performed using an Abaqus user-material (UMAT) Fortran subroutine in which the strains $\{\varepsilon_{11}, \varepsilon_{22}, \gamma_{12}\}$ at different macro-scale integration points are passed as inputs, and the final homogenised stresses $\{\sigma_{11}, \sigma_{22}, \sigma_{12}\}$ evaluated for these strains using the surrogate model are returned back to Abaqus.

The macro-scale simulation resembles a concurrent FE^2 multiscale approach. However, the computationally inefficient procedure of performing concurrent meso-scale RVE simulations in each iteration is replaced by the surrogate model. The latter has been trained using offline RVE simulations to provide a complete damage response under all possible mixed-mode loading conditions.

To perform a reasonable comparison between the macro and meso-scale results, a virtual RVE is constructed around each Gauss point in the macro-scale mesh. It is important to note that the size of macro-elements should be such that they can accommodate equivalent number of RVEs, without the RVEs at adjacent Gauss-points or neighbouring elements overlapping each other [389]. In accordance with this, the macro-element size is chosen equal to the RVE size when using Abaqus S4R shell elements with reduced integration, whereas it's set equal to roughly 2.5 times the RVE size for S4 shell

elements with full-integration. Furthermore, the material axis system in the macro-element must match with the axis system in which the RVE homogenized stresses are predicted.

In Abaqus UMAT, the material tangent matrix needs to be calculated in addition to macro-stresses. An incorrect definition of the tangent matrix does not affect the final results in Abaqus, however, it must be defined as accurately as possible to obtain optimal convergence rates [178]. In the current formulations, this material tangent matrix DDSDDE (C_{ij}) is defined using a central-difference scheme as shown in Eq. (5.11).

$$C_{ij} = \frac{\sigma_i(\varepsilon_j + \Delta\varepsilon_j) - \sigma_i(\varepsilon_j - \Delta\varepsilon_j)}{2\Delta\varepsilon_j} \tag{5.11}$$

where $\Delta\varepsilon_j$ is a small perturbation in the input macro-strains ε_j and σ_i is the corresponding macro-stress component calculated using the surrogate model, with $i, j \in \{11, 22, 12\}$. Since the surrogate model provides a continuous representation of the discrete stress-strain data obtained from the RVE simulations, the derivative C_{ij} exists and is mathematically consistent.

5.6 Benchmarks

5.6.1 Surrogate model validation

In this section, the accuracy of proposed surrogate model is validated against the high-fidelity phase field simulations. The material considered throughout for validation is Textreme-80gsm woven-fabric reinforced composite. The material properties are shown in Table 4.2. The ply-thickness is 0.08 mm with fibre-orientation as $[0^o/90^o]$ within each ply. The mesh-size and length-scale parameter used for the fine-scale phase field simulations are $h_e = 0.05$ mm and $l_o = 0.3$ mm respectively.

To obtain the meso-scale RVE database, 1000 discrete combinations of macro-strains $\{\varepsilon_{11}, \varepsilon_{22}, \gamma_{12}\}$ are generated using the LHC sampling method.

These are uniformly distributed within the ranges $\varepsilon_{11} \in [-0.1, 0.1]$, $\varepsilon_{22} \in [-0.1, 0.1]$ and $\gamma_{12} \in [-\pi/4, \pi/4]$. Unit cell RVE models of size $1 \times 1\,\mathrm{mm}^2$ are subjected to macro-strain combinations applied as averaged strains with periodic boundary conditions, and the damage evolution at the meso-scale is modelled using the anisotropic cohesive phase field model.

A small time-increment $\Delta t = 1.0e^{-5}$ is chosen for analysis, and the field outputs in each RVE simulation are requested at 50 equidistant time-increments. The RVE database is thus populated with total 50000 data-sets of macro-strains $\{\varepsilon_{11}, \varepsilon_{22}, \gamma_{12}\}$ and homogenized stresses $\{\sigma_{11}, \sigma_{22}, \sigma_{12}\}$ stored as input-output response at each time-increment. This type of data-set expansion does not lead to loss of uniqueness in the input strain samples, as explained in Sec. 5.3.2.

The expansion procedure for a randomly chosen meso-scale simulation is illustrated in Fig. 5.12. The RVE database is used to train the PCE or ANN surrogate model that predicts the macro-stress response for arbitrary combination of macro-strain inputs, and thus represents an equivalent constitutive model at the macro-scale. Three separate surrogate models are fitted for each macro-stress as a function of macro-strain combinations, namely $\sigma_{11}(\varepsilon_{11}, \varepsilon_{22}, \gamma_{12})$, $\sigma_{22}(\varepsilon_{11}, \varepsilon_{22}, \gamma_{12})$ and $\sigma_{12}(\varepsilon_{11}, \varepsilon_{22}, \gamma_{12})$. An R^2 fit value of 90% is used as an indicator to determine if the surrogate models have been sufficiently trained. The detailed training procedures for both PCE and ANN surrogate models are described in Appendix A.6.

5.6.1.1 PCE surrogate

In the case of PCE driven surrogates, the probability distribution of input strains plays an important role in determining the type of orthogonal polynomial functions that must be used to obtain the surrogate model. Due to the data-set expansion illustrated in Fig. 5.12, the final probability distribution of the macro-strains is no longer uniform as initially generated via the LHC. A new distribution emerges as a result of this data-set expansion as shown in Fig. 5.13.

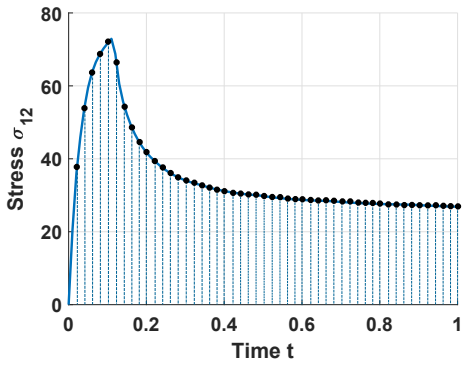

(a)

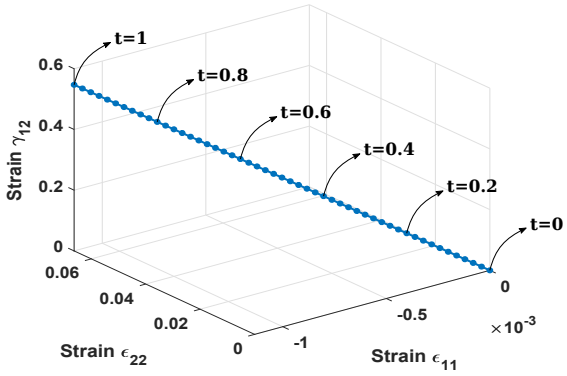

(b)

Time t	Strains $\{\varepsilon_{11}, \varepsilon_{22}, \gamma_{12}\}$	Stress σ_{12} [MPa]
0	{0,0,0}	0
0.02	$\{-2.27e^{-5}, 0.0013, 0.0109\}$	36.009
0.04	$\{-4.54e^{-5}, 0.0026, 0.0219\}$	53.673
0.06	$\{-6.81e^{-5}, 0.0039, 0.0328\}$	63.638
.....	.....	.....
.....	.....	.....
0.98	$\{-0.00111, 0.0650\ 0.5362\}$	26.919
1.0	$\{-0.00113, 0.0663, 0.5471\}$	26.853

(c)

Figure 5.12: Example demonstrating extraction of intermediate stress-strain data from an arbitrary meso-scale RVE simulation to expand the RVE database (a) Extraction of homogenized stress σ_{12} (Shown as black dots) at different intermediate time-increments t (b) Extraction of macro-strain combinations at the same time-increments (c) Sample extracted values for intermediate stresses and strains

To identify the exact type of this new distribution, this is normalised and fitted against the Normal (Gaussian), Laplace and Cauchy probability density functions (PDF) in Fig. 5.14. It can be deduced from the figure that the Laplace PDF fits more closely to this new distribution. Hence, this PDF is chosen to generate the PCE surrogate. The surrogate models for σ_{11}, σ_{22} and σ_{12} are each fitted with a 9^{th} order polynomial using the open-source Python library ChaosPy [478].

The discrete stress-strain responses predicted by the phase field and PCE-surrogate model function for the complete training data-set is shown in Fig. 5.16 and Fig. 5.17. It can be seen from Fig. 5.17 that the PCE surrogate model shows

a reasonable match for sample points away from zero strains. Unfortunately, it poorely fits the region near zero strains, i.e. before the peak stresses are reached. Hence, when the PCE is solely used for the macro-scale simulations, it fails to predict the failure initiation point completely. To circumvent this issue, three additional surrogate models are fitted for the peak (critical) stresses for each failure mode $\{\sigma_{c11}, \sigma_{c22}, \sigma_{c12}\}$ as a function of final macro-strains. The critical stresses are plotted as discrete scattered points in the 3-D space and a convex hull is formed from these points as shown in Fig. 5.15. The convex-hull represents the fracture surface beyond which the failure initiates and evolves in different damage modes.

To use the PCE surrogate model effectively, a pure-elastic and elastic-plastic analysis for the tensile and shear modes respectively, are performed initially. Next, the data point representing the stress-combination $\{\sigma_{11}, \sigma_{22}, \sigma_{12}\}$ at each time-increment is checked against the fracture surface defined by convex-hull. Once the combined stress-state crosses the fracture surface, failure is assumed to have initiated and the post-peak behaviour is henceforth predicted by the PCE surrogate model. Such a strategy helps in obtaining a closer match between the damage response from surrogate and phase field models.

5.6.1.2 ANN surrogate

Next, the response predicted by ANN surrogate model is compared against the meso-scale phase field simulation results. Similar to PCE, the ANN surrogate model is fitted for the RVE database comprising 50000 homogenized stress/strain points obtained from meso-scale simulations. ANN models do not rely on the probability distribution of input dataset and are capable of fitting any type of data, given enough number of training samples are provided. The model is trained using the feed-forward neural network in MATLAB based on Bayesian regularization backpropagation algorithm as explained in Sec. 5.4.2.

The input dataset for the ANN surrogate model comprises the macro-

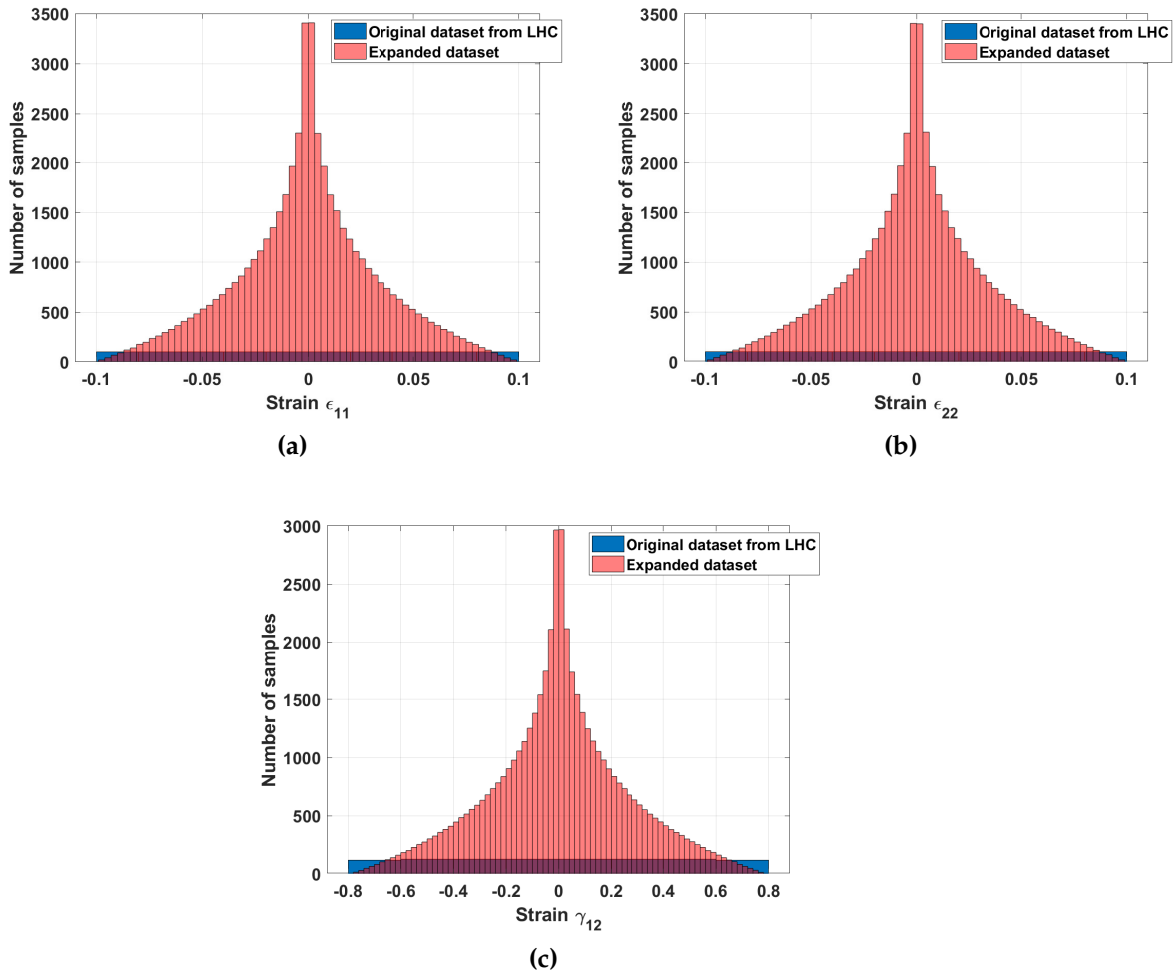

Figure 5.13: Histogram for macro-strains (a) ε_{11} (a) ε_{22} and (a) γ_{12}, showing number of sample points in original dataset generated via LHC and expanded dataset after extraction of intermediate stress-strain points from each meso-scale RVE simulations

scale strains $[\epsilon_{11}, \epsilon_{22}, \gamma_{12}]$, whereas the output dataset is generated with the homogenised macro-scale stresses $[\sigma_{11}, \sigma_{22}, \sigma_{12}]$ obtained from the meso-scale RVE simulations. A single hidden layer, with 80, 80 and 40 neurons respectively, is used to train separate surrogate models for each macro-stress components $\{\sigma_{11}, \sigma_{22}, \sigma_{12}\}$. A symmetric sigmoid activation function as illustrated in Fig. 5.18 is applied for all neurons in the hidden layer. The training is performed on 70% of the total data-set, with remaining 15% each reserved for validation and testing. The complete details of the network architecture are shown in Table 5.1.

The performance or mean-squared error (MSE) is plotted against number

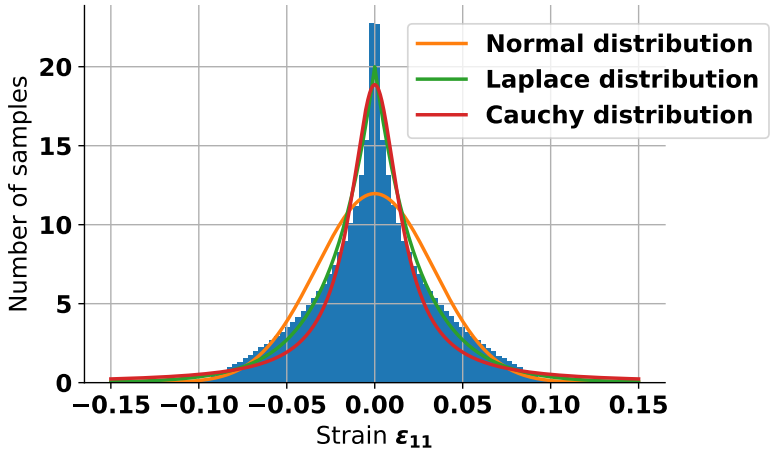

Figure 5.14: Illustration of expanded dataset distribution for macro-strain ε_{11} fitted with (a) Normal probability density function $[\mu = 0, \sigma = 0.0333]$ (b) Laplace probability density function $[\mu = 0, \sigma = 0.025]$ (c) Cauchy probability density function [shift=0, scale=0.0168]

of epochs in Fig. 5.19a, and a histogram depicting number of instances falling within certain error bounds with respect to the zero-error line is shown in Fig. 5.19b. It can be noticed that there are no abrupt jumps in the performance plots for both training and testing data, which indicates that the Bayesian regularization method has successfully prevented over-training of the ANN model. Furthermore, the error histogram in Fig. 5.19b shows that most of the training and test data-sets are close to zero-error line, i.e. the error between their predicted output and the actual output is minimal. The regression plots for training and test data-sets and other training state parameters for ANN are shown in Fig. 5.20a and Fig. 5.20b respectively.

Once the training is complete, the weights, biases, offsets and gains in the trained ANN network are exported to text files, which are later imported into the Abaqus Fortran UMAT to perform macro-scale simulations. The overlapped stress-strain responses from the phase field and ANN surrogate models are shown in Fig. 5.21 and Fig. 5.22 for comparison. It is worth mentioning that the results obtained from ANN are significantly more accurate than PCE, and closely predicts the complete mechanical response in all composite failure modes (Fig. 5.22). As opposed to PCE, ANN does not require ad-hoc techniques to determine the point of failure initiation based on the fracture sur-

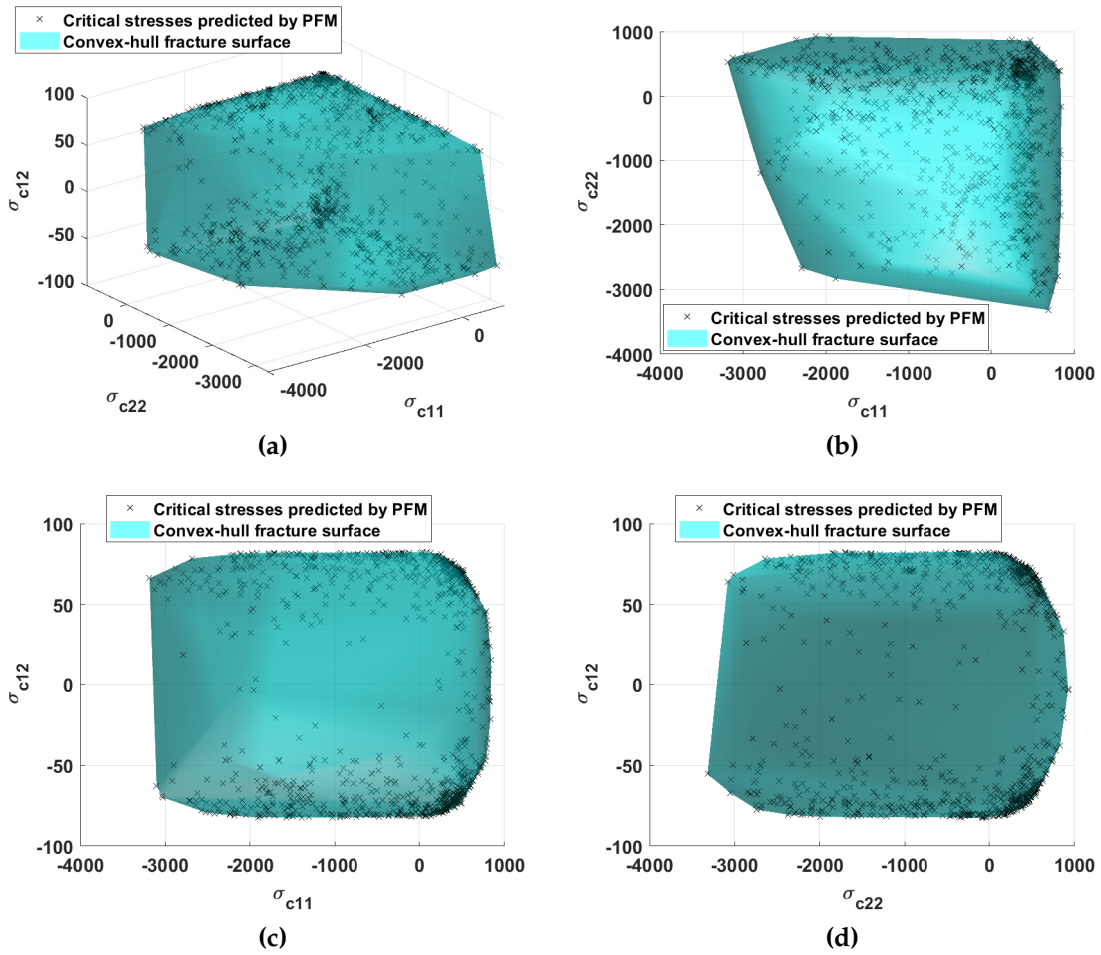

Figure 5.15: (a) Critical stresses $\{\sigma_{c11i}, \sigma_{c22i}, \sigma_{c12i}\}$ predicted by the anisotropic cohesive phase field model for each of i^{th} meso-scale simulation of RVE subjected to i^{th} multi-axial macro-strain combination $\{\varepsilon_{11i}, \varepsilon_{22i}, \gamma_{12i}\}$ and fracture surface represented by convex hull. Sectional cut views are shown as seen along the (b) σ_{c12} axis (c) σ_{c22} axis (d) σ_{c11} axis

face obtained from convex-hull of critical stresses. It accurately captures the complete damage response on its own, including the initial elastic response (elastic-plastic response for shear stress), critical stresses and the post-peak failure behaviour in each mode.

5.6.2 Square plate under mixed-mode loading

The square plate shown in Fig. 5.23 is examined for the purpose of validation of the proposed multiscale numerical procedure. The plate is subjected to arbitrary mixed-mode load combinations with periodic boundary conditions.

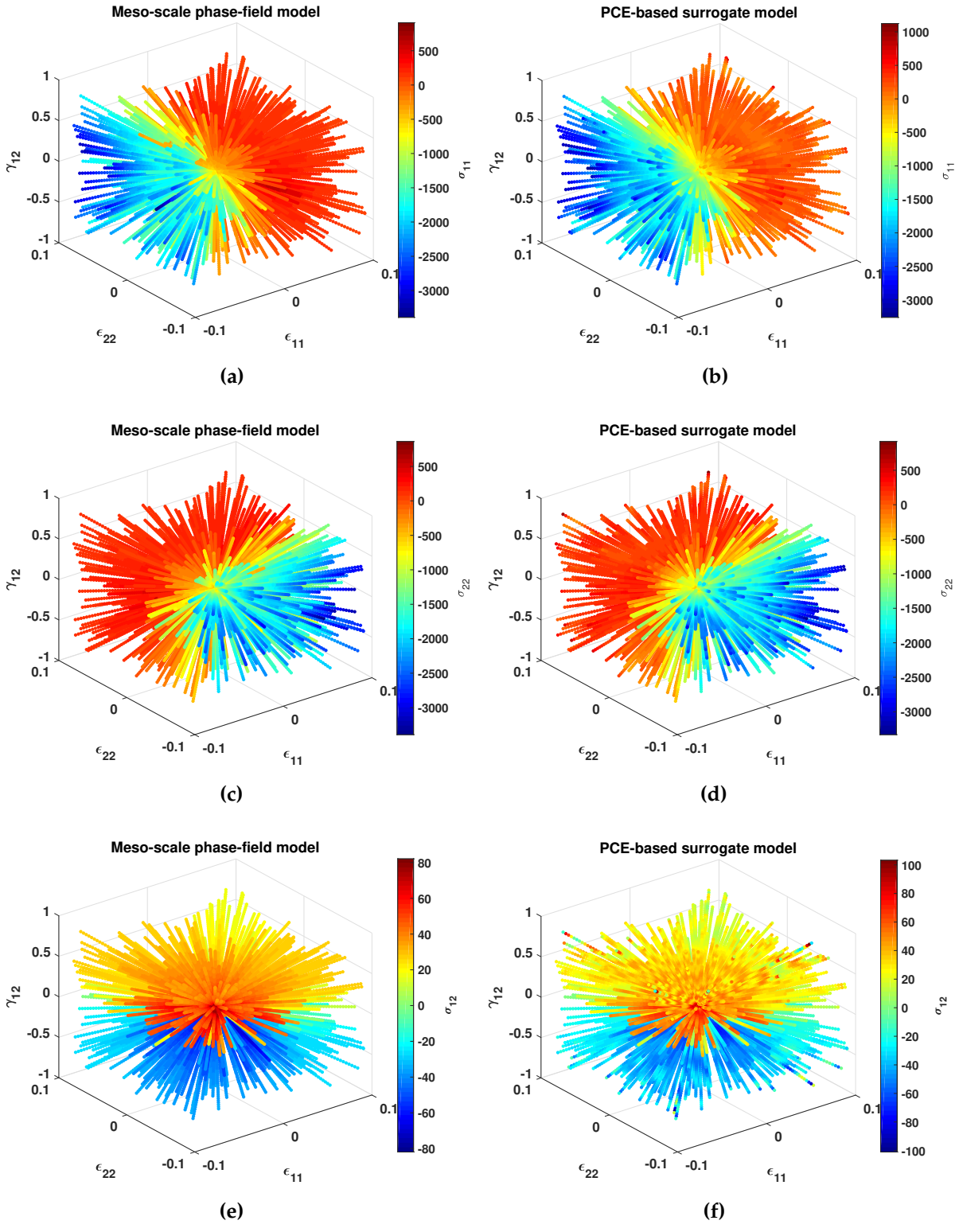

Figure 5.16: PCE-based surrogate model : Macro-stress contours $\{\sigma_{11}, \sigma_{22}, \sigma_{12}\}$ obtained from meso-scale phase field model [(a),(c),(e)] and surrogate model [(b),(d),(f)] plotted as a function of all macro-strains $\{\varepsilon_{11}, \varepsilon_{22}, \gamma_{12}\}$. Surrogate models for σ_{11}, σ_{22} and σ_{12} have been trained with $R^2 = 0.975$, $R^2 = 0.978$ and $R^2 = 0.907$ respectively

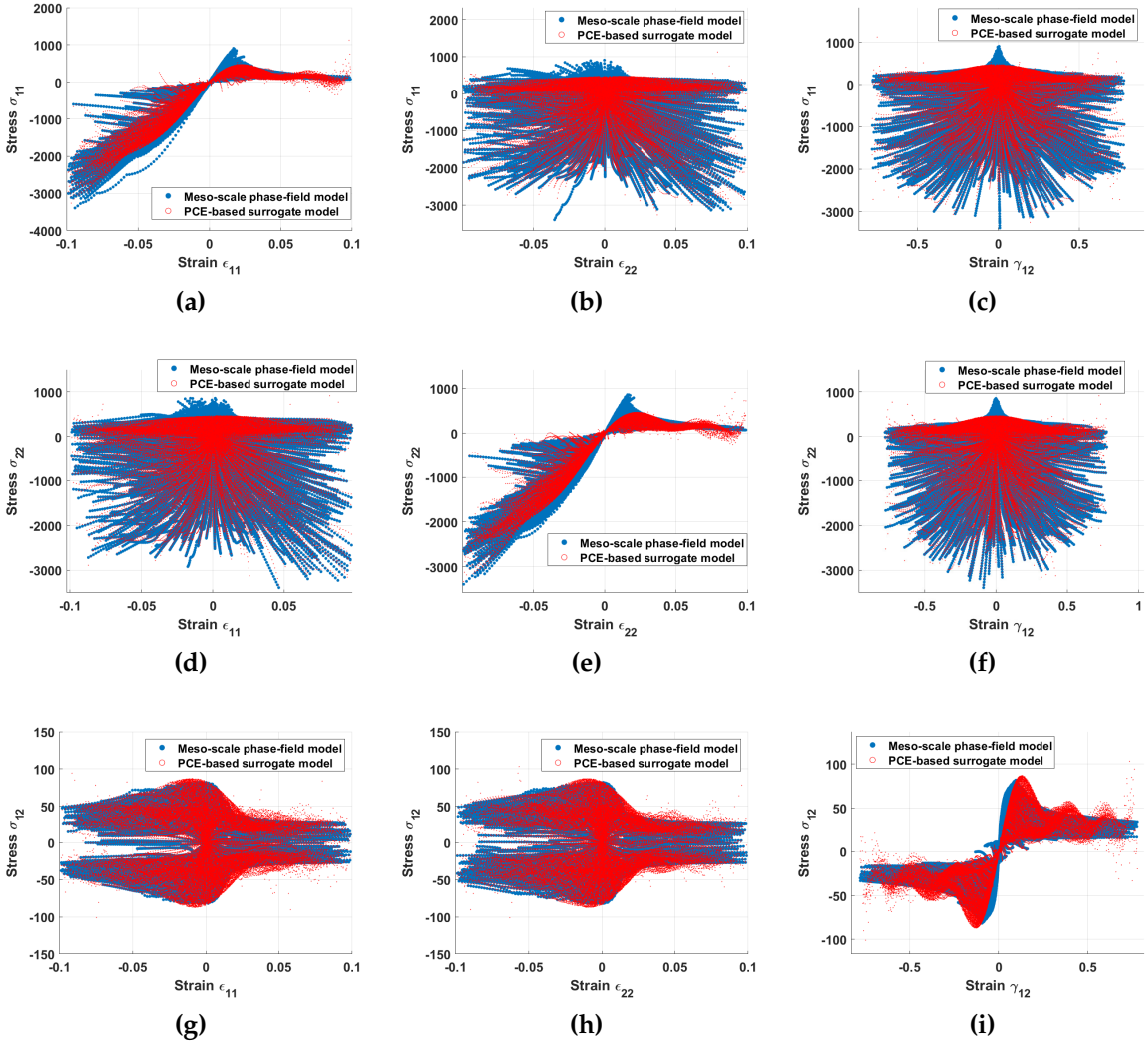

Figure 5.17: PCE-based surrogate model : Macro-stresses σ_{11} [(a)-(c)], σ_{22} [(d)-(f)] and σ_{12} [(g)-(i)] obtained from the meso-scale simulations based on anisotropic cohesive phase field model (shown in blue) and the surrogate model (shown in red), each individually plotted against macro-strain combinations $\{\varepsilon_{11}, \varepsilon_{11}, \gamma_{12}\}$ from training dataset

To achieve a valid and reliable comparison, the loading combinations considered for this example are chosen randomly. Particular care is taken for these combinations to be different from those included in the RVE database, which were used to train the surrogate models. For the phase field model, a fine mesh-discretization with full-integration S4 shell elements of size $h_e = 0.05$ mm and length-scale $l_o = 0.3$ mm is used, and the analysis is performed with a small time-increment $\Delta t = 5.0e^{-5}$.

The PCE and ANN surrogate model simulations are performed using

Input layer	Total hidden layers	Hidden layer neurons	Output layer	Loss function	Training algorithm
$[\epsilon_{11}, \epsilon_{22}, \gamma_{12}]$	1	80× sigmoid	σ_{11}	MSE	Bayesian regularisation backpropagation
$[\epsilon_{11}, \epsilon_{22}, \gamma_{12}]$	1	80× sigmoid	σ_{22}	MSE	Bayesian regularisation backpropagation
$[\epsilon_{11}, \epsilon_{22}, \gamma_{12}]$	1	40× sigmoid	σ_{12}	MSE	Bayesian regularisation backpropagation

Table 5.1: Architecture of separate feed-forward ANN surrogate models trained for each macro-scale stress components σ_{11}, σ_{22} and σ_{12}

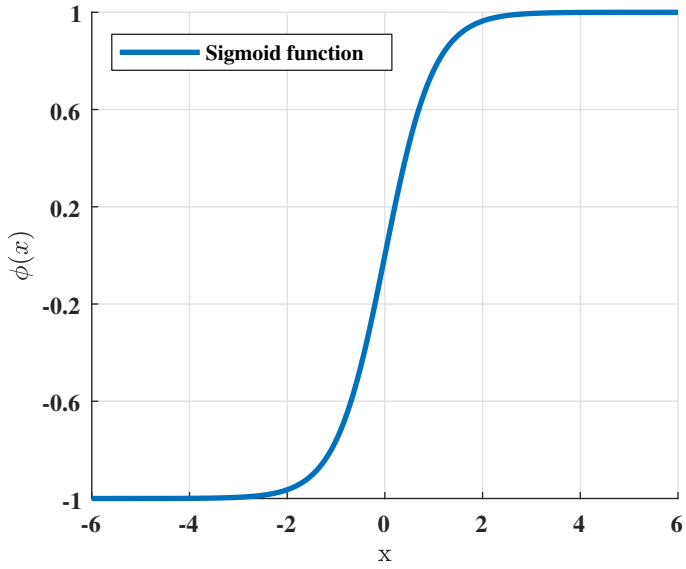

Figure 5.18: Illustration of symmetric sigmoid activation function $\phi(x) = [2/(1 + \exp(-2x)) - 1]$ used for hidden layer neurons in the ANN surrogate model

a very coarse mesh-discretization containing only 4 reduced-integration S4R shell elements with size $h_e = 1$ mm, and the time-increment size is chosen as $\Delta t = 1.0e^{-2}$. The finite element mesh used for the phase field and surrogate models is illustrated in Fig. 5.24a and Fig. 5.24b, respectively.

The force-displacement plots for different failure modes obtained using phase field model, and PCE and ANN surrogate models are shown in Fig. 5.25. The response from the ANN model matches reasonably well with the phase field results. However for the PCE model, it can be seen that an additional

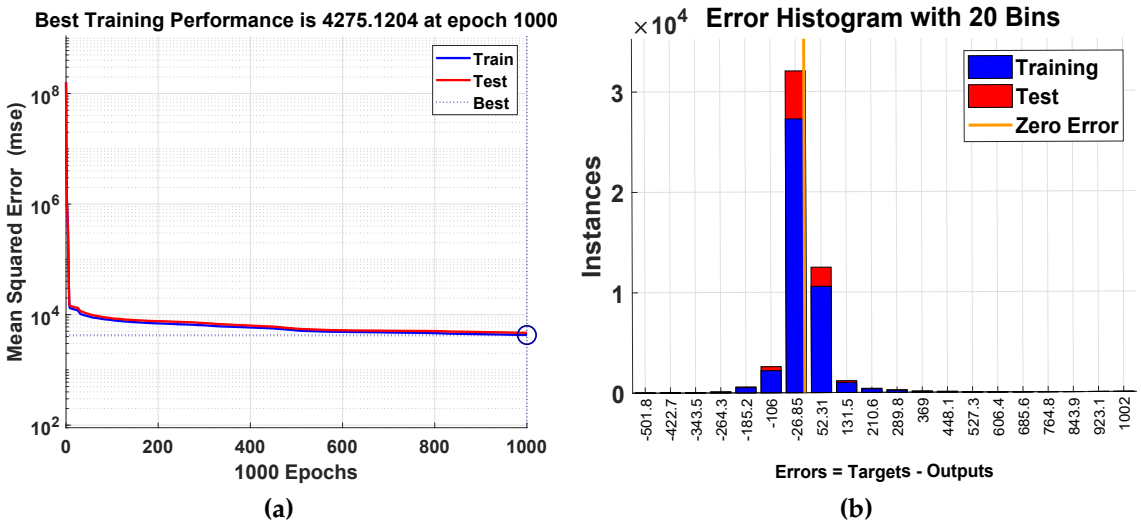

Figure 5.19: (a) Training performance plot showing reduction of mean-squared error with increasing number of epochs for training and test data-sets in ANN surrogate model for macro-stress σ_{11} (b) Error Histogram plot showing number of instances falling within different error-bounds from zero-error line

criteria based on convex-hull of critical stresses is required to determine failure initiation point, otherwise it's accuracy is significantly compromised, especially for the pre-damage initiation response. The time taken by fine-scale phase field model is approximately 3 hours using a single thread, whereas both PCE and ANN surrogate model simulations complete in less than a minute.

5.6.3 Double-edge notched tension test (DENT)

To perform a realistic comparison of the proposed surrogate modelling approach against the phase field method, a double-edge notched tension (DENT) test as shown in Fig. 5.26 is analysed in this section. The example is similar to the DENT test previously simulated in Sec. 4.10.3.

The material properties of Textreme-80gsm is obtained from Table 4.2, and the fibre-orientations are $[0^o/90^o]$. The specimen is clamped at the left edge and a displacement load is applied on the right edge until failure. The mesh used for phase field model comprises full-integration S4 shell elements refined with $h_e = 0.1$ mm in the central-strip surrounding the notch-tips (Fig. 5.27a). For the surrogate models, reduced-integration S4R shell elements with size $h_e = 1$

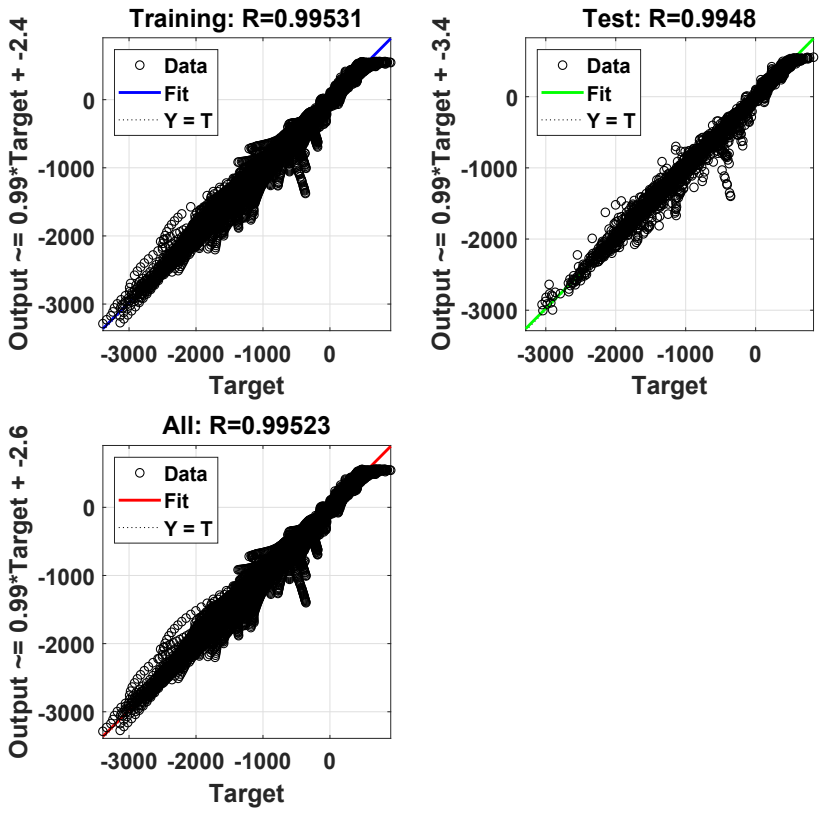

(a)

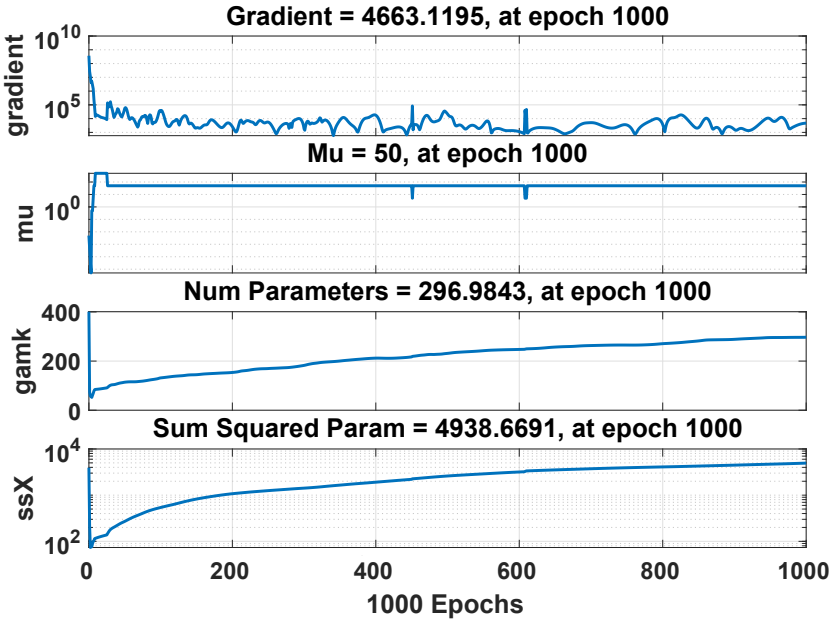

(b)

Figure 5.20: (a) Regression plot and (b) variation of training state parameters over number of epochs for ANN-based surrogate model for macro-stress σ_{11}

mm are used near the notch-tips, in accordance with the RVE size of $1 \times 1\,\text{mm}^2$ used for meso-scale simulations (Fig. 5.27b).

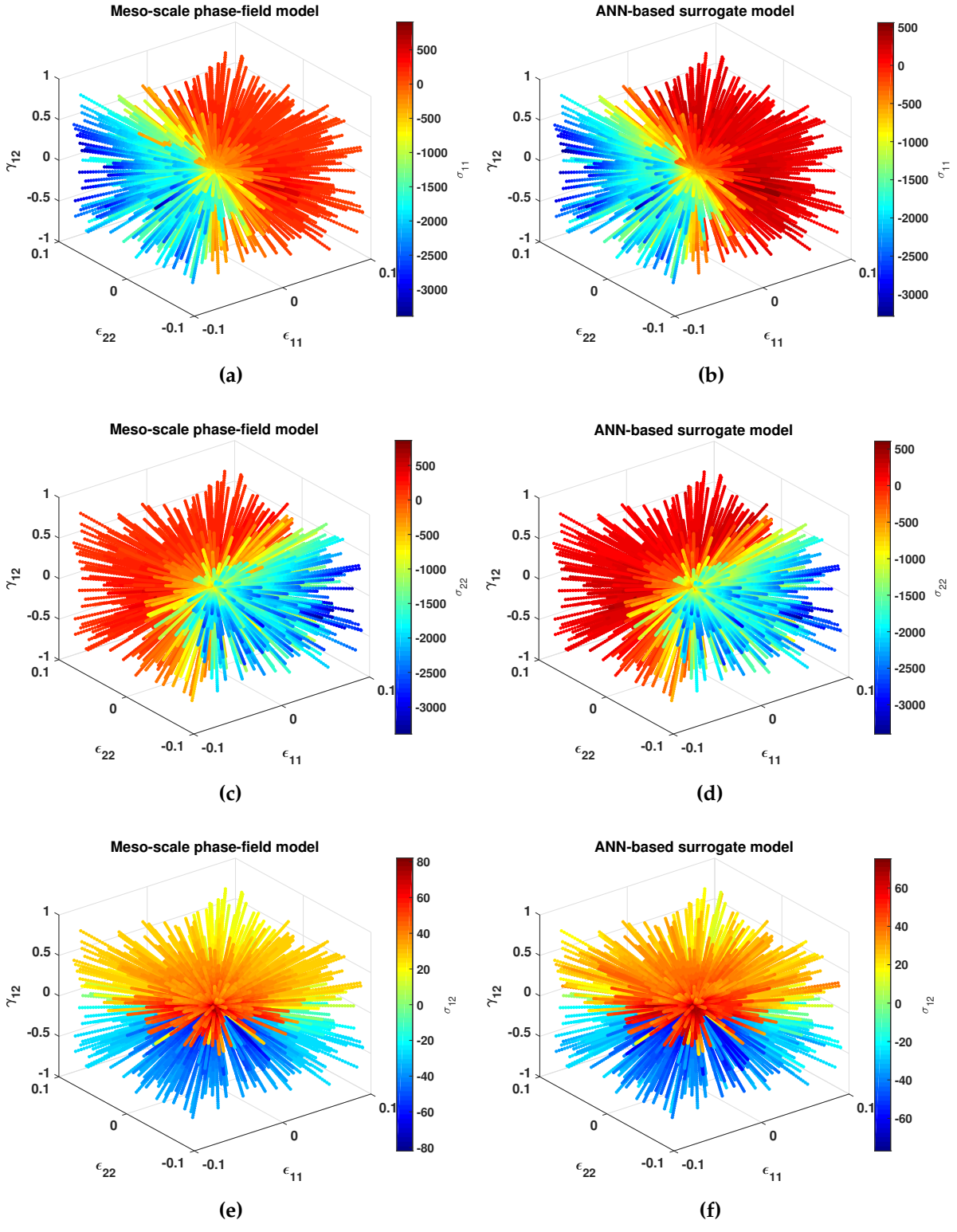

Figure 5.21: ANN-based surrogate model : Macro-stress contours $\{\sigma_{11}, \sigma_{22}, \sigma_{12}\}$ obtained from meso-scale phase field model [(a),(c),(e)] and surrogate model [(b),(d),(f)] plotted as a function of all macro-strains $\{\varepsilon_{11}, \varepsilon_{22}, \gamma_{12}\}$. Surrogate models for σ_{11}, σ_{22} and σ_{12} have been trained with $R^2 = 0.9905$, $R^2 = 0.9924$ and $R^2 = 0.9903$ respectively

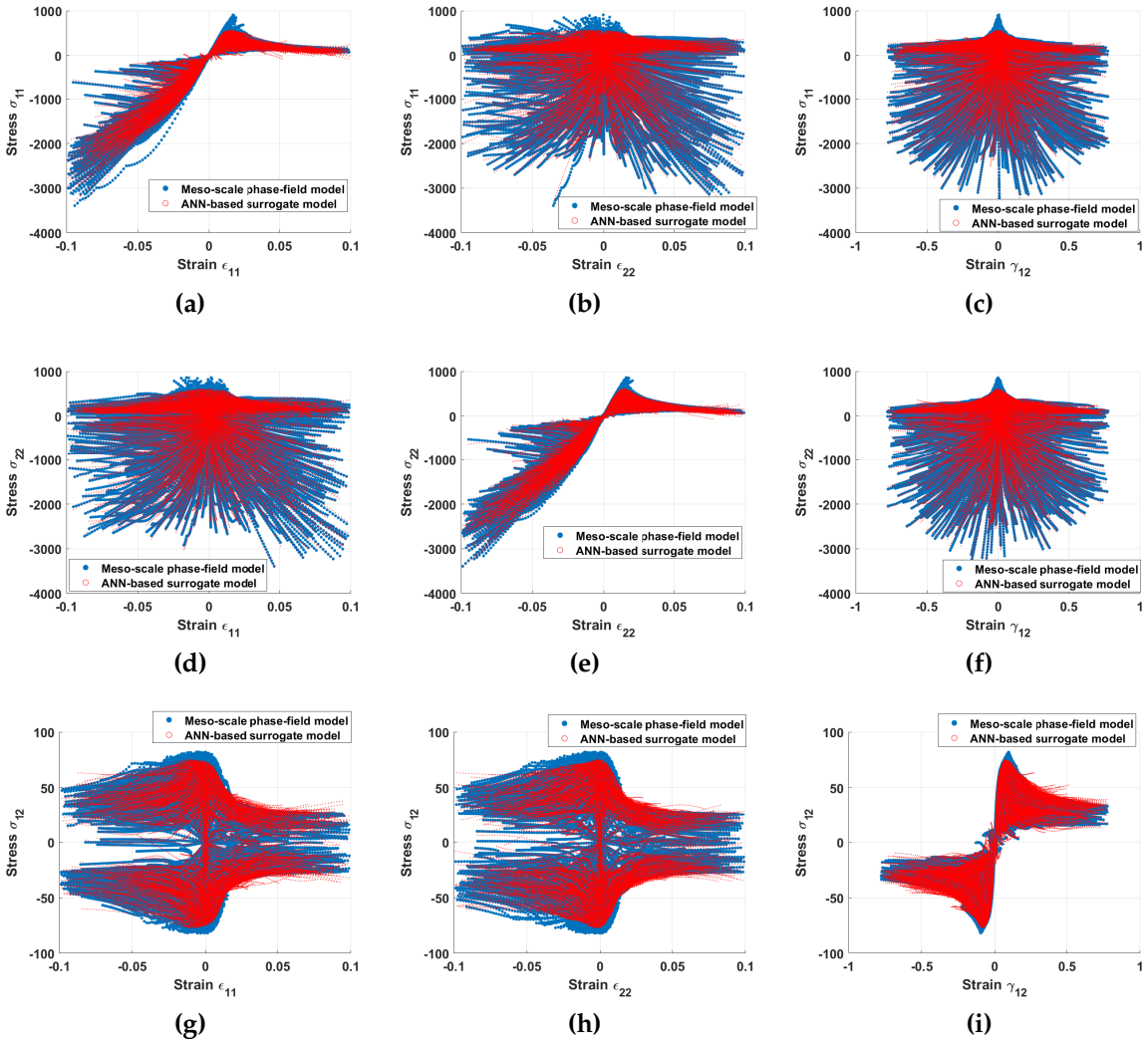

Figure 5.22: ANN-based surrogate model : Macro-stresses σ_{11} [(a)-(c)], σ_{22} [(d)-(f)] and σ_{12} [(g)-(i)] obtained from the meso-scale simulations based on anisotropic cohesive phase field model (shown in blue) and the surrogate model (shown in red), each individually plotted against macro-strain combinations $\{\varepsilon_{11}, \varepsilon_{11}, \gamma_{12}\}$ from training dataset

The mesh in regions 2 mm away in the horizontal direction from the notch-tip contain coarse full-integration S4 elements, thus resulting in total 14151 and 2203 elements for phase field and surrogate models respectively. The ANN surrogate model is triggered right from the start of the simulation, and is used to predict the stresses at each integration point for which the UMAT is called. The force-displacement plot from the phase field model is compared against the ANN surrogate model in Fig. 5.28. The failure behaviour predicted by the ANN surrogate model agrees well with that of physics-based phase field model, both in terms of critical stress (relative error 2.36%) and post-peak frac-

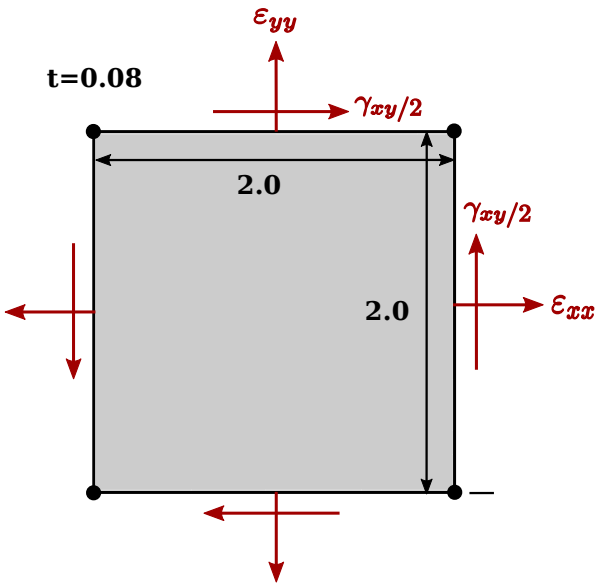

Figure 5.23: Schematic illustration of geometry and boundary conditions for the macro-scale square-plate example subjected to averaged strains applied with periodic boundary conditions. All dimensions in mm

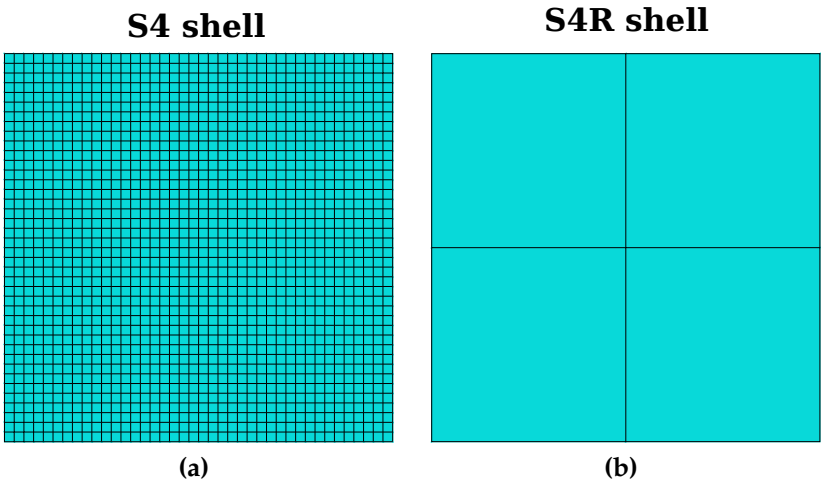

Figure 5.24: Square plate example : Mesh discretization with (a) full-integration S4 shell elements with size $h_e = 0.05$ mm used for the phase field model and (b) reduced-integration S4R shell elements with size $h_e = 1$ mm used for PCE and ANN surrogate models

ture response. The PCE model, however, was unable to capture the drastic reduction of stresses post-damage initiation, and failed to converge as soon as it was triggered once the critical stresses were reached. The total simulation time taken by the high-fidelity phase field and ANN surrogate models using 6 parallel threads is 17.82 and 2.25 hours respectively; hence, the surrogate model is 7.9 times faster than the phase field model and results in significantly

improved computational efficiency.

5.6.4 Open-hole tension test (OHT)

To further validate the prediction accuracy of proposed model, an open-hole tension test is performed. The geometry, boundary conditions and the mesh used for phase field and surrogate models are illustrated in Fig. 5.29 and Fig. 5.30. The material properties for Textreme-80gsm is obtained from Table 4.2, and the fibre-orientations are $[0^o/90^o]$. The open-hole model has lower stress concentrations at the ends of its hole, as compared to the notch-tips in DENT specimen. This enables better comparison of the surrogate and phase field models as the stresses causing damage initiation are highly non-singular unlike DENT test. The model has been analysed previously in Sec. 4.10.4, wherein the damage initiated at opposite ends of the hole, and propagated horizontally towards the specimen edges.

The mesh is refined with fully-integrated S4 shell elements of sizes $h_e = 0.05$ mm for the phase field simulation and $h_e = 2.5$ mm for the simulation using surrogate models, thus resulting in total 23642 and 260 elements respectively. The macro-element size of $h_e = 2.5$ mm for the surrogate model roughly accommodates 4 RVE elements of size $1 \times 1\,\text{mm}^2$ centred at the 4 Gauss points of the S4 shell element. The comparison of force-displacement plots for ANN and phase field model is shown in Fig. 5.31; the relative error in the predicted critical fracture loads is $\sim 6.95\%$. It can be noticed from Fig. 5.22a and Fig. 5.22e that the critical stresses are slightly under-predicted by the ANN surrogate model as compared to the phase field model, which leads to such differences in the predicted peak loads in Fig. 5.31. The prediction accuracy of the surrogate model could be further improved by employing more advanced (recurrent/convolutional) neural networks and deep-learning libraries. The PCE surrogate model failed to converge again for the current analysis. This demonstrates that the surrogate model obtained using ANN is significantly superior than the one with PCE, wherein PCE has been found

inappropriate to predict such highly nonlinear fracture behaviour as displayed by these examples. The high-fidelity phase field model takes approximately 8.5 hours, whereas the surrogate model takes less than 10 minutes to complete using 6 parallel threads, thus making the latter approximately 51 times faster than the former. As compared to DENT example in previous Sec. 5.6.3, a significant increase of computational efficiency is observed in this case due to smoother convergence and much lesser number of elements used for the surrogate model.

5.7 Concluding Remarks

A novel multiscale surrogate modelling technique is presented in this chapter to perform fast and efficient damage simulations at the macro-scale of composites, whilst simultaneously incorporating the complex physics of damage at the meso-scale. Damage modelling approaches, especially the phase field method, are known to be computationally expensive vis-à-vis capturing complex intra-laminar fracture modes in composites. Furthermore, it poses challenges in analysing failure behaviour in larger industrial composite structures, due to the requirements of highly refined mesh and smaller time-increment size for accurate resolution of damage. The proposed two-scale multiscale approach attempts to alleviate such high computational costs associated with the damage modelling of large macro-scale composite structures and bridge the gap between different inherent scales of composites.

The current approach considers the FE^2 multiscale method as the point of departure, and replaces the computationally expensive step of solving meso-scale RVE models at each time-increment, by a surrogate model that provides an equivalent constitutive response at the macro-scale. The surrogate model is trained offline using set of meso-scale simulations comprising unit-cell RVE models, which are solved under periodic boundary conditions with averaged macro-strains applied on their boundaries. The intra-laminar damage modelling at the meso-scale is performed using the anisotropic cohesive phase field

model, and the homogenized stress-strain responses involving damage in each mode are extracted from each meso-scale simulation.

These stress-strain responses contain information about the meso-scale failure behaviour of composite when subjected to a specific mixed-mode loading condition. Multiple meso-scale simulations are performed with varying load-combinations, and a database is populated with macro-strains and macro-stresses as input and output data respectively, on which the surrogate model is trained.

Two different surrogate modelling strategies, namely the Polynomial Chaos Expansion (PCE) and Artificial Neural Networks (ANN) have been examined. It is observed that PCE, which has been shown to be effective for performing linear elastic analysis of multi-layup composites in the literature, performs poorly in predicting the highly nonlinear damage behaviour associated with different composite modes and faces severe convergence issues during macro-scale simulations.

On the contrary, ANN displayed excellent capabilities in predicting accurate macro-scale response even with a simplistic single hidden-layer model. More complex neural networks may be employed to enhance the surrogate model accuracy, however, translating them later to Fortran code to work with Abaqus UMAT subroutine becomes an arduous and challenging task. Once the surrogate model has been trained for a particular composite material, it is capable of reproducing accurate damage behaviour in all failure modes of that material, whilst using a very coarse mesh and larger time-increment size, thus rendering it ideal for macro-scale analysis.

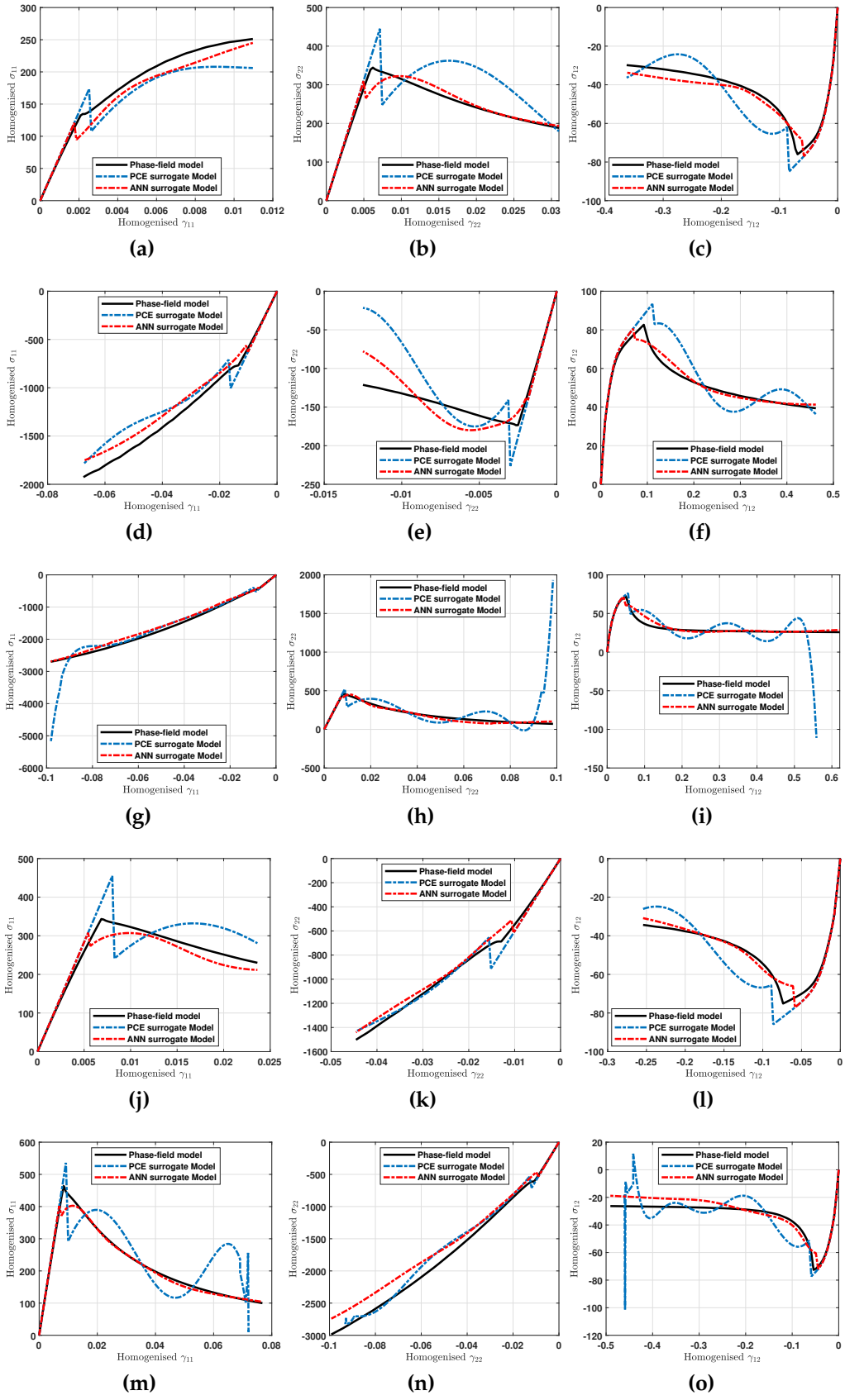

Figure 5.25: Comparison of load-displacement curves obtained from phase field model, and PCE and ANN based surrogate models for random macro-strain combinations from outside of training database

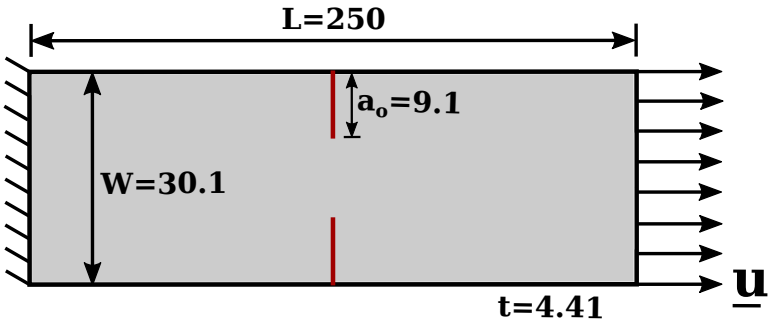

Figure 5.26: Schematic illustration of geometry and boundary conditions for the macro-scale double-edge notched tension (DENT) example on Textreme-80gsm woven fabric-reinforced composite. All dimensions in mm

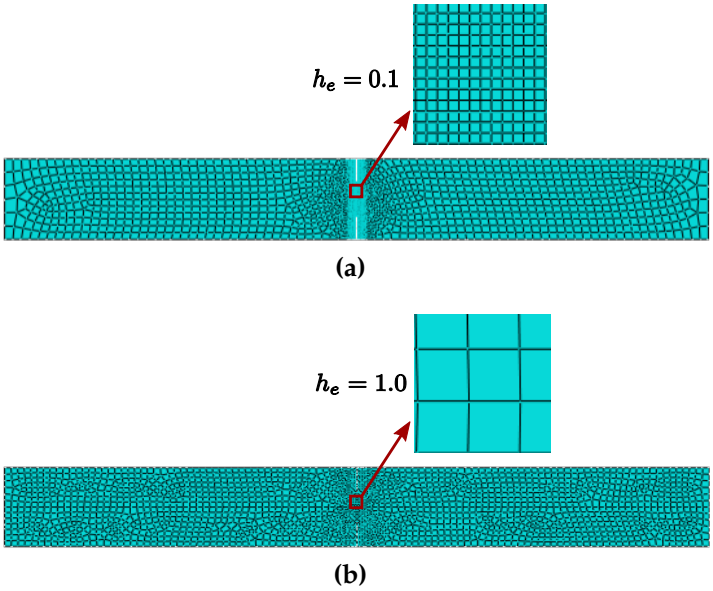

Figure 5.27: Double-edge notched tension (DENT) test : Mesh discretization with (a) full-integration S4 shell elements with size $h_e = 0.1$ mm used for the phase field model and (b) reduced-integration S4R shell elements with size $h_e = 1$ mm used for PCE and ANN surrogate models

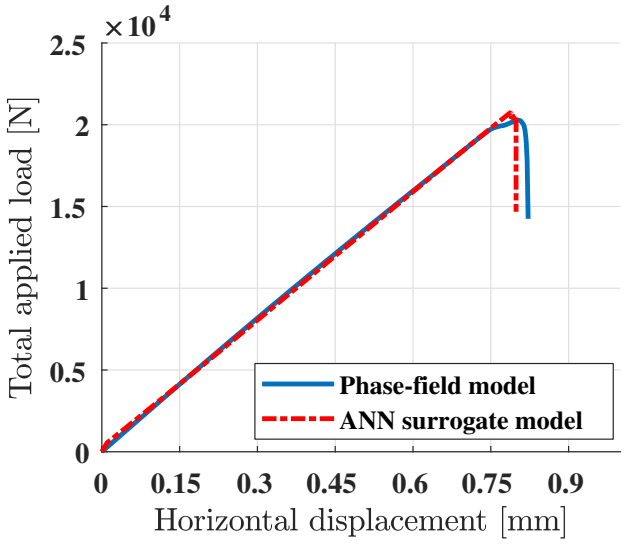

Figure 5.28: Double-edge notched tension (DENT) test on Textreme-80gsm : Comparison of load-displacement curves obtained from the phase field model and ANN surrogate model

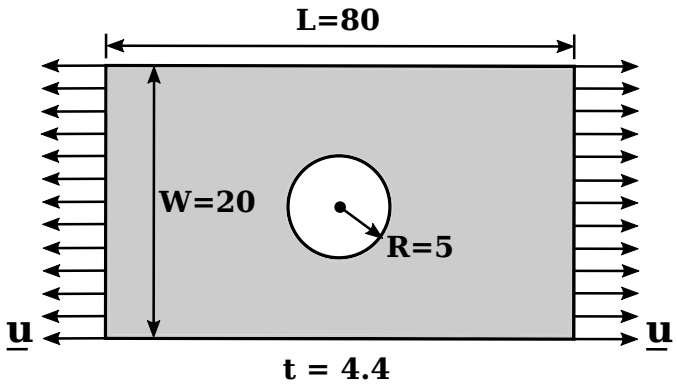

Figure 5.29: Schematic illustration of geometry and boundary conditions for the macro-scale open-hole tension (OHT) example on Textreme-80gsm woven fabric-reinforced composite. All dimensions in mm

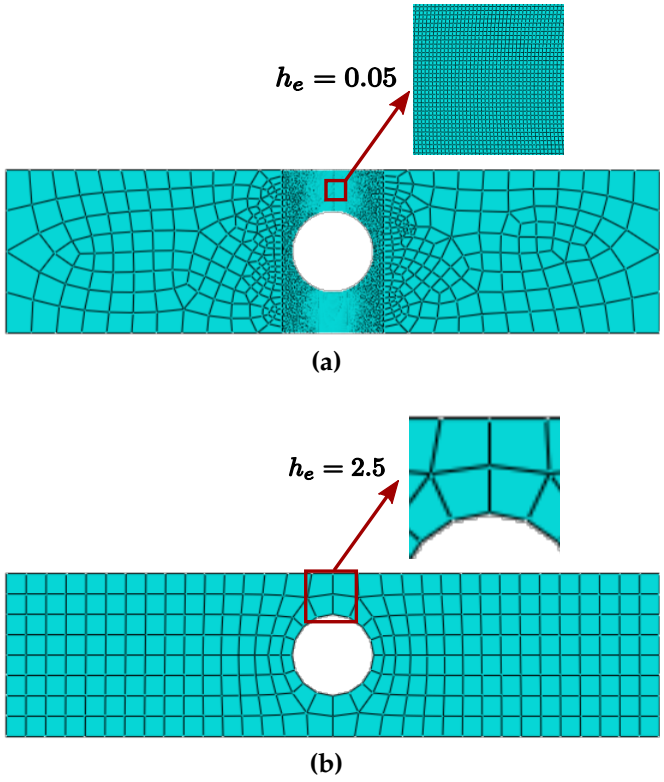

Figure 5.30: Open-hole test : Mesh discretization with (a) full-integration S4 shell elements for both (a) phase field with size $h_e = 0.05$ mm, and (b) PCE and ANN surrogate models with size $h_e = 2.5$ mm

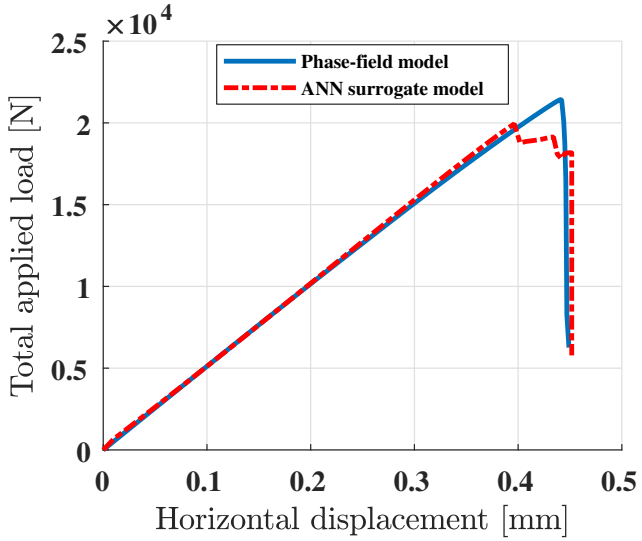

Figure 5.31: Open-hole tension (OHT) test on Textreme-80gsm : Comparison of load-displacement curves obtained from the phase field model and ANN surrogate model

6

Conclusions and future work

6.1 Conclusions

In this PhD thesis, a phase field model to simulate brittle fracture in curved thin-shell plies subjected to coupled in-plane (membrane) and out-of-plane (bending) deformations is proposed using MITC4+ Reissner-Mindlin shell elements. The assumed strain MITC4+ approach successfully alleviates the transverse shear and membrane locking effects that are typically observed in thin shell-like structures.

A novel through-the-thickness crack driving force rule for damage initiation is defined, which accurately simulates the fracture behaviour in bending dominated scenarios. Numerical examples with flat and curved shell geometries that display significant membrane and transverse shear locking are analysed. The results are compared against analytical estimates for both isotropic and anisotropic phase field formulations with spectral decomposition.

Within this context, this research highlights the advantages of using phase field enhanced shell elements in efficiently simulating crack propagation over curved surfaces. The proposed approach provides a robust locking-free alternative to obtain accurate damage predictions in thin-shell plies at significantly lower computational cost compared to traditional 3-D hexahedral finite elements.

Furthermore, a novel damage modelling framework to simulate diverse failure modes in thin-ply spread-tow composite laminates is presented. The anisotropic intra-laminar damage mechanisms, e.g. fibre-fracture, fibre pull-outs, fibre bridging, plastic deformation of matrix and its cracking under tensile/shear loads are analysed for both spread-tow unidirectional and fabric-reinforced composites. Since the crack paths in intra-laminar damage are a-priori unknown, a 3-parameter anisotropic cohesive phase field model that naturally simulates complex curvillinear crack paths is implemented.

The model effectively captures the quasi-brittle fracture behaviour that is displayed by spread-tow composites due to the formation of fracture process zone due to fibre-pullout and bridging effects. Damage evolution is modelled using a single phase field variable, however, anisotropy is accounted in both material as well as fracture behaviour by introducing mode-specific crack-driving force and stress-degradation terms. These depend on elastic and fracture properties, e.g. critical stresses and energy release rates specific to each composite failure mode, and helps delaying, or in some cases, completely avoiding the pre-mature degradation of induced stresses in all modes simultaneously.

The three parameters in the cohesive phase field model control the initial, final and intermediate shape of the post-peak cohesive softening curve accurately. A strategy is provided to calibrate these parameters with experimental softening curves corresponding to different failure modes. Extensive experimental validations are performed with the proposed model for spread-tow woven fabric (carbon-reinforced and glass-reinforced) and quasi-unidirectional flax-ply composites. The model parameters are calibrated using one set of experiments, which are then used to accurately reproduce the complete fracture response including crack paths, load-deflection response and laminate strengths from another set of experiments. The length-scale independence of the predicted critical fracture stresses is demonstrated.

A dynamic explicit cohesive phase field model is proposed, which is combined with the Cohesive Zone Method (CZM) to model delamination, thus

extending it for full-laminate analyses and providing a generalised framework for treating both intra-laminar and inter-laminar fractures. Further extension of the proposed framework for simulating 3-D fracture in thick-ply composites is feasible provided the complex physics of through the thickness damage interactions are properly accounted for, e.g., transverse matrix shear cracks and/or the triggering of delamination. Although in this case the definition of the corresponding crack-driving forces and the corresponding degradation functions would become more involved, no additional complexity would arise from an implementational and computational standpoint.

This research demonstrates that the anisotropic cohesive phase field model effectively simulates the complex quasi-brittle fracture behaviour in composites, and accurately predicts both crack paths and critical stresses in different failure modes. This plays an important role during intra-laminar fracture, wherein the crack paths are unknown a-priori and the crack evolves due to diverse and mutually interacting fibre and matrix based failures. Furthermore, once the cohesive parameters are calibrated, the proposed model accurately and consistently reproduces the experimental fracture response under different loading conditions.

To perform fast and efficient simulation of damage evolution at different inherent scales in composites, a multiscale approach based on surrogate models is proposed. The approach considers FE^2 multiscale method as its foundation, however the computationally expensive procedure of solving a meso-scale RVE model at each time-increment is replaced by an efficient surrogate model. High-fidelity meso-scale simulations are performed on RVE subjected to multi-axial loads during an offline phase. Different macro-strains combinations generated via Latin Hyper Cube method are applied on RVE using periodic boundary conditions, and damage is modelled using the proposed anisotropic cohesive phase field model. To demonstrate the robustness of high-fidelity phase field model, the meso-scale fracture response for the pure-tensile and pure-shear modes are compared against the experimental laminate strengths.

An RVE database containing homogenized stress-strain responses corresponding to different composite failure modes from all meso-scale simulations is eventually populated. The database is used to train ANN and PCE based surrogate models, which provide an equivalent constitutive law at each Gauss point during macro-scale simulations. Macro-scale simulations using surrogate model are performed using a substantially coarser mesh, and the results are compared against high-fidelity phase field simulations performed with finer mesh.

In the presented preliminary study, surrogate models have displayed a promising behaviour in performing complex composite damage simulations at significantly lower computational cost than the current state-of-the-art damage modelling approaches, whilst predicting reasonably accurate failure behaviour. The current study highlights the merits of using surrogate models as an effective multiscale modelling technique to enable fast progressive damage analysis of large industrial composite structures.

6.2 Limitations

6.2.1 Shell Elements for fracture mechanics

The proposed MITC4+ shell element based phase field method captures complete shell-kinematics by accounting for all 6 (translational and rotational) degrees of freedom (DOFs). For modelling of thin-plies, shell elements based on rotational DOFs provide advantages over continuum shell elements with regards to stability and computational efficiency. However, extension of such elements for thick-ply composite laminate analysis requires accurate assessment of ply separation displacement at the interface to model inter-laminar failure (delamination). In composites with thick adhesive layers at ply interfaces, cohesive elements with finite thickness are often used to model delamination. In such case, the proposed method must be extended by coupling the MITC4+ Mindlin shell and cohesive elements at the interface, and defining multi-point

constraints linking their respective degrees of freedom. Whereas the proposed model highlights the capabilities of brittle fracture phase field modelling to harness the advantages of MITC4+ formulations, research should be directed towards realistic and accurate predictions of fracture behaviour in aerospace composites, e.g. during complex high-energy impact scenarios.

Furthermore, the extension of proposed anisotropic cohesive phase field model for the case of thick-ply composites is non-trivial. One of the prominent failure modes that occur in thick-ply composites is the transverse shear cracking of matrix which further evolves to cause delamination. The treatment of such complex anisotropic 3-D fracture requires accurate modelling of through-the-thickness crack propagation in composite plies, and strong coupling between intra-laminar and inter-laminar failure modes.

6.2.2 Surrogate modelling for fracture mechanics

Although the proposed multiscale surrogate model has been validated against a set of benchmarks, there are many limitations which could be addressed as future work. First, since the surrogate model has been trained on a discrete discontinuous data, obtaining accurate tangent stiffness matrix to ensure smooth convergence in implicit Abaqus/Standard analysis becomes a challenging task. To circumvent this, the existing neural network could be trained with more data-points or more complex ANN models could be employed to avoid overtraining and obtain smooth variation of material tangent operator. In addition, the macro-scale simulations could be performed with Abaqus/Explicit, at the cost of using smaller stable time-increment size.

Second, in the current study, only intra-laminar damage with fibre/matrix failures has been analysed at the meso-scale using a single-ply model. To incorporate the true meso-scale composite failure behaviour in the macro-scale simulations, more complex RVE models that also account for inter-laminar (delamination) damage between multiple stacked shell plies could be considered.

In such case, the macro-strain combination applied on the RVE must

also consider transverse shear strains to trigger delamination, which could be modelled with the widespread cohesive zone method (CZM). The macro-scale model, however, would be similar to the coarse-meshed single shell layer model used in the current analysis. Third, a mesh-convergence study could be performed for the macro-scale models, to verify the consistency of predictions from the surrogate model.

6.3 Future work

To extend and improve the work presented in this thesis, following research directions could be pursued:

- The brittle phase field model using MITC4+ shell elements presented in Chapter 3 accounts for intra-laminar damage in both flat and curved shell geometries under combined membrane and bending deformations. This could be employed in full composite laminate analysis by coupling the DOFs of MITC4+ and cohesive element layers at the interface to model delamination. The framework could be subsequently used to simulate realistic impact-driven damage scenarios on aerospace composite structures.

- The MITC4+ based phase field model simulates brittle fracture assuming small-strain deformations. The proposed approach could be enhanced to model more complex fracture problems, e.g. ductile and fatigue damage evolution under finite-strain deformations.

- The anisotropic cohesive phase field model in Chapter 4 captures the complex quasi-brittle fracture modes in spread-tow composites, e.g. fibre-based failures (fibre fracture, bridging and pullouts) under in-plane tension, and matrix-based failures under in-plane tension and in-plane shear modes. Since spread-tow composites comprise thin-plies, matrix cracking under transverse-shear stresses and subsequent triggering of delamination are practically suppressed. The proposed approach could be ex-

tended to model failure in thick-ply composites where such effects are prominent. In such case, the anisotropic crack-driving force and degradation function definitions in Chapter 4 must be extended to account for transverse-shear stresses and capture the complex physics of 3-D crack evolution accurately.

- The current implementation involves a one-pass staggered phase field approach, which decouples the displacement and phase field equations, and requires smaller time-increment size to ensure sufficient accuracy of the solution. To allow larger time-increments, the monolithic approach based on BFGS algorithm could be used which solves both equations in a coupled manner, and also involves lesser iterations and reformulations of the system matrix during each time-increment.

- Experimental validations could be performed for impact simulations that involve combined intra-laminar and inter-laminar damage evolution under the influence of coupled membrane and bending deformations.

- The materials analysed in this thesis involve brittle, quasi-brittle or elastic-plastic ductile fractures only. The damage model could be extended to study rate-dependent fracture behaviour, which is typically observed during high-velocity ballistic impact simulations.

- The unit-cell RVE model used for meso-scale simulations in Chapter 5 considers only intra-laminar fracture evolution in a single-ply shell layer. This could be extended to include multiple plies with adhesive interfaces and also modelling inter-laminar fracture (delamination) to account for complex 3-D fracture behaviour happening at the meso-scale. The macro-scale model could still comprise a single shell layer with a coarse mesh, which could eventually offer significant speedups, as the need for simulating computationally expensive delamination analysis with multiple stacked shell-plies would be eliminated.

- Additionally, the RVE model could also comprise individual fibre inclusions embedded within a matrix section, and cohesive surface in-

teractions can be defined to accurately capture debonding-related stress degradation effects.

- A feed-forward neural network with a single hidden layer is used to construct the surrogate model. Although the model provides considerably accurate results, more advanced neural networks, e.g. recurrent/ convolutional neural networks, and deep-learning libraries (TensorFlow/ PyTorch/ Keras) could be utilised to obtain highly accurate and robust surrogate models. A challenge which needs to be addressed in such case would be to translate the extensive Python code generated by these libraries into Fortran, for it to be effectively used within Abaqus UMAT subroutine.

- The homogenisation-based multiscale modelling approaches rely on the assumption that in real-life macro-scale structures, the effect of stress-concentration around localised features such as notches, holes etc. is practically minimised, and the damage evolution happens under the influence of homogenized macro-scale stresses ignoring the localised stress concentration effects. These multiscale approaches provide accurate fracture estimates in macro-scale simulations and have been extensively validated throughout the literature, rendering such assumptions reasonable and of practical relevance in the case of composites. The proposed surrogate model could be used to perform fast and efficient damage simulations in such large macro-scale industrial composite structures, e.g. aircraft wing's leading edge, wherein the overall strength degradation of the structure is not affected by localised geometrical features. Furthermore, a mesh convergence study could be performed, and the results from surrogate model could be compared with experiments to assess the structural integrity and accuracy of predicted fracture behaviour.

Furthermore, it is also worth exploring the potential extensions of current work in the following broader inter-disciplinary applications:

- Predicting the remaining useful life (RUL) of aircraft composite structures

and identifying an optimal maintenance strategy for them requires coupling of damage propagation and damage identification models. Capturing diverse families of composite damage scenarios during damage identification process, with only a few models that are inexpensive to run, presents a major challenge. The multiscale surrogate damage model presented in Chapter 5 could be employed within a robust damage identification framework to obtain rapid anisotropic characterisation of damage and the rate of crack propagation, which can ultimately be used to predict the RUL of composite structures.

- Structural health monitoring (SHM) of aircraft structures is often performed using sensing techniques based on ultrasonic guided waves. The proposed damage modelling approach could be coupled with efficient wave finite element method to generate different damage signatures, and extend the applicability of sensing techniques by optimising the sensor configuration used for damage detection.

- At the micro-scale, composites display heterogeneous material behaviour due to the presence of random micro-structural cracks and fibre distribution, see for e.g. [495]. This influences both the crack paths as well as the predicted critical forces. To account for such micro-structural heterogeneity, a stochastic analysis could be performed by generating random distributions of fibres/micro-cracks with different probability distribution (e.g. Weibull) and understanding their effect on the predicted fracture behaviour [320].

- The applications of proposed anisotropic cohesive phase field damage model in Chapter 4 could be further explored to perform topology optimization and weight reduction analysis of aircraft composite structures based on the predicted critical stress estimates.

Bibliography

[1] Adrià Quintanas-Corominas, Pere Maimí, Eva Casoni, Albert Turon, Joan Andreu Mayugo, Gerard Guillamet, and Mariano Vázquez. A 3d transversally isotropic constitutive model for advanced composites implemented in a high performance computing code. *European Journal of Mechanics-A/Solids*, 71:278–291, 2018.

[2] Albert Soto, EV González, Pere Maimí, F Martin de la Escalera, JR Sainz de Aja, and E Alvarez. Low velocity impact and compression after impact simulation of thin ply laminates. *Composites Part A: Applied Science and Manufacturing*, 109:413–427, 2018.

[3] DAMTEXproject. Report with a summary of the tests and the data reduction methods applied for fibre fracture toughness characterization, under tension and compression loading (TeXtreme 80 gsm material). Technical Report E2.1 (2013-DAM-01-IT06), Aernnova Engineering Division S.A. (Spain) ; AMADE Polytechnic school, University of Girona (Spain), 2014.

[4] Jung-Kyu Kim, Do-Sik Kim, and Nobuo Takeda. Notched strength and fracture criterion in fabric composite plates containing a circular hole. *Journal of composite materials*, 29(7):982–998, 1995.

[5] E Martín-Santos, P Maimí, EV González, and P Cruz. A continuum con-

stitutive model for the simulation of fabric-reinforced composites. *Composite Structures*, 111:122–129, 2014.

[6] J Modniks, E Spārniņš, J Andersons, and W Becker. Analysis of the effect of a stress raiser on the strength of a ud flax/epoxy composite in off-axis tension. *Journal of Composite Materials*, 49(9):1071–1080, 2015.

[7] J Felger, N Stein, and W Becker. Mixed-mode fracture in open-hole composite plates of finite-width: An asymptotic coupled stress and energy approach. *International Journal of Solids and Structures*, 122:14–24, 2017.

[8] Robert D Cook, David S Malkus, Michael E Plesha, and Robert J Witt. *Concepts and applications of finite element analysis*, volume 4. Wiley New York, 1974.

[9] Ajay Harish. Tips for meshing your cad model for structural analysis. https://www.simscale.com/blog/2016/07/mesh-cad-model-structural-analysis/, June 2021.

[10] E Carrera, AG de Miguel, and A Pagani. Extension of mitc to higher-order beam models and shear locking analysis for compact, thin-walled, and composite structures. *International Journal for Numerical Methods in Engineering*, 112(13):1889–1908, 2017.

[11] A Laulusa, OA Bauchau, JY Choi, VBC Tan, and L Li. Evaluation of some shear deformable shell elements. *International Journal of Solids and Structures*, 43(17):5033–5054, 2006.

[12] L. Noels. Fracture mechanics online class, computational & multi-scale mechanics of materials (cm3). Website, 2015. URL `http://www.ltas-cm3.ulg.ac.be/FractureMechanics/?p=Lecture6_P4`.

[13] Robin Olsson, Alann André, and Peter Hellström. Analytical modelling and fe simulation of impact response and damage growth in a thin-ply laminate. In *20th International Conference on Composite Materials ICCM*, volume 20, pages 19–24, 2015.

[14] Pierre-Olivier Bouchard, François Bay, Yvan Chastel, and Isabelle Tovena. Crack propagation modelling using an advanced remeshing technique. *Computer methods in applied mechanics and engineering*, 189(3):723–742, 2000.

[15] P Jousset and M Rachik. Comparison and evaluation of two types of cohesive zone models for the finite element analysis of fracture propagation in industrial bonded structures. *Engineering Fracture Mechanics*, 132: 48–69, 2014.

[16] Yong Wu, Yongxiang Wang, Waisman Haim, Siming He, and Xinpo Li. Fracture of rocks in the mountains of southeast tibet under hydrothermal conditions at different elevations. *Bulletin of Engineering Geology and the Environment*, pages 1–18, 2020.

[17] Adrian Egger, Udit Pillai, Konstantinos Agathos, Emmanouil Kakouris, Eleni Chatzi, Ian A Aschroft, and Savvas P Triantafyllou. Discrete and phase field methods for linear elastic fracture mechanics: A comparative study and state-of-the-art review. *Applied Sciences*, 9(12):2436, 2019.

[18] Ramesh Talreja. On multi-scale approaches to composites and heterogeneous solids with damage. *Philosophical Magazine*, 90(31-32):4333–4348, 2010.

[19] Emmanouil Kakouris and Savvas P Triantafyllou. Phase-field material point method for dynamic brittle fracture with isotropic and anisotropic surface energy. *Computer Methods in Applied Mechanics and Engineering*, 357(112503), December 2019.

[20] Yanchao Wang and ZhengMing Huang. Analytical micromechanics models for elastoplastic behavior of long fibrous composites: A critical review and comparative study. *Materials*, 11(10):1919, 2018.

[21] UNOTT MARQUESS Technical Team. Review of the state of the art regarding multi-scale methods. Technical Report D11v4, The University of Nottingham (UK), July 2017. URL `https:`

//ec.europa.eu/research/participants/documents/downloadPublic?documentIds=080166e5b4e250b9&appId=PPGMS.

[22] Eduardo N Dvorkin and Klaus-Jürgen Bathe. A continuum mechanics based four-node shell element for general non-linear analysis. *Engineering computations*, 1(1):77–88, 1984.

[23] Yeongbin Ko, Phill-Seung Lee, and Klaus-Jürgen Bathe. A new MITC4+ shell element. *Computers & Structures*, 182:404–418, 2017.

[24] Christian Miehe, Martina Hofacker, and Fabian Welschinger. A phase field model for rate-independent crack propagation: Robust algorithmic implementation based on operator splits. *Computer Methods in Applied Mechanics and Engineering*, 199(45):2765–2778, 2010.

[25] EG Kakouris and SP Triantafyllou. Material point method for crack propagation in anisotropic media: a phase field approach. *Archive of Applied Mechanics*, 88(1-2):287–316, 2018.

[26] E.V. Gonzalez and A. Soto. Material characterization tests (TeXtreme 80 gsm material). Technical Report DAMTEXproject 2013-DAM-01-IT04-SummaryMaterialProperties, Aernnova Engineering Division S.A. (Spain) ; AMADE Polytechnic school, University of Girona (Spain), 2015.

[27] Jeremy Bleyer and Roberto Alessi. Phase-field modeling of anisotropic brittle fracture including several damage mechanisms. *Computer Methods in Applied Mechanics and Engineering*, 336:213–236, 2018.

[28] Peng Zhang, Xiaofei Hu, Tinh Quoc Bui, and Weian Yao. Phase field modeling of fracture in fiber reinforced composite laminate. *International Journal of Mechanical Sciences*, 2019.

[29] *MATLAB version 9.4.0.813654 (R2018a)*. The Mathworks, Inc., Natick, Massachusetts, 2018.

[30] Carl T Herakovich. Mechanics of composites: a historical review. *Mechanics Research Communications*, 41:1–20, 2012.

[31] A Brent Strong. *Fundamentals of composites manufacturing: materials, methods and applications*. Society of Manufacturing Engineers, 2008.

[32] S Rana and R Fangueiro. Advanced composites in aerospace engineering. In *Advanced composite materials for aerospace engineering*, pages 1–15. Elsevier, 2016.

[33] J Cugnoni, R Amacher, S Kohler, J Brunner, E Kramer, C Dransfeld, W Smith, K Scobbie, L Sorensen, and J Botsis. Towards aerospace grade thin-ply composites: Effect of ply thickness, fibre, matrix and interlayer toughening on strength and damage tolerance. *Composites Science and Technology*, 168:467–477, 2018.

[34] Brian N Cox and Gerry Flanagan. Handbook of analytical methods for textile composites. 1997.

[35] K Kawabe, T Matsuo, and Z-i Maekawa. New technology for opening various reinforcing fiber tows. *JOURNAL-SOCIETY OF MATERIALS SCIENCE JAPAN*, 47:727–734, 1998.

[36] Hassan M El-Dessouky and Carl A Lawrence. Ultra-lightweight carbon fibre/thermoplastic composite material using spread tow technology. *Composites Part B: Engineering*, 50:91–97, 2013.

[37] Jianxin Tao and CT Sun. Influence of ply orientation on delamination in composite laminates. *Journal of Composite Materials*, 32(21):1933–1947, 1998.

[38] Albertino Arteiro. *Structural mechanics of thin-ply laminated composites*. PhD thesis, Universidade do Porto (Portugal), 2016.

[39] Nandan Khokar and Fredrik Ohlsson. Spread tow fabrics. NetComposites https://netcomposites.com/guide/reinforcements/spread-tow-fabrics/, January 2019.

[40] JY Zheng and PF Liu. Elasto-plastic stress analysis and burst strength

evaluation of al-carbon fiber/epoxy composite cylindrical laminates. *Computational Materials Science*, 42(3):453–461, 2008.

[41] Ping Xu, JY Zheng, and PF Liu. Finite element analysis of burst pressure of composite hydrogen storage vessels. *Materials & Design*, 30(7):2295–2301, 2009.

[42] PF Liu and JY Zheng. Recent developments on damage modeling and finite element analysis for composite laminates: a review. *Materials & Design*, 31(8):3825–3834, 2010.

[43] Erik A Phillips, Carl T Herakovich, and Lori L Graham. Damage development in composites with large stress gradients. *Composites Science and Technology*, 61(15):2169–2182, 2001.

[44] P Kanouté, DP Boso, JL Chaboche, and BA Schrefler. Multiscale methods for composites: a review. *Archives of Computational Methods in Engineering*, 16(1):31–75, 2009.

[45] A Arteiro, G Catalanotti, J Xavier, and PP Camanho. Notched response of non-crimp fabric thin-ply laminates. *Composites Science and Technology*, 79:97–114, 2013.

[46] TN Bittencourt, PA Wawrzynek, AR Ingraffea, and JL Sousa. Quasi-automatic simulation of crack propagation for 2d lefm problems. *Engineering Fracture Mechanics*, 55(2):321–334, 1996.

[47] Pierre-Olivier Bouchard, François Bay, and Yvan Chastel. Numerical modelling of crack propagation: automatic remeshing and comparison of different criteria. *Computer methods in applied mechanics and engineering*, 192(35):3887–3908, 2003.

[48] RS Barsoum. On the use of isoparametric finite elements in linear fracture mechanics. *International journal for numerical methods in engineering*, 10(1):25–37, 1976.

[49] Ted Belytschko and Tom Black. Elastic crack growth in finite elements with minimal remeshing. *International journal for numerical methods in engineering*, 45(5):601–620, 1999.

[50] Nicolas Moës, John Dolbow, and Ted Belytschko. A finite element method for crack growth without remeshing. *International journal for numerical methods in engineering*, 46(1):131–150, 1999.

[51] Fenghua Zhou and Jean-Francois Molinari. Dynamic crack propagation with cohesive elements: a methodology to address mesh dependency. *International Journal for Numerical Methods in Engineering*, 59(1):1–24, 2004.

[52] Vinh Phu Nguyen, Timon Rabczuk, Stéphane Bordas, and Marc Duflot. Meshless methods: A review and computer implementation aspects. *Mathematics and Computers in Simulation*, 79(3):763–813, dec 2008. ISSN 03784754. doi: 10.1016/j.matcom.2008.01.003. URL `https://linkinghub.elsevier.com/retrieve/pii/S0378475408000062`.

[53] John A Nairn. Material point method calculations with explicit cracks. *Computer Modeling in Engineering and Sciences*, 4(6):649–664, 2003.

[54] EG Kakouris and Savvas P Triantafyllou. Phase-field material point method for brittle fracture. *International Journal for Numerical Methods in Engineering*, 112(12):1750–1776, 2017.

[55] H.-G. Maschke and M. Kuna. A review of boundary and finite element methods in fracture mechanics. *Theoretical and Applied Fracture Mechanics*, 4(3):181–189, dec 1985. ISSN 01678442. doi: 10.1016/0167-8442(85)90003-5. URL `http://linkinghub.elsevier.com/retrieve/pii/0167844285900035`.

[56] V Rokhlin. Rapid solution of integral equations of classical potential theory. *Journal of Computational Physics*, 60(2):187–207, sep 1985. ISSN 00219991. doi: 10.1016/0021-9991(85)90002-6. URL `http://linkinghub.elsevier.com/retrieve/pii/0021999185900026`.

[57] W. Hackbusch. A Sparse Matrix Arithmetic Based on $\Cal H$ -Matrices. Part I: Introduction to ${\Cal H}$ -Matrices. *Computing*, 62(2):89–108, apr 1999. ISSN 0010-485X, 1436-5057. doi: 10.1007/s006070050015. URL http://link.springer.com/10.1007/s006070050015.

[58] Theofanis Strouboulis, Ivo Babuška, and Kevin Copps. The design and analysis of the generalized finite element method. *Computer methods in applied mechanics and engineering*, 181(1-3):43–69, 2000.

[59] John P. Wolf and Chongmin Song. Consistent infinitesimal finite-element cell method: in-plane motion. *Computer Methods in Applied Mechanics and Engineering*, 123(1-4):355–370, jun 1995. ISSN 00457825. doi: 10.1016/0045-7825(95)00781-U. URL http://linkinghub.elsevier.com/retrieve/pii/004578259500781U.

[60] Mahmood M Shokrieh. *Residual stresses in composite materials*. Woodhead publishing, 2014.

[61] Bassam El Said and Stephen R Hallett. Multiscale surrogate modelling of the elastic response of thick composite structures with embedded defects and features. *Composite Structures*, 200:781–798, 2018.

[62] Fujian Zhuang, Puhui Chen, Albertino Arteiro, and Pedro P Camanho. Mesoscale modelling of damage in half-hole pin bearing composite laminate specimens. *Composite Structures*, 214:191–213, 2019.

[63] Cornelia Thieme. Whitepaper - how to create a good quality fe model. Technical report, MSC Software, 2016. URL http://documents.mscsoftware.com/sites/default/files/whitepaper_how_to_create_a_good_fe_model.pdf.

[64] Udit Pillai, Savvas P Triantafyllou, Ian Ashcroft, Yasser Essa, and Federico Martin de la Escalera. Phase-field modelling of brittle fracture in thin shell elements based on the mitc4+ approach. *Computational Mechanics*, pages 1–20, 2020.

[65] Alastair F Johnson, Anthony K Pickett, and Patrick Rozycki. Computational methods for predicting impact damage in composite structures. *Composites Science and Technology*, 61(15):2183–2192, 2001.

[66] Irwan Katili, Imam Jauhari Maknun, Jean-Louis Batoz, and Adnan Ibrahimbegovic. Shear deformable shell element dkmq24 for composite structures. *Composite Structures*, 202:182–200, 2018.

[67] Alastair F Johnson. Modelling fabric reinforced composites under impact loads. *Composites Part A: Applied Science and Manufacturing*, 32(9):1197–1206, 2001.

[68] Erasmo Carrera, Alfonso Pagani, and Stefano Valvano. Shell elements with through-the-thickness variable kinematics for the analysis of laminated composite and sandwich structures. *Composites Part B: Engineering*, 111:294–314, 2017.

[69] Klaus-Jürgen Bathe, Phill-Seung Lee, and Jean-François Hiller. Towards improving the mitc9 shell element. *Computers & structures*, 81(8-11):477–489, 2003.

[70] Nhon Nguyen-Thanh, Timon Rabczuk, H Nguyen-Xuan, and Stéphane PA Bordas. A smoothed finite element method for shell analysis. *Computer Methods in Applied Mechanics and Engineering*, 198(2):165–177, 2008.

[71] Ted Belytschko and Chen-Shyh Tsay. A stabilization procedure for the quadrilateral plate element with one-point quadrature. *International Journal for Numerical Methods in Engineering*, 19(3):405–419, 1983.

[72] Ted Belytschko and Itai Leviathan. Physical stabilization of the 4-node shell element with one point quadrature. *Computer Methods in Applied Mechanics and Engineering*, 113(3-4):321–350, 1994.

[73] OC Zienkiewicz, RL Taylor, and JM Too. Reduced integration technique in general analysis of plates and shells. *International Journal for Numerical Methods in Engineering*, 3(2):275–290, 1971.

[74] Klaus-Jürgen Bathe. *Finite element procedures*. Klaus-Jurgen Bathe, 2006.

[75] Thomas JR Hughes, Robert L Taylor, and Worsak Kanoknukulchai. A simple and efficient finite element for plate bending. *International Journal for Numerical Methods in Engineering*, 11(10):1529–1543, 1977.

[76] Thomas JR Hughes, Martin Cohen, and Medhat Haroun. Reduced and selective integration techniques in the finite element analysis of plates. *Nuclear Engineering and design*, 46(1):203–222, 1978.

[77] Louis NS Chiu, Brian G Falzon, Bernard Chen, and Wen Yi Yan. Numerical considerations for the implementation of a comprehensive composite damage model. In *Applied Mechanics and Materials*, volume 846, pages 217–224. Trans Tech Publ, 2016.

[78] Klaus-Jürgen Bathe and Eduardo N Dvorkin. A formulation of general shell elements—the use of mixed interpolation of tensorial components. *International Journal for Numerical Methods in Engineering*, 22(3):697–722, 1986.

[79] Youngyu Lee, Kyungho Yoon, and Phill-Seung Lee. Improving the mitc3 shell finite element by using the hellinger–reissner principle. *Computers & structures*, 110:93–106, 2012.

[80] Youngyu Lee, Phill-Seung Lee, and Klaus-Jürgen Bathe. The mitc3+ shell element and its performance. *Computers & Structures*, 138:12–23, 2014.

[81] Miguel Luiz Bucalem and Klaus-Jüen Bathe. Higher-order mitc general shell elements. *International Journal for Numerical Methods in Engineering*, 36(21):3729–3754, 1993.

[82] Yeongbin Ko, Phill-Seung Lee, and Klaus-Jürgen Bathe. The mitc4+ shell element and its performance. *Computers & Structures*, 169:57–68, 2016.

[83] Chang-Koon Choi and Jong-Gyun Paik. An efficient four node degenerated shell element based on the assumed covariant strain. *Structural Engineering and Mechanics*, 2(1):17–34, 1994.

[84] Hee Yuel Roh and Maenghyo Cho. The application of geometrically exact shell elements to b-spline surfaces. *Computer methods in applied mechanics and engineering*, 193(23-26):2261–2299, 2004.

[85] GM Kulikov and SV Plotnikova. A family of ans four-node exact geometry shell elements in general convected curvilinear coordinates. *International journal for numerical methods in engineering*, 83(10):1376–1406, 2010.

[86] Phill-Seung Lee and Klaus-Jürgen Bathe. Insight into finite element shell discretizations by use of the "basic shell mathematical model". *Computers & structures*, 83(1):69–90, 2005.

[87] Sangwook Sihn, Ran Y Kim, Kazumasa Kawabe, and Stephen W Tsai. Experimental studies of thin-ply laminated composites. *Composites Science and Technology*, 67(6):996–1008, 2007.

[88] R Amacher, J Cugnoni, J Botsis, L Sorensen, W Smith, and C Dransfeld. Thin ply composites: experimental characterization and modeling of size-effects. *Composites Science and Technology*, 101:121–132, 2014.

[89] Hiroshi Saito, Hiroki Takeuchi, and Isao Kimpara. Experimental evaluation of the damage growth restraining in 90 layer of thin-ply cfrp cross-ply laminates. *Advanced Composite Materials*, 21(1):57–66, 2012.

[90] G Guillamet, A Turon, J Costa, and J Renart. Damage evolution in thin and thick-ply regions of ncf thin-ply laminates under off-axis uniaxial loading. 2014.

[91] Ted L Anderson. *Fracture mechanics: fundamentals and applications*. CRC press, 2017.

[92] Sumio Murakami. *Continuum damage mechanics: a continuum mechanics approach to the analysis of damage and fracture*, volume 185. Springer Science & Business Media, 2012.

[93] Gilles A Francfort and J-J Marigo. Revisiting brittle fracture as an energy minimization problem. *Journal of the Mechanics and Physics of Solids*, 46(8): 1319–1342, 1998.

[94] Blaise Bourdin, Gilles A Francfort, and Jean-Jacques Marigo. The variational approach to fracture. *Journal of elasticity*, 91(1):5–148, 2008.

[95] YR Rashid. Ultimate strength analysis of prestressed concrete pressure vessels. *Nuclear engineering and design*, 7(4):334–344, 1968.

[96] D Ngo and AC Scordelis. Finite element analysis of reinforced concrete beams. In *Journal Proceedings*, volume 64, pages 152–163, 1967.

[97] Mohammed A Msekh, Juan Michael Sargado, Mostafa Jamshidian, Pedro Miguel Areias, and Timon Rabczuk. Abaqus implementation of phase-field model for brittle fracture. *Computational Materials Science*, 96: 472–484, 2015.

[98] AR Ingraffea and V Saouma. Numerical modelling of discrete crack propagation in reinforced and plain concrete. *Fracture Mechanics of concrete*, pages 171–225, 1985.

[99] David Azócar, Marcelo Elgueta, and María Cecilia Rivara. Automatic lefm crack propagation method based on local lepp–delaunay mesh refinement. *Advances in Engineering Software*, 41(2):111–119, 2010.

[100] B Moran and CF Shih. Crack tip and associated domain integrals from momentum and energy balance. *Engineering fracture mechanics*, 27(6): 615–642, 1987.

[101] S. Courtin, C. Gardin, G. Bézine, and H. Ben Hadj Hamouda. Advantages of the J-integral approach for calculating stress intensity factors when using the commercial finite element software ABAQUS. *Engineering Fracture Mechanics*, 72(14):2174–2185, sep 2005. ISSN 00137944. doi: 10.1016/j.engfracmech.2005.02.003. URL `https://linkinghub.elsevier.com/retrieve/pii/S0013794405000767`.

[102] EF Rybicki and MF Kanninen. A finite element calculation of stress intensity factors by a modified crack closure integral. *Engineering fracture mechanics*, 9(4):931–938, 1977.

[103] Ronald Krueger. Virtual crack closure technique: History, approach, and applications. *Applied Mechanics Reviews*, 57(2):109, 2004. ISSN 00036900. doi: 10.1115/1.1595677. URL http://AppliedMechanicsReviews.asmedigitalcollection.asme.org/article.aspx?articleid=1397949.

[104] B. L. Karihaloo and Q. Z. Xiao. Asymptotic fields at the tip of a cohesive crack. *International Journal of Fracture*, 150(1-2):55–74, mar 2008. ISSN 0376-9429, 1573-2673. doi: 10.1007/s10704-008-9218-2. URL http://link.springer.com/10.1007/s10704-008-9218-2.

[105] Yongxiang Wang, Chiara Cerigato, Haim Waisman, and Elena Benvenuti. XFEM with high-order material-dependent enrichment functions for stress intensity factors calculation of interface cracks using Irwin's crack closure integral. *Engineering Fracture Mechanics*, 178:148–168, jun 2017. ISSN 00137944. doi: 10.1016/j.engfracmech.2017.04.021. URL https://linkinghub.elsevier.com/retrieve/pii/S0013794417300619.

[106] Steffen Beese, Stefan Loehnert, and Peter Wriggers. 3D Ductile crack propagation with the XFEM. *PAMM*, 15(1):747–748, 2015.

[107] Pooyan Broumand and A.R. Khoei. Modeling ductile fracture with damage plasticity using XFEM technique, 06 2011.

[108] P Broumand and AR Khoei. The extended finite element method for large deformation ductile fracture problems with a non-local damage-plasticity model. *Engineering Fracture Mechanics*, 112:97–125, 2013.

[109] S Bordas, B Karihaloo, and P Kerfriden. Modeling ductile fracture with damage plasticity using X-FEM technique.

[110] Donald S Dugdale. Yielding of steel sheets containing slits. *Journal of the Mechanics and Physics of Solids*, 8(2):100–104, 1960.

[111] Grigory Isaakovich Barenblatt. The mathematical theory of equilibrium cracks in brittle fracture. *Advances in applied mechanics*, 7:55–129, 1962.

[112] JJC Remmers, Rene de Borst, and A Needleman. A cohesive segments method for the simulation of crack growth. *Computational mechanics*, 31 (1-2):69–77, 2003.

[113] T. Rabczuk and G. Zi. A meshfree method based on the local partition of unity for cohesive cracks. *Computational Mechanics*, 39:743–760, 2007.

[114] E. Barbieri and M. Meo. A meshless cohesive segments method for crack initiation and propagation in composites. *Applied Composite Materials*, 18: 45–63, 2011.

[115] Mark Kachanov. Continuum model of medium with cracks. *Journal of the engineering mechanics division*, 106(5):1039–1051, 1980.

[116] Yan Liu and Sumio Murakami. Damage localization of conventional creep damage models and proposition of a new model for creep damage analysis. *JSME International Journal Series A Solid Mechanics and Material Engineering*, 41(1):57–65, 1998.

[117] Nicolas Moës, Claude Stolz, P-E Bernard, and Nicolas Chevaugeon. A level set based model for damage growth: the thick level set approach. *International Journal for Numerical Methods in Engineering*, 86(3):358–380, 2011.

[118] P Maimí, Pedro Ponces Camanho, JA Mayugo, and CG Dávila. A continuum damage model for composite laminates: Part i–constitutive model. *Mechanics of Materials*, 39(10):897–908, 2007.

[119] P Maimí, Pedro Ponces Camanho, JA Mayugo, and CG Dávila. A continuum damage model for composite laminates: Part ii–computational implementation and validation. *Mechanics of Materials*, 39(10):909–919, 2007.

[120] ST Pinho, L Iannucci, and P Robinson. Physically based failure models and criteria for laminated fibre-reinforced composites with emphasis on fibre kinking. part ii: Fe implementation. *Composites Part A: Applied Science and Manufacturing*, 37(5):766–777, 2006.

[121] Valerio Carollo, J Reinoso, and Marco Paggi. Modeling complex crack paths in ceramic laminates: A novel variational framework combining the phase field method of fracture and the cohesive zone model. *Journal of the European Ceramic Society*, 38(8):2994–3003, 2018.

[122] Jose Reinoso, Giuseppe Catalanotti, Antonio Blázquez, Pedro Areias, PedroP Camanho, and Frederico París. A consistent anisotropic damage model for laminated fiber-reinforced composites using the 3d-version of the puck failure criterion. *International Journal of Solids and Structures*, 126: 37–53, 2017.

[123] Jaan-Willem Simon, Daniel Höwer, Bertram Stier, Stefanie Reese, and Jacob Fish. A regularized orthotropic continuum damage model for layered composites: intralaminar damage progression and delamination. *Computational Mechanics*, 60(3):445–463, 2017.

[124] S Mondal, LM Olsen-Kettle, and L Gross. Regularization of continuum damage mechanics models for 3-d brittle materials using implicit gradient enhancement. *Computers and Geotechnics*, 122:103505, 2020.

[125] Jayesh R Jain and Somnath Ghosh. Homogenization based 3d continuum damage mechanics model for composites undergoing microstructural debonding. *Journal of applied mechanics*, 75(3), 2008.

[126] Luigi Cedolin and Zdeněk P Bažant. Effect of finite element choice in blunt crack band analysis. *Computer Methods in Applied Mechanics and Engineering*, 24(3):305–316, 1980.

[127] Arne Hillerborg, Mats Modéer, and P-E Petersson. Analysis of crack formation and crack growth in concrete by means of fracture mechanics and finite elements. *Cement and concrete research*, 6(6):773–781, 1976.

[128] Zdeněk P Bažant and Byung H Oh. Crack band theory for fracture of concrete. *Matériaux et construction*, 16(3):155–177, 1983.

[129] Michael J Borden, Clemens V Verhoosel, Michael A Scott, Thomas JR Hughes, and Chad M Landis. A phase-field description of dynamic brittle fracture. *Computer Methods in Applied Mechanics and Engineering*, 217: 77–95, 2012.

[130] Mark S Shephard, Nabil AB Yehia, Gary S Burd, and Theodore J Weidner. Automatic crack propagation tracking. *Computers & Structures*, 20(1-3): 211–223, 1985.

[131] Y Sumi. Computational crack path prediction. *Theoretical and applied fracture mechanics*, 4(2):149–156, 1985.

[132] AS Kobayashi, AF Emery, and S Mall. Dynamic-finite-element and dynamic-photoelastic analyses of two fracturing homalite-100 plates. *Experimental Mechanics*, 16(9):321–328, 1976.

[133] J Jung, Jalees Ahmad, MF Kanninen, and CH Popelar. Finite element analysis of dynamic crack propagation. Technical report, BATTELLE COLUMBUS DIV OH, 1981.

[134] I Babuška and BQ Guo. The h, p and hp version of the finite element method; basis theory and applications. *Advances in Engineering Software*, 15(3-4):159–174, 1992.

[135] Bernhard A Schrefler, Stefano Secchi, and Luciano Simoni. On adaptive refinement techniques in multi-field problems including cohesive fracture. *Computer methods in applied mechanics and engineering*, 195(4-6): 444–461, 2006.

[136] Bořek Patzák and Milan Jirásek. Adaptive resolution of localized damage in quasi-brittle materials. *Journal of engineering mechanics*, 130(6):720–732, 2004.

[137] H Moslemi and AR Khoei. 3d adaptive finite element modeling of non-planar curved crack growth using the weighted superconvergent patch recovery method. *Engineering Fracture Mechanics*, 76(11):1703–1728, 2009.

[138] KSRK Murthy and M Mukhopadhyay. Adaptive finite element analysis of mixed-mode crack problems with automatic mesh generator. *International Journal for Numerical Methods in Engineering*, 49(8):1087–1100, 2000.

[139] KSRK Murthy and M Mukhopadhyay. Adaptive finite element analysis of mixed-mode fracture problems containing multiple crack-tips with an automatic mesh generator. *International journal of fracture*, 108(3):251–274, 2001.

[140] AR Khoei, M Eghbalian, H Moslemi, and H Azadi. Crack growth modeling via 3d automatic adaptive mesh refinement based on modified-spr technique. *Applied Mathematical Modelling*, 37(1-2):357–383, 2013.

[141] H Azadi and AR Khoei. Numerical simulation of multiple crack growth in brittle materials with adaptive remeshing. *International journal for numerical methods in engineering*, 85(8):1017–1048, 2011.

[142] Boyang Chen. *Numerical modelling of scale-dependent damage and failure of composites*. PhD thesis, Imperial College London, 2013.

[143] Annika Trädegård, Fred Nilsson, and Sören Östlund. Fem-remeshing technique applied to crack growth problems. *Computer Methods in Applied Mechanics and Engineering*, 160(1-2):115–131, 1998.

[144] Julien Rethore, Anthony Gravouil, and Alain Combescure. A stable numerical scheme for the finite element simulation of dynamic crack propagation with remeshing. *Computer methods in applied mechanics and engineering*, 193(42):4493–4510, 2004.

[145] AR Shahani and MR Amini Fasakhodi. Finite element analysis of dynamic crack propagation using remeshing technique. *Materials & design*, 30(4):1032–1041, 2009.

[146] Alan A Griffith. The phenomena of rupture and flow in solids. *Philosophical transactions of the royal society of london. Series A, containing papers of a mathematical or physical character*, 221:163–198, 1921.

[147] Qingda Yang and Brian Cox. Cohesive models for damage evolution in laminated composites. *International Journal of Fracture*, 133(2):107–137, 2005.

[148] Albert Turon, Carlos G Davila, Pedro Ponces Camanho, and J Costa. An engineering solution for mesh size effects in the simulation of delamination using cohesive zone models. *Engineering fracture mechanics*, 74(10): 1665–1682, 2007.

[149] MGGV Elices, GV Guinea, J Gomez, and J Planas. The cohesive zone model: advantages, limitations and challenges. *Engineering fracture mechanics*, 69(2):137–163, 2002.

[150] Zuorong Chen, AP Bunger, Xi Zhang, and Robert G Jeffrey. Cohesive zone finite element-based modeling of hydraulic fractures. *Acta Mechanica Solida Sinica*, 22(5):443–452, 2009.

[151] AL Saleh and MH Aliabadi. Crack growth analysis in concrete using boundary element method. *Engineering fracture mechanics*, 51(4):533–545, 1995.

[152] Ivo Babuška and Jens M Melenk. The partition of unity method. *International journal for numerical methods in engineering*, 40(4):727–758, 1997.

[153] T. C. Nguyen, H. H. Bui, P. V. Nguyen, and G. D. Nguyen. Modelling rock fracture unsing smoothed particle hydrodynamics and cohesive cracks. *EUROCK*, October:7–10, 2012.

[154] P. A. Klein, J. W. Foulk, E. P. Chen, S. A. Wimmer, and H. J. Gao. Physics-based modeling of brittle fracture: cohesive formulations and the application of meshfree methods. *Theoretical and Applied Fracture Mechanics*, 37:99–166, 2001.

[155] P. Soparat and P. Nanakorn. Analysis of cohesive crack growth by the element-free galerkin method. *Journal of Mechanics*, 24:45–54, 2008.

[156] H Li and N Chandra. Analysis of crack growth and crack-tip plasticity in ductile materials using cohesive zone models. *International Journal of Plasticity*, 19(6):849–882, 2003.

[157] René de Borst, Miguel A Gutiérrez, Garth N Wells, Joris JC Remmers, and Harm Askes. Cohesive-zone models, higher-order continuum theories and reliability methods for computational failure analysis. *International Journal for Numerical Methods in Engineering*, 60(1):289–315, 2004.

[158] De Xie and Anthony M Waas. Discrete cohesive zone model for mixed-mode fracture using finite element analysis. *Engineering fracture mechanics*, 73(13):1783–1796, 2006.

[159] Paul W Harper and Stephen R Hallett. Cohesive zone length in numerical simulations of composite delamination. *Engineering Fracture Mechanics*, 75(16):4774–4792, 2008.

[160] A Turon, PP Camanho, J Costa, and J Renart. Accurate simulation of delamination growth under mixed-mode loading using cohesive elements: definition of interlaminar strengths and elastic stiffness. *Composite structures*, 92(8):1857–1864, 2010.

[161] Paul W Harper and Stephen R Hallett. A fatigue degradation law for cohesive interface elements–development and application to composite materials. *International Journal of Fatigue*, 32(11):1774–1787, 2010.

[162] Pedro Ponces Camanho, C G Davila, and MF De Moura. Numerical simulation of mixed-mode progressive delamination in composite materials. *Journal of composite materials*, 37(16):1415–1438, 2003.

[163] Pedro P Camanho and Carlos G Dávila. Mixed-mode decohesion finite elements for the simulation of delamination in composite materials. 2002.

[164] Bent F Sørensen and Stergios Goutianos. Enhancement of delamination fracture resistance of composites by fiber bridging and mulitple cracks. In *IUTAM Symposium on Size-effect in Microstructure and Damage Evolution 2018*, 2018.

[165] Bent F Sørensen and Peter Kirkegaard. Determination of mixed mode cohesive laws. *Engineering Fracture Mechanics*, 73(17):2642–2661, 2006.

[166] Godofredo T Camacho and M Ortiz. Computational modelling of impact damage in brittle materials. *International Journal of solids and structures*, 33(20-22):2899–2938, 1996.

[167] S R Hallett, B G Green, WG Jiang, and MR Wisnom. An experimental and numerical investigation into the damage mechanisms in notched composites. *Composites Part A: Applied Science and Manufacturing*, 40(5): 613–624, 2009.

[168] Xiangqian Li, Stephen R Hallett, and Michael R Wisnom. Numerical investigation of progressive damage and the effect of layup in overheight compact tension tests. *Composites Part A: Applied Science and Manufacturing*, 43(11):2137–2150, 2012.

[169] OJ Nixon-Pearson, SR Hallett, PW Harper, and LF Kawashita. Damage development in open-hole composite specimens in fatigue. part 2: Numerical modelling. *Composite Structures*, 106:890–898, 2013.

[170] Xia Liu, Ravindra Duddu, and Haim Waisman. Discrete damage zone model for fracture initiation and propagation. *Engineering Fracture Mechanics*, 92:1–18, 2012.

[171] D Feng and Francesco Aymerich. Finite element modelling of damage induced by low-velocity impact on composite laminates. *Composite Structures*, 108:161–171, 2014.

[172] Michael May. Numerical evaluation of cohesive zone models for modeling impact induced delamination in composite materials. *Composite Structures*, 133:16–21, 2015.

[173] Robin Olsson, Rickard Juntikka, and Leif E Asp. High velocity hail impact on composite laminates–modelling and testing. In *Dynamic Failure of Composite and Sandwich Structures*, pages 393–426. Springer, 2013.

[174] EV González, P Maimí, PP Camanho, A Turon, and JA Mayugo. Simulation of drop-weight impact and compression after impact tests on composite laminates. *Composite Structures*, 94(11):3364–3378, 2012.

[175] Ofir Shor and Reza Vaziri. Application of the local cohesive zone method to numerical simulation of composite structures under impact loading. *International Journal of Impact Engineering*, 104:127–149, 2017.

[176] CS Shin and CM Wang. An improved cohesive zone model for residual notched strength prediction of composite laminates with different orthotropic lay-ups. *Journal of composite materials*, 38(9):713–736, 2004.

[177] Ireneusz Lapczyk and Juan A Hurtado. Progressive damage modeling in fiber-reinforced materials. *Composites Part A: Applied Science and Manufacturing*, 38(11):2333–2341, 2007.

[178] SIMULIA. *ABAQUS/Standard User's Manual, Version 2017*. Dassault Systèmes Simulia Corp, Providence, RI, USA, 2016.

[179] MR Wisnom. Modelling discrete failures in composites with interface elements. *Composites Part A: Applied Science and Manufacturing*, 41(7):795–805, 2010.

[180] AC Orifici, I Herszberg, and RS Thomson. Review of methodologies for composite material modelling incorporating failure. *Composite structures*, 86(1):194–210, 2008.

[181] Joris JC Remmers, René de Borst, and Alan Needleman. The simulation of dynamic crack propagation using the cohesive segments method. *Journal of the Mechanics and Physics of Solids*, 56(1):70–92, 2008.

[182] Luiz F Kawashita, Alexandre Bedos, and Stephen R Hallett. Modelling mesh independent transverse cracks in laminated composites with a sim-

plified cohesive segment method. *Computers, Materials, & Continua*, 32(2): 133–158, 2012.

[183] MF Pernice, LF Kawashita, and SR Hallett. Analysis of delamination migration in laminated composites using conventional and mesh-independent cohesive zone models. In *The 19th international conference on composite materials (ICCM 19)*, 2013.

[184] Jagan Selvaraj, Luiz Kawashita, Giuliano Allegri, and Stephen Hallett. Adaptive mesh segmentation for modelling dynamic delamination initiation and propagation in thick composite laminates. 2019.

[185] Ivo Babuška, Gabriel Caloz, and John E Osborn. Special finite element methods for a class of second order elliptic problems with rough coefficients. *SIAM Journal on Numerical Analysis*, 31(4):945–981, 1994.

[186] Jens M Melenk and Ivo Babuška. The partition of unity finite element method: basic theory and applications. In *Research Report/Seminar für Angewandte Mathematik*, volume 1996. Eidgenössische Technische Hochschule, Seminar für Angewandte Mathematik, 1996.

[187] Ted Belytschko, Robert Gracie, and Giulio Ventura. A review of extended/generalized finite element methods for material modeling. *Modelling and Simulation in Materials Science and Engineering*, 17(4):043001, 2009.

[188] Natarajan Sukumar, Nicolas Moës, B Moran, and Ted Belytschko. Extended finite element method for three-dimensional crack modelling. *International Journal for Numerical Methods in Engineering*, 48(11):1549–1570, 2000.

[189] Alireza Asadpoure, Soheil Mohammadi, and Abolhasan Vafai. Crack analysis in orthotropic media using the extended finite element method. *Thin-Walled Structures*, 44(9):1031–1038, 2006.

[190] A Asadpoure and S Mohammadi. Developing new enrichment functions for crack simulation in orthotropic media by the extended finite element

method. *International Journal for Numerical Methods in Engineering*, 69(10): 2150–2172, 2007.

[191] D Motamedi and S Mohammadi. Dynamic analysis of fixed cracks in composites by the extended finite element method. *Engineering Fracture Mechanics*, 77(17):3373–3393, 2010.

[192] D Motamedi and S Mohammadi. Fracture analysis of composites by time independent moving-crack orthotropic xfem. *International Journal of Mechanical Sciences*, 54(1):20–37, 2012.

[193] Chang Ye, Jay Shi, and Gary J Cheng. An eXtended Finite Element Method (XFEM) study on the effect of reinforcing particles on the crack propagation behavior in a metal–matrix composite. *International Journal of Fatigue*, 44:151–156, 2012.

[194] Guodong Nian, Yejie Shan, Qiang Xu, Shaoxing Qu, and Qingda Yang. Failure analysis of syntactic foams: A computational model with cohesive law and xfem. *Composites Part B: Engineering*, 89:18–26, 2016.

[195] Rossana Dimitri, Nicholas Fantuzzi, Yong Li, and Francesco Tornabene. Numerical computation of the crack development and sif in composite materials with xfem and sfem. *Composite structures*, 160:468–490, 2017.

[196] Guangwu Fang, Xiguang Gao, and Yingdong Song. Xfem analysis of the effect of fiber volume fraction on crack propagation in fiber reinforced ceramic matrix composites. In *IOP Conference Series: Materials Science and Engineering*, volume 678, page 012027. IOP Publishing, 2019.

[197] M Kumar, S Ahmad, IV Singh, AV Rao, J Kumar, and V Kumar. Experimental and numerical studies to estimate fatigue crack growth behavior of ni-based super alloy. *Theoretical and Applied Fracture Mechanics*, 96: 604–616, 2018.

[198] M Kumar, IV Singh, and BK Mishra. Fatigue crack growth simulations of plastically graded materials using xfem and j-integral decomposition approach. *Engineering Fracture Mechanics*, 216:106470, 2019.

[199] Chi Duan, Xiuhua Chen, and Ruowei Li. The numerical simulation of fatigue crack propagation in inconel 718 alloy at different temperatures. *Aerospace Systems*, pages 1–9, 2020.

[200] Jianxu Shi, David Chopp, Jim Lua, N Sukumar, and Ted Belytschko. Abaqus implementation of extended finite element method using a level set representation for three-dimensional fatigue crack growth and life predictions. *Engineering Fracture Mechanics*, 77(14):2840–2863, 2010.

[201] Himanshu Pathak, Akhilendra Singh, and Indra Vir Singh. Fatigue crack growth simulations of 3-d problems using xfem. *International Journal of Mechanical Sciences*, 76:112–131, 2013.

[202] Yixiu Shu, Yazhi Li, Minge Duan, and Fan Yang. An x-fem approach for simulation of 3-d multiple fatigue cracks and application to double surface crack problems. *International Journal of Mechanical Sciences*, 130: 331–349, 2017.

[203] Emmanuel De Luycker, David J Benson, Ted Belytschko, Yuri Bazilevs, and Ming Chen Hsu. X-fem in isogeometric analysis for linear fracture mechanics. *International Journal for Numerical Methods in Engineering*, 87 (6):541–565, 2011.

[204] Yue Jia, Cosmin Anitescu, Seyed Shahram Ghorashi, and Timon Rabczuk. Extended isogeometric analysis for material interface problems. *IMA Journal of Applied Mathematics*, 80(3):608–633, 2015.

[205] Nhon Nguyen-Thanh and Kun Zhou. An adaptive extended isogeometric analysis based on pht-splines for crack propagation. *Int. J. Numer. Methods Eng*, pages 1–30, 2017.

[206] SK Singh, IV Singh, BK Mishra, G Bhardwaj, and TQ Bui. A simple, efficient and accurate bézier extraction based t-spline xiga for crack simulations. *Theoretical and Applied Fracture Mechanics*, 88:74–96, 2017.

[207] Jiming Gu, Tiantang Yu, Thanh-Tung Nguyen, Satoyuki Tanaka, Tinh Quoc Bui, et al. Multi-inclusions modeling by adaptive xiga based

on lr b-splines and multiple level sets. *Finite Elements in Analysis and Design*, 148:48–66, 2018.

[208] Nicolas Moës and Ted Belytschko. Extended finite element method for cohesive crack growth. *Engineering fracture mechanics*, 69(7):813–833, 2002.

[209] DM Grogan, CM Ó Brádaigh, and SB Leen. A combined xfem and cohesive zone model for composite laminate microcracking and permeability. *Composite Structures*, 120:246–261, 2015.

[210] Saleh Yazdani, Wilhelm JH Rust, and Peter Wriggers. An xfem approach for modelling delamination in composite laminates. *Composite Structures*, 135:353–364, 2016.

[211] XF Hu, BY Chen, M Tirvaudey, VBC Tan, and TE Tay. Integrated xfem-ce analysis of delamination migration in multi-directional composite laminates. *Composites Part A: Applied Science and Manufacturing*, 90:161–173, 2016.

[212] Eduardo Kausel. Thin-layer method: Formulation in the time domain. *International Journal for Numerical Methods in Engineering*, 37(6):927–941, mar 1994. ISSN 0029-5981, 1097-0207. doi: 10.1002/nme.1620370604. URL `http://doi.wiley.com/10.1002/nme.1620370604`.

[213] Eisuke Kita and Norio Kamiya. Trefftz method: an overview. *Advances in Engineering Software*, 24(1-3):3–12, jan 1995. ISSN 09659978. doi: 10.1016/0965-9978(95)00067-4. URL `http://linkinghub.elsevier.com/retrieve/pii/0965997895000674`.

[214] Anthony T Patera. A spectral element method for fluid dynamics: Laminar flow in a channel expansion. *Journal of Computational Physics*, 54(3):468–488, jun 1984. ISSN 00219991. doi: 10.1016/0021-9991(84)90128-1. URL `https://linkinghub.elsevier.com/retrieve/pii/0021999184901281`.

[215] R.B. Nelson, S.B. Dong, and R.D. Kalra. Vibrations and waves in laminated orthotropic circular cylinders. *Journal of Sound and*

Vibration, 18(3):429–444, oct 1971. ISSN 0022460X. doi: 10.1016/0022-460X(71)90714-0. URL http://linkinghub.elsevier.com/retrieve/pii/0022460X71907140.

[216] ZJ Yang and AJ Deeks. Fully-automatic modelling of cohesive crack growth using a finite element–scaled boundary finite element coupled method. *Engineering Fracture Mechanics*, 74(16):2547–2573, 2007.

[217] Zhenjun Yang. Fully automatic modelling of mixed-mode crack propagation using scaled boundary finite element method. *Engineering Fracture Mechanics*, 73(12):1711–1731, aug 2006. ISSN 00137944. doi: 10.1016/j.engfracmech.2006.02.004. URL http://linkinghub.elsevier.com/retrieve/pii/S0013794406000841.

[218] John P Wolf. *The scaled boundary finite element method*. John Wiley & Sons, 2003.

[219] Steven R. Chidgzey and Andrew J. Deeks. Determination of coefficients of crack tip asymptotic fields using the scaled boundary finite element method. *Engineering Fracture Mechanics*, 72(13):2019–2036, sep 2005. ISSN 00137944. doi: 10.1016/j.engfracmech.2004.07.010. URL https://linkinghub.elsevier.com/retrieve/pii/S0013794404001730.

[220] Chongmin Song. Evaluation of power-logarithmic singularities, t-stresses and higher order terms of in-plane singular stress fields at cracks and multi-material corners. *Engineering Fracture Mechanics*, 72(10):1498–1530, 2005.

[221] John P. Wolf and Chongmin Song. Dynamic-stiffness matrix in time domain of unbounded medium by infinitesimal finite element cell method. *Earthquake Engineering & Structural Dynamics*, 23(11):1181–1198, 1994. doi: 10.1002/eqe.4290231103. URL https://onlinelibrary.wiley.com/doi/abs/10.1002/eqe.4290231103.

[222] P.P. Silvester, D.A. Lowther, C.J. Carpenter, and E.A. Wyatt. Exterior finite elements for 2-dimensional field problems with open boundaries.

Proceedings of the Institution of Electrical Engineers, 124(12):1267, 1977. ISSN 00203270. doi: 10.1049/piee.1977.0267. URL http://digital-library.theiet.org/content/journals/10.1049/piee.1977.0267.

[223] A. J. Deeks and J. P. Wolf. A virtual work derivation of the scaled boundary finite-element method for elastostatics. *Computational Mechanics*, 28(6):489–504, jun 2002. ISSN 0178-7675, 1432-0924. doi: 10.1007/s00466-002-0314-2. URL http://link.springer.com/10.1007/s00466-002-0314-2.

[224] Z. J. Yang and A. J. Deeks. Modelling cohesive crack growth using a two-step finite element-scaled boundary finite element coupled method. *International Journal of Fracture*, 143(4):333–354, jun 2007. ISSN 0376-9429, 1573-2673. doi: 10.1007/s10704-007-9065-6. URL http://link.springer.com/10.1007/s10704-007-9065-6.

[225] E.T. Ooi and Z.J. Yang. Modelling multiple cohesive crack propagation using a finite element–scaled boundary finite element coupled method. *Engineering Analysis with Boundary Elements*, 33(7):915–929, jul 2009. ISSN 09557997. doi: 10.1016/j.enganabound.2009.01.006. URL https://linkinghub.elsevier.com/retrieve/pii/S0955799709000265.

[226] E.T. Ooi and Z.J. Yang. Efficient prediction of deterministic size effects using the scaled boundary finite element method. *Engineering Fracture Mechanics*, 77(6):985–1000, apr 2010. ISSN 00137944. doi: 10.1016/j.engfracmech.2010.01.002. URL https://linkinghub.elsevier.com/retrieve/pii/S0013794410000032.

[227] Ean Tat Ooi and Zhen Jun Yang. Modelling crack propagation in reinforced concrete using a hybrid finite element–scaled boundary finite element method. *Engineering Fracture Mechanics*, 78(2):252–273, jan 2011. ISSN 00137944. doi: 10.1016/j.engfracmech.2010.08.002. URL https://linkinghub.elsevier.com/retrieve/pii/S0013794410003590.

[228] E. T. Ooi, Z. J. Yang, and Z. Y. Guo. Dynamic cohesive crack prop-

agation modelling using the scaled boundary finite element method: DYNAMIC COHESIVE CRACK PROPAGATION MODELLING. *Fatigue & Fracture of Engineering Materials & Structures*, 35(8):786–800, aug 2012. ISSN 8756758X. doi: 10.1111/j.1460-2695.2011.01652.x. URL http://doi.wiley.com/10.1111/j.1460-2695.2011.01652.x.

[229] Chongmin Song. A super-element for crack analysis in the time domain. *International Journal for Numerical Methods in Engineering*, 61(8):1332–1357, oct 2004. ISSN 0029-5981, 1097-0207. doi: 10.1002/nme.1117. URL http://doi.wiley.com/10.1002/nme.1117.

[230] A. Müller, J. Wenck, S. Goswami, J. Lindemann, J. Hohe, and W. Becker. The boundary finite element method for predicting directions of cracks emerging from notches at bimaterial junctions. *Engineering Fracture Mechanics*, 72(3):373–386, feb 2005. ISSN 00137944. doi: 10.1016/j.engfracmech.2004.04.004. URL https://linkinghub.elsevier.com/retrieve/pii/S0013794404000992.

[231] J. Lindemann and W. Becker. Free-Edge Stresses around Holes in Laminates by the Boundary Finite-Element Method. *Mechanics of Composite Materials*, 38(5):407–416, sep 2002. ISSN 1573-8922. doi: 10.1023/A:1020930125415. URL https://doi.org/10.1023/A:1020930125415.

[232] Irene Chiong, Ean Tat Ooi, Chongmin Song, and Francis Tin-Loi. Scaled boundary polygons with application to fracture analysis of functionally graded materials. *International Journal for Numerical Methods in Engineering*, 98(8):562–589, 2014.

[233] X Chen, T Luo, ET Ooi, EH Ooi, and C Song. A quadtree-polygon-based scaled boundary finite element method for crack propagation modeling in functionally graded materials. *Theoretical and Applied Fracture Mechanics*, 94:120–133, 2018.

[234] Zihua Zhang, Dilina Dissanayake, Albert Saputra, Di Wu, and Chongmin

Song. Three-dimensional damage analysis by the scaled boundary finite element method. *Computers & Structures*, 206:1–17, 2018.

[235] Zihua Zhang, Yan Liu, Dilina Dyon Dissanayake, Albert A Saputra, and Chongmin Song. Nonlocal damage modelling by the scaled boundary finite element method. *Engineering Analysis with Boundary Elements*, 99: 29–45, 2019.

[236] Ean Tat Ooi, Chongmin Song, Francis Tin-Loi, and Zhenjun Yang. Polygon scaled boundary finite elements for crack propagation modelling. *International Journal for Numerical Methods in Engineering*, 91(3):319–342, 2012.

[237] Cameron Talischi, Glaucio H. Paulino, Anderson Pereira, and Ivan F. M. Menezes. PolyMesher: a general-purpose mesh generator for polygonal elements written in Matlab. *Structural and Multidisciplinary Optimization*, 45(3):309–328, mar 2012. ISSN 1615-147X, 1615-1488. doi: 10.1007/s00158-011-0706-z. URL `http://link.springer.com/10.1007/s00158-011-0706-z`.

[238] ET Ooi, H Man, S Natarajan, and Ch Song. Adaptation of quadtree meshes in the scaled boundary finite element method for crack propagation modelling. *Engineering Fracture Mechanics*, 144:101–117, 2015.

[239] Adrian W Egger. *A Scaled Boundary Approach to Forward and Inverse Problems with Applications in Computational Fracture Mechanics, Damage Localization and Topology Optimization*. PhD thesis, ETH Zurich, 2019.

[240] Maximilian Praster, Rainer Reichel, and Sven Klinkel. Multiscale analysis of heterogeneous materials in boundary representation. *PAMM*, 19(1): e201900452, 2019.

[241] Adrian W Egger, Savvas P Triantafyllou, and ELENI N CHATZI. A scaled boundary multiscale approach to crack propagation. In *Proceedings of the 10th International Conference on Fracture Mechanics of Concrete and Concrete Structures. IA-FraMCoS*, 2019.

[242] Gao Lin, Yong Zhang, ZhiQiang Hu, and Hong Zhong. Scaled boundary isogeometric analysis for 2d elastostatics. *Science China Physics, Mechanics and Astronomy*, 57(2):286–300, 2014.

[243] Sundararajan Natarajan, JunChao Wang, Chongmin Song, and Carolin Birk. Isogeometric analysis enhanced by the scaled boundary finite element method. *Computer Methods in Applied Mechanics and Engineering*, 283:733–762, 2015.

[244] F Auricchio, Francesco Calabro, Thomas JR Hughes, A Reali, and G Sangalli. A simple algorithm for obtaining nearly optimal quadrature rules for nurbs-based isogeometric analysis. *Computer Methods in Applied Mechanics and Engineering*, 249:15–27, 2012.

[245] J Austin Cottrell, Thomas JR Hughes, and Yuri Bazilevs. *Isogeometric analysis: toward integration of CAD and FEA*. John Wiley & Sons, 2009.

[246] Y Khudari Bek, KM Hamdia, Timon Rabczuk, and C Könke. Micromechanical model for polymeric nano-composites material based on sbfem. *Composite Structures*, 194:516–526, 2018.

[247] Chao Li, Hou Man, Chongmin Song, and Wei Gao. Analysis of cracks and notches in piezoelectric composites using scaled boundary finite element method. *Composite Structures*, 101:191–203, 2013.

[248] Chao Li, Chongmin Song, Hou Man, Ean Tat Ooi, and Wei Gao. 2d dynamic analysis of cracks and interface cracks in piezoelectric composites using the sbfem. *International Journal of Solids and Structures*, 51(11-12): 2096–2108, 2014.

[249] Sascha Hell and Wilfried Becker. Hypersingularities in three-dimensional crack configurations in composite laminates. In *Key Engineering Materials*, volume 577, pages 209–212. Trans Tech Publ, 2014.

[250] S Dölling, J Hahn, J Felger, S Bremm, and W Becker. A scaled boundary finite element method model for interlaminar failure in composite laminates. *Composite Structures*, 241:111865, 2020.

[251] Nikhil Garg, Nilanjan Das Chakladar, B Gangadhara Prusty, Chongmin Song, and Andrew W Phillips. Modelling of laminated composite plates with weakly bonded interfaces using scaled boundary finite element method. *International Journal of Mechanical Sciences*, 170:105349, 2020.

[252] Chao Li, Hou Man, Chongmin Song, and Wei Gao. Fracture analysis of piezoelectric materials using the scaled boundary finite element method. *Engineering Fracture Mechanics*, 97:52–71, 2013.

[253] Albert Artha Saputra, Vladimir Sladek, Jan Sladek, and Chongmin Song. Micromechanics determination of effective material coefficients of cement-based piezoelectric ceramic composites. *Journal of Intelligent Material Systems and Structures*, 29(5):845–862, 2018.

[254] Adrian W Egger, Savvas P Triantafyllou, and Eleni N Chatzi. The scaled boundary finite element method for the efficient modeling of linear elastic fracture. 2016.

[255] Yu N Rabotnov. Creep problems in structural members. 1969.

[256] Ramesh Talreja and Chandra Veer Singh. *Damage and failure of composite materials*. Cambridge University Press, 2012.

[257] Zvi Hashin. Fatigue failure criteria for unidirectional fiber composites. *ASME, Transactions, Journal of Applied Mechanics*, 48:846–852, 1981.

[258] Carlos G Dávila and Pedro P Camanho. Failure criteria for frp laminates in plane stress. *NASA TM*, 212663(613), 2003.

[259] Silvestre T Pinho, Carlos G Dávila, Pedro P Camanho, Lorenzo Iannucci, and Paul Robinson. Failure models and criteria for frp under in-plane or three-dimensional stress states including shear non-linearity. 2005.

[260] ST Pinho, R Darvizeh, P Robinson, C Schuecker, and PP Camanho. Material and structural response of polymer-matrix fibre-reinforced composites. *Journal of Composite Materials*, 46(19-20):2313–2341, 2012.

[261] ST Pinho, GM Vyas, and P Robinson. Material and structural response of polymer-matrix fibre-reinforced composites: Part b. *Journal of Composite Materials*, 47(6-7):679–696, 2013.

[262] Zvi Hashin and Assa Rotem. A fatigue failure criterion for fiber reinforced materials. *Journal of composite materials*, 7(4):448–464, 1973.

[263] Assa Rotem and Zvi Hashin. Failure modes of angle ply laminates. *Journal of Composite Materials*, 9(2):191–206, 1975.

[264] Assa Rotem and Howard G Nelson. Fatigue behavior of graphite-epoxy laminates at elevated temperatures. In *Fatigue of Fibrous Composite Materials*. ASTM International, 1981.

[265] A Puck and H Schürmann. Failure analysis of frp laminates by means of physically based phenomenological models. *Composites Science and Technology*, 58(7):1045–1067, 1998.

[266] A Puck and M Mannigel. Physically based non-linear stress–strain relations for the inter-fibre fracture analysis of frp laminates. *composites science and technology*, 67(9):1955–1964, 2007.

[267] Stephen W Tsai and Edward M Wu. A general theory of strength for anisotropic materials. *Journal of composite materials*, 5(1):58–80, 1971.

[268] Stephen W Tsai. Strength theories of filamentary structure. *Fundamental aspects of fiber reinforced plastic composites*, 1968.

[269] Peter A Zinoviev, Sergei V Grigoriev, Olga V Lebedeva, and Ludmilla P Tairova. The strength of multilayered composites under a plane-stress state. *Composites science and technology*, 58(7):1209–1223, 1998.

[270] Oscar Hoffman. The brittle strength of orthotropic materials. *Journal of Composite Materials*, 1(2):200–206, 1967.

[271] SE Yamada and CT Sun. Analysis of laminate strength and its distribution. *Journal of composite materials*, 12(3):275–284, 1978.

[272] JL Chaboche. Continuum damage mechanics. ii: Damage growth, crack initiation, and crack growth. *Journal of applied mechanics*, 55(1):65–72, 1988.

[273] Nicola Bonora. A nonlinear cdm model for ductile failure. *Engineering fracture mechanics*, 58(1):11–28, 1997.

[274] Ever J Barbero and Liliana De Vivo. A constitutive model for elastic damage in fiber-reinforced pmc laminae. *International Journal of Damage Mechanics*, 10(1):73–93, 2001.

[275] Ramesh Talreja. A continuum mechanics characterization of damage in composite materials. In *Proceedings of the Royal Society of London A: mathematical, physical and engineering sciences*, volume 399, pages 195–216. The Royal Society, 1985.

[276] Ramesh Talreja. Damage mechanics of composite materials based on thermodynamics with internal variables. *Durability of Polymer Based Composite Systems for Structural Applications*, pages 65–79, 1990.

[277] Ramesh Talreja. Damage and fatigue in composites–a personal account. *Composites Science and Technology*, 68(13):2585–2591, 2008.

[278] Olivier Allix, Pierre Ladevèze, Daniel Gilletta, and Roger Ohayon. A damage prediction method for composite structures. *International Journal for Numerical Methods in Engineering*, 27(2):271–283, 1989.

[279] Pierre Ladevèze, Olivier Allix, Jean-François Deü, and David Lévêque. A mesomodel for localisation and damage computation in laminates. *Computer methods in applied mechanics and engineering*, 183(1):105–122, 2000.

[280] Pedro Ponces Camanho, Pere Maimí, and CG Dávila. Prediction of size effects in notched laminates using continuum damage mechanics. *Composites science and technology*, 67(13):2715–2727, 2007.

[281] ALJTR Matzenmiller, J Lubliner, and RL Taylor. A constitutive model

for anisotropic damage in fiber-composites. *Mechanics of materials*, 20(2): 125–152, 1995.

[282] Ren-Horng Maa and Jung-Ho Cheng. A cdm-based failure model for predicting strength of notched composite laminates. *Composites Part B: Engineering*, 33(6):479–489, 2002.

[283] D Perreux and F Thiebaud. Damaged elasto-plastic behaviour of [+ ϑ,- ϑ] n fibre-reinforced composite laminates in biaxial loading. *Composites science and technology*, 54(3):275–285, 1995.

[284] P F Liu and JY Zheng. Progressive failure analysis of carbon fiber/epoxy composite laminates using continuum damage mechanics. *Materials Science and Engineering: A*, 485(1-2):711–717, 2008.

[285] ST Pinho, L Iannucci, and P Robinson. Physically-based failure models and criteria for laminated fibre-reinforced composites with emphasis on fibre kinking: Part i: Development. *Composites Part A: Applied Science and Manufacturing*, 37(1):63–73, 2006.

[286] Jose Reinoso, Giuseppe Catalanotti, Antonio Blázquez, Pedro Areias, PedroP Camanho, and Frederico París. A consistent anisotropic damage model for laminated fiber-reinforced composites using the 3d-version of the puck failure criterion. *International Journal of Solids and Structures*, 126: 37–53, 2017.

[287] Mahdi Fakoor and Seyed Mohammad Navid Ghoreishi. Experimental and numerical investigation of progressive damage in composite laminates based on continuum damage mechanics. *Polymer Testing*, 70:533–543, 2018.

[288] Jiefei Gu, Ke Li, and Lei Su. A continuum damage model for intralaminar progressive failure analysis of cfrp laminates based on the modified puck's theory. *Materials*, 12(20):3292, 2019.

[289] Christian Gerendt, Aamir Dean, Thorsten Mahrholz, and Raimund Rolfes. On the progressive failure simulation and experimental validation of fiber metal laminate bolted joints. *Composite Structures*, 229: 111368, 2019.

[290] Bijan Mohammadi, Babak Fazlali, and Davood Salimi-Majd. Development of a continuum damage model for fatigue life prediction of laminated composites part a applied science and manufacturing. 2017.

[291] Sergej Diel and Otto Huber. A continuum damage mechanics model for the static and cyclic fatigue of cellular composites. *Materials*, 10(8):951, 2017.

[292] Arafat I Khan, Satchi Venkataraman, and Ian Miller. Fatigue failure predictions of laminated composites using mechanical properties degradation and continuum damage models. In *2018 AIAA/ASCE/AHS/ASC Structures, Structural Dynamics, and Materials Conference*, page 1642, 2018.

[293] Nadeem Ali Bhatti, Kyvia Pereira, and Magd Abdel Wahab. A continuum damage mechanics approach for fretting fatigue under out of phase loading. *Tribology International*, 117:39–51, 2018.

[294] Jordi Llobet, Pere Maimí, Albert Turon, Brian Lau Verndal Bak, Esben Lindgaard, Yasser Essa, and F Martin de la Escalera. Progressive damage modelling of notched carbon/epoxy laminates under tensile fatigue loadings. In *Proceedings of the 18th European Conference on Composite Materials, ECCM18, Athens, Greece, 25-28 June 2018*, 2018.

[295] Liang Zhang, Zhenyuan Gao, Robert A Haynes, Todd C Henry, and Wenbin Yu. An anisotropic continuum damage model for high-cycle fatigue. *Mechanics of Advanced Materials and Structures*, pages 1–15, 2020.

[296] Kevin V Williams, Reza Vaziri, and Anoush Poursartip. A physically based continuum damage mechanics model for thin laminated composite structures. *International Journal of Solids and Structures*, 40(9):2267–2300, 2003.

[297] Eun-Ho Kim, Mi-Sun Rim, In Lee, and Tae-Kyung Hwang. Composite damage model based on continuum damage mechanics and low velocity impact analysis of composite plates. *Composite Structures*, 95:123–134, 2013.

[298] Amir Shojaei, Guoqiang Li, PJ Tan, and Jacob Fish. Dynamic delamination in laminated fiber reinforced composites: A continuum damage mechanics approach. *International Journal of Solids and Structures*, 71:262–276, 2015.

[299] Aswani Kumar Bandaru and Suhail Ahmad. Modeling of progressive damage for composites under ballistic impact. *Composites Part B: Engineering*, 93:75–87, 2016.

[300] EV González, P Maimí, E Martín-Santos, A Soto, P Cruz, F Martín de la Escalera, and JR Sainz de Aja. Simulating drop-weight impact and compression after impact tests on composite laminates using conventional shell finite elements. *International Journal of Solids and Structures*, 144: 230–247, 2018.

[301] Rahul Singh Dhari, Nirav P Patel, Hongxu Wang, and Paul J Hazell. Progressive damage modeling and optimization of fibrous composites under ballistic impact loading. *Mechanics of Advanced Materials and Structures*, pages 1–18, 2019.

[302] Zdenek P Bazant and Gilles Pijaudier-Cabot. Nonlocal continuum damage, localization instability and convergence. *Journal of applied mechanics*, 55(2):287–293, 1988.

[303] René de Borst. Some recent issues in computational failure mechanics. *International Journal for Numerical Methods in Engineering*, 52(1-2):63–95, 2001.

[304] Erwan Tanné, Tianyi Li, Blaise Bourdin, J-J Marigo, and Corrado Maurini. Crack nucleation in variational phase-field models of brittle fracture. *Journal of the Mechanics and Physics of Solids*, 110:80–99, 2018.

[305] Stella Brach, Erwan Tanné, Blaise Bourdin, and Kaushik Bhattacharya. Phase-field study of crack nucleation and propagation in elastic–perfectly plastic bodies. *Computer Methods in Applied Mechanics and Engineering*, 353:44–65, 2019.

[306] Guowei Liu, Qingbin Li, Mohammed A Msekh, and Zheng Zuo. Abaqus implementation of monolithic and staggered schemes for quasi-static and dynamic fracture phase-field model. *Computational Materials Science*, 121:35–47, 2016.

[307] C Miehe, F Welschinger, and M Hofacker. Thermodynamically consistent phase-field models of fracture: Variational principles and multi-field fe implementations. *International Journal for Numerical Methods in Engineering*, 83(10):1273–1311, 2010.

[308] Osman Gültekin, Hüsnü Dal, and Gerhard A Holzapfel. A phase-field approach to model fracture of arterial walls: theory and finite element analysis. *Computer methods in applied mechanics and engineering*, 312:542–566, 2016.

[309] Alexander Schlüter, Adrian Willenbücher, Charlotte Kuhn, and Ralf Müller. Phase field approximation of dynamic brittle fracture. *Computational Mechanics*, 54(5):1141–1161, 2014.

[310] Charlotte Kuhn and Ralf Müller. A continuum phase field model for fracture. *Engineering Fracture Mechanics*, 77(18):3625–3634, 2010.

[311] M Hofacker and C Miehe. A phase field model of dynamic fracture: Robust field updates for the analysis of complex crack patterns. *International Journal for Numerical Methods in Engineering*, 93(3):276–301, 2013.

[312] Christian Miehe, Lisa-Marie Schaenzel, and Heike Ulmer. Phase field modeling of fracture in multi-physics problems. part i. balance of crack surface and failure criteria for brittle crack propagation in thermo-elastic solids. *Computer Methods in Applied Mechanics and Engineering*, 294:449–485, 2015.

[313] Marreddy Ambati, Tymofiy Gerasimov, and Laura De Lorenzis. Phase-field modeling of ductile fracture. *Computational Mechanics*, 55(5):1017–1040, 2015.

[314] Marreddy Ambati and Laura De Lorenzis. Phase-field modeling of brittle and ductile fracture in shells with isogeometric nurbs-based solid-shell elements. *Computer Methods in Applied Mechanics and Engineering*, 312: 351–373, 2016.

[315] Marreddy Ambati, Roland Kruse, and Laura De Lorenzis. A phase-field model for ductile fracture at finite strains and its experimental verification. *Computational Mechanics*, 57(1):149–167, 2016.

[316] Michael J Borden, Thomas JR Hughes, Chad M Landis, Amin Anvari, and Isaac J Lee. A phase-field formulation for fracture in ductile materials: Finite deformation balance law derivation, plastic degradation, and stress triaxiality effects. *Computer Methods in Applied Mechanics and Engineering*, 312:130–166, 2016.

[317] Charlotte Kuhn, Timo Noll, and Ralf Müller. On phase field modeling of ductile fracture. *GAMM-Mitteilungen*, 39(1):35–54, 2016.

[318] Y Heider and B Markert. A phase-field modeling approach of hydraulic fracture in saturated porous media. *Mechanics Research Communications*, 80:38–46, 2017.

[319] Wolfgang Ehlers and Chenyi Luo. A phase-field approach embedded in the theory of porous media for the description of dynamic hydraulic fracturing. *Computer Methods in Applied Mechanics and Engineering*, 315: 348–368, 2017.

[320] Udit Pillai, Yousef Heider, and Bernd Markert. A diffusive dynamic brittle fracture model for heterogeneous solids and porous materials with implementation using a user-element subroutine. *Computational Materials Science*, 153:36–47, 2018.

[321] Christian Miehe, HÜSNÜ Dal, L-M Schänzel, and A Raina. A phase-field model for chemo-mechanical induced fracture in lithium-ion battery electrode particles. *International Journal for Numerical Methods in Engineering*, 106(9):683–711, 2016.

[322] Markus Klinsmann, Daniele Rosato, Marc Kamlah, and Robert M McMeeking. Modeling crack growth during li insertion in storage particles using a fracture phase field approach. *Journal of the Mechanics and Physics of Solids*, 92:313–344, 2016.

[323] Thanh-Tung Nguyen, Danièle Waldmann, and Tinh Quoc Bui. Computational chemo-thermo-mechanical coupling phase-field model for complex fracture induced by early-age shrinkage and hydration heat in cement-based materials. *Computer Methods in Applied Mechanics and Engineering*, 348:1–28, 2019.

[324] Alexander Schlüter, Charlotte Kuhn, Ralf Müller, Marilena Tomut, Christina Trautmann, Helmut Weick, and Carolin Plate. Phase field modelling of dynamic thermal fracture in the context of irradiation damage. *Continuum Mechanics and Thermodynamics*, 29(4):977–988, 2017.

[325] S Masoud Marandi, S Hassan Nourbakhsh, M Botshekanan Dehkordi, and Hojjat Badnava. Finite element implementation of coupled temperature-rate dependent fracture using the phase field model. *Mechanics of Materials*, page 103449, 2020.

[326] Giovambattista Amendola, Mauro Fabrizio, and JM Golden. Thermomechanics of damage and fatigue by a phase field model. *Journal of Thermal Stresses*, 39(5):487–499, 2016.

[327] Roberto Alessi, Stefano Vidoli, and Laura De Lorenzis. A phenomenological approach to fatigue with a variational phase-field model: The one-dimensional case. *Engineering fracture mechanics*, 190:53–73, 2018.

[328] P Carrara, M Ambati, R Alessi, and L De Lorenzis. A framework to model the fatigue behavior of brittle materials based on a variational

phase-field approach. *Computer Methods in Applied Mechanics and Engineering*, 361:112731, 2020.

[329] Young-Jo Cheon and Hyun-Gyu Kim. An adaptive material point method coupled with a phase-field fracture model for brittle materials. *International Journal for Numerical Methods in Engineering*, 120(8):987–1010, 2019.

[330] Fadi Aldakheel, Blaž Hudobivnik, Ali Hussein, and Peter Wriggers. Phase-field modeling of brittle fracture using an efficient virtual element scheme. *Computer Methods in Applied Mechanics and Engineering*, 341:443–466, 2018.

[331] Fadi Aldakheel, Blaž Hudobivnik, and Peter Wriggers. Virtual element formulation for phase-field modeling of ductile fracture. *International Journal for Multiscale Computational Engineering*, 17(2), 2019.

[332] Michael J Borden, Thomas JR Hughes, Chad M Landis, and Clemens V Verhoosel. A higher-order phase-field model for brittle fracture: Formulation and analysis within the isogeometric analysis framework. *Computer Methods in Applied Mechanics and Engineering*, 273:100–118, 2014.

[333] Fatemeh Amiri, Daniel Millán, Yongxing Shen, Timon Rabczuk, and M Arroyo. Phase-field modeling of fracture in linear thin shells. *Theoretical and Applied Fracture Mechanics*, 69:102–109, 2014.

[334] Heike Ulmer, Martina Hofacker, and Christian Miehe. Phase field modeling of fracture in plates and shells. *PAMM*, 12(1):171–172, 2012.

[335] Josef Kiendl, Marreddy Ambati, Laura De Lorenzis, Hector Gomez, and Alessandro Reali. Phase-field description of brittle fracture in plates and shells. *Computer Methods in Applied Mechanics and Engineering*, 312:374–394, 2016.

[336] José Reinoso, Marco Paggi, and Christian Linder. Phase field modeling of brittle fracture for enhanced assumed strain shells at large deformations:

formulation and finite element implementation. *Computational Mechanics*, 59(6):981–1001, 2017.

[337] Jian-Ying Wu, Vinh Phu Nguyen, Chi Thanh Nguyen, Danas Sutula, Stephane Bordas, and Sina Sinaie. Phase field modeling of fracture. *Advances in Applied Mechancis: Multi-scale Theory and Computation*, 52, 2018.

[338] Gergely Molnár and Anthony Gravouil. 2d and 3d abaqus implementation of a robust staggered phase-field solution for modeling brittle fracture. *Finite Elements in Analysis and Design*, 130:27–38, 2017.

[339] Jian-Ying Wu, Yuli Huang, and Vinh Phu Nguyen. On the bfgs monolithic algorithm for the unified phase field damage theory. *Computer Methods in Applied Mechanics and Engineering*, 360:112704, 2020.

[340] T Gerasimov and L De Lorenzis. A line search assisted monolithic approach for phase-field computing of brittle fracture. *Computer Methods in Applied Mechanics and Engineering*, 312:276–303, 2016.

[341] Jian-Ying Wu and Yuli Huang. Comprehensive implementations of phase-field damage models in abaqus. *Theoretical and Applied Fracture Mechanics*, 106:102440, 2020.

[342] Siobhan Burke, Christoph Ortner, and Endre Süli. An adaptive finite element approximation of a variational model of brittle fracture. *SIAM Journal on Numerical Analysis*, 48(3):980–1012, 2010.

[343] Marco Artina, Massimo Fornasier, Stefano Micheletti, and Simona Perotto. Anisotropic mesh adaptation for crack detection in brittle materials. *SIAM Journal on Scientific Computing*, 37(4):B633–B659, 2015.

[344] Tymofiy Gerasimov, Ulrich Römer, Jaroslav Vondřejc, Hermann G Matthies, and Laura De Lorenzis. Stochastic phase-field modeling of brittle fracture: computing multiple crack patterns and their probabilities. *Computer Methods in Applied Mechanics and Engineering*, 372:113353, 2020.

[345] Hanen Amor, Jean-Jacques Marigo, and Corrado Maurini. Regularized formulation of the variational brittle fracture with unilateral contact: Numerical experiments. *Journal of the Mechanics and Physics of Solids*, 57(8): 1209–1229, 2009.

[346] Kim Pham, Jean-Jacques Marigo, and Corrado Maurini. The issues of the uniqueness and the stability of the homogeneous response in uniaxial tests with gradient damage models. *Journal of the Mechanics and Physics of Solids*, 59(6):1163–1190, 2011.

[347] A Quintanas-Corominas, J Reinoso, E Casoni, A Turon, and JA Mayugo. A phase field approach to simulate intralaminar and translaminar fracture in long fiber composite materials. *Composite Structures*, 220:899–911, 2019.

[348] T Wu, A Carpiuc-Prisacari, Martin Poncelet, and L De Lorenzis. Phase-field simulation of interactive mixed-mode fracture tests on cement mortar with full-field displacement boundary conditions. *Engineering Fracture Mechanics*, 182:658–688, 2017.

[349] KH Pham, K Ravi-Chandar, and CM Landis. Experimental validation of a phase-field model for fracture. *International Journal of Fracture*, 205(1): 83–101, 2017.

[350] A Dean, J Reinoso, NK Jha, E Mahdi, and R Rolfes. A phase field approach for ductile fracture of short fibre reinforced composites. *Theoretical and Applied Fracture Mechanics*, page 102495, 2020.

[351] Rudy JM Geelen, Yingjie Liu, Tianchen Hu, Michael R Tupek, and John E Dolbow. A phase-field formulation for dynamic cohesive fracture. *Computer Methods in Applied Mechanics and Engineering*, 348:680–711, 2019.

[352] Jian-Ying Wu. A unified phase-field theory for the mechanics of damage and quasi-brittle failure. *Journal of the Mechanics and Physics of Solids*, 103: 72–99, 2017.

[353] Tushar Kanti Mandal, Vinh Phu Nguyen, and Jian-Ying Wu. Length scale and mesh bias sensitivity of phase-field models for brittle and cohesive fracture. *Engineering Fracture Mechanics*, 217:106532, 2019.

[354] Jian-Ying Wu, Tushar Kanti Mandal, and Vinh Phu Nguyen. A phase-field regularized cohesive zone model for hydrogen assisted cracking. *Computer Methods in Applied Mechanics and Engineering*, 358:112614, 2020.

[355] Pascal J Loew, Bernhard Peters, and Lars AA Beex. Fatigue phase-field damage modeling of rubber using viscous dissipation: Crack nucleation and propagation. *Mechanics of Materials*, 142:103282, 2020.

[356] Guangda Lu and Jianbing Chen. A new nonlocal macro-meso-scale consistent damage model for crack modeling of quasi-brittle materials. *Computer Methods in Applied Mechanics and Engineering*, 362:112802, 2020.

[357] Peng Zhang, Xiaofei Hu, Shangtong Yang, and Weian Yao. Modelling progressive failure in multi-phase materials using a phase field method. *Engineering Fracture Mechanics*, 209:105–124, 2019.

[358] De-Cheng Feng and Jian-Ying Wu. Phase-field regularized cohesive zone model (czm) and size effect of concrete. *Engineering Fracture Mechanics*, 197:66–79, 2018.

[359] Clemens V Verhoosel and René Borst. A phase-field model for cohesive fracture. *International Journal for numerical methods in Engineering*, 96(1): 43–62, 2013.

[360] Julien Vignollet, Stefan May, René De Borst, and Clemens V Verhoosel. Phase-field models for brittle and cohesive fracture. *Meccanica*, 49(11): 2587–2601, 2014.

[361] Thanh-Tung Nguyen, Julien Yvonnet, Q-Z Zhu, Michel Bornert, and Camille Chateau. A phase-field method for computational modeling of interfacial damage interacting with crack propagation in realistic microstructures obtained by microtomography. *Computer Methods in Applied Mechanics and Engineering*, 312:567–595, 2016.

[362] Pranesh Roy, SP Deepu, Anil Pathrikar, Debasish Roy, and JN Reddy. Phase field based peridynamics damage model for delamination of composite structures. *Composite Structures*, 180:972–993, 2017.

[363] Bensingh Dhas, Masiur Rahaman, Kiran Akella, Debasish Roy, JN Reddy, et al. A phase-field damage model for orthotropic materials and delamination in composites. *Journal of Applied Mechanics*, 85(1), 2018.

[364] A Quintanas-Corominas, A Turon, J Reinoso, E Casoni, M Paggi, and JA Mayugo. A phase field approach enhanced with a cohesive zone model for modeling delamination induced by matrix cracking. *Computer Methods in Applied Mechanics and Engineering*, 358:112618, 2020.

[365] Valerio Carollo, José Reinoso, and Marco Paggi. A 3d finite strain model for intralayer and interlayer crack simulation coupling the phase field approach and cohesive zone model. *Composite Structures*, 182:636–651, 2017.

[366] S Teichtmeister, D Kienle, F Aldakheel, and M-A Keip. Phase field modeling of fracture in anisotropic brittle solids. *International Journal of Non-Linear Mechanics*, 97:1–21, 2017.

[367] Bin Li, Christian Peco, Daniel Millán, Irene Arias, and Marino Arroyo. Phase-field modeling and simulation of fracture in brittle materials with strongly anisotropic surface energy. *International Journal for Numerical Methods in Engineering*, 102(3-4):711–727, 2015.

[368] José Reinoso, A Arteiro, Marco Paggi, and PP Camanho. Strength prediction of notched thin ply laminates using finite fracture mechanics and the phase field approach. *Composites Science and Technology*, 150:205–216, 2017.

[369] Sundararajan Natarajan, Ratna Kumar Annabattula, et al. Modeling crack propagation in variable stiffness composite laminates using the phase field method. *Composite Structures*, 209:424–433, 2019.

[370] José Reinoso, Percy Durand, Pattabhi Ramaiah Budarapu, and Marco Paggi. Crack patterns in heterogenous rocks using a combined phase field-cohesive interface modeling approach: A numerical study. *Energies*, 12(6):965, 2019.

[371] T Guillén-Hernández, IG García, J Reinoso, and M Paggi. A micromechanical analysis of inter-fiber failure in long reinforced composites based on the phase field approach of fracture combined with the cohesive zone model. *International Journal of Fracture*, pages 1–23, 2019.

[372] Marco Paggi and José Reinoso. Revisiting the problem of a crack impinging on an interface: a modeling framework for the interaction between the phase field approach for brittle fracture and the interface cohesive zone model. *Computer Methods in Applied Mechanics and Engineering*, 321: 145–172, 2017.

[373] Peng Zhang, Yaoqi Feng, Tinh Quoc Bui, Xiaofei Hu, and Weian Yao. Modelling distinct failure mechanisms in composite materials by a combined phase field method. *Composite Structures*, 232:111551, 2020.

[374] T Guillén-Hernández, A Quintana-Corominas, IG García, J Reinoso, M Paggi, and A Turón. In-situ strength effects in long fibre reinforced composites: a micro-mechanical analysis using the phase field approach of fracture. *Theoretical and Applied Fracture Mechanics*, page 102621, 2020.

[375] A Dean, PK Asur Vijaya Kumar, J Reinoso, C Gerendt, M Paggi, E Mahdi, and R Rolfes. A multi phase-field fracture model for long fiber reinforced composites based on the puck theory of failure. *Composite Structures*, page 112446, 2020.

[376] Sindhu Nagaraja, Mohamed Elhaddad, Marreddy Ambati, Stefan Kollmannsberger, Laura De Lorenzis, and Ernst Rank. Phase-field modeling of brittle fracture with multi-level hp-fem and the finite cell method. *Computational Mechanics*, pages 1–18, 2017.

[377] RU Patil, BK Mishra, and IV Singh. An adaptive multiscale phase field method for brittle fracture. *Computer Methods in Applied Mechanics and Engineering*, 329:254–288, 2018.

[378] Savvas P Triantafyllou and Emmanouil G Kakouris. A generalized phase field multiscale finite element method for brittle fracture. *International Journal for Numerical Methods in Engineering*, 121(9):1915–1945, 2020.

[379] Tymofiy Gerasimov, Nima Noii, Olivier Allix, and Laura De Lorenzis. A non-intrusive global/local approach applied to phase-field modeling of brittle fracture. *Advanced Modeling and Simulation in Engineering Sciences*, 5(1):14, 2018.

[380] W. E and J. Lu. Multiscale modeling. *Scholarpedia*, 6(10):11527, 2011. doi: 10.4249/scholarpedia.11527. revision #91540.

[381] E Weinan. *Principles of multiscale modeling*. Cambridge University Press, 2011.

[382] Marco AR Ferreira and Herbert KH Lee. *Multiscale modeling: a Bayesian perspective*. Springer Science & Business Media, 2007.

[383] José E Andrade and Xuxin Tu. Multiscale framework for behavior prediction in granular media. *Mechanics of Materials*, 41(6):652–669, 2009.

[384] Young W Kwon, David H Allen, and Ramesh Talreja. *Multiscale modeling and simulation of composite materials and structures*, volume 47. Springer, 2008.

[385] E Weinan and B Engquist. The heterogeneous multi-scale methods. *Communications in Mathematical Sciences*, 2003.

[386] Assyr Abdulle, E Weinan, Björn Engquist, and Eric Vanden-Eijnden. The heterogeneous multiscale method. *Acta Numerica*, 21:1–87, 2012.

[387] Lionel Gendre, Olivier Allix, Pierre Gosselet, and François Comte. Non-intrusive and exact global/local techniques for structural problems with local plasticity. *Computational Mechanics*, 44(2):233–245, 2009.

[388] Maxence Wangermez, Olivier Allix, Pierre-Alain Guidault, Oana Ciobanu, and Christian Rey. Interface coupling method for the global–local analysis of heterogeneous models: A second-order homogenization-based strategy. *Computer Methods in Applied Mechanics and Engineering*, 365:113032, 2020.

[389] Bassam El Said, Federica Daghia, Dmitry Ivanov, and Stephen R Hallett. An iterative multiscale modelling approach for nonlinear analysis of 3d composites. *International Journal of Solids and Structures*, 132:42–58, 2018.

[390] Charbel Farhat, Michel Lesoinne, Patrick LeTallec, Kendall Pierson, and Daniel Rixen. Feti-dp: a dual–primal unified feti method—part i: A faster alternative to the two-level feti method. *International journal for numerical methods in engineering*, 50(7):1523–1544, 2001.

[391] Margarita Akterskaia, Eelco Jansen, Stephen R Hallett, Paul M Weaver, and Raimund Rolfes. Progressive failure analysis using global-local coupling including intralaminar failure and debonding. *AIAA Journal*, pages 3078–3089, 2019.

[392] Sina Hühne, José Reinoso, Eelco Jansen, and Raimund Rolfes. A two-way loose coupling procedure for investigating the buckling and damage behaviour of stiffened composite panels. *Composite Structures*, 136:513–525, 2016.

[393] Margarita Akterskaia, Eelco Jansen, Sina Hühne, and Raimund Rolfes. Efficient progressive failure analysis of multi-stringer stiffened composite panels through a two-way loose coupling global-local approach. *Composite Structures*, 183:137–145, 2018.

[394] Pierre Kerfriden, Olivier Allix, and Pierre Gosselet. A three-scale domain decomposition method for the 3d analysis of debonding in laminates. *Computational mechanics*, 44(3):343–362, 2009.

[395] Federica Daghia and Pierre Ladevèze. A micro–meso computational

strategy for the prediction of the damage and failure of laminates. *Composite structures*, 94(12):3644–3653, 2012.

[396] Pierre Kerfriden, Jean-Charles Passieux, and Stephane Pierre-Alain Bordas. Local/global model order reduction strategy for the simulation of quasi-brittle fracture. *International Journal for Numerical Methods in Engineering*, 89(2):154–179, 2012.

[397] Pierre Kerfriden, Olivier Goury, Timon Rabczuk, and Stephane Pierre-Alain Bordas. A partitioned model order reduction approach to rationalise computational expenses in nonlinear fracture mechanics. *Computer methods in applied mechanics and engineering*, 256:169–188, 2013.

[398] Karel Matouš, Marc GD Geers, Varvara G Kouznetsova, and Andrew Gillman. A review of predictive nonlinear theories for multiscale modeling of heterogeneous materials. *Journal of Computational Physics*, 330: 192–220, 2017.

[399] OH Aliyu. Analytical, numerical and computational multiscale modelling techniques for heterogenous materials: A review. *ARID ZONE JOURNAL OF ENGINEERING, TECHNOLOGY AND ENVIRONMENT*, 15(3):488–509, 2019.

[400] Jean-Claude Michel, Hervé Moulinec, and Pierre Suquet. Effective properties of composite materials with periodic microstructure: a computational approach. *Computer methods in applied mechanics and engineering*, 172(1-4):109–143, 1999.

[401] Christian Miehe, Jörg Schröder, and Martin Becker. Computational homogenization analysis in finite elasticity: material and structural instabilities on the micro-and macro-scales of periodic composites and their interaction. *Computer Methods in Applied Mechanics and Engineering*, 191 (44):4971–5005, 2002.

[402] Shuguang Li. General unit cells for micromechanical analyses of unidi-

rectional composites. *Composites Part A: applied science and manufacturing*, 32(6):815–826, 2001.

[403] Shuguang Li. Boundary conditions for unit cells from periodic microstructures and their implications. *Composites Science and technology*, 68(9):1962–1974, 2008.

[404] Jacob Fish and Rong Fan. Mathematical homogenization of nonperiodic heterogeneous media subjected to large deformation transient loading. *International Journal for numerical methods in engineering*, 76(7):1044–1064, 2008.

[405] Andrea Bacigalupo, Lorenzo Morini, and Amdrea Piccolroaz. Multiscale asymptotic homogenization analysis of thermo-diffusive composite materials. *International Journal of Solids and Structures*, 85:15–33, 2016.

[406] A Visrolia and M Meo. Multiscale damage modelling of 3d weave composite by asymptotic homogenisation. *Composite Structures*, 95:105–113, 2013.

[407] Qing-Xiang Meng, Huan-Ling Wang, Wei-Ya Xu, and Yu-Long Chen. Numerical homogenization study on the effects of columnar jointed structure on the mechanical properties of rock mass. *International Journal of Rock Mechanics and Mining Sciences*, 124:104127, 2019.

[408] YJ Cao, WQ Shen, Jian-Fu Shao, and Wei Wang. Numerical homogenization of elastic properties and plastic yield stress of rock-like materials with voids and inclusions at same scale. *European Journal of Mechanics-A/Solids*, 81:103958, 2020.

[409] Saeid Nezamabadi, Michel Potier-Ferry, Hamid Zahrouni, and Julien Yvonnet. Compressive failure of composites: A computational homogenization approach. *Composite Structures*, 127:60–68, 2015.

[410] Xinxing Han, Chenghai Xu, Weihua Xie, and Songhe Meng. Multiscale computational homogenization of woven composites from microscale to

mesoscale using data-driven self-consistent clustering analysis. *Composite Structures*, 220:760–768, 2019.

[411] Frédéric Feyel. A multilevel finite element method (fe2) to describe the response of highly non-linear structures using generalized continua. *Computer Methods in applied Mechanics and engineering*, 192(28-30):3233–3244, 2003.

[412] Frédéric Feyel and Jean-Louis Chaboche. Fe2 multiscale approach for modelling the elastoviscoplastic behaviour of long fibre sic/ti composite materials. *Computer methods in applied mechanics and engineering*, 183(3-4): 309–330, 2000.

[413] Frédéric Feyel and Jean-Louis Chaboche. Multi-scale non-linear fe2 analysis of composite structures: damage and fiber size effects. *Revue Européenne des Éléments Finis*, 10(2-4):449–472, 2001.

[414] I Özdemir, WAM Brekelmans, and Marc GD Geers. Fe2 computational homogenization for the thermo-mechanical analysis of heterogeneous solids. *Computer Methods in Applied Mechanics and Engineering*, 198(3-4): 602–613, 2008.

[415] F El Halabi, D González, A Chico, and M Doblaré. Fe2 multiscale in linear elasticity based on parametrized microscale models using proper generalized decomposition. *Computer Methods in Applied Mechanics and Engineering*, 257:183–202, 2013.

[416] Shibo Yan, Xi Zou, Mohammad Ilkhani, and Arthur Jones. An efficient multiscale surrogate modelling framework for composite materials considering progressive damage based on artificial neural networks. *Composites Part B: Engineering*, page 108014, 2020.

[417] Sadik L Omairey, Peter D Dunning, and Srinivas Sriramula. Multiscale surrogate-based framework for reliability analysis of unidirectional frp composites. *Composites Part B: Engineering*, 173:106925, 2019.

[418] Sadik L Omaireya, Peter D Dunninga, and Srinivas Sriramulaab. Multiscale fea-based reliability analysis framework for frp composites. 2019.

[419] Georgios Balokas, Steffen Czichon, and Raimund Rolfes. Neural network assisted multiscale analysis for the elastic properties prediction of 3d braided composites under uncertainty. *Composite Structures*, 183:550–562, 2018.

[420] Michael J Bogdanor, Caglar Oskay, and Stephen B Clay. Multiscale modeling of failure in composites under model parameter uncertainty. *Computational mechanics*, 56(3):389–404, 2015.

[421] Chunwang He, Jingran Ge, Dexing Qi, Jiaying Gao, Yanfei Chen, Jun Liang, and Daining Fang. A multiscale elasto-plastic damage model for the nonlinear behavior of 3d braided composites. *Composites Science and Technology*, 171:21–33, 2019.

[422] Amir Shojaei, Guoqiang Li, Jacob Fish, and PJ Tan. Multi-scale constitutive modeling of ceramic matrix composites by continuum damage mechanics. *International Journal of Solids and Structures*, 51(23-24):4068–4081, 2014.

[423] Ling Wu, Ludovic Noels, L Adam, and Issam Doghri. A multiscale mean-field homogenization method for fiber-reinforced composites with gradient-enhanced damage models. *Computer Methods in Applied Mechanics and Engineering*, 233:164–179, 2012.

[424] Ling Wu, Federico Sket, Jon M Molina-Aldareguia, Ahmed Makradi, Laurent Adam, Issam Doghri, and Ludovic Noels. A study of composite laminates failure using an anisotropic gradient-enhanced damage mean-field homogenization model. *Composite Structures*, 126:246–264, 2015.

[425] RU Patil, BK Mishra, Indra Vir Singh, and TQ Bui. A new multiscale phase field method to simulate failure in composites. *Advances in Engineering Software*, 126:9–33, 2018.

[426] M Holl, S Loehnert, and P Wriggers. An adaptive multiscale method for crack propagation and crack coalescence. *International Journal for Numerical Methods in Engineering*, 93(1):23–51, 2013.

[427] RU Patil, BK Mishra, and IV Singh. A new multiscale xfem for the elastic properties evaluation of heterogeneous materials. *International Journal of Mechanical Sciences*, 122:277–287, 2017.

[428] Ritukesh Bharali, Fredrik Larsson, and Ralf Jänicke. Computational homogenisation of phase-field fracture. *European Journal of Mechanics-A/Solids*, page 104247, 2021.

[429] Luigi Ambrosio and Vincenzo Maria Tortorelli. Approximation of functional depending on jumps by elliptic functional via t-convergence. *Communications on Pure and Applied Mathematics*, 43(8):999–1036, 1990.

[430] Kim Pham, Hanen Amor, Jean-Jacques Marigo, and Corrado Maurini. Gradient damage models and their use to approximate brittle fracture. *International Journal of Damage Mechanics*, 20(4):618–652, 2011.

[431] Luigi Ambrosio and VINCENZO Tortorelli. On the approximation of free discontinuity problems. 1992.

[432] Marreddy Ambati, Tymofiy Gerasimov, and Laura De Lorenzis. A review on phase-field models of brittle fracture and a new fast hybrid formulation. *Computational Mechanics*, 55(2):383–405, 2015.

[433] Kim Pham and Jean-Jacques Marigo. Approche variationnelle de l'endommagement: I. les concepts fondamentaux. *Comptes Rendus Mécanique*, 338(4):191–198, 2010.

[434] Tymofiy Gerasimov and Laura De Lorenzis. On penalization in variational phase-field models of brittle fracture. *Computer Methods in Applied Mechanics and Engineering*, 2019.

[435] M Schwab, M Todt, M Wolfahrt, and HE Pettermann. Failure mechanism based modelling of impact on fabric reinforced composite lam-

inates based on shell elements. *Composites Science and Technology*, 128: 131–137, 2016.

[436] George C Sih, PC Paris, and Fazil Erdogan. Crack-tip, stress-intensity factors for plane extension and plate bending problems. *Journal of Applied Mechanics*, 29(2):306–312, 1962.

[437] S J Rouzegar and M Mirzaei. Modeling dynamic fracture in kirchhoff plates and shells using the extended finite element method. *Scientia Iranica*, 20(1):120–130, 2013.

[438] Xue Zhang, Chet Vignes, Scott W Sloan, and Daichao Sheng. Numerical evaluation of the phase-field model for brittle fracture with emphasis on the length scale. *Computational Mechanics*, 59(5):737–752, 2017.

[439] Pedro Areias and Timon Rabczuk. Finite strain fracture of plates and shells with configurational forces and edge rotations. *International Journal for Numerical Methods in Engineering*, 94(12):1099–1122, 2013.

[440] G Kikis, M Ambati, L De Lorenzis, and S Klinkel. Phase-field model of brittle fracture in reissner–mindlin plates and shells. *Computer Methods in Applied Mechanics and Engineering*, 373:113490, 2021.

[441] I Scheider and W Brocks. Cohesive elements for thin-walled structures. *Computational Materials Science*, 37(1-2):101–109, 2006.

[442] Ingo Scheider and Wolfgang Brocks. Residual strength prediction of a complex structure using crack extension analyses. *Engineering Fracture Mechanics*, 76(1):149–163, 2009.

[443] Wolfgang Brocks, Ingo Scheider, and Manfred Schödel. Simulation of crack extension in shell structures and prediction of residual strength. *Archive of Applied Mechanics*, 76(11-12):655–665, 2006.

[444] Eric Lorentz. A nonlocal damage model for plain concrete consistent with cohesive fracture. *International Journal of Fracture*, 207(2):123–159, 2017.

[445] Udit Pillai, Savvas P Triantafyllou, Yasser Essa, and Federico Martin de la Escalera. An anisotropic cohesive phase field model for quasi-brittle fractures in thin fibre-reinforced composites. *Composite Structures*, 252: 112635, 2020.

[446] Zdeněk P Bažant. Concrete fracture models: testing and practice. *Engineering fracture mechanics*, 69(2):165–205, 2002.

[447] Christian G Hoover and Zdeněk P Bažant. Cohesive crack, size effect, crack band and work-of-fracture models compared to comprehensive concrete fracture tests. *International Journal of Fracture*, 187(1):133–143, 2014.

[448] Thanh Tung Nguyen, Julien Réthoré, and Marie-Christine Baietto. Phase field modelling of anisotropic crack propagation. *European Journal of Mechanics-A/Solids*, 65:279–288, 2017.

[449] LMA Cahill, Sundararajan Natarajan, Stephane Pierre Alain Bordas, Ronan M O'Higgins, and Conor T McCarthy. An experimental/numerical investigation into the main driving force for crack propagation in unidirectional fibre-reinforced composite laminae. *Composite Structures*, 107: 119–130, 2014.

[450] Jian-Ying Wu, Vinh Phu Nguyen, Hao Zhou, and Yuli Huang. A variationally consistent phase-field anisotropic damage model for fracture. *Computer Methods in Applied Mechanics and Engineering*, 358:112629, 2020.

[451] Mary F Wheeler, T Wick, and W Wollner. An augmented-lagrangian method for the phase-field approach for pressurized fractures. *Computer Methods in Applied Mechanics and Engineering*, 271:69–85, 2014.

[452] Xue Zhang, Scott W Sloan, Chet Vignes, and Daichao Sheng. A modification of the phase-field model for mixed mode crack propagation in rock-like materials. *Computer Methods in Applied Mechanics and Engineering*, 322:123–136, 2017.

[453] Vinh Phu Nguyen and Jian-Ying Wu. Modeling dynamic fracture of solids with a phase-field regularized cohesive zone model. *Computer Methods in Applied Mechanics and Engineering*, 340:1000–1022, 2018.

[454] Jian-Ying Wu. A geometrically regularized gradient-damage model with energetic equivalence. *Computer Methods in Applied Mechanics and Engineering*, 328:612–637, 2018.

[455] Jian-Ying Wu. Robust numerical implementation of non-standard phase-field damage models for failure in solids. *Computer Methods in Applied Mechanics and Engineering*, 340:767–797, 2018.

[456] Jian-Ying Wu and Vinh Phu Nguyen. A length scale insensitive phase-field damage model for brittle fracture. *Journal of the Mechanics and Physics of Solids*, 119:20–42, 2018.

[457] *Developer Reference for Intel Math Kernel Library - Fortran*. Intel Corporation, May 2019. URL `https://software.intel.com/en-us/mkl-developer-reference-fortran-intel-mkl-pardiso-parallel-direct-sparse-s`

[458] Tao Wang, Xuan Ye, Zhanli Liu, Dongyang Chu, and Zhuo Zhuang. Modeling the dynamic and quasi-static compression-shear failure of brittle materials by explicit phase field method. *Computational Mechanics*, 64 (6):1537–1556, 2019.

[459] M L Benzeggagh and MJCS Kenane. Measurement of mixed-mode delamination fracture toughness of unidirectional glass/epoxy composites with mixed-mode bending apparatus. *Composites science and technology*, 56(4):439–449, 1996.

[460] OxeonAB. TeXtreme. http://www.textreme.com/, 2003.

[461] DAMTEXproject. Report of FE models for the prediction of impact and compression after impact tests. Technical Report E4.2, E4.3, E5.1 (2013-DAM-01-IT10), Aernnova Engineering Division S.A. (Spain) ; AMADE Polytechnic school, University of Girona (Spain), 2014.

[462] Ahmed Wagih, P Maimí, EV González, N Blanco, JR Sainz de Aja, FM De La Escalera, R Olsson, and E Alvarez. Damage sequence in thin-ply composite laminates under out-of-plane loading. *Composites Part A: Applied Science and Manufacturing*, 87:66–77, 2016.

[463] Zdenek P Bazant. *Fracture and size effect in concrete and other quasibrittle materials*. Routledge, 2019.

[464] Hilton Ahmad. *Finite element-based strength prediction for notched and mechanically fastened woven fabric composites*. PhD thesis, University of Surrey, 2012.

[465] FLAXPREG. https://eco-technilin.com/en/!products/vstc3=flaxpreg, 2012.

[466] Robert A Gingold and Joseph J Monaghan. Smoothed particle hydrodynamics: theory and application to non-spherical stars. *Monthly notices of the royal astronomical society*, 181(3):375–389, 1977.

[467] MH Siemann and Stefan Andreas Ritt. Novel particle distributions for sph bird-strike simulations. *Computer Methods in Applied Mechanics and Engineering*, 343:746–766, 2019.

[468] MA Lavoie, A Gakwaya, M Nejad Ensan, DG Zimcik, and D Nandlall. Bird's substitute tests results and evaluation of available numerical methods. *International Journal of Impact Engineering*, 36(10-11):1276–1287, 2009.

[469] Christian Miehe. Strain-driven homogenization of inelastic microstructures and composites based on an incremental variational formulation. *International Journal for numerical methods in engineering*, 55(11):1285–1322, 2002.

[470] JFW Bishop and Rodney Hill. Xlvi. a theory of the plastic distortion of a polycrystalline aggregate under combined stresses. *The London, Edinburgh, and Dublin Philosophical Magazine and Journal of Science*, 42(327): 414–427, 1951.

[471] D Garoz, FA Gilabert, RDB Sevenois, SWF Spronk, and Wim Van Paepegem. Consistent application of periodic boundary conditions in implicit and explicit finite element simulations of damage in composites. *Composites Part B: Engineering*, 168:254–266, 2019.

[472] Jacob Aboudi and Michael Ryvkin. The effect of localized damage on the behavior of composites with periodic microstructure. *International Journal of Engineering Science*, 52:41–55, 2012.

[473] Yunfa Zhang, Zihui Xia, and Fernand Ellyin. Nonlinear viscoelastic micromechanical analysis of fibre-reinforced polymer laminates with damage evolution. *International journal of solids and structures*, 42(2):591–604, 2005.

[474] AR Melro, PP Camanho, FM Andrade Pires, and ST Pinho. Micromechanical analysis of polymer composites reinforced by unidirectional fibres: Part ii–micromechanical analyses. *International Journal of Solids and Structures*, 50(11-12):1906–1915, 2013.

[475] E Tikarrouchine, Adil Benaarbia, George Chatzigeorgiou, and Fodil Meraghni. Non-linear fe2 multiscale simulation of damage, micro and macroscopic strains in polyamide 66-woven composite structures: analysis and experimental validation. *Composite Structures*, 255:112926, 2021.

[476] Norbert Wiener. The homogeneous chaos. american journal of mathematics. 1938.

[477] S. Tyson, D. Donovan, B. Thompson, S. Lynch, and M. Tas. Uncertainty modelling with polynomialchaos expansion: Stage 1 – final report. Technical Report 978-1-74272-173-6, The University of Queensland, Australia, 2015.

[478] Jonathan Feinberg and Hans Petter Langtangen. Chaospy: An open source tool for designing methods of uncertainty quantification. *Journal of Computational Science*, 11:46–57, 2015.

[479] John J Hopfield. Neural networks and physical systems with emergent collective computational abilities. *Proceedings of the national academy of sciences*, 79(8):2554–2558, 1982.

[480] Anshul Agarwal and Lorenz T Biegler. A trust-region framework for constrained optimization using reduced order modeling. *Optimization and Engineering*, 14(1):3–35, 2013.

[481] Jun Han and Claudio Moraga. The influence of the sigmoid function parameters on the speed of backpropagation learning. In *International Workshop on Artificial Neural Networks*, pages 195–201. Springer, 1995.

[482] Mian Mian Lau and King Hann Lim. Investigation of activation functions in deep belief network. In *2017 2nd international conference on control and robotics engineering (ICCRE)*, pages 201–206. IEEE, 2017.

[483] Konstantin Eckle and Johannes Schmidt-Hieber. A comparison of deep networks with relu activation function and linear spline-type methods. *Neural Networks*, 110:232–242, 2019.

[484] Rob A Dunne and Norm A Campbell. On the pairing of the softmax activation and cross-entropy penalty functions and the derivation of the softmax activation function. In *Proc. 8th Aust. Conf. on the Neural Networks, Melbourne*, volume 181, page 185. Citeseer, 1997.

[485] Girish Chandra Tripathi, Meenakshi Rawat, and Karun Rawat. Swish activation based deep neural network predistorter for rf-pa. In *TENCON 2019-2019 IEEE Region 10 Conference (TENCON)*, pages 1239–1242. IEEE, 2019.

[486] David E Rumelhart, Geoffrey E Hinton, and Ronald J Williams. Learning representations by back-propagating errors. *nature*, 323(6088):533–536, 1986.

[487] Sepp Hochreiter and Jürgen Schmidhuber. Long short-term memory. *Neural computation*, 9(8):1735–1780, 1997.

[488] Yann LeCun, Yoshua Bengio, et al. Convolutional networks for images, speech, and time series. *The handbook of brain theory and neural networks*, 3361(10):1995, 1995.

[489] Teuvo Kohonen. Self-organized formation of topologically correct feature maps. *Biological cybernetics*, 43(1):59–69, 1982.

[490] T. Kohonen and T. Honkela. Kohonen network. *Scholarpedia*, 2(1):1568, 2007. doi: 10.4249/scholarpedia.1568. revision #127841.

[491] David S Broomhead and David Lowe. Radial basis functions, multivariable functional interpolation and adaptive networks. Technical report, Royal Signals and Radar Establishment Malvern (United Kingdom), 1988.

[492] JMJ Murre, RH Phaf, and G Wolters. Calm networks: a modular approach to supervised and unsupervised learning. In *Proceedings of the International Joint Conference on Neural Networks*, volume 1, pages 649–656, 1989.

[493] Jacob MJ Murre. *Learning and categorization in modular neural networks*. Psychology Press, 2014.

[494] F Dan Foresee and Martin T Hagan. Gauss-newton approximation to bayesian learning. In *Proceedings of International Conference on Neural Networks (ICNN'97)*, volume 3, pages 1930–1935. IEEE, 1997.

[495] Wei Tan and Emilio Martínez-Pañeda. Phase field predictions of microscopic fracture and r-curve behaviour of fibre-reinforced composites. *Composites Science and Technology*, 202:108539, 2021.

A

Appendices

A.1 Jacobian matrix for coordinate transformation in Reissner-Mindlin shell elements

The Jacobian $[\mathbf{J}]$ for coordinate transformation mapping in a Reissner-Mindlin shell element and its first column are defined as in Eq. (A.1) and (A.2). Eq. (A.2) can be subsequently used to derive expressions for second and third column in a similar manner.

$$[\boldsymbol{J}] = \begin{bmatrix} x_{,\xi} & y_{,\xi} & z_{,\xi} \\ x_{,\eta} & y_{,\eta} & z_{,\eta} \\ x_{,\zeta} & y_{,\zeta} & z_{,\zeta} \end{bmatrix} \tag{A.1}$$

where,

$$\begin{bmatrix} x_{,\xi} \\ x_{,\eta} \\ x_{,\zeta} \end{bmatrix} = \begin{bmatrix} \sum N_{i,\xi} \left(x_i + \dfrac{\zeta t_i l_{3i}}{2} \right) \\ \sum N_{i,\eta} \left(x_i + \dfrac{\zeta t_i l_{3i}}{2} \right) \\ \sum N_i \left(\dfrac{t_i l_{3i}}{2} \right) \end{bmatrix} \tag{A.2}$$

where, $\mathbf{x} = [x, y, z]$ is the position vector of any arbitrary point within the shell element, $\{\xi, \eta, \zeta\}$ are the shell parametric coordinates, t_i is the shell thickness and $\{l_{3i}, m_{3i}, n_{3i}\}$ are the direction cosines of normal vector V_{3i} to the shell mid-surface at any node i. Here, N_i are the two-dimensional shape-functions

as shown in Eq. (A.3).

$$\begin{aligned} N_i &= \frac{1}{4}(1+\xi_i\xi)(1+\eta_i\eta) \quad , i \in \{1,2,3,4\} \\ \xi_i &= [-1,+1,+1,-1] \\ \eta_i &= [-1,-1,+1,+1] \end{aligned} \tag{A.3}$$

A.2 Coordinate-transformation matrix for rotation of strain tensors

The strains can be rotated from one coordinate system (say C_1 with normalized basis vectors $\vec{e}$) to another coordinate system (C_2 with normalized basis vectors $\hat{e}$) by multiplying them with the strain-transformation matrix $\mathcal{T}_\varepsilon$ shown in eq. (A.4).

$$\mathcal{T}_\varepsilon = \begin{bmatrix} \mathcal{T}_{11} & \mathcal{T}_{12} \\ \mathcal{T}_{21} & \mathcal{T}_{22} \end{bmatrix} \tag{A.4}$$

with,

$$\mathcal{T}_{11} = \begin{bmatrix} l_1^2 & m_1^2 & n_1^2 \\ l_2^2 & m_2^2 & n_2^2 \\ l_3^2 & m_3^2 & n_3^2 \end{bmatrix} \tag{A.5}$$

$$\mathcal{T}_{12} = \begin{bmatrix} l_1m_1 & m_1n_1 & n_1l_1 \\ l_2m_2 & m_2n_2 & n_2l_2 \\ l_3m_3 & m_3n_3 & n_3l_3 \end{bmatrix} \tag{A.6}$$

$$\mathcal{T}_{21} = \begin{bmatrix} 2l_1l_2 & 2m_1m_2 & 2n_1n_2 \\ 2l_2l_3 & 2m_2m_3 & 2n_2n_3 \\ 2l_3l_1 & 2m_3m_1 & 2n_3n_1 \end{bmatrix} \tag{A.7}$$

$$\mathcal{T}_{22} = \begin{bmatrix} l_1m_2+l_2m_1 & m_1n_2+m_2n_1 & n_1l_2+n_2l_1 \\ l_2m_3+l_3m_2 & m_2n_3+m_3n_2 & n_2l_3+n_3l_2 \\ l_3m_1+l_1m_3 & m_3n_1+m_1n_3 & n_3l_1+n_1l_3 \end{bmatrix} \tag{A.8}$$

where, the terms $[l_1, m_1, n_1]$, $[l_2, m_2, n_2]$ and $[l_3, m_3, n_3]$ correspond to the direction cosines of the shell nodal-vectors V_{1i}, V_{2i} and V_{3i} respectively, defined according to Eq. (A.9) [74].

$$\begin{aligned} l_1 &= \cos[\bar{e}_x, \hat{e}_x]\,;\; m_1 = \cos[\bar{e}_y, \hat{e}_x]\,;\; n_1 = \cos[\bar{e}_z, \hat{e}_x] \\ l_2 &= \cos[\bar{e}_x, \hat{e}_y]\,;\; m_2 = \cos[\bar{e}_y, \hat{e}_y]\,;\; n_2 = \cos[\bar{e}_z, \hat{e}_y] \\ l_3 &= \cos[\bar{e}_x, \hat{e}_z]\,;\; m_3 = \cos[\bar{e}_y, \hat{e}_z]\,;\; n_3 = \cos[\bar{e}_z, \hat{e}_z] \end{aligned} \tag{A.9}$$

The resulting $\mathcal{T}_\varepsilon$ is a (6×6) matrix which can be multiplied to (6×1) strain vector (expressed in Voigt notation) to transform it from coordinate system C_1 to coordinate system C_2. Similar coordinate transformations can also be applied directly to the strain-displacement matrix (B-matrix) shown in Eq. (A.13).

A.3 Strain-displacement matrix (B-matrix) for Reissner-Mindlin shell elements

The 6-strain components in Reissner-Mindlin shell elements can be expressed in terms of displacement derivatives as shown in Eq. (A.10)

$$[\varepsilon_x, \varepsilon_y, \varepsilon_z, \gamma_{xy}, \gamma_{yz}, \gamma_{zx}]^T = [\boldsymbol{H}][\boldsymbol{J}_{inv}][u_{,\xi},\, u_{,\eta},\, u_{,\zeta},\, v_{,\xi},\, ...,\, ...,\, w_{,\zeta}]^T \tag{A.10}$$

where $[\boldsymbol{H}]$ and $[\boldsymbol{J}_{inv}]$ are (6×9) and (9×9) matrices expressed as:

$$[\boldsymbol{H}] = \begin{bmatrix} 1 & 0 & 0 & 0 & 0 & 0 & 0 & 0 & 0 \\ 0 & 0 & 0 & 0 & 1 & 0 & 0 & 0 & 0 \\ 0 & 0 & 0 & 0 & 0 & 0 & 0 & 0 & 1 \\ 0 & 1 & 0 & 1 & 0 & 0 & 0 & 0 & 0 \\ 0 & 0 & 0 & 0 & 0 & 1 & 0 & 1 & 0 \\ 0 & 0 & 1 & 0 & 0 & 0 & 1 & 0 & 0 \end{bmatrix} \qquad [\boldsymbol{J}_{inv}] = \begin{bmatrix} \boldsymbol{J}^{-1} & 0 & 0 \\ 0 & \boldsymbol{J}^{-1} & 0 \\ 0 & 0 & \boldsymbol{J}^{-1} \end{bmatrix} \tag{A.11}$$

Here, $\boldsymbol{J}^{-1}$ is the inverse of (3×3) Jacobian matrix $[\boldsymbol{J}]$ shown in Appendix A.1, $\{u, v, w\}$ are displacement components in global $\{x, y, z\}$ coordinates, and

$\{\xi, \eta, \zeta\}$ are parametric coordinates of the shell element.

The displacement derivative vector in Eq. (A.10) can be evaluated based on shell local degrees of freedom $[u_i, v_i, w_i, \alpha_i, \beta_i, \gamma_i]$ as in Eq. (A.12).

$$\begin{bmatrix} u_{,\xi} \\ u_{,\eta} \\ u_{,\zeta} \\ v_{,\xi} \\ . \\ . \\ w_{,\zeta} \end{bmatrix} = \sum_i \begin{bmatrix} N_{i,\xi} & 0 & 0 & -\zeta t_i N_{i,\xi} l_{2i}/2 & \zeta t_i N_{i,\xi} l_{1i}/2 & 0 \\ N_{i,\eta} & 0 & 0 & -\zeta t_i N_{i,\eta} l_{2i}/2 & \zeta t_i N_{i,\eta} l_{1i}/2 & 0 \\ 0 & 0 & 0 & -t_i N_i l_{2i}/2 & t_i N_i l_{1i}/2 & 0 \\ 0 & N_{i,\xi} & 0 & -\zeta t_i N_{i,\xi} m_{2i}/2 & \zeta t_i N_{i,\xi} m_{1i}/2 & 0 \\ . & . & . & . & . & . \\ . & . & . & . & . & . \\ 0 & 0 & 0 & -t_i N_i n_{2i}/2 & t_i N_i n_{1i}/2 & 0 \end{bmatrix} \begin{bmatrix} u_i \\ v_i \\ w_i \\ \alpha_i \\ \beta_i \\ \gamma_i \end{bmatrix} \tag{A.12}$$

where i is the node number, N_i is the shape-function corresponding to node i, t_i is the shell thickness, and $\{l_i, m_i, n_i\}$ are the direction cosines of shell-normal vectors given in Appendix A.2. Combining Eq. (A.12) and Eq. (A.10), the strain-displacement transformation matrix $[\boldsymbol{B}_i]$ can be obtained.

$$[\varepsilon_x, \varepsilon_y, \varepsilon_z, \gamma_{xy}, \gamma_{yz}, \gamma_{zx}]^T = \sum [\boldsymbol{B}_i^{\boldsymbol{u}}][u_i,\, v_i,\, w_i,\, \alpha_i,\, \beta_i,\, \gamma_i]^T \tag{A.13}$$

A.4 Treatment of 6^{th} (drilling) DOF in MITC4+ Mindlin shell elements

For shell-element nodes that are surrounded completely by co-planar elements, only 5 DOFs per node are sufficient to capture the shell kinematics and the 6^{th} (drilling) DOF can be simply removed from the list of overall DOFs. However, when the surrounding elements are not coplanar, the drilling DOF need to be accounted to avoid over-constraining and stiffening of the structure as explained in Remark 1 of Chapter 3.

In the current work, the 6^{th} drilling DOF of MITC4+ elements is formulated by explicitly introducing zero-values in the 6^{th} column of the B-matrix corresponding to shell-aligned local coordinate system [1, 2, 3]. Herein, the

zero-valued columns indicate zero-stiffness associated with the drilling DOFs. The local B-matrix in $[1,2,3]$ system can be obtained from the global B-matrix in $[x,y,z]$ system [Eq. (A.13)] using the strain transformation matrix $\mathcal{T}_\varepsilon$ shown in Eq. (A.4).

$$[\boldsymbol{B}_i^{\boldsymbol{u}}]_{123} = [\mathcal{T}_\varepsilon][\boldsymbol{B}_i^{\boldsymbol{u}}]_{xyz} \tag{A.14}$$

For a 4-noded shell element with 6-DOFs per node, the $[\boldsymbol{B}_i^{\boldsymbol{u}}]_{123}$ matrix can be modified by adding zero values in the 6^{th}, 12^{th}, 18^{th} and 24^{th} columns, resulting in the structure shown in Eq. (A.15).

$$[\boldsymbol{B}^{\boldsymbol{u}}]_{123} = \begin{bmatrix} - & - & - & - & - & 0 & - & - & - & - & - & 0 & - & - & - & - & - & 0 & - & - & - & - & - & 0 \\ - & - & - & - & - & 0 & - & - & - & - & - & 0 & - & - & - & - & - & 0 & - & - & - & - & - & 0 \\ - & - & - & - & - & 0 & - & - & - & - & - & 0 & - & - & - & - & - & 0 & - & - & - & - & - & 0 \\ - & - & - & - & - & 0 & - & - & - & - & - & 0 & - & - & - & - & - & 0 & - & - & - & - & - & 0 \\ - & - & - & - & - & 0 & - & - & - & - & - & 0 & - & - & - & - & - & 0 & - & - & - & - & - & 0 \\ - & - & - & - & - & 0 & - & - & - & - & - & 0 & - & - & - & - & - & 0 & - & - & - & - & - & 0 \end{bmatrix} \tag{A.15}$$

It is of interest to note that instead of local B-matrix, the zero-valued 6^{th} column could also be directly inserted in the shape-function derivative matrix given in Eq. (A.12).

Following this, the local element stiffness matrix $[\mathcal{K}_{loc}^{\boldsymbol{u}}]$ can be formulated in $[1,2,3]$ coordinates based on Eq. (3.53) and using the modified local $[\boldsymbol{B}_i^{\boldsymbol{u}}]_{123}$ matrix in Eq. (A.15). The $[\mathcal{K}_{loc}^{\boldsymbol{u}}]$ matrix is then transformed to global $[\mathcal{K}^{\boldsymbol{u}}]$ matrix in $[x,y,z]$ system (see Eq. (3.53)), and the global stiffness matrix is assembled from individual element matrices.

It must be highlighted that the local $[\mathcal{K}_{loc}^{\boldsymbol{u}}]$ matrix would still contain zero values in its 6^{th}, 12^{th}, 18^{th} and 24^{th} rows and columns, and hence would be singular as there is no stiffness to drilling rotational DOF in local $[1,2,3]$ system. However, when $[\mathcal{K}_{loc}^{\boldsymbol{u}}]$ is transformed and assembled into the global $[\mathcal{K}^{\boldsymbol{u}}]$ matrix, these zero-values are replaced by non-zero values and the singularity is resolved, due to the resistance offered from the coupling of element's drilling DOFs with the bending stiffness of adjacent elements.

A.5 Transformation of membrane strains in MITC4+ shell element formulations

Membrane strain components within the Reissner-Mindlin shell element $\{\varepsilon_{rr}, \varepsilon_{ss}, \varepsilon_{rs}\}$ are modified [Eq. (A.16)] based on the strain values at membrane tying points $\{A, B, C, D, E\}$ shown in Fig. 3.3b, using the MITC4+ approach proposed by Ko et al. [23]. The membrane strains at tying points $\{\varepsilon_{rr}^{m(A)}, \varepsilon_{ss}^{m(B)}, \varepsilon_{rr}^{m(C)}, \varepsilon_{ss}^{m(D)}\}$ are calculated directly using standard displacement-based interpolation Eq. (3.4).

$$
\begin{aligned}
\varepsilon_{rr} &= \frac{1}{2}(1 - 2a_A - \eta + 2a_A\eta^2)\varepsilon_{rr}^{m(A)} + a_B(-1+\eta^2)\varepsilon_{ss}^{m(B)} \\
&\quad + \frac{1}{2}(1 - 2a_C + \eta + 2a_C\eta^2)\varepsilon_{rr}^{m(C)} + a_D(-1+\eta^2)\varepsilon_{ss}^{m(D)} \\
&\quad + a_E(-1+\eta^2)\varepsilon_{rs}^{m(E)} \\
\varepsilon_{ss} &= a_A(-1+\xi^2)\varepsilon_{rr}^{m(A)} + \frac{1}{2}(1 - 2a_B + \xi + 2a_B\xi^2)\varepsilon_{ss}^{m(B)} \\
&\quad + a_C(-1+\xi^2)\varepsilon_{rr}^{m(C)} + \frac{1}{2}(1 - 2a_D - \xi + 2a_D\xi^2)\varepsilon_{ss}^{m(D)} \\
&\quad + a_E(-1+\xi^2)\varepsilon_{rs}^{m(E)} \\
\varepsilon_{rs} &= \frac{1}{4}(-\xi + 4a_A\xi\eta)\varepsilon_{rr}^{m(A)} + \frac{1}{4}(\eta + 4a_B\xi\eta)\varepsilon_{ss}^{m(B)} \\
&\quad + \frac{1}{4}(\xi + 4a_C\xi\eta)\varepsilon_{rr}^{m(C)} + \frac{1}{4}(-\eta + 4a_D\xi\eta)\varepsilon_{ss}^{m(D)} \\
&\quad + (1 + a_E\xi\eta)\varepsilon_{rs}^{m(E)}
\end{aligned}
\tag{A.16}
$$

The coefficients $\{a_A, a_B, a_C, a_D, a_E\}$ are as shown in eq. (A.17).

$$
\begin{aligned}
a_A &= \frac{c_\xi(c_\xi+1)}{2d} \;;\; a_B = \frac{c_\eta(c_\eta-1)}{2d} \;;\; a_C = \frac{c_\xi(c_\xi-1)}{2d} \\
a_D &= \frac{c_\eta(c_\eta+1)}{2d} \;;\; a_E = \frac{2c_\xi c_\eta}{d}
\end{aligned}
\tag{A.17}
$$

where the magnitudes of in-plane distortions (c_ξ, c_η) and total distortion vector (d) are obtained from [23].

A.6 Training procedure for PCE/ANN multi-scale surrogate damage models

A.6.1 PCE surrogate

The PCE surrogate model is trained using ChaosPy [478] library. For ChaosPy to use the correct orthogonal polynomials, the modified probability distribution for expanded strain (input) dataset needs to be identified. This is done by plotting a histogram for the expanded dataset $[\varepsilon_{11}, \varepsilon_{22}, \gamma_{12}]$, and fitting an appropriate PDF to it (see e.g. Fig. 5.12 and Fig. 5.14). Subsequently, the mean and variance of the fitted PDF is evaluated to define the probability distribution in ChaosPy. The complete training procedure for the PCE model is summarised below:

- First, the ChaosPy library is imported in Python.
- The distribution for $[\varepsilon_{11}, \varepsilon_{22}, \gamma_{12}]$ is defined as:
  $distr\_eps11 = chaospy.Laplace(mu = \langle mean \rangle, scale = \langle scale \rangle)$
- Subsequently, the joint probability distribution for $[\varepsilon_{11}, \varepsilon_{22}, \gamma_{12}]$ is generated using:
  $joint\_distr = chaospy.J(distr\_eps11, distr\_eps22, distr\_eps12)$
- The ChaosPy PCE model is defined using the *orth_ttr* command:
  $poly\_order = 9$
  $poly\_sig11 = chaospy.orth\_ttr(poly\_order, joint\_distr, normed = True)$
- One PCE surrogate model is trained for each of $[\sigma_{11}, \sigma_{22}, \sigma_{12}]$/ $[\sigma_{c11}, \sigma_{c22}, \sigma_{c12}]$ datasets. Each training is performed using macro-strain combination $[\varepsilon_{11}, \varepsilon_{22}, \gamma_{12}]$ as the input dataset:
  $rules = [''LHC'']$
  $fitted\_pce\_sig11 = \{rule : chaospy.fit\_regression(\ poly\_sig11, input, output)$
  $for\ rule\ in\ rules\ \}$

- Finally, the PCE coefficients and exponents are extracted and written to external text files, which are read into Abaqus UMAT subroutine later.
  $coeff\_sig11 = fitted\_pce\_sig11["LHC"].coefficients$
  $expon\_sig11 = fitted\_pce\_sig11["LHC"].exponents$

A.6.2 ANN surrogate

The ANN surrogate model is trained using MATLAB's neural net fitting toolbox $(nftool)$, see Fig. 5.11 [29]. The training procedure for ANN is as follows:

- In *nftool*, the input and output datasets are chosen as the macro-scale strains $[\varepsilon_{11}, \varepsilon_{22}, \gamma_{12}]$ obtained after dataset expansion (Fig. 5.12), and macro-scale stresses $[\sigma_{11}, \sigma_{22}, \sigma_{12}]$ respectively.
- The percentage of samples to be used for training, validation and testing datasets are set to default values (70%, 15% and 15% respectively).
- The number of neurons for $[\sigma_{11}, \sigma_{22}, \sigma_{12}]$ are set based on Table 5.1.
- The training algorithm is selected as *Bayesian Regularisation*, and the performance is monitored regularly to avoid over-training.
- Once trained, the testing performance plot is checked for any abrupt jumps. The error histogram, regression plot and R^2 fit value are assessed for sufficient accuracy.
- If the trained ANN model lacks accuracy, it is retrained and further tested with additional samples.
- The trained model is exported into a MATLAB function using $Matrix-Only\ Function$ $(genFunction)$ tool.
- Finally, the MATLAB function and ANN matrices/ constants like biases, weights, offsets and gains are translated into Abaqus UMAT subroutine.

A.7 Algorithms

Algorithm A.1 Implementation of phase field model for brittle fractures (Chapter 3) in MITC4+ Mindlin shell elements (One-pass staggered algorithm)

Data: Define computational domain Ω. Get E, ν, l_o, η, $\mathcal{G}_c$. Set initial $\boldsymbol{u}_o$ and ϕ_o to 0

for *each time-step n=1, 2, .., n_{steps}* **do**

`// Solution procedure for phase field evolution equation`

for *each element e=1, 2, .., n_{elem}* **do**

Obtain crack-driving force $\mathcal{D}_{n-1}$ at time-step t_{n-1}

for *each thickness integration point th=1, 2, .., n_{th}* **do**

for *each Gauss-point gp=1, 2, .., n_{gp}* **do**

Compute: N, $[\boldsymbol{J}]$, and $[\boldsymbol{B}_i^{\boldsymbol{u}}]$ based on A.1 and A.3.

Transform $[\boldsymbol{B}_i^{\boldsymbol{u}}]$ matrix from $[x, y, z] \rightarrow [1, 2, 3] \rightarrow [r, s, t]$ coordinate system [Eq. (3.7), (3.8) and (3.10)]

Apply MITC4+ corrections to $[\boldsymbol{B}_i^{\boldsymbol{u}}]$ matrix rows [Eq. (3.5) and A.5]

Transform $[\boldsymbol{B}_i^{\boldsymbol{u}}]$ to $[1, 2, 3]$ coordinate system [Eq. (3.8), (3.10)]

Formulate $[\boldsymbol{B}_i^{\phi}]$ matrix from specific entries of $[\boldsymbol{B}_i^{\boldsymbol{u}}]$ [Eq. (3.55)]

Calculate local to global transformation matrix $\mathcal{T}_{rot}$ [Eq. (3.14)]

Evaluate $\left[\mathcal{R}_i^{\phi}\right]$ and $\left[\mathcal{K}_i^{\phi}\right]$ for each element [Eq. (3.52), Eq. (3.54)]

Assemble global $\left[\mathcal{K}^{\phi}\right]$ and $\left[\mathcal{R}^{\phi}\right]$ for all elements. Solve $\left[\mathcal{K}^{\phi}\right]\left[\phi_n\right] = \left[\mathcal{R}^{\phi}\right]$ for ϕ_n

`// Solution procedure for linear momentum balance`

for *each element e=1, 2, .., n_{elem}* **do**

Obtain $\boldsymbol{u}_{n-1}$ and ϕ_n at t_{n-1} and t_n respectively

for *each thickness integration point th=1, 2, .., n_{th}* **do**

for *each Gauss-point gp=1, 2, .., n_{gp}* **do**

Calculate $[\boldsymbol{\varepsilon}]_{\mathbf{123}} = [\boldsymbol{B}_i^{\boldsymbol{u}}][\boldsymbol{u_{n-1}}]$. Evaluate $\boldsymbol{\varepsilon}'_{\pm}$ / $\boldsymbol{\varepsilon}_{\pm}$ [Eq. (3.21), (3.23), (3.24)]

Calculate σ^{IP}/σ^{OP} and $\sigma_{\pm}^{IP}/\sigma_{\pm}^{OP}$ [Eq. (3.27), (3.30)]

Calculate ψ_e^{IP}/ψ_e^{OP}, $\psi_{\pm}^{IP}/\psi_{\pm}^{OP}$ and $\psi_{\pm}$ [Eq. (3.26), (3.29), (3.32)]

Calculate $\boldsymbol{\mathcal{D}'}_n$ and $\boldsymbol{\mathcal{D}}_n$ based on Eq. (3.45), (3.46) and Fig. 3.6

Evaluate $\left[\mathcal{R}_i^{\boldsymbol{u}}\right]$ and $\left[\mathcal{K}_i^{\boldsymbol{u}}\right]$ for each element [Eq. (3.51) and (3.53)]

Assemble global $[\mathcal{K}^{\boldsymbol{u}}]$ and $[\mathcal{R}^{\boldsymbol{u}}]$ for all elements. Solve $[\mathcal{K}^{\boldsymbol{u}}]\,[\boldsymbol{u}_n] = [\mathcal{R}^{\boldsymbol{u}}]$ for $\boldsymbol{u}_n$

Store $\boldsymbol{u}_n$ and $\boldsymbol{\mathcal{D}}_n$ to be used in next time-step t_{n+1}

Algorithm A.2 Abaqus UMAT implementation of anisotropic cohesive phase field model (Chapter 4) for composites (staggered approach for $t_{n-1} \rightarrow t_n$)

Data: Define computational domain Ω. Get E_{11}, E_{22}, G_{12}, ν_{12}, σ_{ci}, $\mathcal{G}_{ci}$, S_{LP}, ζ_E, ζ_E^T, ζ_L, l_o, p_i, q_i [$i \in \{11, 22, 12\}$]. Set initial ϕ_o to 0

`// Abaqus UEXTERNALDB subroutine`

Get Lagrange parameter λ_{n-1}, phase field ϕ_{n-1} and crack driving force $\tilde{\mathcal{D}}_{n-1}$

Get n_{11}/n_{22} within the ply and calculate $\mathcal{A}$ [Eq. (4.13)]

Set $k = 0$, $\lambda_k = \lambda_{n-1}$ and $\phi_k = \phi_{n-1}$

Import mesh and section data from Abaqus input file into UEXTERNALDB

do

`// Solution procedure for phase field evolution equation`

Set $\phi_{k-1} = \phi_k$; $\lambda_k \leftarrow (\langle \lambda_k + \gamma(\phi_{n-1} - \phi_k) \rangle_+ + \langle \lambda_k + \gamma(1 - \phi_k) \rangle_-)$ [Fig. 4.8]

for *each element e=1, 2, .., n_{elem}* **do**

for *each thickness integration point th=1, 2, .., n_{th}* **do**

for *each Gauss-point gp=1, 2, .., n_{gp}* **do**

Transform shell coordinates from $[x, y, z]$ to $[1, 2, 3]$ using $\mathcal{T}_{rot}$ [Eq. (3.14)]

Compute: N, $[\boldsymbol{J}]$, and $[\boldsymbol{B}_i^{\phi}]$ matrix based on A.1 and Eq. (3.55)

Evaluate $\left[\mathcal{R}_i^{\phi}\right]$ and $\left[\mathcal{K}_i^{\phi}\right]$ using λ_k, ϕ_{k-1} for each element [Eq. (4.56)]

Assemble global $\left[\mathcal{K}^{\phi}\right]$ and $\left[\mathcal{R}^{\phi}\right]$ from individual element matrices

Solve $\left[\mathcal{K}^{\phi}\right]$ $[\phi_k]$ = $\left[\mathcal{R}^{\phi}\right]$ for ϕ_k using external MKL PARDISO solver

Perform Newton-Raphson interations until $\mathcal{R}^{\phi} \rightarrow 0$. Set $k \rightarrow k + 1$

while $\|\phi_k - \phi_{k-1}\| \ll \mathcal{R}_{\gamma}$;

Set $\phi_n = \phi_k$, and store ϕ_n in an external Fortran module

`// Abaqus UMAT subroutine to solve linear momentum balance`

for *each call to Abaqus UMAT* **do**

Calculate $\varepsilon_{12}^e/\varepsilon_{12}^p$ [Eq. (4.49), (4.51)]. Obtain $\varepsilon^{\pm}$ [Eq. (4.19), (4.20)]

Calculate $\bar{\sigma}^{\pm}$ [Eq. (4.24), (4.25)]

Calculate $\psi_i^{\pm}$ components [Eq. (4.26), (4.50)]

Calculate anisotropic $g_i(\phi)$ components [Eq. (4.29)-(4.31)]

Calculate anisotropic $\tilde{\mathcal{D}}_i$ components [Eq. (4.41)-(4.43)]

Obtain degraded σ based on Eq. (4.59). Set this as *stress* variable in UMAT

Obtain material stiffness (*ddsdde*) with numerical tangent approach [Eq. (5.11)]

Store ϕ_n, $\tilde{\mathcal{D}}_i$, ε_{12}^p as *STATEV* in Abaqus

Solve linear momentum balance with Abaqus (Standard) for displacements $\boldsymbol{u}_n$

Algorithm A.3 Implementation of multi-scale surrogate modelling approach (Chapter 5). Each sub-step must be automated using Abaqus Python scripting.

`// Meso-scale simulations`

Generate meso-scale RVE model with periodic mesh in Abaqus

Apply PBC for each node-pair on opposite edges/faces [Sec. 5.3.1]

Perform meso-scale damage simulations for pure tensile $\{11, 22\}$ and shear $\{12\}$ loading modes (Fig. 5.5/ 5.8) using anisotropic cohesive PFM in A.2

Estimate max limits for applied $\{\varepsilon_{11m}, \varepsilon_{22m}, \gamma_{12m}\}$ that cause full/significant damage evolution in $\{11, 22, 12\}$ modes

Generate n macro-strain combinations between $\{-\varepsilon_{11m}, -\varepsilon_{22m}, -\gamma_{12m}\}$ and $\{\varepsilon_{11m}, \varepsilon_{22m}, \gamma_{12m}\}$ using LHC [Fig. 5.3]

for *each of n macro-strain combination* **do**

- Apply $[\varepsilon_{11}, \varepsilon_{22}, \gamma_{12}]$ on the RVE boundary with PBC [Sec. 5.3.1 and Fig. 5.5]
- Perform meso-scale damage simulations on RVE using PFM
- Evaluate homogenised stresses/ strains within RVE [Sec. 5.2 and Eq. (5.2)]
- Extract final stresses $[\sigma_{11}, \sigma_{22}, \sigma_{12}]$ and critical stresses $[\sigma_{c11}, \sigma_{c22}, \sigma_{c12}]$ from the homogenised stress-strain response [Fig. 5.12]
- Create RVE database with $[\varepsilon_{11}, \varepsilon_{22}, \gamma_{12}]$ as input, and $[\sigma_{11}, \sigma_{22}, \sigma_{12}]/[\sigma_{c11}, \sigma_{c22}, \sigma_{c12}]$ as output datasets [Fig. 5.7]

Train PCE and ANN based surrogate models with the RVE database, using ChaosPy and MATLAB's nftool respectively (see A.6)

`// Macro-scale simulations`

For trained PCE surrogate model, extract the coefficients and exponents [Sec. 5.4.1]

For trained ANN surrogate model, extract the weights, biases, and other constants like offsets and gains [Sec. 5.4.2]

Translate the trained PCE/ANN model into a new Abaqus UMAT subroutine

Read the matrices/vectors/constants extracted above into this UMAT

Set-up macro-scale model with macro-element size chosen based on Sec. 5.5

for *each call to Abaqus UMAT at Gauss-points within macro-scale element* **do**

- Obtain $[\varepsilon_{11}, \varepsilon_{22}, \gamma_{12}]$ supplied by Abaqus into UMAT
- **for** *PCE surrogate only* **do**
  - Evaluate critical $[\sigma_{c11}, \sigma_{c22}, \sigma_{c12}]$ using trained PCE model
  - Perform pure elastic/elastic-plastic analysis until $[\sigma_{c11}, \sigma_{c22}, \sigma_{c12}]$ crosses convex hull surface. Activate PCE model henceforth
- Evaluate degraded $[\sigma_{11}, \sigma_{22}, \sigma_{12}]$ using trained PCE/ANN surrogate model
- Evaluate material stiffness (*ddsdde*) using numerical tangent approach [Eq. (5.11)]
- Return *stress* $[\sigma_{11}, \sigma_{22}, \sigma_{12}]$ and *ddsdde* back to Abaqus

Solve linear momentum balance with Abaqus (Standard) for displacements $\boldsymbol{u}_n$